DESIGN AND PROPERTIES OF SELF-COMPACTING CONCRETE MIXES AND THEIR SIMULATION IN THE J-RING TEST

by

Mohammed Shamil Mohammed Abo Dhaheer

B.Sc., M.Sc.

Thesis submitted in candidature for the degree of Doctor of Philosophy at Cardiff University

School of Engineering

Cardiff University

United Kingdom

November 2016

In the Name of God.

The Most Compassionate and the Most Merciful

DECLARATION AND STATEMENTS

DECLARATION

This work has not previously been accepted in substance for any degree and is not concurrently submitted in candidature for any degree.

Signed ………………………………… (Mohammed Abo Dhaheer) Date …………………………

STATEMENT 1

This thesis is being submitted in partial fulfilment of the requirements for the degree of Doctor of Philosophy.

Signed ………………………………… (Mohammed Abo Dhaheer) Date …………………………

STATEMENT 2

This thesis is the result of my own independent work/investigations, except where otherwise stated. Other sources are acknowledged by explicit references.

Signed ………………………………… (Mohammed Abo Dhaheer) Date …………………………

STATEMENT 3

I hereby give consent for my thesis, if accepted, to be made available for photocopying and for inter-library loan, and for the title and summary to be made available to outside organisations.

Signed ………………………………… (Mohammed Abo Dhaheer) Date …………………………

ACKNOWLEDGEMENT

SYNOPSIS

Although self-compacting concrete (SCC) has matured beyond laboratory studies and has now become an industrial product, its characteristics behaviour and performance, in the fresh and hardened states alike, still need to be thoroughly comprehended. This thesis presents the results of a study on behaviour of SCC in the fresh and hardened states. The work was divided into three main parts of research. In the first part, the focus was to develop a simple and rational method for designing SCC mixes based on the desired target plastic viscosity and compressive strength of the mix. The expression for the plastic viscosity of an SCC mix developed using the so-called micromechanical principles has been exploited to develop this rational method. The simplicity and usefulness of this method was enhanced by the provision of design charts for choosing the mix proportions that achieve the mix target plastic viscosity and compressive strength. Experimental work was performed attesting the validity of this mix design procedure via a series of SCC mixes in both the fresh and hardened states. The test mixes were found to meet the necessary self-compacting and the compressive strength criteria, thus fully validating the proposed mix proportioning method. Therefore, this method reduces considerably the extent of laboratory work, the testing time and the materials used.

The second part addressed the other important properties of hardened SCC: specific fracture energy (G_F), direct tensile strength (f_{ct}), critical crack opening (w_c), characteristic length (l_{ch}), which are no less important than the compressive strength. Combined work with two other PhD candidates (in Cardiff University) has been carried out in order to get a much clearer picture by investigating in detail the role of several parameters - coarse aggregate volume, paste volume and strength grade - of SCC mixes in their G_F, f_{ct}, w_c and l_{ch}. Also addressed in this part is the corresponding bilinear approximation of the tension softening diagram using a procedure based on the non-linear hinge model. It is found that all the mentioned properties are dominated by the coarse aggregate volume (or, conversely the paste volume) in the mix and the mix grade.

The third part of this thesis is dedicated to simulating the flow of SCC through gaps in reinforcing bars using the J-ring test. This has been performed by implementing an incompressible mesh-less smooth particle hydrodynamics (SPH) methodology. A suitable Bingham-type constitutive model has been coupled with the Lagrangian momentum and continuity equations to simulate the flow. The capabilities of SPH methodology were validated by comparing the experimental and simulation results of different SCC mixes. The comparison showed that the simulations were in very good agreement with experimental results for all the test mixes. The free surface profiles around the J-ring bars, the spread at 500 mm diameter and the final flow pattern are all captured accurately by SPH. In term of segregation assessment, it is revealed that SPH allows the distribution of large aggregates in the mixes to be examined in order to ensure that they have not segregated from the mortar. The SPH simulation methodology can therefore replace the time-consuming laboratory J-ring test, thereby saving time, effort and materials.

TABLE OF CONTENTS

Chapter 1

Introduction

1.1 Introduction

This chapter highlights the scope of the research, presents the research objectives and methodology, outlines the structure of the thesis and presents the research output.

1.2 Scope of the research

"Necessity is the mother of invention". Increasing population and modern cities require new aspirant structural design ideas and increase the demands on reinforced concrete structures. The shapes and sections of elements have become more complex and their reinforcement becomes denser and clustered, which have raised problems of casting, compacting and filling of concrete elements. With increasing complexity, the durability problem of concrete structures has become a major issue of interest facing engineers for many years. Achieving durable concrete structures requires adequate compaction by skilled labour. During the eighties of the last century, the shortage in skilled site operatives and its consequential shortage in the quality of construction was a serious issue in Japan (Okamura and Ouchi, 2003). Consequently, the necessity for a revolutionary innovation in concrete construction has arisen from the perspectives of concrete quality assurance and improvement of working conditions. For this reason, a Japanese researcher (Okamura) in 1986 successfully pioneered what is popularly known today as "self-compacting concrete" (SCC).

Since its early use in Japan, SCC has now started to be an alternative to vibrated concrete (VC) across the world as its ability to rationalise the construction systems by offering several economic and technical advantages over VC (Omran and Khayat, 2016). These involve: overcoming problems associated with cast-in-situ concrete, ensuring a good structural performance and robustness, shortening construction time, providing a safe and healthy working environment by minimizing job-site equipment and noise levels.

Self-compacting concrete is a liquid particle suspension that can compact itself solely by means of its own weight without the need for vibration effort, and fill the gaps in highly congested reinforcement and geometrically complicated structural members without any

segregation and bleeding (EFNARC, 2005). In other words, it can fulfil the following main functional requirements: filling ability, passing ability and segregation resistance. To achieve such requirements, major work should take into account designing appropriate volume fractions of the mix ingredients. Although SCC has passed from the research phase into actual application, until recently no unique mix design method has widely been followed for proportioning SCC mixes, but rather different methods have been adopted based on a trial and error using time and materials-consuming laboratory tests. The latter would be significantly reduced if practical guidelines on how to select the most appropriate volume fractions of mix constituents were introduced in designing SCC.

The volume fractions of the mix constituents, i.e. cement, cement replacement materials, aggregates, water and admixtures have a significant effect on the rheology of SCC, which in turn affects its hardened state. Since the SCC main characteristic is flow-ability, its fresh property cannot be thoroughly comprehended without understanding its rheology. The quality control and accurate prediction of the SCC rheology is a crucial parameter for the success of its production.

The quality control and accurate prediction of the SCC flowing behaviour is not a simple task, particularly in the presence of heavy reinforcement, complex shapes and large size of aggregate. In this regard, an indispensable and inexpensive approach offering considerable potential is by performing numerical simulation. This approach will deepen the understanding of the SCC mix flow behaviour and evaluate its ability to meet the necessary self-compacting criteria while maintaining adequate suspension and distribution of coarse particles in the matrix.

Apart from its fresh state, the properties of SCC in its hardened state cannot be overlooked for its successful proportioning and production. Although the literature is rich in reporting on SCC, much of the research has primarily focused on the fresh properties, rather than hardened properties, to produce an SCC mix that possesses the features of being self-compacting. From an engineering point of view, strength remains the most important property of hardened concrete as it plays an essential part in its successful development and gives an indication of its overall quality (Neville, 1995). Thus, to

simultaneously achieve the adequate fresh and hardened properties of an SCC mix, the reliable approach is one which pays implicit attention to its strength along with its rheological properties, i.e., strength together with rheological properties need to be imposed as design criteria to successfully produce SCC.

Another important property of hardened SCC, which is no less important than strength, is its fracture behaviour. An energy based failure theory is needed for this that could be used in designing cement-based structures since it studies the response and failure of structures as a consequence of crack initiation and propagation (Karihaloo, 1995). The most important parameters describing the fracture behaviour of a concrete mix are its specific fracture energy and the tension softening diagram. They form a basis for the assessment of the load carrying capacity of cracked concrete structures (Karihaloo, 1995; Bazant and Planas, 1997). Given the fact that SCC requires relatively large amounts of fine material and paste but low coarse aggregate content, to control its fundamental parameters (yield stress and plastic viscosity), its fracture behaviour becomes an issue and raises concerns among researchers that need to be borne in mind and fully addressed.

1.3   Research objectives

The main objectives of this thesis are:

❖ **firstly**, to develop a simple and rational method for designing SCC mixes based on the desired target plastic viscosity and compressive strength of the mix. The simplicity and usefulness of this method will be enhanced by the provision of design charts for choosing the mix proportions that achieve the mix target plastic viscosity and compressive strength.

❖ **secondly**, to provide an experimental validation of the proposed mix design method and to investigate whether the produced SCC mixes meet the necessary self-compacting criteria in both the fresh and hardened states.

❖ **thirdly**, to examine in detail the role of several compositional parameters - coarse aggregate volume, paste to solid volume ratio and strength grade - of SCC mixes in their size-independent fracture energy (G_F) and the corresponding bilinear approximation of the tension softening diagram (TSD).

❖ **fourthly**, to simulate the non-Newtonian viscous SCC mixes in a standard test configuration (J-ring test) using the three-dimensional mesh-less smooth particle hydrodynamic methodology (SPH). This methodology aims to provide a thorough understanding of whether or not an SCC mix can satisfy the self-compactibility criterion of passing ability through narrow gaps in reinforcement besides the flow-ability criterion.

❖ **fifthly**, to monitor the distribution of coarse aggregate particles in the mixes during the simulation in order to check whether or not they are homogeneously distributed after the flow has stopped.

1.4   Research methodology

The above objectives are achieved as follows:

❖ **firstly**, the expression for the plastic viscosity of an SCC mix developed using micromechanical principles (Ghanbari and Karihaloo, 2009) will be exploited to develop the method for proportioning SCC mixes. To aid the user in making an informed choice of mix constituents, a software program will be developed from which the design charts are constructed. A regression analysis is performed on the data collected from many published sources to construct a reliable formula between water to cementitious material (w/cm) and compressive strength.

❖ **secondly**, the validity of the proposed mix design method will be proved by preparing a series of SCC mixes differing in target plastic viscosity and compressive strength. All these mixes will be extensively tested in the fresh state using the slump cone, J–ring, L–box and V–funnel apparatus and in the hardened state using compressive strength test.

❖ **thirdly**, the fracture behaviour of SCC will be experimentally studied on a series of mixes differing in the coarse aggregate volume, paste volume and strength grade. The size-dependent fracture energy (G_f) will be measured using the RILEM work-of-fracture test on three point bend specimens containing shallow and deep starter notches. Then the size-independent fracture energy (G_F) will be calculated using the simplified boundary effect approach (SBE). Finally, the corresponding bilinear approximation of the tension softening diagram will be obtained using a procedure based on the non-linear hinge model.

❖ **fourthly**, the smooth particle hydrodynamics (SPH) approach will be used for simulating the flow of SCC in J-ring test. SCC is regarded as a non-Newtonian incompressible fluid whose behaviour is described by a Bingham-type model, which contains two material properties: the yield stress and the plastic viscosity. For the investigated mixes, the former is predicted in an inverse manner using the SPH simulation and the latter is estimated by a micromechanical procedure from the known plastic viscosity of the paste and the SCC mix proportions. The results of the numerical simulation will be benchmarked against actual J-ring tests carried out in the laboratory to examine the efficiency of the proposed methodology (SPH) to predict accurately the flow behaviour of SCC.

❖ **fifthly**, the distribution of coarse aggregate in the SCC mix will be simulated and evaluated along two diametrical planes, in four quadrants and in three concentric circular regions. The statistics of the coarse aggregate distribution in all cut regions should be nearly the same to confirm that the flow was homogeneous.

1.5   Outline of the thesis

This thesis is organised into eight chapters, followed by bibliographical references and appendices. The contents of each chapter can be summarised as follows:

Chapter 1 highlights the scope of the research, presents the research objectives and methodology, outlines the structure of the thesis and presents the research output.

Chapter 2 reviews the properties of SCC, approaches to its achievement, materials used in its production and their influence on its characteristics in the fresh and hardened states, proportioning of its constituents and standard tests employed for its assessment. Also presented in this chapter is a brief review of the mechanical properties of SCC.

Chapter 3 provides a concise review of the rheology of SCC and the methods of simulating its flow. It also highlights the three-dimensional Lagrangian form of the governing equations used to model the flow of SCC, which are the mass and momentum conservation equations. A brief overview of smooth particle hydrodynamic (SPH) approach is also presented in this chapter.

Chapter 4 describes the systematic steps taken to develop the SCC mix design method based on the micromechanical procedure. Here, it is worth mentioning that the micromechanical procedure has enriched this research work far beyond the scope of its original intended use for the determination of SCC mix plastic viscosity; it forms the backbone of this rational mix design method. This method has then been enhanced by the provision of design charts as a guide for proportioning SCC mixes. Several examples on the use of these charts to proportion mixes with different target plastic viscosity and compressive strength are given in this chapter.

Chapter 5 is dedicated to the experimental work attesting the validity of the mix design procedure via a series of SCC mixes in both the fresh and hardened states. To these mixes, standard tests employed for SCC have been extensively applied.

Chapter 6 presents the results of a combined experimental study on the fracture behaviour of SCC mixes. This combined work has been carried out with two other PhD students in order to get a much more clear picture by investigating in detail the role of several parameters - coarse aggregate volume, paste volume and strength grade - of SCC mixes in their specific fracture energy (G_F). Also given in this chapter is the corresponding bilinear approximation of the tension softening diagram using a procedure based on the non-linear hinge model.

Chapter 7 describes the three-dimensional SPH method used to simulate all the developed SCC mixes in the J-ring test. The results of the numerical simulation are compared with experimental tests carried out in the laboratory to validate the efficiency of the proposed methodology (SPH) to predict precisely the behaviour of SCC. The distribution of coarse aggregate in the mix is also evaluated and given in this chapter.

Chapter 8 summarises the conclusions from this research work along with recommendations for further study.

1.6   Thesis output

The work described in this thesis has been published in different Journals and conferences. For easy reference, the publications are listed below.

[1] **Abo Dhaheer, M.S.**, Kulasegaram, S. and Karihaloo, B.L. 2016. Simulation of self-compacting concrete flow in the J-ring test using smoothed particle hydrodynamics (SPH). Cement and Concrete Research, 89, pp. 27-34.

[2] **Abo Dhaheer, M.S.**, Al-Rubaye, M.M., Alyhya, W.S., Karihaloo, B.L. and Kulasegaram, S. 2016. Proportioning of self-compacting concrete mixes based on target plastic viscosity and compressive strength: mix design procedure. Journal of Sustainable Cement-Based Materials, 5(4), pp. 199–216.

[3] **Abo Dhaheer, M.S.**, Al-Rubaye, M.M., Alyhya, W.S., Karihaloo, B.L. and Kulasegaram, S. 2016. Proportioning of self-compacting concrete mixes based on target plastic viscosity and compressive strength: experimental validation. Journal of Sustainable Cement-Based Materials, 5(4), pp. 217–232.

[4] **Abo Dhaheer, M.S.**, Karihaloo, B.L. and Kulasegaram, S. 2016. Simulation of self-compacting concrete flow in J-ring test using smoothed particle hydrodynamics. In: Proceedings of the 24th UK Conference of the Association for Computational Mechanics in Engineering, ACME, Cardiff, UK.

[5]   Alyhya, W.S., **Abo Dhaheer, M.S.**, Al-Rubaye M.M., Karihaloo, B.L. and Kulasegaram, S. 2016. A rational method for the design of self-compacting concrete mixes. In: 8th International RILEM Symposium on Self-Compacting Concrete, Washington DC, USA, pp. 85–94.

[6]   Alyhya, W.S., **Abo Dhaheer, M.S.**, Al-Rubaye, M.M. and Karihaloo, B.L. 2016. Influence of mix composition and strength on the fracture properties of self-compacting concrete. Construction and Building Materials, 110, pp. 312–322.

[7]   Alyhya, W.S., **Abo Dhaheer, M.S.**, Al-Rubaye, M.M., Karihaloo, B.L. and Kulasegaram, S. 2015. A rational method for the design of self-compacting concrete mixes based on target plastic viscosity and compressive strength. In: 35th Cement and Concrete Science Conference, CCSC35, Aberdeen, UK.

[8]   Al-Rubaye, M.M., Alyhya, W.S., **Abo Dhaheer, M.S.** and Karihaloo, B.L. 2016. Influence of composition variations on the fracture behaviour of self-compacting concrete. In: 21st European Conference on Fracture, ECF21, Catania, Italy.

Chapter 2

Self-compacting concrete (SCC)

2.1   Introduction

The key reason why concrete is considered a successful structural material, which has steadily gained popularity since its inception, is that it can be molded into any desired structure with the advantages of strength, durability, fire resistance, cost-effectiveness and on-site manufacturing. Nevertheless, concrete that is cast and compacted under conditions far from ideal could be prone to flaws such as air voids, honeycombs, lenses of bleed water and aggregate segregation (Patzák and Bittnar, 2009). These flaws can be a serious problem in a concrete structure affecting its durability and integrity, irrespective of the mix strength. The aforementioned shortcomings, especially in structures with congested reinforcement and restricted areas, can be overcome by the use of self-compacting concrete (SCC) (Desnerck et al., 2014). This chapter reviews the properties of SCC, approaches to its achievement, materials used in its production and their influence on its characteristics in the fresh and hardened states, proportioning of its constituents and standard tests employed for its assessment. Also presented in this chapter is a brief review of the mechanical properties of SCC.

2.2   Definition of SCC

Self-compacting concrete (SCC) is a super workable concrete that can compact itself only by means of its own weight, achieve impressive deformability in its fresh state, fill every corner, even with restricted areas and geometrically complex shapes, and form a compact, uniform and void-free mass, while maintaining homogeneity; no vibration is required and no segregation or bleeding occurs (Desnerck et al., 2014; BS EN 206-9, 2010).

SCC has three fundamental requirements: (1) filling ability which is the characteristic of SCC to flow under its own weight and to completely fill the formwork; (2) passing ability which is the characteristic of SCC to flow through and around obstacles such as reinforcement and narrow openings without blocking, and (3) segregation resistance which is the characteristic of SCC to remain homogeneous during and after transporting and placing (BS EN 206-9, 2010; Khayat, 1999).

2.3   Development of SCC

The development of SCC can be divided into two periods: its initial development in Japan in the mid-1980s and its subsequent spreading into Europe in the late-1990s. In Japan, the first practical prototype of SCC was produced by 1988, and the first research publications that looked into the principles required for SCC were around 1989 to 1991 (Goodier, 2003). After these developments, Japan has undergone intensive research in many places, particularly within the research institutes of large construction companies, and accordingly, SCC has been used in its many practical applications. The successful interest and use of SCC in Japan has drawn the attention of many European countries. The first country in Europe to begin development of SCC was Sweden, from which the technology spread then to other Scandinavian countries at the end of the 1990s (Goodier, 2003).

Since SCC has gained widespread acceptance in different structural applications, extensive research work on SCC has been dedicated by different research institutes. To extract the benefits from its intended use, SCC has to be successfully integrated into the whole design and construction processes from the viewpoint of making it a standard concrete. As a result, guidelines and specifications for SCC have been proposed by individual institutions with the objectives of mix proportions, material requirements and test methods necessary to produce and test SCC (EFNARC, 2002; EFNARC, 2005; BS EN 206-9, 2010). Simultaneously with the development of its guidelines and specifications, different parts of the world have embraced SCC and a lot of amazing structures have been built with this concrete. Examples of structures made with SCC could be found in (Deeb, 2013; Pamnani, 2014; Badry, 2015).

2.4   Advantages and limitations of SCC

2.4.1   Advantages of SCC

SCC has many advantages over VC. These advantages are as follows (Khayat, 1999; EFNARC, 2005; Okamura and Ouchi, 2003).

➢ Eliminating the need for vibration as it flows through and around obstacles (e.g. reinforcing steel) under self-weight;

➢ Allowing for the placement of a large amount of reinforcement in small sections, especially in high-rise buildings;

➢ Improving work environment and safety as it requires fewer workers for transport and placement of concrete;

➢ Reducing the noise pollution and improving the construction environment in the absence of concrete vibrating equipment;

➢ Decreasing the construction time and labour cost;

➢ Ensuring a uniform architectural surface finish (appearance of concrete) with little to no remedial surface work;

➢ Decreasing the permeability and thus, improving strength and durability of concrete.

2.4.2   Limitations of SCC

The possible limitations of using SCC compared with VC are its material costs: it will be higher than that of VC. However, the reduction of costs caused by better productivity, shorter construction time and improved working conditions will compensate the higher material costs and, in many cases, may result in more favourable prices of the final product. Therefore, when casting in highly congested areas, SCC is more productive, efficient, and has better constructability than VC.

Another limitation can be related to the nature of SCC: because of its high fluidity, handling and transporting SCC becomes a bit delicate, although the outstanding results would overcome these limitations.

2.5   Functional requirements of SCC

In order to be classified as an SCC, the concrete must have the characteristics of filling ability, passing ability and segregation resistance (Figure 2.1). All these characteristics

should remain throughout the entire construction process (mixing, transporting, handling, placing and casting).
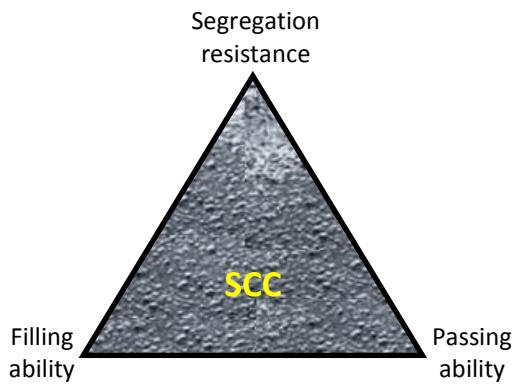
Figure 2.1: Functional requirements of SCC

2.5.1   Filling ability

Filling ability describes the ability of concrete to flow under its own weight and completely fill formwork. To achieve the filling ability, the friction between SCC solid particles (coarse and fine aggregates) has to be reduced. This can be achieved by adding more water or super-plasticiser. The former could decrease the particle friction and improve filling ability on the one hand, but on the other hand it leads to segregation in addition to its consequential reduction in strength and durability. The latter, unlike water addition, decreases the particle friction by dispersing cement particles and maintains the deformability and homogeneity of SCC mix.

In order to obtain a better filling ability in SCC, enough paste must be provided to cover the surface area of the aggregates, and that the excess paste serves to minimize the friction among the aggregates. Without the paste layer, too much friction would be generated between the aggregates resulting in extremely limited workability. Figure 2.2 shows the formation of cement paste layers around aggregates.
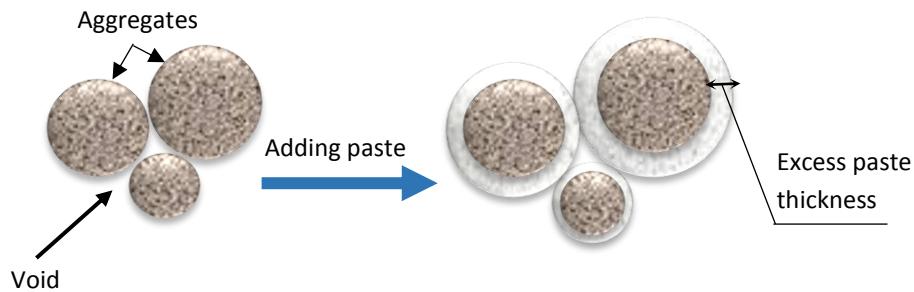
Figure 2.2: Excess paste layer around aggregates (After: Deeb, 2013)

2.5.2   Passing ability

Passing ability refers to the ability of SCC mix to pass through densely reinforced structures and narrow spaces, while maintaining good suspension of coarse particles in the matrix without blocking. The passing ability is related to different parameters. Increasing paste volume and limiting the size and coarse aggregate content, whose energy consumption is high, can effectively increase the passing ability and reduce the risk of blockage. The latter could be attributed to the interaction among aggregate particles and between the aggregate particles and reinforcement; when concrete approaches a narrow space, the different flowing velocities of the mortar and coarse aggregate result in a locally increased content of coarse aggregate (Roussel et al., 2009; Noguchi et al., 1999). Some aggregates may bridge or arch at small openings which block the rest of the concrete, as shown in Figure 2.3.
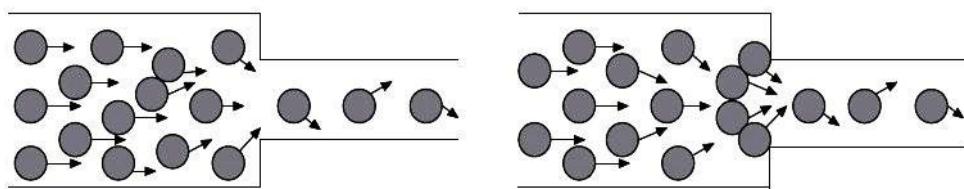
Figure 2.3: Schematic of blocking, aggregates may bridge or arch at small openings which block the rest of the concrete (After: RILEM TC 174 SCC, 2000)

Also related to the SCC passing ability is paste viscosity: highly viscous paste prevents localised increases in internal stress due to the approach of coarse aggregate particles (Okamura and Ouchi, 2003) and therefore increases the passing ability of SCC.

2.5.3   Segregation resistance

Segregation resistance or stability is the concrete's ability to keep the coarse aggregate evenly distributed during flow as well as when it is at rest, until the concrete has set. Enhancement of mix stability can be achieved by providing proper viscosity which is a consequence of increasing the powder content and/or using a viscosity modifying agent (VMA). Limiting the size and content of coarse aggregate are also effective in inhibiting segregation.

It can be mentioned that the above three key requirements are to some extent related and inter-connected. A variation in one property will lead to a change in one or both of the others. Both insufficient filling ability and segregation result in unsatisfactory passing ability. Segregation resistance increases as filling ability increases. SCC is therefore a trade-off between these parameters (Pamnani, 2014).

2.6   Approaches to achieve SCC

Over the last decade, extensive research has been devoted to achieving self-compactibility of concrete. Three different approaches have been identified to produce this type of concrete:

2.6.1   Powder-type SCC

This type of SCC is achieved by using greater amount of cementitious material and filler along with super-plasticiser at low water to powder ratio (w/p) (Khayat, 1999). Increasing the powder leads to increased viscosity and improved stability of the fresh concrete. The flow performance is mainly affected by the super-plasticiser. However, the balance between flow and stability is very important for the behaviour of fresh concrete.

2.6.2   VMA-type SCC

Addition of VMA enhances the stability of SCC mixes, preventing the concrete from segregation without increasing powder content (Khayat, 1998; EFNARC, 2005). Similar to

the use of powder in SCC, addition of VMA increases the concrete robustness. However, from an economical perspective, most VMAs type are expensive and in general more expensive than powder type using, e.g. limestone filler.

2.6.3   Combination-type SCC

The third main approach of SCC is based on both approaches: powder-type and VMA-type (EFNARC, 2005). In such type the VMA content is less than that in the VMA-type SCC and the powder content is less than that in the powder-type SCC. Addition of VMA reduces the powder needed, and vice versa. The viscosity is provided by the VMA along with the powder. This type of SCC was reported to have high filling ability, high segregation resistance and improved robustness (Rozière et al., 2007).

2.7   Constituent materials of SCC

2.7.1   Cement

EFNARC (2005) states that the selection of the type of cement depends on the overall requirements for the concrete such as strength and durability. Ordinary Portland cement is most widely used to produce various types of SCC. It is used alone or in combination with cement replacement materials (CRM). Cement improves the flowing ability of SCC when used with water to lubricate the aggregates. Cement can also affect the segregation resistance of SCC by affecting the density of cement paste matrix of concrete.

2.7.2   Water

The amount of water in VC and SCC is important for the properties at the fresh and hardened stages. However, SCC is more sensitive to the water content in the mix than traditional vibrated concrete. Adequate water is required for the hydration of cement, leading to the formation of paste to bind the aggregates. In addition, water is required in conjunction with super-plasticiser to achieve the self-compactibility of SCC by lubricating

the fine and coarse aggregates in the mix. Typical range of water content in SCC, as per EFNARC (2005), is 150-210 l/m^3.

2.7.3   Aggregate

Aggregate (coarse or fine) characteristics such as size, gradation, shape, volume fraction, have a significant impact on self-compactibility of SCC (Koehler and Fowler, 2007). With the reference to the coarse aggregate, it significantly affects the performance of SCC by influencing its flowing ability, passing ability and segregation resistance as well as its strength (EFNARC, 2005). All standard sizes of coarse aggregate are generally suitable to produce SCC. It should be selected in consideration of the performance need for fresh and hardened concrete (Koehler and Fowler, 2007). Most SCC applications have used coarse aggregate with a maximum size in the range of 16~20 mm depending on local availability and particular application (Domone, 2006). Nevertheless, sizes higher than 20 mm could possibly be used. However, SCC with higher volume fraction or maximum size of coarse aggregate relative to the gap will be more sensitive to segregation, and will likely need either higher powder content or a viscosity modifying agent (VMA).

The fine aggregates are also a key component of SCC, which plays a major role in its workability and stability. EFNARC (2005) reports that the effect of fine aggregates on the fresh properties of SCC mixes is significantly higher than that of coarse aggregate. The fine aggregates addressed as sand/total aggregate (S/A) ratio is an important material parameter of SCC that influences its rheological properties (Su et al., 2001).

2.7.4   Powders

During the transportation and placement of SCC the increased flow-ability may cause segregation and bleeding which can be overcome by enhancing the viscosity of concrete mix. This is usually supplied by using a high volume fraction of paste, by limiting the maximum aggregate size or by using viscosity modifying admixtures (VMA) (Khayat, 1999). For this purpose, if only cement and chemical admixtures are used, it will be more costly, and at the same time lead to more heat of hydration and drying shrinkage. To

avoid such issues, it is necessary to use powder materials, which are greatly beneficial for concrete properties and durability (Kim et al., 2012). They not only decrease the SCC materials' cost but also enhance its particle packing density, self-compactibility and stability as well as its durability. The term 'powder' used in SCC refers to a material of particle size smaller than 0.125 mm. It will also include this size fraction of the sand. These materials include cement replacement materials (CRM) and fillers (e.g. limestone powder).

2.7.4.1   Cement replacement materials (CRM)

CRM are used as a partial replacement of Portland cement in SCC mixes. All CRMs have two common features; their particle size is smaller or the same as Portland cement particle and they become involved in the hydration reactions mainly because their ability to exhibit pozzolanic behaviour. By themselves, pozzolans which contain silica (SiO_2) in a reactive form have little or no cementitious value. However, in a finely divided form and in the presence of moisture they will chemically react with calcium hydroxide at ordinary temperatures to form cementitious compounds (Domone and Illston, 2010). The most common CRMs used are ground granulated blast furnace slag (ggbs), silica fume (SF) and fly ash (FA). More details of CRMs can be found in (Dinakar et al., 2013a,b; Obla et al., 2003; Sonebi, 2004; Siddique and Khan, 2011).

2.7.4.2   Fillers

Fillers, such as limestone powder, are used as a portion of total powder content to enhance certain properties of SCC. It is not a pozzolanic material and its action can be related to a change in the microstructure of the cement matrix associated with the small size of the particles (Ye et al., 2007). The filler increases the paste volume required to achieve the desirable workability of SCC, resulting in an enhancement in the packing density of powder and in the stability and cohesiveness of fresh SCC (Bosiljkov, 2003; Topçu and Uğurlu, 2003).

However, excessive quantities of fine particles can result in a significant rise in the surface area of powder and an increase in inter-particle friction, due to solid-solid contact, which may influence the passing ability of the SCC mix and also a substantial rise in the viscosity (Yahia et al., 2005).

2.7.5 Chemical Admixtures

The most commonly used chemical admixtures in SCC are high range water reducers (HRWR), or super-plasticiser (SP), and viscosity modifying agent (VMA).

2.7.5.1 High range water reducers (HRWR)

High range water reducer (HRWR) or super-plasticiser (SP) is an essential component of SCC to provide the necessary workability (Okamura and Ouchi, 2003). The main purpose of using a super-plasticiser (SP) is to improve the flow-ability of concrete with low water to binder ratio by deflocculating the cement particles and freeing the trapped water through their dispersing action, as illustrated in Figure 2.4.
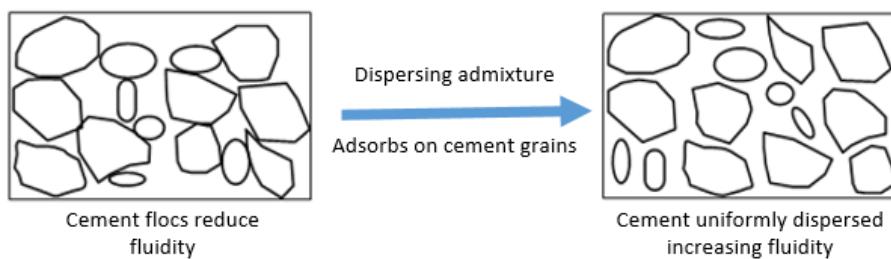
Figure 2.4: Effect of dispersing admixtures in breaking up cement flocs (After: Dransfield, 2003)

SP contributes to the achievement of denser packing and lower porosity in concrete by increasing the flow-ability, and thus assisting in producing SCCs of high strength and good durability. For achieving the SCC, an optimum combination of water and SP dosage can be derived for fixed w/c ratio in concrete (i.e., compressive strength). However, a high SP

amount could cause segregation and bleeding. The new generation super-plasticiser, which is particularly useful for production of SCC, is Poly-Carboxylate Ether (PCE) based, although SCC can be made with different types of SP (Assaad et al., 2003; Lachemi et al., 2003).

2.7.5.2   Viscosity Modifying Agent (VMA)

Viscosity modifying agents (VMA), also known as anti-washout admixtures or anti-bleeding admixtures, are water-soluble polymers that increase the viscosity of mixing water and enhance the ability of concrete to retain its constituted suspension. VMA may also be used as an alternative to increasing the powder content or reducing the water content of a concrete mix, and mitigating the influences of variations in materials and proportions in SCC mix, especially when gap-graded aggregates are used (Koehler and Fowler, 2007). The commonly used viscosity-modifying agent in concrete is welan gum. It can absorb some of the free water in the system, thus increasing the viscosity of the cement paste which, in turn, enables the paste to hold aggregate particles in a stable suspension. As a result, less free water is available for bleeding.

2.8   Proportioning of SCC mixes

Proportioning of SCC can be defined as combining optimum fractions of the constituent materials to fulfill the requirements of fresh properties (filling ability, passing ability, and segregation resistance) as well as hardened properties for a particular application (Desnerck et al., 2014). The complexity of SCC mix proportioning has increased with the increasing variety of components available for its production: different types of cement and aggregate (crushed, rounded, etc.), cement replacement materials (ggbs, fly ash, silica fume, etc.), fillers, chemical admixtures (SP, VMA) (Sandra et al., 2009). Consequently, different variables must be considered in the proportioning of SCC and different tests have to be carried out to optimize its constituents. Here, the proportioning of SCC mix will be discussed in terms of its comparison with VC, quantity ranges of its constituent materials and the methods developed for its design.

2.8.1   Comparison of mix proportions of SCC with VC

With regard to its proportioning, SCC consists of almost the same constituent materials as VC, which are cement, aggregates, water and with the addition of chemical and mineral admixtures (fly ash, silica fume, ggbs, limestone powder, etc.) in different proportions. However, the reduction of coarse aggregates, the large amount of powder, the incorporation of SP, the low water to powder (w/p) ratio, are what leads to self-compactibility. The schematic composition of SCC versus VC is shown in Figure 2.5.
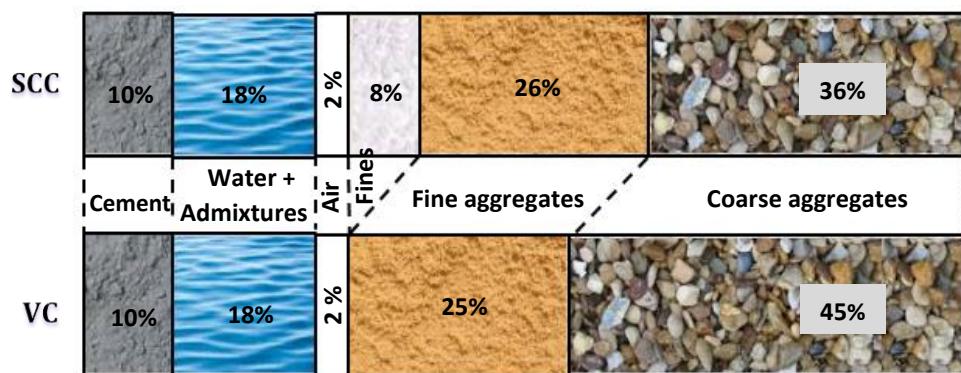
Figure 2.5: The schematic composition of SCC versus VC (After: Okamura and Ouchi, 2003)

There are two main differences in the mix proportioning methods between SCC and VC. First, the design of VC starts from determining the water to cementicious materials (w/cm) ratio to satisfy the strength requirement and finishes by the amount of aggregates. SCC on the other hand is usually proportioned beginning with the fresh property requirements. Owing to its high cementitious and powder content, which often ensuring higher strength than is required, designs of SCC usually do not take strength criterion into account (Ghazi and Al Jadiri, 2010). Second, the fresh and hardened properties of SCC are more difficult to predict than those of VC and more testing after design is required. Therefore, the constituent materials of SCC must be carefully proportioned.

2.8.2   Quantity ranges of the constituent materials for SCC

Typical ranges of quantities of the constituent materials for producing SCC are given by EFNARC (2005) (Table 2.1); the actual amounts depend on the desired strength and other performance requirements.

Table 2.1: Typical range of SCC mix compositions according to EFNARC (2005)

Ingredients	Typical range by mass, kg/m^3	Typical range by volume, litres/m^3
Powder (cementitious materials + filler)	380–600	–
Water	150–210	150–210
Coarse aggregate	750–1000	270–360
Water to powder ratio by volume	0.85–1.10	
Fine aggregate	Typically 48–55% of the total aggregate	

Among 56 case studies of SCC applications, Domone (2006) reported that it can be produced using a wide range of possible constituent materials such that there are still no clear rules for proportioning SCC mixes. These case studies revealed that coarse aggregate contents ranged from 28 to 38% of concrete volume, fine aggregate content varied from 38 to 54% of mortar volume, w/p ratio (by weight) ranged from 0.26 to 0.48, paste content varied from 30 to 42% of concrete volume, powder content ranged from 445 to 605 kg/m^3.

2.8.3   Mix design methods for SCC

Over the years, a number of different mix design methods, based on different principles (Desnerck et al., 2014; Shi et al., 2015; Koehler and Fowler, 2007) have been proposed by researchers from various countries around the world. According to their design principles, these methods could be classified into five categories: (1) empirical design approach; (2) statistical approach; (3) packing approach; (4) compressive strength approach, and (5)

rheological approach (Shi et al., 2015). The following is a brief overview of these approaches to each of them an example will be included.

2.8.3.1   Empirical approach

Empirical design method is based on empirical data available for mix parameter to determine the initial ingredients. The best estimates of the SCC mix proportions for required properties are performed through several trial mixes and alteration. The Japanese method was the pioneering work in the SCC mix proportioning based on the empirical design approach (Shi et al., 2015). It has been adopted and used in many European countries as a starting point for the development of SCC (Brouwers and Radix, 2005). The main aspects were to fix the coarse aggregate content at 50% of solid volume and the fine aggregate content at 40% of mortar volume so that self-compactibility can be achieved easily by adjusting the water-powder ratio (initial value is in the range of 0.9-1 by volume) and super-plasticiser dosage only. In spite of its simplicity, the empirical design method requires intensive laboratory testing on available raw materials to achieve satisfactory mix proportions (Shi et al., 2015).

2.8.3.2   Statistical approach

Statistical design approach is used to derive design charts which correlate input mix-design variables to output material properties, mainly consisting of the measurements of fresh state properties. Khayat et al. (1999) proposed a mix design method for SCC based on a statistical model. Their design procedure included five mix parameters: the volume of coarse aggregate, the cementitious material content, the ratio of water to cementicious materials, dosage of VMA by mass of water and SP dosage by mass of binder. The fine aggregate content was varied to achieve the total volume. These parameters were evaluated and fitted to the results of each measured property (slump flow, filling ability, V-funnel time and compressive strength) in a statistical manner. It is however worth mentioning that although the statistical method is valid for a wide range

of SCC mix proportions, establishment of statistical relationships requires intensive laboratory tests on available raw materials (Shi et al., 2015).

2.8.3.3   Packing approach

In this approach the SCC mix ingredients are obtained by determining the minimum voids between aggregates according to their packing factor (PF), which is the mass ratio of closely packed aggregate to that of loosely packed aggregate. The key consideration of this approach is to fill aggregate voids with an optimum paste volume depending on the PF value. Su et al. (2001), based on this approach, developed a mix proportion method to design a medium strength SCC. This method was successfully applied in the Netherlands (Brouwers and Radix, 2005) and adapted for lightweight SCC in South Korea (Choi et al., 2006). Given the fact that the design principle of this approach is based on minimum paste volume, which could save the most expensive constituents (namely cement and filler), the produced SCC tends to segregate easily, causing a problem for the constructed structures.

2.8.3.4   Compressive strength approach

An alternative approach for the design of SCC mix was developed based on the requirement of mix compressive strength. Ghazi and Al Jadiri (2010) constructed a mix proportioning approach based on two well-known mix design methods, which are the ACI 211.1 (1991) for proportioning VC and the EFNARC (2005) for proportioning SCC. The requirements of these methods (ACI 211.1 and EFNARC) were combined with certain modifications to develop this method. The original ACI 211.1 had a range of design compressive strength of 15 to 40 MPa. This range was widened to cover the proportioning of SCC with a compressive strength range of 15 to 75 MPa. A modification on the mix parameters such as coarse aggregate content, cementitious materials, powder content and w/p ratio were introduced to be within the practical values specified by EFNARC (2005). It could be mentioned that the compressive strength based approach gives a clear procedure for proportioning SCC mix ingredients and minimizing the need for

trial mixes. Nevertheless, adjustments to all the mix ingredients are needed to obtain an optimal mix proportions (Shi et al., 2015).

2.8.3.5   Rheological approach

The rheological properties (plastic viscosity and yield stress) can also be incorporated into SCC mix design methods, as for instance in the one proposed recently by Karihaloo and Ghanbari (2012). They have developed a rigorous method for proportioning high strength SCC mixes with and without steel fibres based on their plastic viscosity. The key consideration of this method is to exploit the expression for the plastic viscosity of an SCC mix developed using micro-mechanical principles (Ghanbari and Karihaloo, 2009). Deeb and Karihaloo (2013) have extended this method to proportioning SCC mixes that contain traditional coarse aggregate and whose characteristic cube strength ranges between 35 and 100 MPa. Although this method covers a wide range of SCC mixes and reduces the need for trial mixes, it does not give practical guidelines on how to choose the most appropriate mix. Also, the compressive strength was not explicitly imposed as a design criterion in this method.

For more detailed information about SCC mix design methods, we refer the reader to a very recent work by Shi et al. (2015), where the state of the art review (from 1995 to 2014) on this issue is thoroughly discussed. This review provides valuable scientific basis for selection of suitable mix design methods of SCC. The procedures, advantages and drawbacks of the surveyed methods are presented and discussed in this review.

2.9   Testing methods for self-compactibility of SCC

The unique characteristics of SCC do not allow the standard tests employed for VC to be applied to monitor correctly the fresh properties of the produced SCC. The self-compactibility tests commonly employed on SCC mixes are briefly described below.

2.9.1   Slump cone test

The slump test is used to assess the deformability of SCC in the absence of obstacles. It is a simple test such that it can be performed either on site or in laboratory (BS EN 12350-8, 2010). This test measures three different aspects: filling ability, viscosity and resistance to segregation. The filling ability of SCC is evaluated by measuring the horizontal flow diameter; the larger the slump flow value, the greater is the ability of SCC mix to fill formwork under its own weight. Two horizontal perpendicular diameters (d_1 and d_2) as illustrated in Figure 2.6 are recorded and the average flow spread diameter (SF) is calculated.

$$SF = \frac{(d_1 + d_2)}{2}$$

(2.1)
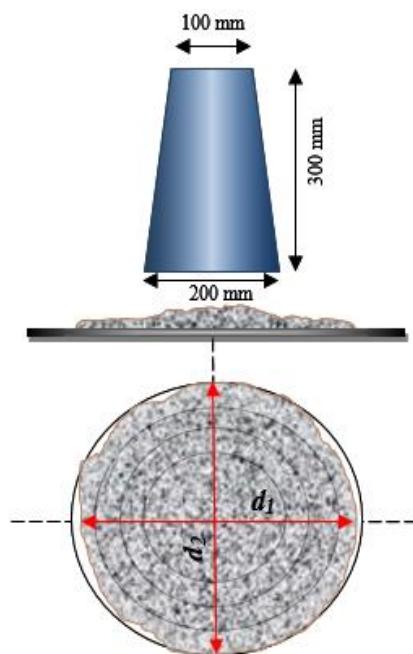
Figure 2.6: Slump test apparatus

The mix viscosity is assessed by measuring the time needed for SCC to reach 500 mm flow (t_{500}); the longer the t_{500}, the higher the mix viscosity will be. Two viscosity classes are introduced: viscosity class 1 (VS$_1$) and viscosity class 2 (VS$_2$) depending on whether $t_{500} < 2$ s or ≥ 2 s (BS EN 206-9, 2010).

Moreover, the slump test gives an indication of resistance to segregation in SCC mixes, which can be detected by visually inspecting the mix periphery after concrete stops to flow. Segregation is indicated by the occurrence of a halo of paste or unevenly distributed coarse aggregate in the mix.

2.9.2   J-ring test

The J-ring test in combination with a slump test is used to assess the passing ability of SCC with or without fibres through gaps in the reinforcement. The apparatus is composed of a ring with different numbers of vertical reinforcing bars, a slump cone and a rigid plate (BS EN 12350-12, 2010) as shown in Figure 2.7. Flow spread of the J-ring (SF_J) indicates the restricted deformability of SCC and can be expressed as:

$$SF_J = \frac{(d_1 + d_2)}{2}$$

(2.2)

The J-ring can be assessed relative to the flow spread (SF_J) of the same mix using the slump test as reported in ASTM C 1621/C 1621M (2008). If the difference between spread diameters ($D_{flow} - D_{J\text{-}ring}$) of the two tests is less than 25 mm, then there is no visible blockage. If it is between 25 and 50 mm, then there is minimal to noticeable blockage.

The SCC passing ability can also be judged in terms of the height difference between the concrete inside and outside the steel bars of the J-ring using the following equation.

$$P_J = \frac{\Delta h_{x1} + \Delta h_{x2} + \Delta h_{y1} + \Delta h_{y2}}{4} - \Delta h_0$$

(2.3)

Here, P_J is the blocking step, Δh_0 is the height measurement at the centre of flow and Δh_{x1}, Δh_{x2}, Δh_{y1}, Δh_{y2} are the four measurement heights at positions just outside the J-ring. The acceptance criterion of SCC passing ability is that the blocking step (P_J) should be ≤ 10 mm (BS EN 206-9, 2010).

The J-ring test can give an indication of resistance to segregation in SCC mixes, which can be detected by visually inspecting the mix periphery after concrete stops; a ring of cement paste/mortar in the edge of flow after the concrete has stopped flowing.
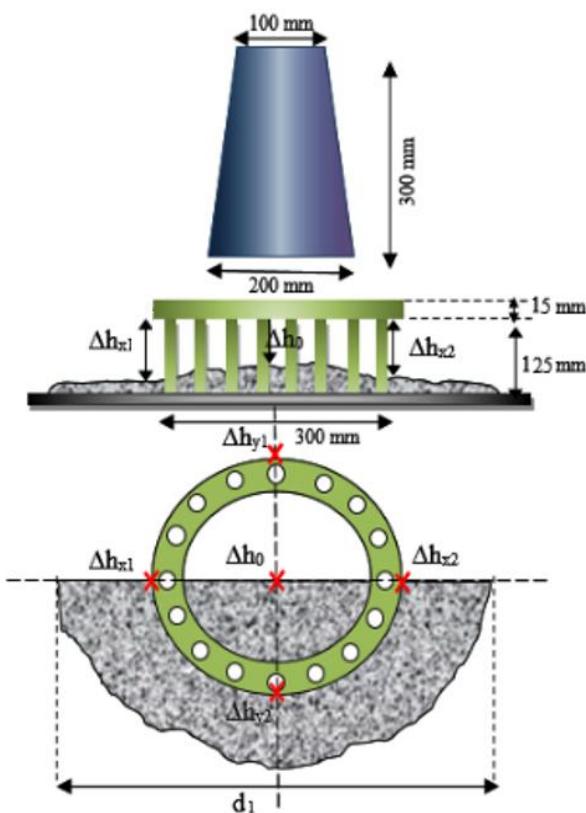
Figure 2.7: J-ring test apparatus

2.9.3   L-box test

The L-box test is used to assess the filling and passing ability of SCC. The test is carried out in accordance with BS EN 12350-10 (2010) and EFNARC (2005). The dimensions of the L-box are shown in Figure 2.8. The times for the SCC to reach a distance of 200 mm (t_{200}) and 400 mm (t_{400}) along the horizontal part are measured. Also measured is the height of concrete at the two ends of the horizontal section of box (H_1 and H_2) after the concrete has stopped flowing. The ratio H_2/H_1 represents the filling ability, and typically, this value should be 0.8~1. The passing ability can be detected visually by inspecting the area around the rebars.
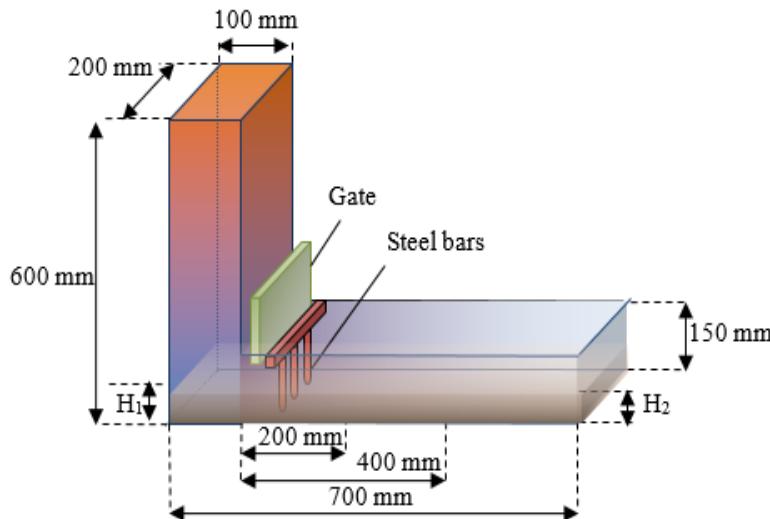
Figure 2.8: L-box test apparatus

2.9.4   V-funnel test

The V-funnel test, which is shown in Figure 2.9, is used to evaluate the viscosity and filling ability of self-compacting concrete (BS EN 12350-9, 2010; EFNARC, 2005). The V-funnel test is performed by measuring the time for the concrete to flow out of the funnel under its own weight. Two viscosity classes are introduced: viscosity class 1 (VF_1) and viscosity class 2 (VF_2) depending on whether $VF_1 < 8.0$ s or VF_2 between 8.0 to 25.0 s (BS EN 206-9, 2010). Segregation resistance of concrete flow can be evaluated by assessing the homogeneity of concrete flow from the funnel test. In this regards, Alyhya (2016) have examined (by SPH simulation) the distribution of coarse aggregates in the mix: (1) along three zones of the V-funnel at different times during the flow, and (2) along three portions of the collecting container at the outlet of the funnel. He found that, as the simulation allows the distribution of large coarse aggregates embedded in the homogeneous mixes to be tracked, it is possible to check whether or not they are homogeneously distributed during the flow and after the flow has stopped.
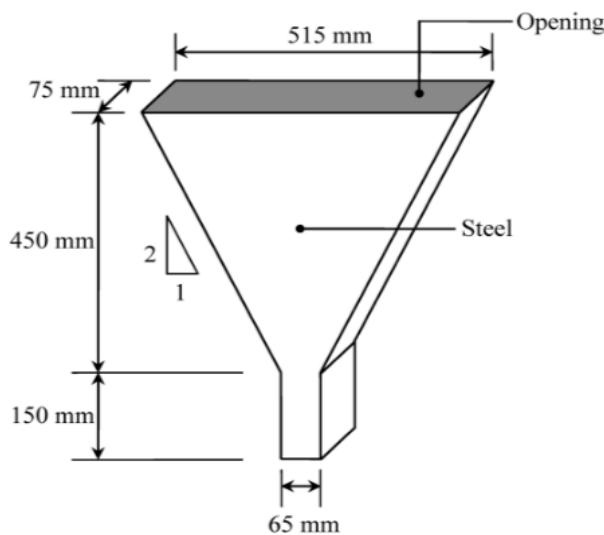
Figure 2.9: V-funnel test apparatus

2.10   Hardened properties of SCC

Generally, the hardened behaviour of concrete is governed by its compressive strength. Numerous papers have been published concerning all aspects of the hardened properties of SCC, often in comparison with VC (Desnerck et al., 2014; Domone, 2007; Hoffmann and Leemann, 2005; Persson, 2001). A brief review of the hardened properties is given in this section. It will emphasise the compressive strength, tensile strength, modulus of rupture and fracture mechanics properties. The other hardened properties will not be involved as they are outside the scope of this study.

2.10.1   Compressive Strength

Compressive strength is the key property of hardened concrete that dominates other mechanical properties and gives an indication of its overall quality (Neville, 1995). Under given curing conditions, the compressive strength of VC and SCC is mostly determined by the ratio of water to cementitious material (w/cm). In addition to w/cm ratio, numerous researchers (Desnerck et al., 2014; Parra, 2011; Vilanova et al., 2011; Domone, 2007; Hoffmann and Leemannn, 2005; Persson, 2001) have pointed out that compressive

strength of SCC is also influenced by other factors such as type of cement and CRM, use of materials having pozzolanic activity, type and size of aggregates, type and dosage of admixtures. However, achieving low compressive strength in SCC is more difficult than medium and high strength due to the presence of high powder contents.

In general, SCC should exhibit higher compressive strength than VC for a constant w/cm. This is due to better microstructure and homogeneity in SCC which are the consequences of significant reduction of segregation and bleeding and reduction of w/p ratio and air pores. The improved microstructure in SCC is related to the interfacial transition zone (ITZ) which is denser and significantly more uniform than in VC.

2.10.2   Tensile strength

The tensile strength is one of the key properties that affects the safety, durability and serviceability of concrete structures (Parra et al., 2011). The tensile strength of SCC is superior relative to VC (Desnerck et al., 2014; Domone, 2007; Persson, 2001). This is attributed to the high paste content in SCC and better homogeneity resulting from vibration free production compared to VC (Nikbin et al., 2014a).

The SCC tensile strength, as VC, has been assessed by splitting, flexural and direct tensile tests. Many relationships have been built, based on different parameters, to convert these test results from one to another or as a function of compressive strength (Craeye et al., 2014; Nikbin et al., 2014a; Parra et al., 2011). This is however not the case for the direct tensile strength as very limited results are available due to high complexity of this test. Thus, more test results are necessary to build reliable conclusions with regard to parametric influences on the direct tensile strength of SCC (Craeye et al., 2014).

2.10.3   Modulus of elasticity

It is known that the modulus of elasticity of concrete depends on the modulus of elasticity of the individual mix ingredients. It increases with high content of aggregates, whereas it

decreases with increasing paste volume and increasing porosity (Neville, 1995). However, the increase in the SCC modulus of elasticity due to the decrease in porosity cannot compensate for the reduction induced by the lowering of coarse aggregate content and/or increasing paste volume. Accordingly, lower values of modulus of elasticity can be expected for SCC, as it has relatively higher content of paste and lower content of coarse aggregate than VC.

Craeye et al. (2014) reported that due to the significant contribution of aggregates to the overall stiffness of concrete, it is expected that SCC, with its higher paste volume, tends to reach a slightly lower modulus of elasticity than VC. Similar conclusions have been drawn by other researchers (Desnerck et al., 2014; Domone, 2007; Nikbin et al., 2014a; Parra et al., 2011).

2.10.4   Fracture mechanics

Concrete structure, because of its heterogeneity, can be prone to flaws such as irregularly distributed pockets of entrapped air voids, lenses of bleed water and shrinkage cracks, even prior to the application of load. These flaws grow stably under external load, coalesce with existing or newly-formed small cracks until large fractures are formed which cause the collapse of the structure. When a load is applied there will be high stress concentrations around these cracks, higher than those at other points within the structure. These cracks propagate during service and can be a serious problem in such structures. Since it studies the response and failure of structures as a consequence of crack initiation and propagation, fracture mechanics provides an energy based failure theory that could be used in designing cement-based structures (Karihaloo, 1995).

2.10.4.1   Linear elastic fracture mechanics (LEFM)

Linear elastic fracture mechanics (LEFM) has been available since 1920 (Karihaloo, 1995). However, it is absent from the Codes because the Griffith fracture theory is only applicable to elastic homogeneous brittle materials such as glass (Karihaloo, 1995). Thought to be a brittle material, attempts were made to apply LEFM to concrete, but

these proved unsuccessful due to the fact that cement-based materials indeed show a different response. For a quasi-brittle material like concrete, a substantial non-linearity exists before the maximum stress is reached (region AB in Figure 2.10a). This is the strain hardening response of the material. There is also a region of softening after the attainment of the maximum load (region BC in Figure 2.10a). These are mainly a result of randomly formed micro-cracks. The tail region of tension softening (region CD in Figure 2.10a) is caused by the aggregate interlock and other frictional effects.

The pre-peak non-linearity has only a minor impact on the fracture behaviour of concrete. In fact, the major impact comes from the tension softening response because it reduces the flux of energy which can be released into the crack tip and thereby leads to an increase in the fracture surface area. Therefore, the LEFM application to concrete structures is limited, due to the presence of the tension softening response. In other words, the fracture behaviour of concrete is affected by the formation of an extensive fracture process zone (FPZ) ahead of the pre-existing crack (Figure 2.10b).
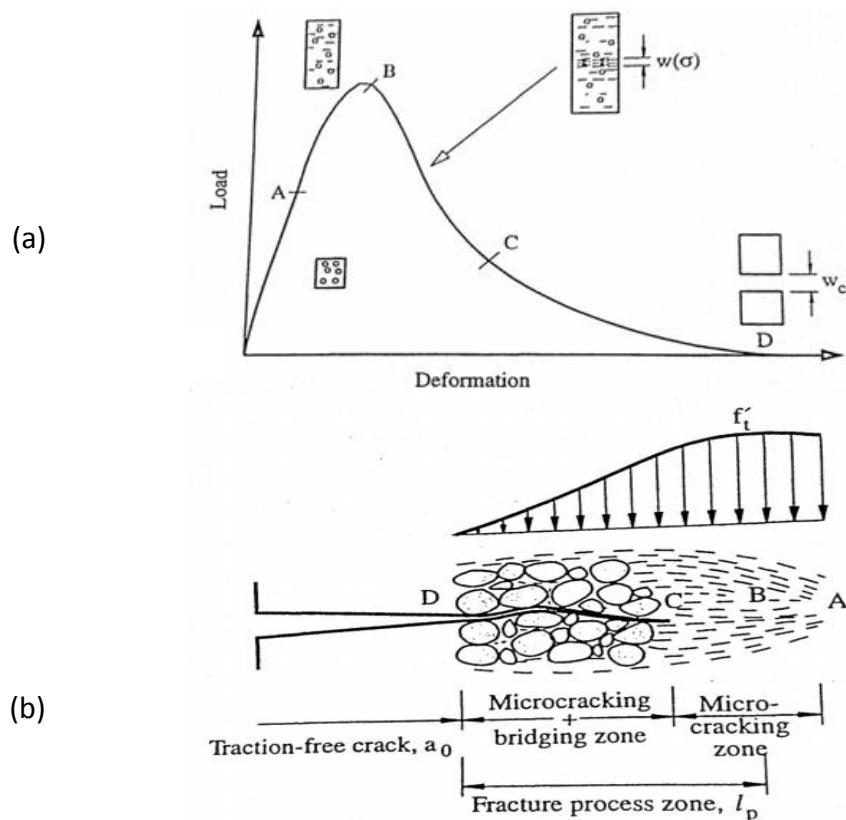
Figure 2.10: Typical load-deformation response of a quasi-brittle material in tension/flexure (a) and the fracture process zone ahead of the real traction-free crack (b) (After: Karihaloo, 1995).

2.10.4.2 Fracture process zone (FPZ)

The fracture process zone (FPZ) is defined as the inelastic zone around the crack tip and corresponds to the region of tension softening of the load-deformation curve (Figure 2.10). Many mechanisms that are responsible for fracture process in concrete are related to the development of the fracture process zone. Some of these mechanisms are indicated in Figure 2.11 such as, micro-cracking at aggregate due to the presence of a macro-crack, de-bonding and micro-cracking, coalescence of de-bond crack with a macro-crack and the crack bridging.
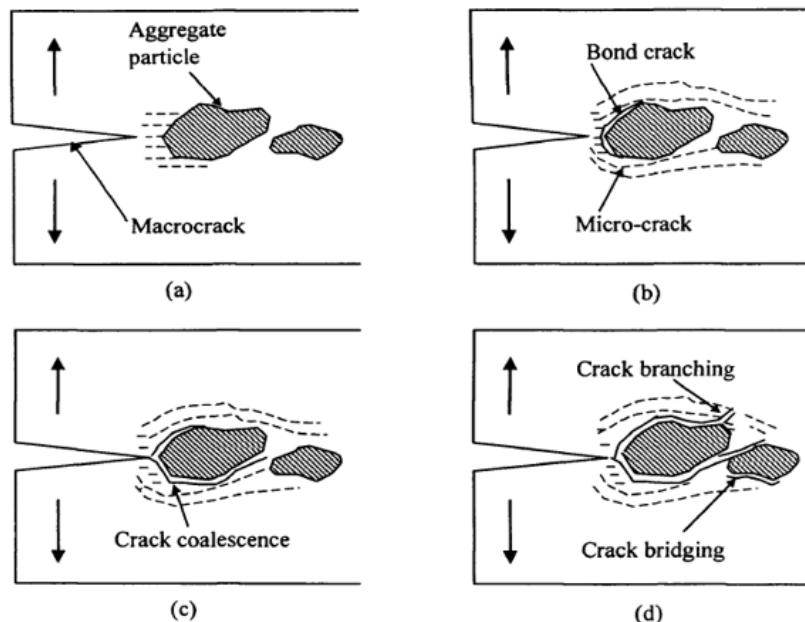
Figure 2.11: Schematic representation of the fracture process zone (After: Karihaloo, 1995).

Fracture behaviour of concrete is significantly influenced by the FPZ. Since the FPZ consumes a substantial amount of the energy supplied by the applied load, a crack can propagate steadily prior to failure. The FPZ is responsible for the quasi-brittle fracture response of concrete after the peak load. Since some parts of crack surfaces may still be in contact after cracking, stress gradually decreases after the peak load, and a softening type of concrete stress-strain relationship is obtained.

2.10.4.3   Nonlinear fracture mechanics (NLFM)

LEFM is not applicable to concrete due to the existence of the inelastic toughening mechanisms (i.e. FPZ) that appear around a crack when it propagates. A fracture theory capable to describe the material softening process that takes place in the fracture process zone must be a non-linear fracture theory (Karihaloo, 1995). The first non-linear theory of fracture mechanics for quasi-brittle materials like concrete is the fictitious crack model (FCM) proposed by Hillerborg et al. (1976). Bažant (1984) proposed the second non-linear theory of fracture, which is the crack band model. The two non-linear theories were covered in detail by Karihaloo (1995).

The fictitious crack model set a benchmark for fracture mechanics of concrete and is widely used in various applications (Hu and Wittmann, 2000). The applications of this model require the knowledge of two important parameters: the size-independent fracture energy, G_F and the tension softening diagram, σ(w) of the concrete mix. These parameters form the basis for the assessment of the load carrying capacity of cracked concrete structures (Karihaloo, 1995; Bazant and Planas, 1997).

G_F can be simply calculated using the simplified boundary effect (SBE) formalism (Abdalla and Karihaloo, 2003) from notched three-point bend test of single size specimens with only two distinctly-different notch to depth ratios, while σ(w) could ideally be obtained from the direct tension test. However, as the determination of σ(w) using such test is not a simple task, it is often approximated by a bilinear relationship whose parameters are determined in an inverse manner by matching the experimental load-displacement curve of a notched three-point bend beam. To avoid unnecessary duplication, detailed information about the above parameters will be presented and discussed together with results from this study in Chapter 6.

2.10.4.4   Fracture behaviour of SCC versus VC

The fracture behaviour of concrete, as a specific type of composite material, is significantly influenced by the properties of matrix (Akçaoğlu et al., 2004), which in turn are governed by the mix ingredients in VC and SCC, as well. Based on the experimental

results obtained from different researchers (Karihaloo, 1995; Akcay et al., 2012; Prokopski and Langier, 2000), reduction of the aggregate size and content in VC leads to decrease in fracture energy. This is the consequence of the decrease in aggregate bridging and interlocking across the crack resulting in the reduction of energy absorption. In SCC, concerns have been raised among researchers as it may have inferior fracture behaviour compared to VC (Beygi et al., 2014a,b,c; Domone, 2006). This is primarily due to the fact that SCC requires comparatively low coarse aggregate content but large amounts of fine material and paste in order to control its fundamental parameters (yield stress and plastic viscosity).

The differences in SCC mix composition lead to change in its pore structure, resulting in modified mechanical behaviour, especially fracture properties, and consequently different cracking behaviour. These conclusions were confirmed by previous studies (Beygi et al., 2014a,b,c; Nikbin et al., 2014b,c; Cifuentes and Karihaloo, 2013; Beygi et al., 2013a; Rozière et al., 2007). These studies, apart from the study of Cifuentes and Karihaloo (2013), were indeed based on the size-dependent specific fracture energy (G_f), not on the true fracture energy (size-independent fracture energy (G_F)). However, since a lack of adequate knowledge on the SCC fracture behaviour (specifically G_F), due to a limited amount of test results from literature, the use of the fracture assumptions and relations that are valid for VC might be risky for SCC (Beygi et al., 2014c).

2.11 Concluding remarks

Self-compacting concrete, which is characterised in its fresh state by high flow-ability and rheological stability, has excellent applicability for elements with complicated shapes and congested reinforcement. It has rationalised the construction systems by offering several economic and technical advantages over VC. A concrete mix can only be classified as SCC if its main functional requirements (filling ability, passing ability and segregation resistance) are fulfilled. These are mainly achieved by exploiting the benefits of super-plasticisers (SP) and viscosity modifying agents (VMA) (if required), cement replacement material (CRM) and fillers. The above three key requirements are to some extent related

and inter-connected. In other words, SCC is a trade-off between these parameters; a variation in one property will lead to a change in one or both of the others.

Since the SCC requirements are mostly influenced by the fractions of the mix ingredients, it becomes crucial to develop an appropriate procedure for its proportioning. A review of the mix design methods indicates that SCC can be designed using a wide range of possible constituent materials such that there is no unique mix design method has widely been followed for proportioning SCC mixes. To all of the surveyed methods, a significant number of time and material-consuming trial mixes are inevitably needed before an optimum mix proportion is reached. However, in most of the reviewed methods, it should be pointed out that attention has primarily been paid to the fresh properties, rather than hardened properties, to produce an SCC mix that possesses the features of being self-compacting.

Recently, a rigorous method for proportioning high strength SCC mixes with and without steel fibres has been developed. The key consideration of this method is to exploit the expression for the plastic viscosity of an SCC mix developed using micro-mechanical principles. Although this method covers a wide range of SCC mixes and reduces the need for trial mixes, it does not give practical guidelines on how to choose the most appropriate mix. In addition, the compressive strength was not explicitly imposed as a design criterion in this method. As a result, there is a scope in this study (Chapters 4 and 5) to overcome the shortcomings of this method, in which practical guidelines in the form of design charts will be developed as a guide for proportioning SCC mixes.

A review of the literature concerning the hardened properties shows that SCC mixes are often, but not always, accompanied with improvements in these properties. The compressive and tensile strengths of SCC are always higher than that of VC due to the improvement in mix microstructures. Many relationships have been built for VC to convert the test results of compressive and tensile strength (which is assessed by splitting, flexural and direct tensile strength) from one to another. However, it is not quite clear whether these conversion factors are still valid for SCC and therefore, more experimental results are necessary to reach reliable conclusions. In this thesis, we will develop relationships between the direct and indirect tensile strength of SCC mixes of

different paste to solid ratio, coarse aggregate volume and mix grades. This will give a better understanding of the contribution of these compositional parameters on the tensile strength of SCC.

Based on the results obtained from different studies, it is indicated that SCC, with its high paste volume and low coarse aggregate contents, tends to have a lower fracture energy than VC, which raises concerns among researchers. A limited number of studies has debated the parameters affecting the SCC fracture behaviour (specifically the size-independent fracture energy, G_F) such as coarse aggregate content, paste volume and strength grade. In Chapter 6, we will examine in detail the role of these compositional parameters of SCC mixes in their G_F and the corresponding bilinear approximation of the tension softening diagram (TSD).

The next chapter will look concisely at the rheology of SCC and simulating its flow, which are the two key issues in the scope of this study.

Chapter 3

Rheology of SCC and simulation of its flow

3.1   Introduction

A key phase, when producing SCC, lies in understanding its workability to provide a quantitative fundamental way of characterising its self-compactibility so as to obtain adequate properties of fresh concrete. Without understanding this property, SCC will continue to be designed by trial and error to satisfy the performance required for a particular application. Several tools are available to assess the workability of SCC. These tools can be classified into three categories (Tattersall, 1991): qualitative assessment, quantitative empirical assessment and quantitative fundamental assessment. In the previous chapter, the qualitative assessment of SCC was reviewed via its functional requirements (flow-ability, passing ability and stability), and quantitative empirical assessment via classical tests recommended by the British standard (BS EN 206-9, 2010) such as slump flow, J-ring, L-box and V-funnel tests. In this chapter, the SCC workability will be quantitatively reviewed in terms of its fundamental rheological properties, which is crucial for the success of its production. However, the prediction of SCC rheological behaviour is not a simple task, particularly in the presence of heavy reinforcement, complex shapes of formwork and large size of aggregates. In this regard, a useful and worthwhile approach offering considerable potential is by performing numerical simulation. Such an approach will deepen the understanding of the SCC mix flow behaviour and allow an evaluation of its ability to meet the necessary self-compacting criteria. In this chapter, the simulation of SCC flow will be briefly looked at, with an emphasis on the smooth particle hydrodynamics (SPH) approach that will be used later in this thesis (Chapter 7). Detailed information may be found in Deeb (2013).

3.2   Rheology of SCC

Rheology is the science of the flow and deformation of matter under the effect of an applied force. The necessity to define and control the properties and performance of materials is part of the technological development, and the rheology of cementitious materials is no exception to this development (Banfill, 2006). The rheological study of concrete is of prime importance for the construction industry because concrete is placed in its plastic state. Thanks to an increasingly scientific approach, the rheology of fresh

concrete has been studied extensively for several decades to achieve a set of engineering properties required for its successful performance, including understanding its fresh properties, designing and selecting its materials and modelling its processes. This is especially the case in SCC (Heirman et al., 2008; Petit et al., 2007) in which the processes such as transporting, pumping, injection, spraying, spreading, self-levelling, moulding and compaction depend on the rheology of the material.

In SCC, the rheology has to be deeply understood to provide a quantitative fundamental way of characterising its flow-ability, passing ability and stability, which are the key for the concrete industry as they affect all the mechanical properties in the hardened state. The rheological parameters that characterise the fresh behaviour of the SCC mix are yield stress (τ_y) and plastic viscosity (η), as will be explained in the following section.

3.3   Rheological parameters of fresh SCC

From a rheological perspective, SCC, which is dominated by its fluid-like behaviour, is a viscous non-Newtonian fluid, usually described by a bi-linear Bingham-type rheological model (Heirman et al., 2008). This model contains two parameters: plastic viscosity (η) and yield stress (τ_y). η is the measure of the resistance to flow due to internal friction, which is mainly due to the interaction between fluid particles. SCC should have a relatively high viscosity to ensure that there is no tendency for coarse aggregate and water to sink downwards from paste through the fresh SCC mass. τ_y is the measure of the minimum amount of energy required to make SCC flow, which starts once the shear stress becomes higher than the yield stress. However, when it becomes equal or lower than the yield stress, the flow stops. To be considered SCC, concrete must flow easily under its own weight, so its τ_y should be as low as possible. In comparison with vibrated concrete (VC) the yield stress of SCC, as shown in Figure 3.1, is low and it remains so over a wide range of plastic viscosity (Dransfield et al., 2003; Badry, 2016).
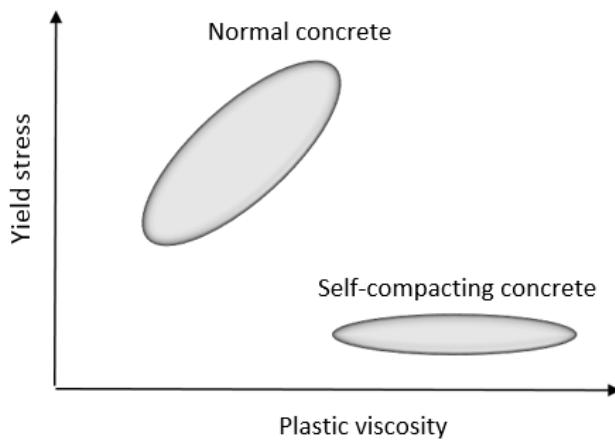
Figure 3.1: Rheology of normal and self-compacting concrete (After: Dransfield et al., 2003)

The potential of a relationship between the SCC rheological characteristics (η and τ_y) and the measured parameters in the slump flow test (namely, slump flow diameter and t_{500}) has been investigated by many researchers (Thrane et al., 2007; Tregger et al., 2007; Roussel, 2006a; Kasemchaisiri and Tangtermsirikul, 2008; Zerbino et al., 2009). They recognised that η is closely related to the time t_{500} (the higher the η the longer the t_{500} time) but that the slump flow spread is a function of both the τ_y and the density of SCC.

3.3.1   Measuring the rheological parameters

The relationship between the shear stress and strain rate are routinely measured by an instrument called rheometer. To obtain the rheological characteristics of general viscous liquids (such as cement pastes) and solid-liquid suspensions (such as SCCs), a rheometer is to be used. Several types of this instrument have been proposed to evaluate the η and τ_y of cementitious materials (Ghanbari, 2011). The plastic viscosity of a homogeneous viscous fluid, such as a paste (mixture of cement, cement replacement material, water and super–plasticiser) can be measured rather accurately with a viscometer which is not possible for a non–homogeneous viscous fluid such as an SCC mix. There is a large scatter in η of one and the same SCC mix measured with different rheometers, as has been reported by many researchers (Feys et al., 2007; Wallevik and Wallevik, 2011). In this regard it is also reported (Vasilić, 2015) that ''due to the complexity of the material behaviour and the concrete rheometer setups, it is nearly impossible to obtain the set of

actual rheological parameters (plastic viscosity and yield stress) in fundamental units from rheometer measurements''. It is therefore necessary to seek alternative methods for estimating the plastic viscosity of an SCC mix accurately and reliably. Ghanbari and Karihaloo (2009) have proposed a micromechanical procedure for estimating accurately the plastic viscosity of an SCC mix knowing the plastic viscosity of the paste used in it. The description of this procedure will be given in the next chapter (Chapter 4).

As the complex material behaviour disallows the rheological parameters of SCC to be measured accurately using rheometers, there is a large scatter in the measured yield stress as there is in the measured plastic viscosity (Vasilić, 2015). It is therefore again necessary to seek alternative methods for estimating the yield stress of an SCC mix accurately and reliably. In this regard, numerical simulations could be a tool for determining this unknown parameter. One such method is to estimate it in an inverse manner from the measured t$_{500}$ and flow spread of the mix in a cone flow test using the three-dimensional smooth particle hydrodynamics (SPH) method for simulating the flow of SCC (Badry et al., 2016).

3.3.2   Models describing SCC flow

To describe the non-Newtonian flow behaviour of concrete, the two commonly used models are those of Bingham and Herschel-Bulkley. The Bingham model is the simplest and most commonly used relation to show the behaviour of a fluid having a τ_y. This could be explained by the fact that this model is most practical: the model parameters can be measured independently, and the flow of concrete in most cases seems to follow this relation (Ferraris, 1999). This model is written as:

$$\tau = \tau_y + \eta\dot{\gamma} \qquad\qquad \tau > \tau_y \qquad\qquad\qquad (3.1)$$

$$\dot{\gamma} = 0 \qquad\qquad\qquad \tau \le \tau_y \qquad\qquad\qquad (3.2)$$

Because SCC can exhibit shear thickening behaviour (Roussel et al., 2010; Heirman et al., 2009), which means that the plastic viscosity (η) increases with the shear rate ($\dot{\gamma}$), it can be modelled by the Herschel-Bulkley model (Vasilić et al., 2010). This model is a

generalisation of the Bingham model in such a way that, upon deformation, the viscosity can be shear thinning or shear thickening. The constitutive equation in this model is

$$\tau = \tau_y + \eta\dot{\gamma}^n \qquad\qquad \tau > \tau_y \qquad\qquad\qquad (3.3)$$

$$\dot{\gamma} = 0 \qquad\qquad\qquad \tau \leq \tau_y \qquad\qquad\qquad (3.4)$$

The fluid exhibits shear thinning, Bingham behaviour and shear thickening behaviour for n <1, n =1 and n >1, respectively.

3.4   Simulation of SCC flow

Since concrete is put into place in its plastic form, its fresh properties have a direct influence on the strength and durability in the hardened state (Zerbino et al., 2009). This is of prime importance in SCC as the prediction of its fresh behaviour is very difficult and sensitive to the composition and characteristics of its constituents. Although being verified to satisfy fresh properties by classical experimental tests, SCC may be prone to defects arising from problems accompanying its production like bleeding, segregation, incomplete filling, which are particularly problematic when SCC is cast in complex and heavily reinforced structural members. This could explain the reason why the classical tests such as slump flow, L-Box, J-ring and V-funnel tests are not always sufficient to fulfil the SCC self-compactibility criteria and to predict its behaviour. Therefore, performing numerical simulation of SCC can be a promising aid in overcoming these issues from the view point of:

➢ providing a useful tool for predicting the SCC rheological parameters (plastic viscosity and yield stress);

➢ examining whether or not the formwork is completely filled;

➢ investigating the blocking and passing behaviour of the mix as particles migrate through narrow gaps in reinforcements, especially when large aggregates and/or fibres are present;

➤ assisting in proportioning an SCC mix and optimising its ingredients, thus improving on the traditional trial and error SCC mix design;

➤ investigating the distribution of large aggregates during the flow of concrete and therefore avoiding segregation and ensuring the homogeneity of the mix;

➤ examining the distribution of fibres and their orientation in the formwork, therefore optimising the durability and strength of concrete.

3.4.1   Methods for simulating SCC

The simulation methods of concrete flow can be divided into two main groups. First, methods that treat it as a homogeneous medium in which SCC is regarded as a viscous fluid without particle inclusions. It is the easiest and fastest way to simulate fresh concrete. The drawback of this method is that the particle blocking and segregation cannot be predicted (Roussel, 2007). Second, methods that treat concrete as a heterogeneous medium in which attention is paid to the differences in the physical properties between the liquid and granular components used in the concrete and their effects on the flow. This method highlights the distribution of the large aggregates in this mix, allowing the actual distribution of coarse aggregates and/or fibres (and their orientations) to be revealed during the flow. However, selecting the right technique depends on the purpose of the simulation and whether the solid components of concrete are considered as separate particles or are embedded in the mortar.

3.4.2   Numerical solution strategy of simulation techniques

In the numerical simulation, there are, in principle, some basic steps as shown in Figure 3.2. In the first step, the focus is on the observed physical phenomenon, which will be represented by a mathematical model with a set of governing equations. To numerically solve the governing equations, the next step involves dividing the continuum problem domain into a discrete number of elements or components. This forms the computational frame for the numerical approximation which is based on a theory of function

approximations and includes discrete representation of the governing equations according to the discretization technique used.
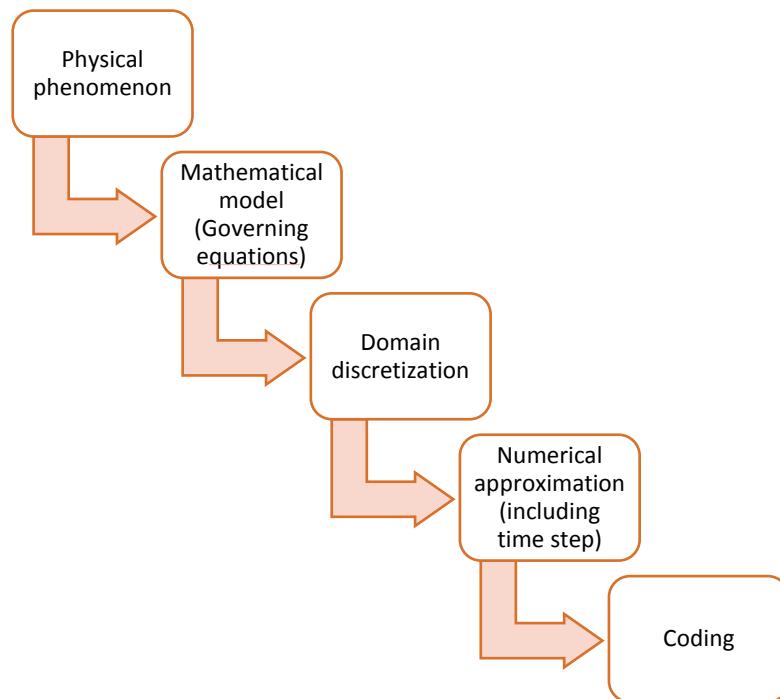
Figure 3.2: The numerical strategy of the simulation technique

3.4.3   The governing equations used in SCC simulation

SCC is represented as a fluid and its flow is governed by the equations of fluid motion: the continuity, momentum and energy conservation equations which are based on the fundamental physical laws of conservation. However, when there is no change in the temperature during a test and the heat flux in the continuum is absent, the energy can be assumed to be identically conserved. Also, since the viscosity and density are not affected by the temperature, the energy conservation equation can be omitted.

The continuity equation or the mass conservation equation in the Lagrangian form is

$$\frac{D\rho}{Dt} + \rho \nabla \cdot \mathbf{v} = 0 \tag{3.5}$$

Here ρ, t, and $\mathbf{v}$ are respectively, the fluid particle density, time, and particle velocity. $\nabla \cdot \mathbf{v}$ is the time rate of change of the volume of a moving fluid element. *D* denotes the substantial or material derivative.

For an incompressible fluid, the density is constant, and therefore (3.5) becomes

$$\nabla \cdot \mathbf{v} = 0 \qquad\qquad\qquad (3.6)$$

If gravity (g) is the only body force acting on the continuum, the momentum conservation equations in the Lagrangian form can be written in the compact vectorial form as

$$\frac{D\mathbf{v}}{Dt} = -\frac{1}{\rho}\nabla P + \frac{1}{\rho}\nabla . \boldsymbol{\tau} + g \qquad\qquad (3.7)$$

where *P*, g and $\boldsymbol{\tau}$ are pressure, gravitational acceleration, and shear stress, respectively.

3.4.4   Fundamental approaches describing the physical governing equations

To describe the physical governing equations, there are two fundamental approaches: Eulerian and Lagrangian. The Eulerian approach is a spatial description used to track a certain fixed location in the flow field and follows the change in properties (velocity, temperature, density, mass, or concentration, etc.) as different fluid elements pass through that location.

Suppose that the velocity is being followed at a location in the fluid flow through which different fluid elements pass at different times (Figure 3.3)

$$t_1 \rightarrow \mathbf{v}_1 \quad , \quad t_2 \rightarrow \mathbf{v}_2$$

The time rate of change of the velocity in such a measurement is denoted as $\left.\dfrac{\partial \mathbf{v}}{\partial t}\right|_{(x,y,z)}$, which is the partial derivative of the velocity with respect to time. Note that the suffix (*x, y, z*) implies that the observer records the change in the property at the fixed location (*x, y, z*). $\left(\dfrac{\partial \mathbf{v}}{\partial t}\right)$ is also called the local rate of change of that property (velocity in this case).
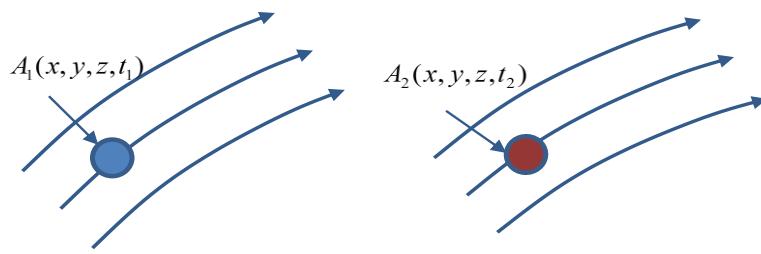
Figure 3.3: Different fluid elements at different times at a fixed location in the fluid flow (After: Deeb, 2013)

The Lagrangian approach is used to track a material element of the fluid as it moves and the changes in its properties, e.g. velocity are monitored. Figure 3.4 illustrates that at time t_1, the 'material' or 'particle' of the fluid '*A*' has moved from location (x_1, y_1, z_1) to another location (x_2, y_2, z_2) at time t_2. Its property, say velocity, is recorded, as the material moves in the flow-field. The recorded property is associated with the same fluid particle, but at different locations and at different times.
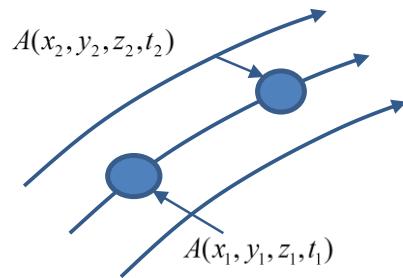
Figure 3.4: Fluid particle motion from time t_1 to time t_2 (After: Deeb, 2013)

The time change of the velocity in such a measurement is denoted as $\dfrac{D\mathbf{v}}{Dt}$, which is called material derivative or substantial derivative. It reflects time rate of change in the velocity (or any other properties) of the tagged fluid particle as observed by an observer moving with the fluid. An example of the Lagrangian method is the smooth particle hydrodynamics (SPH) method.

The two derivatives, Lagrangian and Eulerian, are related to each other, e.g. for velocity

$$\frac{D\mathbf{v}}{Dt} = \frac{\partial \mathbf{v}}{\partial t} + \left(\mathbf{v}.\nabla\right)\mathbf{v} \qquad\qquad (3.8)$$

where the term $\mathbf{v}.\nabla$ is the convective derivative, which defines the time rate of change as the fluid element moves from one location to another in the flow field.

3.4.5   Domain Discretization

In the numerical simulations, the continuum problem domain needs to be divided into a finite number of discrete components in order to numerically solve the governing equations. This technique is different according to the numerical method used. From a graphical point of view, computational modelling can be divided into two main categories, grid and particle-based methods. Figure 3.5 illustrates the two different discretizations of the same geometrical domain.
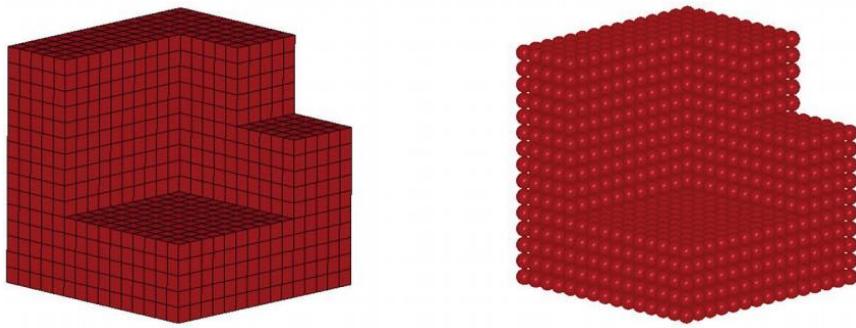
Figure 3.5: Comparison between grid method (left) and particle method (right) for the same geometry (After: Vesenjak and Ren, 2007)

In the grid or mesh-based method, the continuum domain is divided into small discrete domains connected to each other by nodes. The accuracy of the numerical approximation is closely related to the mesh topography (i.e. shape, size...etc.). Examples of the mesh-based method are the finite element method (FEM), the finite difference method (FDM), and the finite volume method (FVM). Because the generation of the mesh for a grid method is a prerequisite, for complicated problems it can be more difficult than solving

the problem itself since the results are based on the quality of the mesh (Vesenjak and Ren, 2007). Therefore, mesh-less methods become more attractive to treat problems where it is difficult to use grid based methods.

In particle (or mesh-less) methods, a domain is represented by a set of nodal points or particles without using any mesh to connect those nodes. In these methods, large deformations, moving interfaces, difficult boundary conditions and complex geometries are easy to handle, since the connectivity among nodes is generated as part of the computation. As an example of mesh-free methods, which will be used for the analysis of fluid flow in this thesis (Chapter 7), is the smooth particle hydrodynamics (SPH) (Kulasegaram and Karihaloo, 2013; Deeb et al., 2014a,b).

3.4.6   Numerical approximation- Smooth Particle Hydrodynamics (SPH)

In engineering computational mechanics, mesh-based numerical methods are the primary computational methodology. However, its efficiency in many complex problems (e.g. free surface problems, large deformations) is still limited, and therefore the necessity for developing other computational methods has arisen to avoid the mesh dependency. In this regard, one of the attractive mesh-free formulations is the Smooth Particle Hydrodynamics (SPH). It is a Lagrangian particle-based technique for approximating the continuum fluid through the use of particles. SPH was originally developed to solve particular astrophysical problems in three-dimensional open space (Lucy, 1977; Gingold and Monaghan, 1977). Because the motion of SPH particles is similar to liquid or gas flow, those particles can be simulated using the governing equations of hydrodynamics (Liu and Liu, 2003).

Thanks to its completely mesh-free nature, with SPH it is easier to model flows with complex geometry, free surfaces, discontinuity and large deformation. The Lagrangian nature of SPH allows the grid to be embedded in the material and thus reduces some of the material interface problems associated with Eulerian techniques. Since it was first proposed, SPH has gained significant popularity, and with the continuing improvement and modifications its accuracy, stability and adaptability have reached an acceptable level

for different engineering applications. In the field of self-compacting concrete (SCC), which is recognised as a homogeneous fluid that consists of particles of different sizes and shapes, SPH has been used and proved to be efficient and accurate in simulating the flow and monitoring the movement of large aggregates and/or short steel fibres (Deeb et al., 2014a,b,c). It also plays an essential role in the mix proportioning to achieve appropriate mix ingredients, thereby saving time, effort and materials (Karihaloo and Ghanbari, 2012; Deeb and Karihaloo, 2013). In addition, SPH provides a useful tool for predicting the yield stress (τ_y) of SCC mixes accurately in an inverse manner from the flow spread (Badry et al., 2016).

3.4.6.1   Key characteristics employed to solve problems in SPH

SPH is an integral interpolation method to approximate values and derivatives of continuous field quantities by using discrete sample points (Gingold and Monaghan, 1977). As reported by Liu and Liu (2003), the key characteristics employed to solve problems in SPH are:

SPH support domain: The support domain for a particle, say particle '*a*', is the domain where all the information for all particles inside this domain is used to determine the information at the point '*a*' (see Figure 3.6). This means that any physical property of a particle '*a*' can be obtained by summing the same property of particles that lie in the support domain Ω within a radius *r* of the observed particle '*a*' and multiplying the sum by a smoothing function *W*.

Figure 3.6 shows the support domain of particle '*a*' and all the neighbouring particles '*b*' that lie in it. Particles which are closer to the centre have a greater contribution to the property unlike particles outside the influence domain that have no contribution at all, the influence area of each particle will be therefore defined using the kernel function. This part is very important in terms of computational effort; for instance, problems with large deformation that require a huge number of particles could take unacceptably long CPU time to solve.
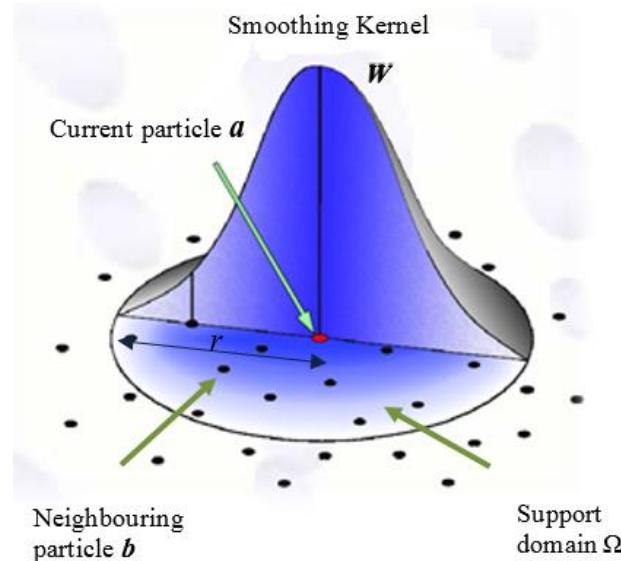
Figure 3.6: Distribution of physical properties of a particle (After: Deeb, 2013)

Kernel approximation: SPH provides a concept to approximate the spatial derivative using particles, which therefore makes computing the spatial derivatives in particle-based method as easy as in grid-based methods. Each particle, say particle '*a*' as illustrated in Figure 3.6, carries the field variables such as the mass (m_a), density (ρ_a), pressure (P_a), velocity ($\boldsymbol{v}_a$), position ($\boldsymbol{r}_a$), temperature (T_a), colour (c_a) and any other quantities depending on the nature of the flow and of the fluid. The mass is constant through the simulations. However, the other physical quantities are updated every time step. These field variables are represented by integral functions, the so-called kernel or smoothing functions (Figure 3.6).

Particle interpolation: Particle approximation in SPH involves discretising the entire domain problem into a limited number of particles N, and then approximately calculating all the field variables on these particles. The finite volume (V_b) of the particle, say particle '*b*' that lies in the support domain, is calculated as $V_b = \dfrac{m_b}{\rho_b}$, where ρ_b and m_b are density and mass of the particle, respectively. The inclusion of these properties makes SPH the ideal numerical solution to simulate dynamic fluid flow applications such as the flow of SCC.

A quantity $f(\mathbf{x})$ (Figure 3.7) at an arbitrary position **x** is approximated using quantities f_b at sample positions $\mathbf{x}_b$. The kernel function *W* realises a diminishing influence of particles at larger distances. Over all the particles N in the support domain, $f(\mathbf{x})$ can be expressed in the equivalent forms of discretized particle approximation (Bonet and Lok, 1999)

$$f(\mathbf{x}) = \sum_{b=1}^{N} V_b f(\mathbf{x}_b) W_b(\mathbf{x}) \tag{3.9}$$

where $W_b(\mathbf{x})$ is an interpolating kernel, representing the kernel with compact support domain of radius *r* (Figure 3.7). There are different possibilities in selecting the kernel function *W*. Spline kernel functions are the most common as they can be designed to have specific characteristics and possess a compact support (Bonet and Kulasegaram, 2000).

The differential of equation (3.9) is given by

$$\nabla f(\mathbf{x}) = \sum_{b=1}^{N} V_b f(\mathbf{x}_b) \nabla W_b(\mathbf{x}) \tag{3.10}$$

where the quantity $\nabla W_b(\mathbf{x})$ denotes the gradient of the kernel, which is taken as centred on the position of particle *a* (Figure 3.7).
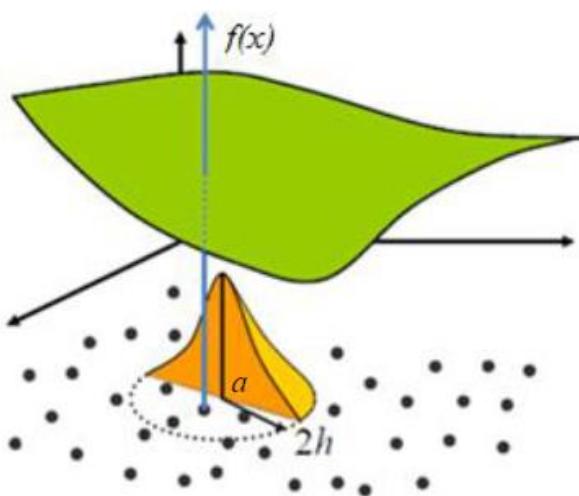
Figure 3.7: Particle approximation of function *f(x)* (After: Deeb, 2013)

Equations (3.9) and (3.10) state that the value of any function (or its differential) at any position is approximated using the average of the values of the function at all the particles within the support domain (particles b=1,2,…N) of that particle weighted by the smoothing function, $W_b(\mathbf{x})$. The application of equation (3.9) to compute the approximate value for the density of a continuum leads to the classical SPH equation

$$\rho(\mathbf{x}) = \sum_{b=1}^{N} m_b W_b(\mathbf{x}) \tag{3.11}$$

3.4.6.2   Boundary conditions

Boundary conditions in SPH should be imposed to ensure balancing the inner particle forces to prevent those particles from penetrating the wall. To impose boundary conditions in SPH, different methods are available, such as repulsive forces (Monaghan, 1994), mirror particles (Takeda et al., 1994; Cummins and Rudman, 1999) and dummy particles (Shao and Lo, 2003; Lee et al., 2008; Amini et al., 2011). In this thesis, the dummy particle approach will be used as will be explained in Chapter 7.

3.4.6.3   Numerical solution strategies in SPH

In SPH enforcing incompressibility can be pursued using two different approaches - the truly incompressible SPH (ISPH) (Kulasegaram et al., 2011) and the weakly compressible SPH (WCSPH) (Monaghan, 1994; Lee et al., 2008). In ISPH approach, a projection method based on the predictor-corrector time stepping scheme is used to track the flow in which the SCC incompressibility has been imposed exactly through the pressure Poisson equation (as will be explained in Chapter 7). In WCSPH approach, the incompressibility condition is imposed approximately through the so-called weakly or quasi-compressible SPH (Monaghan, 1994). It leads to the replacement of the real incompressible fluid by an artificial quasi-compressible fluid having a small, user-defined, fluctuation in the density in which the time-consuming solution of the Poisson equation can be avoided (Becker and Teschner, 2007). However, WCSPH requires a much smaller time step in order to keep the density fluctuation down to 1% to avoid numerical instability (Lee et al., 2008). This can

be circumvented by implementing ISPH (as shown in Chapter 7) in which the pressure and velocity are computed separately.

3.5   Concluding remarks

In this chapter, the rheology of SCC was introduced, with an overview of the rheological parameters, the methods of their measurement and the models describing a fluid flow. In addition to its rheology, the simulation of SCC flow, highlighting the numerical strategy used in its techniques, was briefly looked at. A review of SPH as a suitable method to model the SCC flow has also been given briefly in this chapter.

A review of the methods used for measuring the rheological parameters indicates that, due to the complexity of the material behaviour and the concrete rheometers setups, it is nearly impossible to obtain these rheological properties reliably from rheometer measurements. For this reason alternative methods have been developed to determine these parameters. The yield stress is estimated in an inverse manner from the measured t_{500} and flow spread of the mix in a cone flow test using SPH. The plastic viscosity can be determined using the micromechanical procedure based on the plastic viscosity of the paste (as will be described in Chapter 4). Here, the micromechanical procedure has not only been used for determining the SCC plastic viscosity, it also paved the way for developing a rational mix design method for proportioning SCC mixes. The steps taken to develop this rational method will be described in Chapter 4.

As we have seen from the reviewed literature, SPH can assist in different areas of SCC application, such as proportioning SCC mixes, providing a useful tool for predicting the SCC rheological parameters and modelling the flow and monitoring the movement of large aggregates and/or short steel fibres in the cone slump flow and L-box tests. Beyond the scope of its mentioned capabilities, there is another scope for SPH methodology to simulating SCC mixes in the J-ring test. This will be used to examine whether or not the produced mixes meet the passing ability criterion and flow homogeneously with no blockage in complex and heavily reinforced structural members. In Chapter 7 we will report on the simulation of the flow of fresh SCC in the J-ring test using the SPH approach.

Chapter 4

Proportioning of SCC mixes based on target plastic viscosity and compressive strength: mix design procedure

4.1   Introduction

Self-compacting concrete (SCC) requirements are mostly influenced by the fractions of the mix ingredients. In other words, to fulfil its main functional requirements (filling ability, passing ability and segregation resistance), major work in SCC should take into account designing appropriate volume fractions of the mix ingredients. Without paying attention to its mix proportioning, SCC will remain to be designed by a number of time and material-consuming trials before an optimum mix proportion is reached. Although it has passed from the research phase into real application, methods for proportioning SCC mixes have not kept pace with their production techniques. This chapter develops a rational mix design method for SCC based on the desired target plastic viscosity and compressive strength of the mix. The simplicity and usefulness of this method are enhanced by the provision of design charts as a guide for mix proportioning. The characteristic cube strength of these charts varied between 30 and 80 MPa at 28 days age, and the target plastic viscosity between 3 and 15 Pa s: the upper bound of all mix grades was 15 Pa s, whereas the lower bound varied between 3 – 8 Pa s in mix grade range 30 – 80 MPa. Several examples on the use of the design charts are given. In the next chapter, experimental validation of the mix design procedure is provided on a series of SCC mixes in both the fresh and hardened states.

The contents of this chapter have been published in the journal 'Journal of Sustainable Cement-Based Materials' (see publication 2 in the list in Chapter 1).

4.2   Exploitation of an idea: mix design development

The proportioning of self-compacting concrete (SCC) mixes requires a balance between their flow and passing ability on the one hand and the resistance to segregation on the other (Corinaldesi and Moriconi, 2004; Wu and An, 2014; Okamura and Ouchi, 2003). The early mix proportioning approaches proposed by Okumara and Ouchi (1999) and Domone (2000) and later developed by others (Okamura et al., 2000) were all heuristic in nature requiring many trial mixes. However, the extensive research work carried out on the rheological properties of SCC (Roussel, 2006b; Tregger et al., 2012; Saak et al., 2001;

Chidiac and Mahmoodzadeh, 2009; Figueiras et al., 2014; Wallevik and Wallevik, 2011; Petersson and Billberg, 1999; Li and Kwan, 2011; Li and Kwan, 2013) has greatly improved the proportioning of SCC mixes. A summary of different mix proportioning approaches can be found in Shi et al. (2015). The European Federation of National Trade Associations (EFNARC) guidelines (EFNARC, 2005) give typical ranges of primary ingredients; the actual amounts depend on the desired strength and other performance requirements. Thus the mix proportioning still involves considerable trial and error.

A rigorous method for proportioning normal and high strength SCC mixes based on their plastic viscosity has been proposed in (Karihaloo and Ghanbari, 2012 and Deeb and Karihaloo, 2013). It exploits the expression for the plastic viscosity of an SCC mix developed by Ghanbari and Karihaloo (2009) using micro-mechanical principles. This expression shows how the known plastic viscosity of the paste is increased by the addition of solid phase particles, i.e. filler, fine and coarse aggregates. The contribution of each of the solid phases to the overall increase depends on its volume fraction and shape of its particles. As a result, the final expression for the plastic viscosity of an SCC mix is the product of the known plastic viscosity of the paste and contributions of each of the solid phases.

While the method proposed in (Karihaloo and Ghanbari, 2012 and Deeb and Karihaloo, 2013) is rigorous and based on sound physical principles, it produces a bewildering array of mixes that reach the target plastic viscosity but does not give any practical guidelines on how to choose the most appropriate mix. Moreover, the method was developed on the basis of reference mixes of a range of known cube compressive strength, but the latter was not explicitly imposed as a design criterion.

This chapter will overcome the above shortcomings of this method for proportioning SCC mixes. Practical guidelines in the form of design charts will be provided for choosing the mix proportions that achieve the target compressive strength and the target plastic viscosity.

4.3   Target compressive strength

The compressive strength of a concrete mix is mostly determined by the ratio of water to cementitious material (w/cm) under given curing conditions. A regression analysis was performed on the data collected from many published sources (Deeb and Karihaloo, 2013; Beygi et al., 2013a,b; Dinakar et al., 2013a,b; Panesar and Shindman, 2011; Felekoğlu et al., 2007; Rozière et al., 2007; Nikbin et al., 2014a,b; Boukendakdji et al., 2012; Persson, 2001; Leemann and Hoffmann, 2005; Parra et al., 2011; Nuruddin et al., 2014; Zhu and Gibbs, 2005; Carpinteri and Brighenti, 2010; Rabehi et al., 2013; Beygi et al., 2014a; Dinakar et al., 2008; Collepardi et al., 2007; Khaloo et al., 2014; Bui et al., 2002; Domone, 2007; Ferrara et al., 2007) and on the data obtained in various studies in Cardiff University (Figure 4.1). It was found that the compressive strength of SCC (MPa) could be best fitted by an Abrams-type relation (R^2 =0.94):

$$f_{cu} = \frac{195}{12.65^{(w/cm)}}$$ (4.1)

where f_{cu} is the 28-day equivalent cube compressive strength (MPa) and w/cm is the ratio of water to cementitious materials (i.e. cement + cement replacement material, e.g. ggbs). The large scatter in the surveyed data is no doubt a reflection of the differences in the curing conditions, the cement type, the type of cement replacement material and replacement levels up to 30% and the amount and the maximum size of coarse aggregate. The values have been adjusted for the size of the cube test specimens to that of 100 mm cubes. It was found however (see later) that formula (4.1) overestimates the cube compressive strength of low strength (30 – 40 MPa) SCC mixes. This is perhaps a result of the presence of high powder content in these mixes, as has also been stated in (Nanthagopalan and Santhanam, 2009). For 30 MPa mix, the w/cm predicted by (4.1) needs to be decreased by approximately 14% and that for 40 MPa mix by 8%.
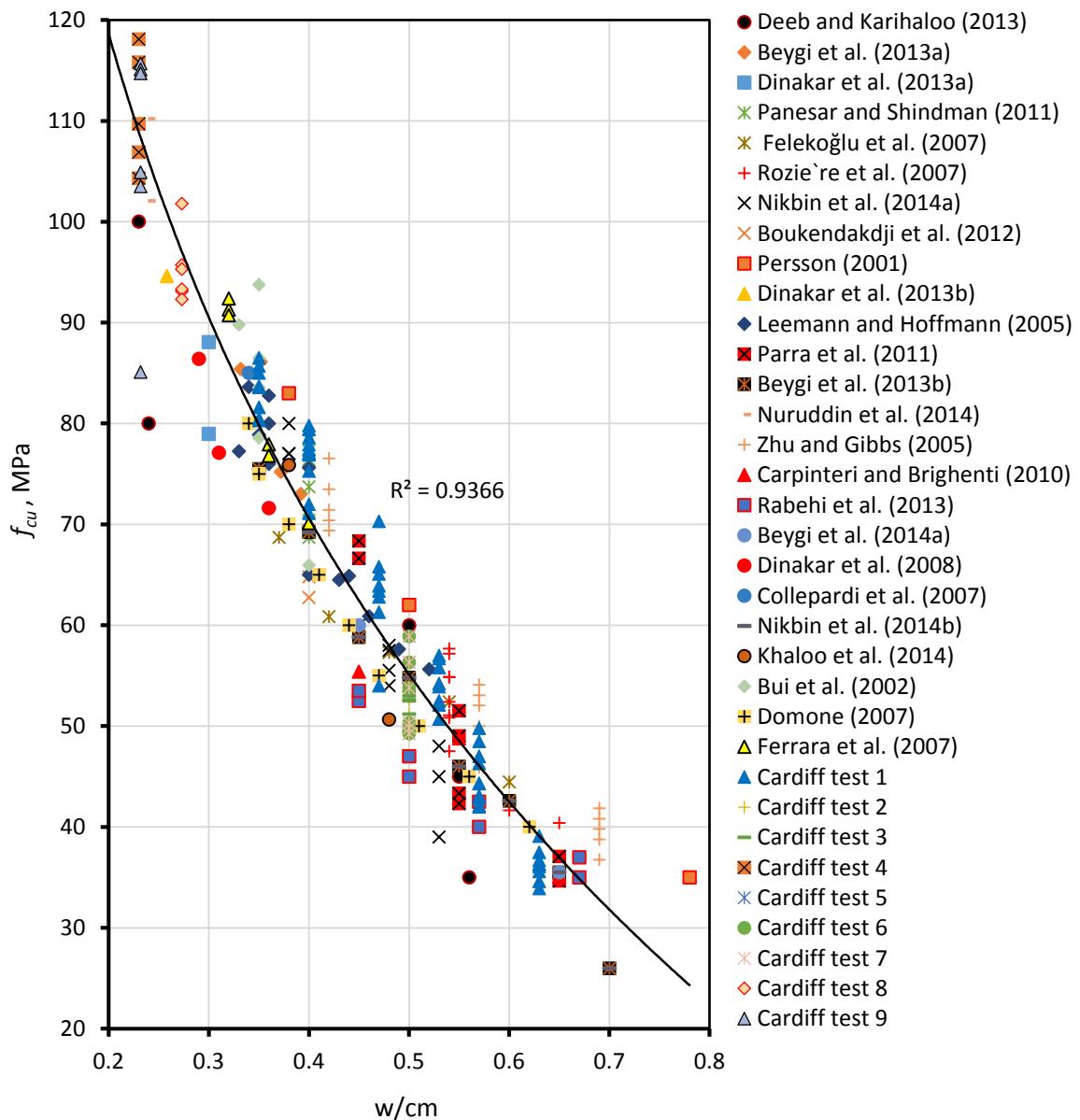
Figure 4.1: Relation between compressive strength and water to cementitious material ratio

4.4   Target plastic viscosity

Fresh SCC is a non–Newtonian fluid best described by a Bingham–type model. This model contains two rheological parameters of SCC, namely its yield stress and plastic viscosity (Dransfield, 2003). It is known however, that the yield stress of SCC mixes is low (in the order of tens of Pa) in comparison with vibrated concrete mixes and it remains so over a wide range of plastic viscosity (Dransfield, 2003; Badry, 2016). Thus the most important parameter is the plastic viscosity which changes with the plastic viscosity of the paste and the mix composition.

The plastic viscosity of a homogeneous viscous fluid, such as a paste (mixture of cement, cement replacement material, water and super-plasticiser) can be measured rather accurately with a viscometer which is not possible for a non-homogenous viscous fluid such as an SCC mix. There is a large scatter in the plastic viscosity of the same SCC mix measured with different rheometers, as has been noticed by many researchers (Wallevik and Wallevik, 2011; Banfill et al., 2000; Feys et al., 2007). Ghanbari and Karihaloo (2009) have therefore proposed a micromechanical procedure for estimating the plastic viscosity of an SCC mix knowing the plastic viscosity of the paste used in it. In this procedure, SCC is regarded as a two–phase suspension in which the solid phase is suspended in a viscous liquid phase. The increase in the plastic viscosity of the liquid phase as a result of the addition of the solid phase (filler, fine and coarse aggregates) is estimated in a stepwise manner from the two-phase suspension model. In the first step, the solid phase is the finest solid material, for example the filler in the viscous fluid phase i.e. the paste. In the next step, the finest solid i.e. fine aggregate is the solid phase suspended in the viscous fluid phase now formed by the two-phase suspension from the first step. This procedure is continued until all the solid phase ingredients have been added. The plastic viscosity of the i–th liquid-solid suspension can be estimated from the plastic viscosity of the preceding (i–1)th phase as

$$\eta_{ci} = \eta_{ci-1} \times f_i(\phi_i) \tag{4.2}$$

Here,

η_{ci} = plastic viscosity of the i–th liquid–solid suspension; η_{ci-1} = plastic viscosity of the preceding (i–1)th phase. In the first step i = 1, η_{c0} is the known plastic viscosity of the paste; $f_i(\phi_i)$ = a factor larger than unity that predicts the increase in the plastic viscosity induced the solid phase with a volume fraction ϕ_i. Figure 4.2 shows the hierarchy of these two-phase (liquid-solid) suspensions used in the estimation of the plastic viscosity of all mixes developed based on the viscosity of the cement paste used in them.

$$\eta_{C1} = \eta_p \, f_1(\phi_1) \qquad \eta_{C2} = \eta_{C1} \, f_2(\phi_2) \qquad \eta_{C3} = \eta_{C2} \, f_3(\phi_3) \qquad \eta_{C4} = \eta_{C3} \, f_4(\phi_4)$$
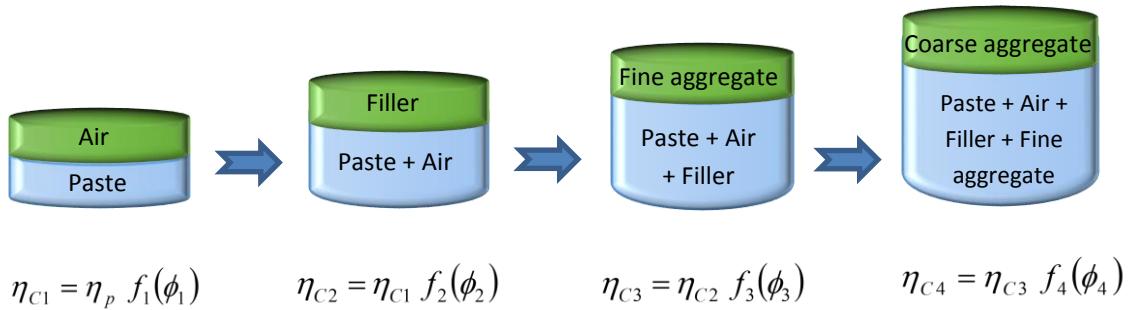
Figure 4.2: Hierarchy of two-phase liquid-solid suspensions constituting an SCC mix

According to this procedure, the plastic viscosity of an SCC mix is given by:

$$\eta_{mix} = \eta_{paste} \times f_1(\phi_1) \times f_2(\phi_2) \dots \times f_n(\phi_n) \tag{4.3}$$

where n is the total number of solid phases in the mix. Besides the filler, fine and coarse aggregates, air voids can also be treated as a second phase in a viscous suspension. Einstein was the first to develop an expression $f_i(\phi_i)$ for dilute suspensions (second phase volume fraction less than 10%) containing randomly distributed rigid or hollow spheres with no hydrodynamic interactions (Koehler and Fowler, 2007):

$$f_i(\phi_i) = 1 + [\eta]\phi_i \tag{4.4}$$

The numerical factor $[\eta]$ is equal to 2.5 for rigid spherical particles and to 1 for spherical air bubbles that are packed randomly in a hexagonal arrangement. Subsequent investigations have proved that the numerical factor 2.5 is quite accurate even for rigid ellipsoidal particles with an aspect ratio less than 3.

However, at higher concentrations of the solid phase (volume fraction >10% up to the maximum possible volume fraction, ϕ_m), the hydrodynamic interactions between the particles and the Brownian motions cannot be ignored. In this situation, the Krieger–Dougherty (Krieger, 1959) formula (Eq. (4.5)) has been found to be appropriate for cement–based suspensions. The value of ϕ_m is 0.74 for hexagonal close packing, 0.63 for random hexagonal packing, and 0.524 for cubic packing

$$f_i(\phi_i) = (1 - \frac{\phi_i}{\phi_m})^{-[\eta]\phi_m} \tag{4.5}$$

The particle size distribution significantly affects ϕ_m. Furthermore, the numerical factor $[\eta]$ and ϕ_m depend upon the shear rate; the former tends to decrease with increasing shear rate, whereas the latter shows the opposite trend. However, $[\eta]$ and ϕ_m change in such a way that a decrease in the first leads to an increase in the second, but the product of both changes remains practically the same and equal, on average, to 1.9 (de Kruif et al., 1985). In most SCC mixes, the volume fractions of the filler, fine and coarse aggregates generally exceed 10%, so that their contribution to the increase in the known plastic viscosity of the paste is given by Eq. (4.5). The volume fraction of the trapped air bubbles is however low, around 2%, such that Eq. (4.4) with the numerical factor equal to 1 is appropriate. For simplicity, this 2% increase due to trapped air is included in the plastic viscosity of the paste in Eq. (4.6):

$$\eta_{mix} = \eta_{paste} \times \left(1 - \frac{\phi_{Filler}}{\phi_m}\right)^{-1.9} \times \left(1 - \frac{\phi_{Fine\ Agg.}}{\phi_m}\right)^{-1.9} \times \left(1 - \frac{\phi_{Coarse\ Agg.}}{\phi_m}\right)^{-1.9} \qquad (4.6)$$

Note that the packing density (i.e. the maximum volume fraction, ϕ_m) increases with the addition of solid phases. When the first solid phase is added to the paste, the packing is loose so that it is appropriate to assume cubic packing. When however, the last solid phase is added to the suspension, the packing is very dense and it is appropriate to assume hexagonal close packing.

4.5   Calculating the plastic viscosity of SCC mixes

The calculation of the plastic viscosity will be demonstrated on a mix 40A (as it is designed in Chapter 5) as an example and it is the same procedure for all developed SCC mixes.

Step 1: Estimating the plastic viscosity of the liquid phase (η_{paste}).

The plastic viscosity of the cement paste (cement + ggbs + SP + water + air) is estimated by using the literature (Sun et al., 2006; Nehdi and Rahman, 2004) and it equals to 0.18 Pa s (see Table 4.1).

Table 4.1: Estimated plastic viscosity of the paste (cement +ggbs + SP+ water+ air)

w/cm	η_{paste}, Pa s	$\eta_{paste+air\ voids}$, Pa s
0.63	0.104	0.11
0.57	0.176	0.18
0.53	0.224	0.23
0.47	0.286	0.29
0.40	0.330	0.34
0.35	0.365	0.37

Step 2: Adding the first solid phase i.e. limestone powder (LP)

In this case, limestone powder (LP) is considered the solid phase and cement paste (cement + ggbs + SP + water + air) is the liquid phase. The volume fraction of the solid phase is determined using Eq. (4.7):

$$(\phi_{LP} = \frac{v_{LP}}{v_{LP}+v_p})$$ (4.7)

Here, $v_{LP:}$ is the volume fraction of the solid phase (limestone powder), v_p: is the volume of the continuous matrix phase (paste volume) in which the solid phase is suspended. After calculating the volume of each ingredient in the mix, the volume of paste is $v_p = 0.346$ m³, limestone powder is considered the solid phase and the components within the container are the liquid phase. The volume fraction of LP is:

$$\phi_{LP} = \frac{0.041}{0.041+0.346} = 0.106 > 0.10$$

Using Eq. (4.5); ($[\eta]\times\phi_m$) = -1.9 and ϕ_m= 0.524, gives;

$$f_{LP}(\phi_{LP}) = \left(1 - \frac{0.106}{0.524}\right)^{-1.9} = 1.536$$

Based on Eq. (4.2); the plastic viscosity of the suspension is:

$$\eta(\phi_{LP+air+p}) = \eta_{paste}\times f_{LP}(\phi_{LP}) = 0.18\times 1.536 = 0.276 \text{ Pa s}$$

Step 3: Adding the fine aggregate (FA)

Fine aggregate (FA) is now considered as the solid phase and the ingredients in the container as the liquid phase. The volume fraction of FA is

$$\phi_{FA} = 0.420 > 0.10$$

Using Eq. (4.5); ($[\eta]\times\phi_m$) = -1.9 and ϕ_m = 0.63, gives;

$$f_{FA}(\phi_{FA}) = \left(1 - \frac{0.420}{0.630}\right)^{-1.9} = 8.064$$

Based on Eq. (4.2); the plastic viscosity of the mix so far is:

$$\eta(\phi_{FA+LP+air+p}) = \eta_{paste}\times f_{LP}(\phi_{LP})\times f_{FA}(\phi_{FA})$$

$$= 0.18\times1.536\times8.064 = 2.230 \text{ Pa s}$$

Step 4: Adding the coarse aggregates (CA)

Coarse aggregates are now considered as the solid phase and the ingredients in the container as the liquid phase. The volume fraction of CA is

$$\phi_{CA} = 0.330 > 0.10$$

Using Eq. (4.5); ($[\eta]\times\phi_m$) = -1.9 and ϕ_m = 0.74, gives;

$$f_{CA}(\phi_{CA}) = (1 - \frac{0.330}{0.740})^{-1.9} = 3.071$$

Based on Eq. (4.2); the plastic viscosity of the final mix is:

$$\eta(\phi_{CA+FA+LP+air+p}) = \eta_{paste}\times f_{LP}(\phi_{LP})\times f_{FA}(\phi_{FA})\times f_{CA}(\phi_{CA})$$

$$= 0.18\times1.536\times8.064\times3.071 = 6.847\text{Pa s}$$

The results of the plastic viscosity calculation of mix 40A are summarised in Table 4.2.

Table 4.2: Summarising the results of the plastic viscosity calculation of mix 40A

Ingredients	Mass, kg/m³	Volume, m³	ϕ	$f(\phi)$
Paste	–	0.346	–	–
Limestone powder	100	0.041	0.106	1.536
Fine Aggregate	748	0.282	0.420	8.064
Coarse Aggregate	924	0.330	0.330	3.071

4.6   Basic steps of the proposed mix design method

The basic steps of the proposed mix design method are summarised below.

1. Select the desired plastic viscosity of the mix within the range of 3–15 Pa s, remembering that the slump cone t_{500} time increases with increasing plastic viscosity of the mix. EFNARC (2005) will be helpful in the choice of the desired plastic viscosity depending on the application;

2. Calculate the ratio of water to cementitious materials (w/cm) that produces the target cube characteristic strength from Eq. (4.1);

3. Choose the water content in the range of 150–210 kg/m³, following EFNARC (2005), and calculate the mass of cementitious materials (cm) in kg/m³. The amount of ggbs is assumed to be 25% of cementitious material (cm). It is known (Nehdi and Rahman, 2004) that the replacement of 25% cement (c) by ggbs has little or no effect on the paste viscosity;

4. Assume a trial super-plasticiser (SP) dosage as a per cent of the cementitious material mass in the range of 0.4–0.8 % for the MasterGlenium super-plasticiser used in this work. For this super-plasticiser the manufacturer's recommended dosage is 0.2 – 1.2 kg per 100 kg of cementitious material (BASF, 2014).

5. Estimate the plastic viscosity of the paste from the w/cm and SP/cm ratios (Sun et al., 2006; Nehdi and Rahman, 2004) (see Table 4.1). It is known that SP/cm has little impact on the paste viscosity; the major impact is on the yield stress (Domone, 2003);

6. Calculate the mass of the solid phase ingredients (filler, fine aggregate and coarse aggregate) according to their volume fractions, as explained in the examples below;

7. Check if the total volume of the produced mix is equal to 1.0 m^3. If not, scale the ingredient masses to achieve a total volume of 1.0 m^3;

8. Calculate the plastic viscosity of the mix using Eq. (4.6) and compare it with the desired one (step 1). If the difference is within ±5%, adopt the mix proportions. If not, choose a different combination of the volume fractions of the solid phase ingredients (step 6) and repeat steps 7–8.

The steps of the proposed mix design method are shown in the flow-chart below (Figure 4.3).
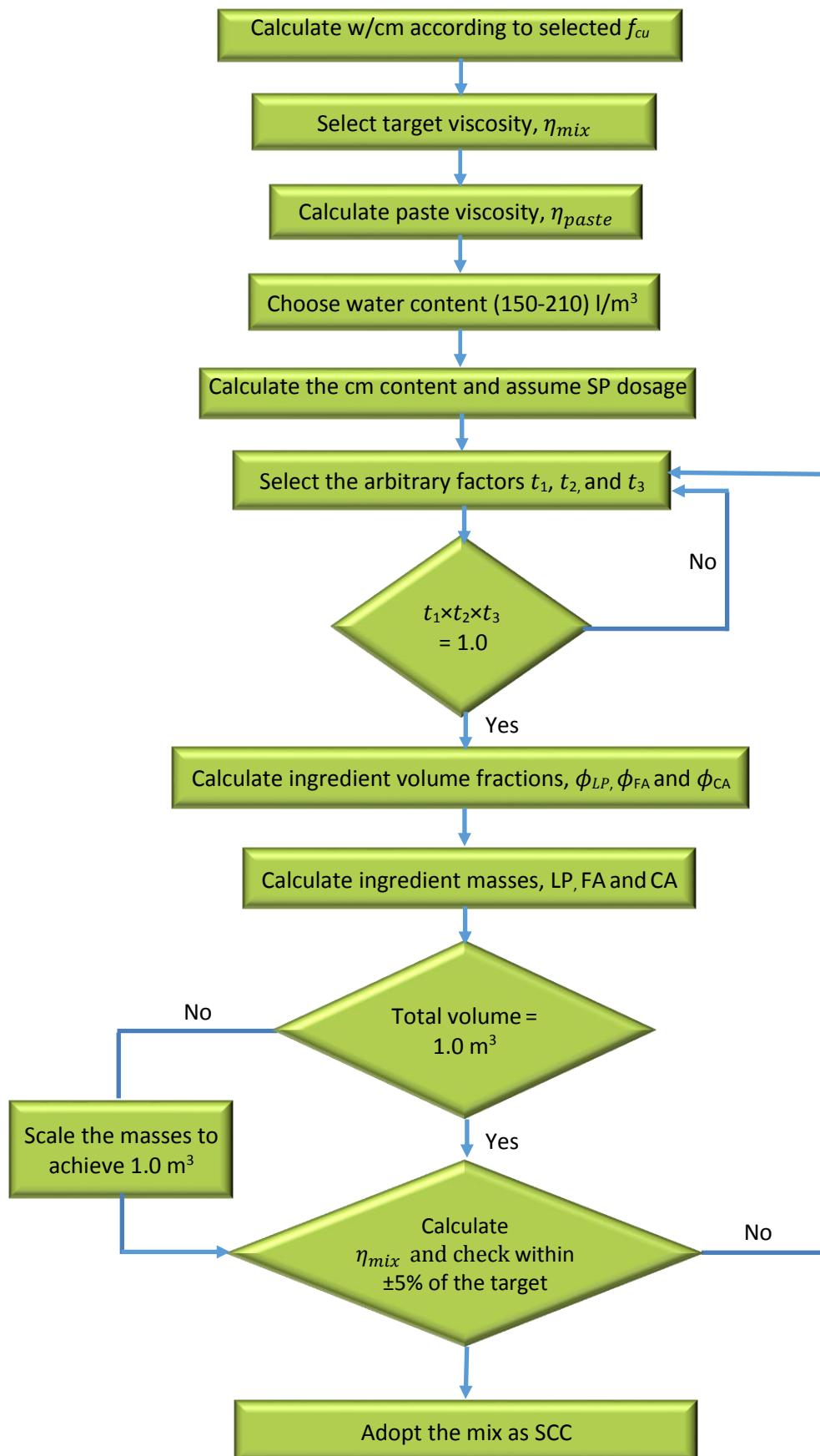
Figure 4.3: Flow-chart of the proposed mix design method

4.7   Examples of mix proportioning

As an example, let us proportion the mix of an SCC having a 28-day target cube compressive strength of 50 MPa. The procedure is as follows:

1. Suppose that the desired target plastic viscosity of the mix is equal to 7 Pa s;

2. Calculate the w/cm ratio from Eq. (4.1) corresponding to strength grade C50. It works out to be 0.53;

3. Assume the water content, w to be $200 \, \text{kg/m}^3$, then the mass of cementitious materials (cm);

$$cm = \frac{w}{(w/cm)} = \frac{200}{0.53} = 377.4 \, \text{kg/m}^3;$$

4. Assume a trial SP dosage as a per cent of mass of cementitious materials (say 0.65%) which equals $2.45 \, \text{kg/m}^3$;

5. Estimate the plastic viscosity of the paste; η_{paste} = 0.23 Pa s (Table 4.1);

6. In order to estimate the volume fractions of filler (LP), fine aggregate (FA) and coarse aggregate (CA), we first rewrite Eq. (4.6) as (note the use of different packing densities, as explained above);

$$\eta_{mix} = \eta_{paste} \times \left(1 - \frac{\phi_{LP}}{0.524}\right)^{-1.9} \times \left(1 - \frac{\phi_{FA}}{0.63}\right)^{-1.9} \times \left(1 - \frac{\phi_{CA}}{0.74}\right)^{-1.9}$$

$$\text{Let } u = \left(\frac{\eta_{mix}}{\eta_{paste}} \times 0.524^{-1.9} \times 0.63^{-1.9} \times 0.74^{-1.9}\right)^{\frac{1}{-1.9}}$$

so that the above equation becomes $u = (0.524 - \phi_{LP}) \times (0.63 - \phi_{FA}) \times (0.74 - \phi_{CA})$

Substituting η_{mix} = 7 Pa s and η_{paste} = 0.23 Pa s, gives

$u = 0.0405 = (0.524 - \phi_{LP}) \times (0.63 - \phi_{FA}) \times (0.74 - \phi_{CA})$

Let $x = \sqrt[3]{u} = 0.343$,

then the values of ϕ_{LP}, ϕ_{FA} and ϕ_{CA} are given by

$\phi_{LP} = 0.524 - t_1 \times x$, $\phi_{FA} = 0.63 - t_2 \times x$, $\phi_{CA} = 0.74 - t_3 \times x$

where, t_1, t_2, and t_3 are arbitrarily chosen factors such that $t_1 \times t_2 \times t_3 = 1.0$ Let us choose $t_1 = 1.0$, $t_2 = 1.0$ and $t_3 = 1.0$, in the first instance.

For this choice of t_1, t_2, and t_3, the volume fractions of solid phases will be

ϕ_{LP}= 0.524−$t_1 \times x$= 0.524−1×0.343= 0.181

ϕ_{FA}= 0.63−$t_2 \times x$= 0.63−1×0.343= 0.287

ϕ_{CA}= 0.74−$t_3 \times x$= 0.74−1×0.343= 0.397

The amounts of solid phases, i.e. limestone filler (LP), fine aggregate (FA) and coarse aggregate (CA) that are suspended in the liquid paste are calculated according to their volume fractions (ϕ_i), knowing that the densities of cement, ggbs, water, super-plasticiser, limestone powder, fine aggregate and coarse aggregate are 2950, 2400, 1000, 1070, 2400, 2650 and 2800 kg/m^3, respectively:

$$\phi_{LP} = \frac{\frac{LP}{\rho_{LP}}}{\left(\frac{c}{\rho_c}+\frac{ggbs}{\rho_{ggbs}}+\frac{w}{\rho_w}+\frac{SP}{\rho_{SP}}+0.02\right)+\frac{LP}{\rho_{LP}}} \qquad \rightarrow \quad LP = 189 \text{ kg/m}^3$$

$$\phi_{FA} = \frac{\frac{FA}{\rho_{FA}}}{\left(\frac{c}{\rho_c}+\frac{ggbs}{\rho_{ggbs}}+\frac{w}{\rho_w}+\frac{SP}{\rho_{SP}}+\frac{LP}{\rho_{LP}}+0.02\right)+\frac{FA}{\rho_{FA}}} \qquad \rightarrow \quad FA = 465 \text{ kg/m}^3$$

$$\phi_{CA} = \frac{\frac{CA}{\rho_{CA}}}{\left(\frac{c}{\rho_c}+\frac{ggbs}{\rho_{ggbs}}+\frac{w}{\rho_w}+\frac{SP}{\rho_{SP}}+\frac{LP}{\rho_{LP}}+\frac{FA}{\rho_{FA}}+0.02\right)+\frac{CA}{\rho_{CA}}} \qquad \rightarrow \quad CA = 1126 \text{ kg/m}^3$$

7. The total volume of the SCC mix that the above ingredients will yield (including the volume occupied by trapped air bubbles, 0.02)

$$\text{Total Vol.} = \frac{c}{\rho_c} + \frac{ggbs}{\rho_{ggbs}} + \frac{w}{\rho_w} + \frac{SP}{\rho_{SP}} + \frac{LP}{\rho_{LP}} + \frac{FA}{\rho_{FA}} + \frac{CA}{\rho_{CA}} + 0.02$$

$$\text{Total Vol.} = \frac{377.4 \times 0.75}{2950} + \frac{377.4 \times 0.25}{2400} + \frac{200}{1000} + \frac{2.45}{1070} + \frac{189}{2400} + \frac{465}{2650} + \frac{1126}{2800} + 0.02 =$$

1.014 m^3

As the yield does not equal 1.0 m^3, the amounts of materials are adjusted, and the mix plastic viscosity is recalculated using Eq. (4.6).

cm= 377.4/1.014= 372.2 kg/m^3

w=200/1.014= 197.2 kg/m^3

SP= 2.45/1.014= 2.42 kg/m^3

LP= 189/1.014= 186 kg/m^3

FA= 465/1.014= 459 kg/m^3

CA= 1126/1.014= 1110 kg/m^3

$$\text{Total Vol.} = \frac{c}{\rho_c} + \frac{ggbs}{\rho_{ggbs}} + \frac{w}{\rho_w} + \frac{SP}{\rho_{SP}} + \frac{LP}{\rho_{LP}} + \frac{FA}{\rho_{FA}} + \frac{CA}{\rho_{CA}} + 0.02 = 1.0 \text{ m}^3$$

8. The mix plastic viscosity is calculated by using Eq. (4.6). As the difference between the target plastic viscosity and the actual mix plastic viscosity is within ±5%, the mix proportions after adjustment are acceptable. The mix masses before and after scaling to 1.0 m^3 are given in Table 4.3.

<p align="center">**Table 4.3: Mix constituents and plastic viscosity of an SCC mix**</p>

	Ingredient, kg/m^3							η, Pa s	Difference
	cement	ggbs	w	SP	LP	FA	CA		
Before adjust.	283	94	200	2.45	189	465	1126	–	
After adjust.	279	93	197	2.42	186	459	1110	7.04	0.6%
Density	2950	2400	1000	1070	2400	2650	2800	–	

However, the amount of coarse aggregate exceeds the limit in the guidelines (EFNARC, 2005), so it is necessary to reduce it and to adjust the mix proportions by choosing different arbitrary values of t_1, t_2 and t_3 for the same target plastic viscosity and strength:

Steps 1-5 are the same as described above.

6. In order to calculate the volume fractions of solid phases, let choose values of t_1, t_2, and t_3 different from those used above. Let t_1 = 1.1, t_2 = 0.7 and t_3 = 1.3 such that $t_1 \times t_2 \times t_3$ = 1.0. Accordingly, the volume fractions of solid phases work out to be ϕ_{LP} = 0.147, ϕ_{FA} = 0.390 and ϕ_{CA} = 0.294. The amounts of solid phases, i.e. limestone filler (LP), fine aggregate (FA) and coarse aggregate (CA) that are suspended in the liquid paste are calculated according to their volume fractions (ϕ_i);

$$\phi_{LP} = \frac{\frac{LP}{\rho_{LP}}}{\left(\frac{c}{\rho_c}+\frac{ggbs}{\rho_{ggbs}}+\frac{w}{\rho_w}+\frac{SP}{\rho_{SP}}+0.02\right)+\frac{LP}{\rho_{LP}}} \qquad \rightarrow \quad LP = 147 \text{ kg/m}^3$$

$$\phi_{FA} = \frac{\frac{FA}{\rho_{FA}}}{\left(\frac{c}{\rho_c}+\frac{ggbs}{\rho_{ggbs}}+\frac{w}{\rho_w}+\frac{SP}{\rho_{SP}}+\frac{LP}{\rho_{LP}}+0.02\right)+\frac{FA}{\rho_{FA}}} \qquad \rightarrow \quad FA = 707 \text{ kg/m}^3$$

$$\phi_{CA} = \frac{\frac{CA}{\rho_{CA}}}{\left(\frac{c}{\rho_c}+\frac{ggbs}{\rho_{ggbs}}+\frac{w}{\rho_w}+\frac{SP}{\rho_{SP}}+\frac{LP}{\rho_{LP}}+\frac{FA}{\rho_{FA}}+0.02\right)+\frac{CA}{\rho_{CA}}} \qquad \rightarrow \quad CA = 799 \text{ kg/m}^3$$

7. The total volume of the SCC mix that the above ingredients will yield (including the volume occupied by trapped air bubbles, 0.02);

$$\text{Total Vol.} = \frac{c}{\rho_c} + \frac{ggbs}{\rho_{ggbs}} + \frac{w}{\rho_w} + \frac{SP}{\rho_{SP}} + \frac{LP}{\rho_{LP}} + \frac{FA}{\rho_{FA}} + \frac{CA}{\rho_{CA}} + 0.02 = \ 0.972 \text{ m}^3$$

As the yield does not equal to 1.0 m^3, the amounts of ingredients are adjusted. The results are shown in Table 4.4.

8. The mix plastic viscosity is calculated by using Eq. (4.6). As the difference between the target plastic viscosity and the actual mix plastic viscosity is within ±5%, the mix proportions after adjustment are acceptable.

Table 4.4: Mix constituents and plastic viscosity of an SCC mix

| | Ingredient, kg/m³ | | | | | | | η, Pa s | Difference |
	cement	ggbs	w	SP	LP	FA	CA		
Before adjust.	283	94	200	2.45	147	707	799	–	
After adjust.	291	97	206	2.52	151	727	822	7.02	0.3 %
Density	2950	2400	1000	1070	2400	2650	2800	–	

In view of the arbitrariness in the choice of t_i, it is clear that there are many (theoretically infinite) combinations of the volume fractions of the solid phases that can be chosen for an SCC mix and still reach the target cube compressive strength and mix plastic viscosity. It is however possible that some of these combinations may not yield a satisfactory SCC mix. It is therefore necessary to use other sources of information based on accumulated knowledge of SCC mixes, e.g. the EFNARC (2005) and survey report (Domone, 2006), as was done above. To aid the user in making a knowledgeable choice, a software program (Appendix A) was developed from which design charts were constructed which are presented below.

4.8   Design charts for mix proportioning of normal and high strength SCC mixes

Thousands of solid phase volume fraction combinations (i.e. t_1, t_2, and t_3) were produced using a software program. These combinations covered wide ranges of target cube compressive strength and mix plastic viscosity. They have been collected in groups according to the target strength for ease of SCC mix proportioning. It was found convenient for presentation of a huge body of data to normalise the amounts of dry phases by the plastic viscosity and to present the amounts in separate plots, beginning with the cementitious materials (cm), and ending with the content of all dry phases (cm + LP + FA + CA). These design charts are given in Figures 4.4–4.9. The scatter reflects the multiplicity of combinations. It is however interesting to note that the scatter is the least in the bottom (cm) and the top (cm + LP + FA + CA) curves. This is because the amount of

cm calculated from the target compressive strength is according to the water content which varies in the narrow range of 150-210 l/m^3 (EFNARC, 2005) and the amounts of all dry ingredients contribute to the target plastic viscosity of the mix.

Moreover, it should be mentioned that the target plastic viscosity of the constructed design charts varies between 3 and 15 Pa s: the upper bound of all mix grades is 15 Pa s, whereas the lower bound varies between 3 – 8 Pa s for the mix grades 30 – 80 MPa, respectively. This is because some of the SCC mix parameters and fresh flow characteristics (cement replacement level, water content, super-plasticiser dosage and flow spread) have been chosen within certain restricted limits. For example, the replacement level of cement by ggbs was only allowed up to 25%, the target flow spread was restricted to the range of 700±50 mm, the water content was allowed to vary between 150 and 210 l/m^3 and the SP dosage was in the range of 0.4–0.8 % as a per cent of the mass of the cementitious material (cement + ggbs).
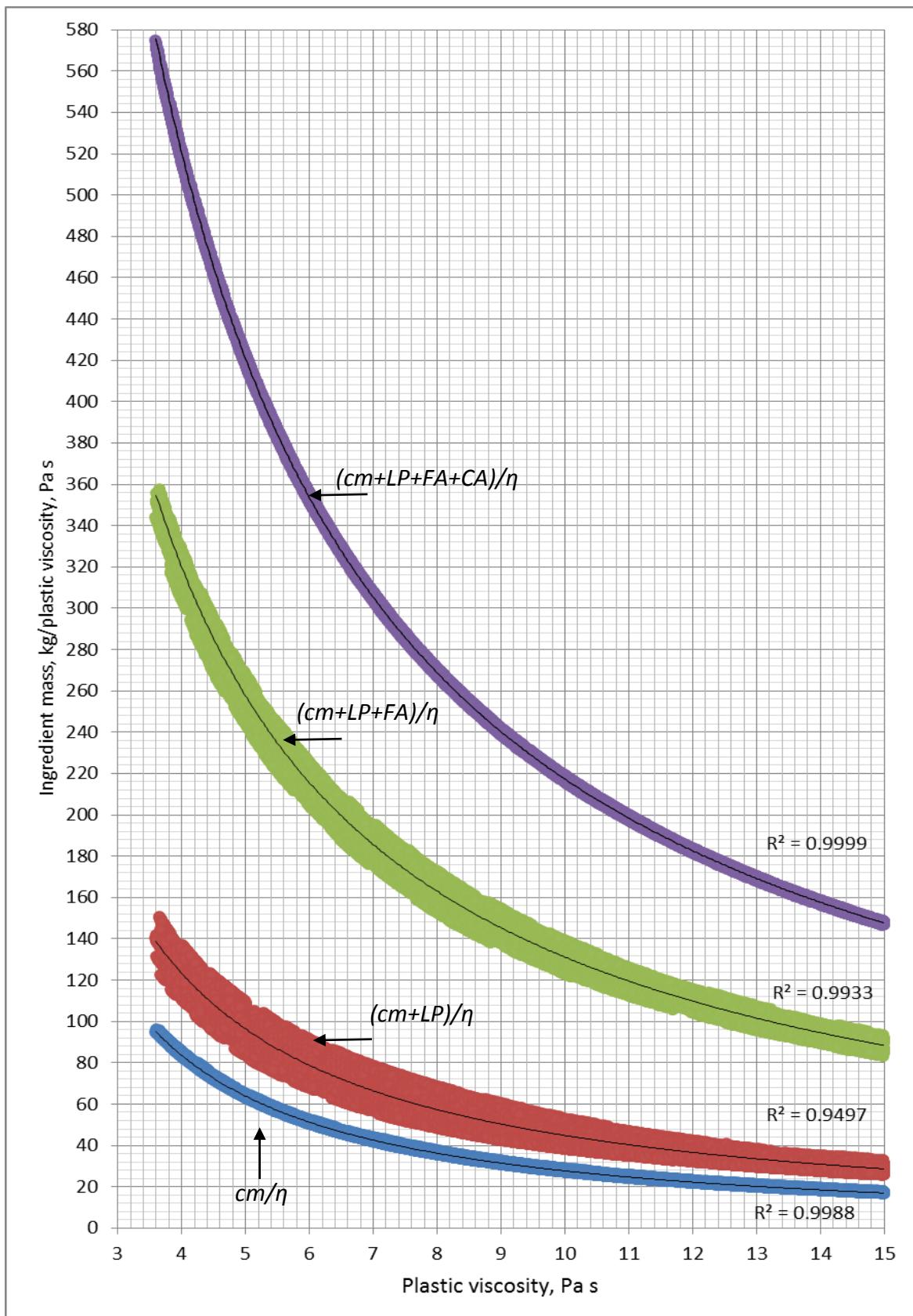
Figure 4.4: Ingredient mass (kg) normalised by mix plastic viscosity vs plastic viscosity for 30 MPa mix
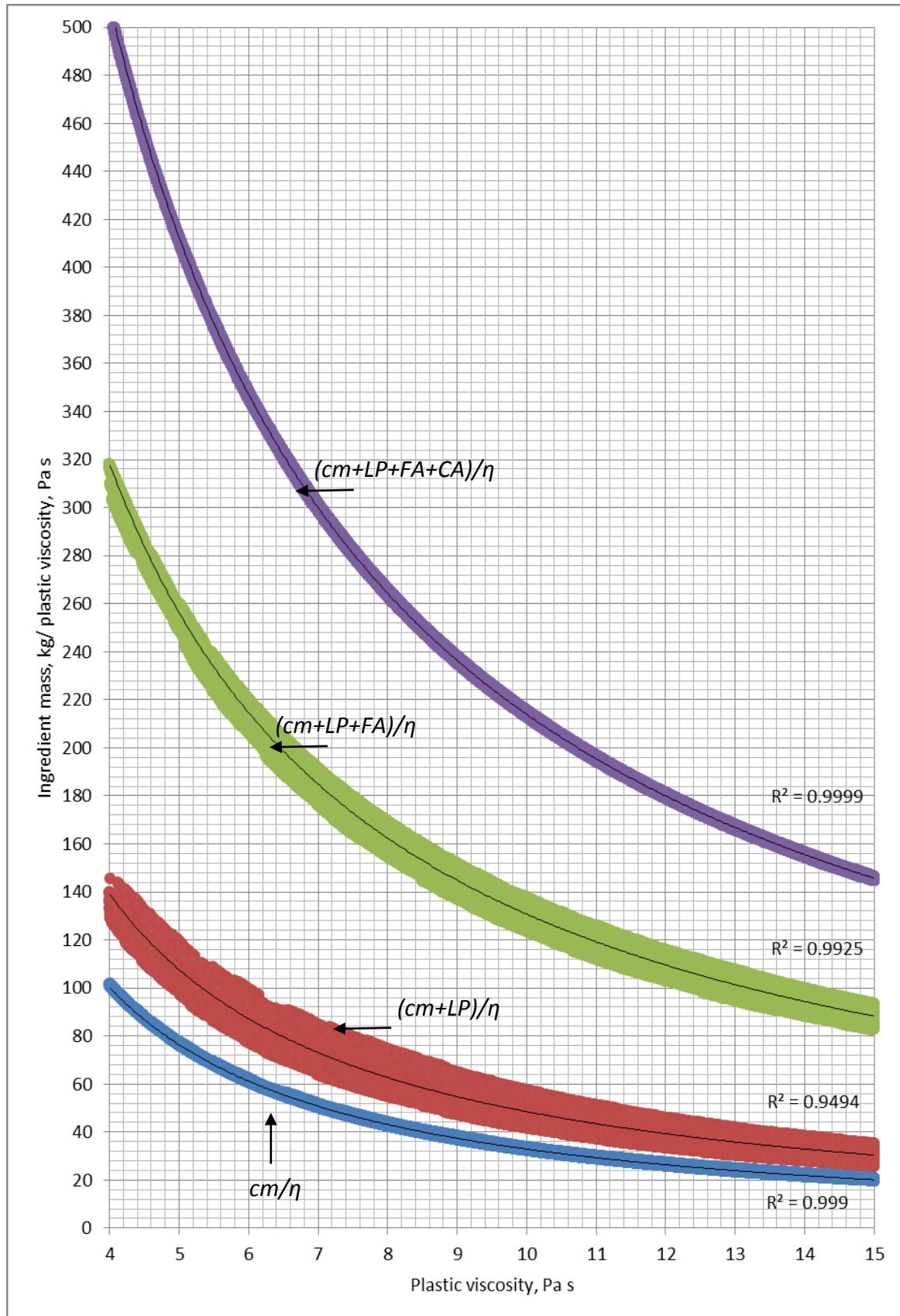
Figure 4.5: Ingredient mass (kg) normalised by mix plastic viscosity vs plastic viscosity for 40 MPa mix
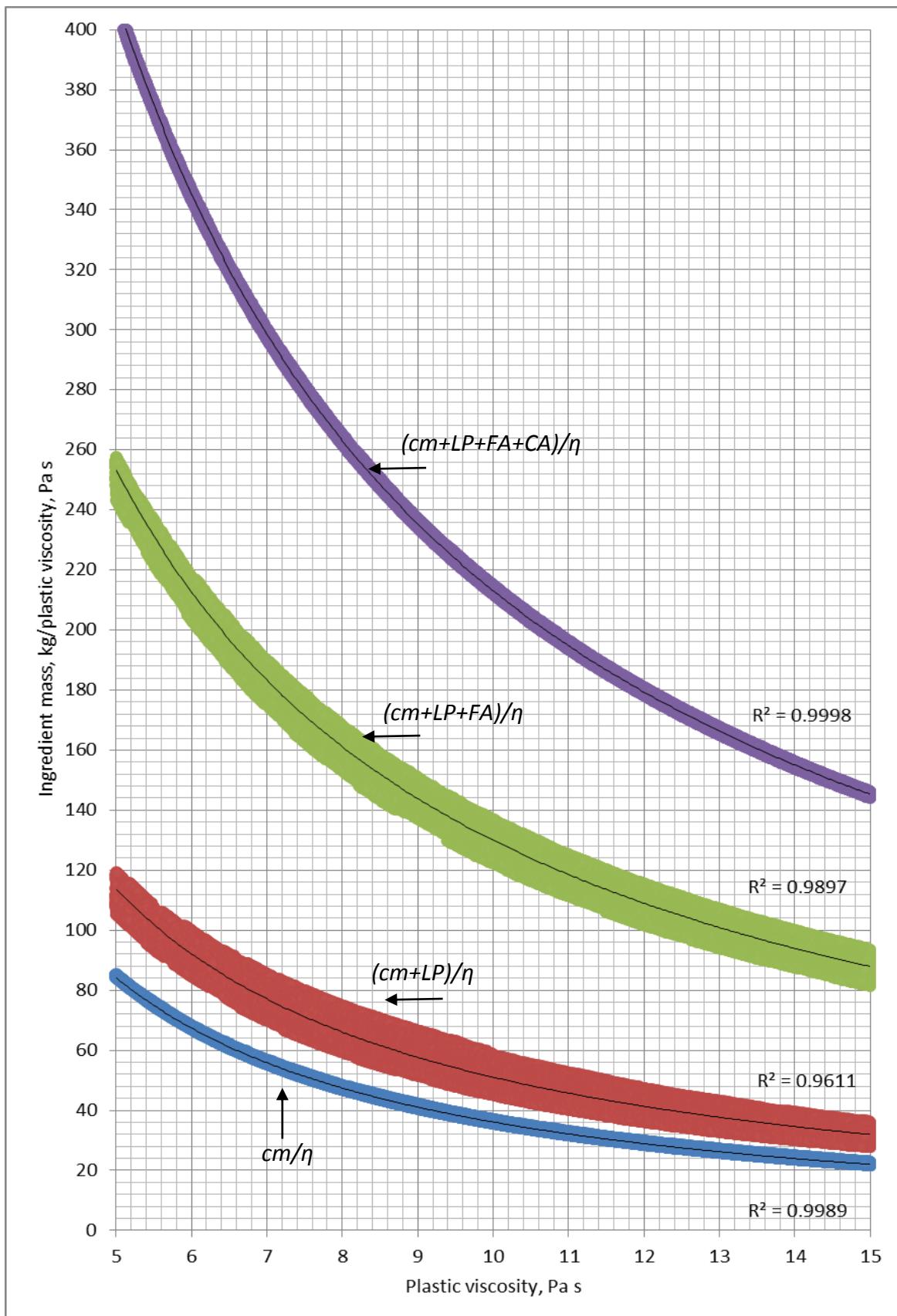
Figure 4.6: Ingredient mass (kg) normalised by mix plastic viscosity vs plastic viscosity for 50 MPa mix
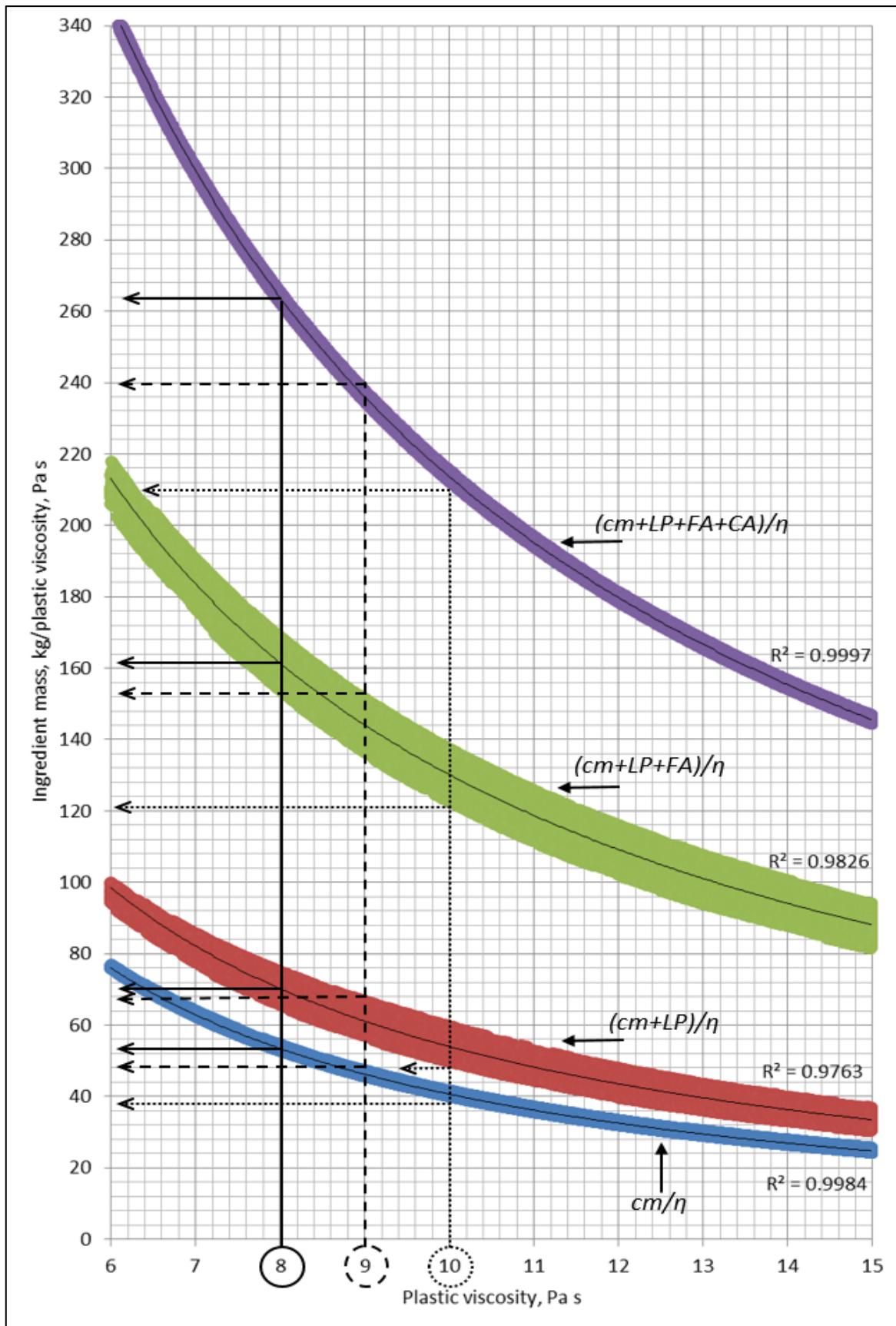
Figure 4.7: Ingredient mass (kg) normalised by mix plastic viscosity vs plastic viscosity for 60 MPa mix
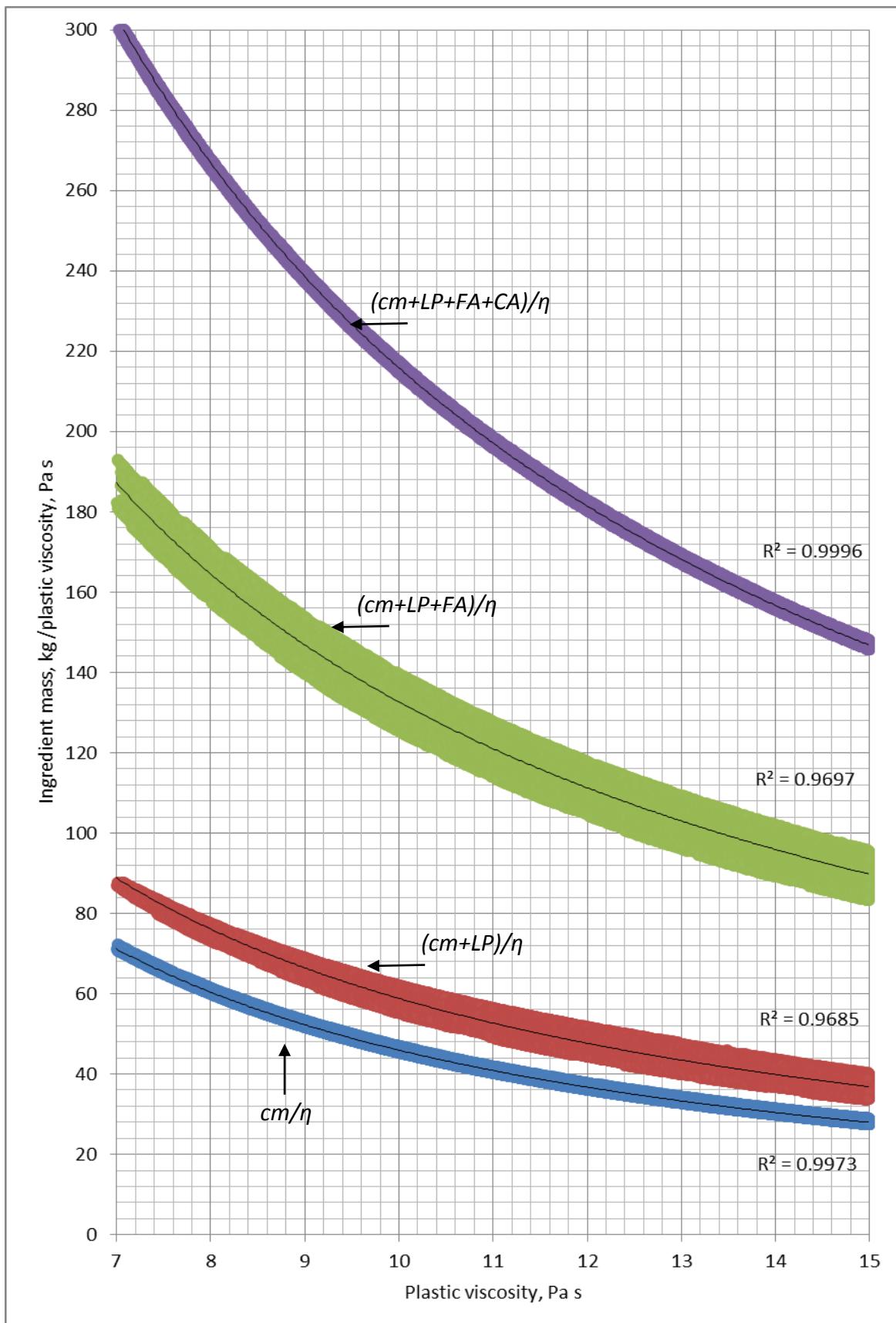
Figure 4.8: Ingredient mass (kg) normalised by mix plastic viscosity vs plastic viscosity for 70 MPa mix
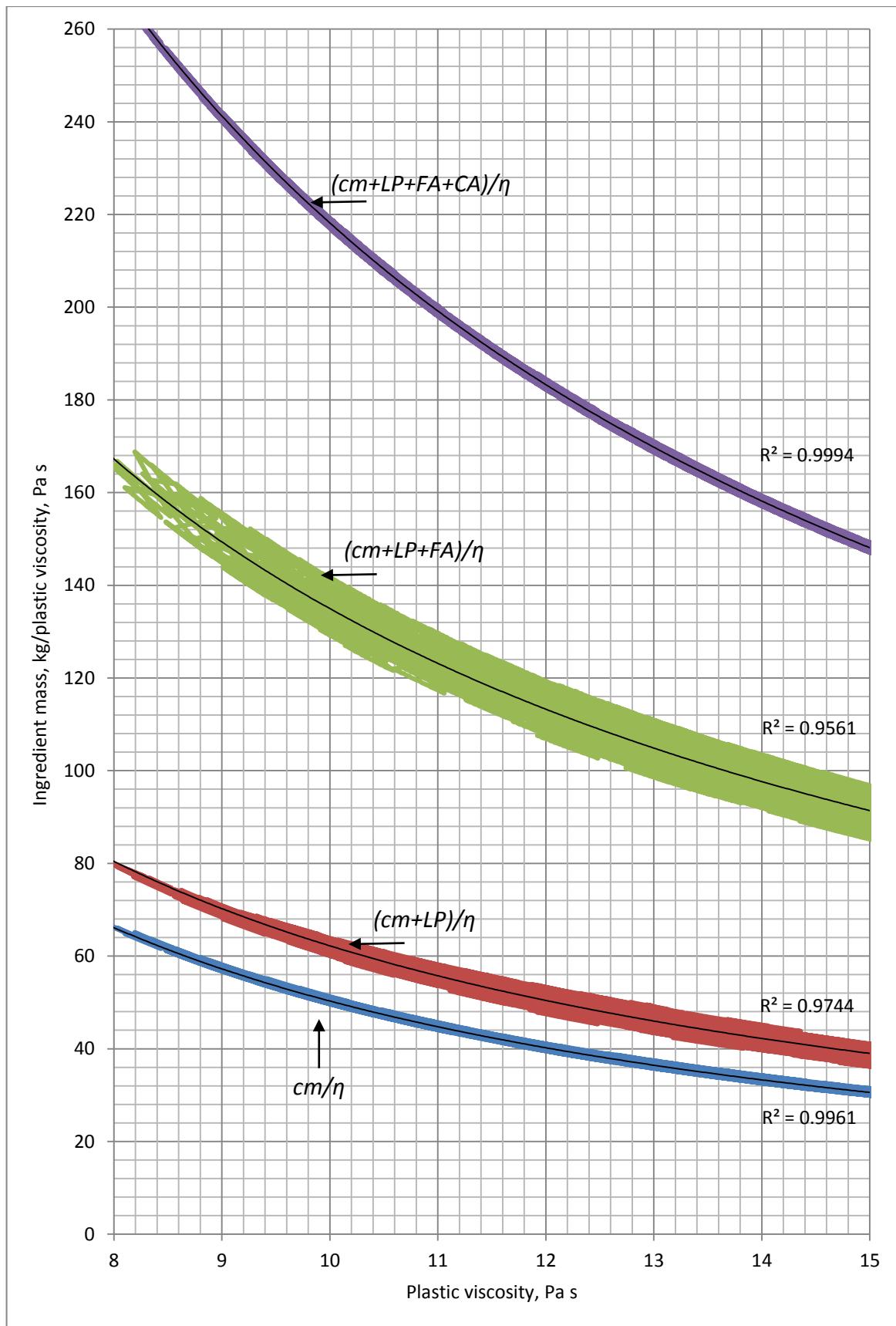
Figure 4.9: Ingredient mass (kg) normalised by mix plastic viscosity vs plastic viscosity for 80 MPa mix

4.9   Examples of the use of design charts

In order to demonstrate how easy it is to use the design charts (Figures 4.4–4.9), let us assume we wish to design an SCC mix with a target cube compressive strength of 60 MPa (Figure 4.7).

1. Suppose further that the desired target plastic viscosity of mix is 8 Pa s;

2. For the desired target strength= 60 MPa $\longrightarrow$ w/cm= 0.47 (Eq. (4.1));

3. Calculate the cementitious material content (cm);

   For $\eta_{mix} = 8$ Pa s $\longrightarrow$ $\frac{cm}{\eta}$ = 53.5 (bottom curve)

   cm= 53.5×8= 428 kg/m^3;

   c = 0.75×428= 321 kg/m^3, ggbs = 0.25×428= 107 kg/m^3;

   As w/cm= 0.47 $\longrightarrow$ w= 0.47×428= 201.2 l/m^3

4. Assume a trial SP dosage as a per cent of mass of cementitious materials (say 0.60%) which equals to 2.6 kg/m^3;

5. The plastic viscosity of the paste according to its w/cm and SP/cm ratios is equal to 0.29 (Table 4.1);

6. Calculate the solid phase ingredient contents (LP, FA and CA);

   For $\eta_{mix} = 8$ Pa s;

   $\frac{(cm+LP)}{\eta}$ = 70 (second curve from bottom)

   $(cm + LP)$= 70×8= 560 kg/m^3 $\longrightarrow$ LP= 560 − 428= 132 kg/m^3

   $\frac{(cm+LP+FA)}{\eta}$= 162 (second curve from top)

   $(cm + LP + FA)$= 162×8= 1296 kg/m^3 $\longrightarrow$ FA = 1296 − 428 −132= 736 kg/m^3

   $\frac{(cm+LP+FA+CA)}{\eta}$ = 264 (top curve)

   $(cm + LP + FA + CA)$ = 264×8 = 2112 kg/m^3

   CA= 2112 − 428 −132−736= 816 kg/m^3

7. Calculate the total volume of the mix;

   $$\text{Total vol.} = \frac{c}{\rho_c} + \frac{ggbs}{\rho_{ggbs}} + \frac{w}{\rho_W} + \frac{SP}{\rho_{SP}} + \frac{LP}{\rho_{LP}} + \frac{FA}{\rho_{FA}} + \frac{CA}{\rho_{CA}} + 0.02$$

   $$= \frac{321}{2950} + \frac{107}{2400} + \frac{201.2}{1000} + \frac{2.6}{1070} + \frac{132}{2400} + \frac{736}{2650} + \frac{816}{2800} + 0.02 = 1.0 \text{ m}^3$$

8. Check the plastic viscosity using Eq. (4.6);

$$\eta_{mix} = \eta_{paste} \times \left(1 - \frac{\phi_{LP}}{\phi_m}\right)^{-1.9} \times \left(1 - \frac{\phi_{FA}}{\phi_m}\right)^{-1.9} \times \left(1 - \frac{\phi_{CA}}{\phi_m}\right)^{-1.9}$$

$$\eta_{mix} = 0.29 \times \left(1 - \frac{0.127}{0.524}\right)^{-1.9} \times \left(1 - \frac{0.391}{0.63}\right)^{-1.9} \times \left(1 - \frac{0.291}{0.74}\right)^{-1.9} = 8.01 \text{ Pa s}$$

Viscosity diff. $= \frac{(calculated\ \eta_{mix} - target\ \eta_{mix})}{target\ \eta_{mix}} \times 100 = \frac{(8.01 - 8)}{8} \times 100 = +0.13\%$

This is within the acceptable difference $\pm 5\%$.

It is interesting to observe that in this example we chose the mix combinations corresponding to the best-fit lines in the curves (see Figure 4.7). That is why the total mix volume worked out to be exactly 1.0 m³, so that the plastic viscosity of the mix is within the acceptable deviation from the desired target value. This would not have been so, had we chosen the mix combinations different from the best-fit lines within the scatter band. As a rule, the more the deviation from the best-fit lines, the more the total mix volume deviates from 1.0 m³ and consequently the more the plastic viscosity of the resultant mix deviates from the target value. If the deviation is more than ±5%, then as mentioned above the procedure would need to be repeated (see step 8 in the mix design procedure §4.6).

In order to demonstrate this we chose two examples with ingredient proportions (Figures 4.4–4.9) away from the best fit-lines, and nearer the upper and lower limits of scatter. Let us design an SCC mix with a target cube compressive strength of 60 MPa (Figure 4.7) and choose the starting ingredient amounts at the upper limits of scatter in the design chart (Figure 4.7).

1. Suppose the desired target plastic viscosity of mix is 9 Pa s;

2. For the desired target strength= 60 MPa ⟶ w/cm= 0.47 (Eq. (4.1));

3. Calculate the cementitious material content (cm);

    For $\eta_{mix} = 9$ Pa s ⟶ $\frac{cm}{\eta}$ = 48 (bottom curve) ⟶ cm= 48×9= 432 kg/m³;

    c = 0.75×432= 324 kg/m³, ggbs = 0.25×432= 108 kg/m³;

    As w/cm= 0.47 ⟶ w= 0.47×432= 203 l/m³

4. Assume a trial SP dosage as a per cent of mass of cementitious materials (say 0.65%) which equals to 2.8 kg/m³;

5. The plastic viscosity of the paste according to its w/cm and SP/cm ratios is equal to 0.29 (Table 4.1);

6. Calculate the solid phase ingredient contents (LP, FA and CA);

   For $\eta_{mix} = 9$ Pa s;

   $\frac{(cm+LP)}{\eta} = 68$ (second curve from bottom)

   $(cm + LP)= 68{\times}9= 612$ kg/m^3 $\longrightarrow$ LP= $612 - 432= 180$ kg/m^3

   $\frac{(cm+LP+FA)}{\eta}= 153$ (second curve from top)

   $(cm + LP + FA)= 153{\times}9= 1377$ kg/m^3 $\longrightarrow$ FA = $1377 - 432 - 180= 765$ kg/m^3

   $\frac{(cm+LP+ FA+CA\ )}{\eta} = 240$ (top curve)

   $(cm + LP + FA + CA)= 240{\times}9= 2160$ kg/m^3

   CA= $2160 - 432 - 180 - 765= 783$ kg/m^3

7. Calculate the total volume of the mix;

   Total vol. $= \frac{324}{2950} + \frac{108}{2400} + \frac{203}{1000} + \frac{2.8}{1070} + \frac{180}{2400} + \frac{765}{2650} + \frac{783}{2800} + 0.02 = 1.024$ m^3

Owing to the total mix volume exceeding 1.0 m^3, it must be scaled to 1.0, so the ingredient amounts will be:

   cm= 432 /1.024 = 422 kg/m^3

   w= 203 /1.024= 198 kg/m^3

   SP= 2.8 /1.024= 2.7 kg/m^3

   LP= 180 /1.024= 176 kg/m^3

   FA=765 /1.024= 747 kg/m^3

   CA=783 /1.024= 765 kg/m^3

   Total vol. $= \frac{422{\times}0.75}{2950} + \frac{422{\times}0.25}{2400} + \frac{198}{1000} + \frac{2.7}{1070} + \frac{176}{2400} + \frac{747}{2650} + \frac{765}{2800} + 0.02=1.0$ m^3

8. Check the plastic viscosity using Eq. (4.6);

   $\eta_{mix} = \eta_{paste}{\times}\left(1 - \frac{\phi_{LP}}{\phi_m}\right)^{-1.9} \times \left(1 - \frac{\phi_{FA}}{\phi_m}\right)^{-1.9} \times \left(1 - \frac{\phi_{CA}}{\phi_m}\right)^{-1.9}$

   $\eta_{mix} = 0.29 \times \left(1 - \frac{0.164}{0.524}\right)^{-1.9} \times \left(1 - \frac{0.388}{0.63}\right)^{-1.9} \times \left(1 - \frac{0.273}{0.74}\right)^{-1.9} = 8.74$ Pa s

   Viscosity diff. $= \frac{(calculated\ \eta_{mix} - target\ \eta_{mix})}{target\ \eta_{mix}}{\times}100 = \frac{(8.74 - 9)}{9}{\times}100 = -2.9\%$

   This is within the acceptable difference $\pm 5\%$.

The next example deals with the design of an SCC mix with a target cube compressive strength of 60 MPa. In this example, we choose the starting ingredient amounts at the lower limits of scatter in the design chart (Figure 4.7).

1. Suppose the desired target plastic viscosity of mix is 10 Pa s;

2. For the desired target strength= 60 MPa $\longrightarrow$ w/cm= 0.47 (Eq. (4.1));

3. Calculate the cementitious material content (cm);

   For $\eta_{mix} = 10$ Pa s $\longrightarrow$ $\frac{cm}{\eta}$ = 38 (bottom curve)

   cm= 38×10= 380 kg/m^3;

   c $= 0.75×380= 285$ kg/m^3, ggbs $= 0.25×380= 95$ kg/m^3 ;

   As w/cm= 0.47 $\longrightarrow$ w= 0.47×380= 178.6 l/m^3

4. Assume a trial SP dosage as a per cent of mass of cementitious materials (say 0.65%) which equals to 2.5 kg/m^3 ;

5. The plastic viscosity of the paste according to its w/cm and SP/cm ratios is equal to 0.29 (Table 4.1);

6. Calculate the solid phase ingredient contents (LP, FA and CA);

   For $\eta_{mix} = 10$ Pa s;

   $\frac{(cm+LP)}{\eta}$ = 48 (second curve from bottom)

   $(cm + LP)$= 48×10= 480 kg/m^3 $\longrightarrow$ LP = 480–380= 100 kg/m^3

   $\frac{(cm+LP+FA)}{\eta}$= 121 (second curve from top)

   $(cm + LP + FA)$= 121×10= 1210 kg/m^3 $\longrightarrow$ FA = 1210 – 380 –100= 730 kg/m^3

   $\frac{(cm+LP+ FA+CA)}{\eta}$ = 210 (top curve)

   $(cm + LP + FA + CA)$= 210×10= 2100 kg/m^3

   CA= 2100 – 380 –100– 730= 890 kg/m^3

7. Calculate the total volume of the mix;

   Total vol. $= \frac{285}{2950} + \frac{95}{2400} + \frac{178.6}{1000} + \frac{2.5}{1070} + \frac{100}{2400} + \frac{730}{2650} + \frac{890}{2800} + 0.02 = 0.972$ m^3

Owing to the total mix volume not being equal to 1.0 m^3, it must be scaled to 1.0, so the ingredients amounts will be:

cm = 380 /0.972= 391 kg/m^3

w = 178.6 /0.972= 183.8 kg/m^3

SP = 2.5 /0.972= 2.60 kg/m^3

LP = 100 /0.972 = 103 kg/m^3

FA=730 /0.972= 751 kg/m^3

CA=890 /0.972= 917 kg/m^3

Total vol. $= \frac{391 \times 0.75}{2950} + \frac{391 \times 0.25}{2400} + \frac{183.8}{1000} + \frac{2.6}{1070} + \frac{103}{2400} + \frac{751}{2650} + \frac{917}{2800} + 0.02 = 1.0$ m^3

8. Check the plastic viscosity using Eq. (4.6);

$$\eta_{mix} = 0.29 \times \left(1 - \frac{0.110}{0.524}\right)^{-1.9} \times \left(1 - \frac{0.421}{0.63}\right)^{-1.9} \times \left(1 - \frac{0.327}{0.74}\right)^{-1.9} = 11.3 \text{ Pa s}$$

Viscosity diff. $= \frac{(calculated\ \eta_{mix} - target\ \eta_{mix})}{target\ \eta_{mix}} \times 100 = \frac{(11.3 - 10)}{10} \times 100 = +13\%$

The difference exceeds the acceptable value, ±5%, so different ingredient masses need to be chosen from the design chart (Figure 4.7), beginning with the cementitious materials ($\frac{cm}{\eta}$).

For $\eta_{mix} = 10$ Pa s, choose

$\frac{cm}{\eta}$ = 39 (bottom curve) $\longrightarrow$ cm= 39×10= 390 kg/m^3;

c = 0.75×390= 292.5 kg/m^3, ggbs $= 0.25 \times 390$= 97.5 kg/m^3 ;

As w/cm= 0.47 $\longrightarrow$ w= 0.47×390= 183.3 l/m^3

$\frac{(cm+LP)}{\eta}$ = 48 (second curve from bottom) $\longrightarrow$ LP = 480 − 390= 90 kg/m^3

$\frac{(cm+LP+FA)}{\eta}$ = 121 (second curve from top) $\longrightarrow$ FA =1210 − 390 − 90= 730 kg/m^3

$\frac{(cm+LP+FA+CA)}{\eta}$ = 210 (top curve) $\longrightarrow$ CA= 2100 − 390 − 90 − 730= 890 kg/m^3

Total vol. $= \frac{c}{\rho_c} + \frac{ggbs}{\rho_{ggbs}} + \frac{w}{\rho_W} + \frac{SP}{\rho_{SP}} + \frac{LP}{\rho_{LP}} + \frac{FA}{\rho_{FA}} + \frac{CA}{\rho_{CA}} + 0.02 = 0.976$ m^3

The volume must be scaled to 1.0 m^3, so the ingredient amounts will be:

cm = 390 /0.976= 400 kg/m^3

w = 183.3 /0.976= 187.8 kg/m^3

SP = 2.5 /0.976= 2.60 kg/m^3

LP = 90 /0.976= 92 kg/m^3

FA=730 /0.976= 748 kg/m^3

CA=890 /0.976= 912 kg/m^3

$$\text{Total Vol.} = \frac{c}{\rho_c} + \frac{ggbs}{\rho_{ggbs}} + \frac{w}{\rho_W} + \frac{SP}{\rho_{SP}} + \frac{LP}{\rho_{LP}} + \frac{FA}{\rho_{FA}} + \frac{CA}{\rho_{CA}} + 0.02 = 1.0 \text{ m}^3$$

$\eta_{mix} = 10.37$ Pa s from Eq. (4.6).

Viscosity diff. $= \frac{(calculated\ \eta_{mix} - target\ \eta_{mix})}{target\ \eta_{mix}} \times 100 = \frac{(10.37-10)}{10} \times 100 = +3.7\%.$

This is within the acceptable difference, so the mix design is complete.

Typical SCC mixes (differing by target compressive strength and target plastic viscosity) designed using the procedure described above are given in Appendix B (Tables B.1–B.6).

4.10   Concluding remarks

An easy-to-use method for the design of SCC mixes based on the desired target plastic viscosity and compressive strength of the mix was developed in this chapter. The simplicity and usefulness of this method are enhanced by the provision of design charts as a guide for mix proportioning. The characteristic cube strength of these charts varied between 30 and 80 MPa at 28 days age, and the target plastic viscosity between 3 and 15 Pa s: the upper bound of all mix grades was 15 Pa s, whereas the lower bound varied between 3 − 8 Pa s in mix grade range 30 − 80 MPa. Several examples have been given explaining the use of these design charts.

The method of proportioning is simple as evidenced by the examples. The procedure and design charts can also be used when the mix ingredients have different densities (apart from type II/B-V 32.5R cement) because the plastic viscosity depends only on the volume fractions (Eq. (4.6)). For designing a mix whose target compressive strength is different from those of design charts in Figures 4.4–4.9, for example, a mix with target compressive strength 65 MPa, the values of ingredient masses can be interpolated from charts for mixes with target compressive strengths 60 and 70 MPa (Figures 4.7 and 4.8).

Chapter 5

Proportioning of SCC mixes based on target plastic viscosity and compressive strength: experimental validation

5.1   Introduction

The previous chapter described the mix design procedure and gave several examples on the use of the design charts. The present chapter is concerned with the experimental validation of the mix design procedure on a series of SCC mixes in both the fresh and hardened states. A series of SCC mixes differing in target plastic viscosity and target compressive strength were prepared using the design charts. All these mixes were extensively tested in the fresh state using the slump cone, J–ring, L–box and V–funnel apparatus and in hardened state using compressive strength test.

The contents of this chapter have been published in the journal 'Journal of Sustainable Cement-Based Materials' (see publication 3 in the list in Chapter 1).

5.2   Materials and mix proportions

The verification of the proposed SCC mix design method using the design charts was carried out by testing many mixes of differing cube compressive strength and plastic viscosity. These mixes were designated A for paste to solids (p/s) ratio. In order to get a reliable assessment of the proposed mix design method, investigations have also been conducted on SCC mixes in the same laboratory by two other PhD students (Alyhya, 2016; Al-Rubaye, 2016) on two different p/s ratios: they were designated B and C for medium and high p/s ratios, respectively. It is for this reason that the mixes in this chapter are qualified with the letter A (see Table 5.1) corresponding to their low p/s ratios.

Different mixes of strength 30, 40, 50, 60, 70, and 80 MPa and different target plastic viscosity (4.5-10.5 Pa s) were prepared and subjected to the slump flow, J–ring, L–box and V–funnel tests in the fresh state to ensure that they met the flow and passing ability criteria without segregation. Standard cubes (100 mm) were then cast, cured in water and tested for compressive strength at 7, 28 and 90 days of age. The amounts and details of the ingredients used in the test mixes are given in Tables 5.1 and 5.2. These were chosen using the design charts and the procedure described in Chapter 4.

Locally available type II cement (CEM II/B-V 32.5R according to BS EN 197-1 (2011)) and ground granulated blast furnace slag (ggbs) with a specific gravity of 2.95 and 2.40,

respectively were used. The super-plasticiser used was a poly-carboxylic ether-based type with specific gravity of 1.07. Crushed limestone coarse aggregate with a maximum size of 20 mm and a specific gravity of 2.80 was used, while the fine aggregate was river sand having a specific gravity of 2.65. Limestone powder as filler with maximum particle size of 125 μm was used (specific gravity 2.40). A part of the river sand was replaced by an equivalent volume of the coarser fraction of limestone filler in the size range 125 μm - 2 mm.

Table 5.1: Mix proportions of test SCC mixes, kg/m³

Mix design.	cm [a]		water	SP [b]	w/cm	SP/cm, %	LP [c]	FA [d]		CA [e]
	cem	ggbs						FA**	FA***	
30A*	240	80	201.6	1.4	0.63	0.44	109	164	579	924
40A	262.5	87.5	199.5	1.5	0.57	0.43	100	150	582	924
50A(50A)	281.2	93.8	198.8	1.6	0.53	0.43	95	143(0)	573(730)	924
60A	315	105	197.5	[2.3]2.0	0.47	0.55	94	141	536	924
70A	345	115	184	2.5	0.40	0.54	93	140	536	924
80A	367.5	122.5	171.5	2.8	0.35	0.57	94	141	536	924

* A refers to the selected low paste/solid ratio as explained above.

a: cementitious materials.

b: super–plasticiser. Figure in square brackets refers to increase in SP needed for satisfying passing ability.

c: limestone powder <125 μm.

d: fine aggregate < 2 mm (Note: a part of the fine aggregate is the coarser fraction of the limestone powder, FA**125 μm –2 mm, whereas FA *** refers to natural river sand < 2 mm).

e: coarse aggregate < 20 mm.

Table 5.2: Further details of test SCC mixes

Mix designation	Target plastic viscosity, Pa s	Actual plastic* viscosity, Pa s	Paste vol. fraction	Solid vol. fraction	Paste/solid (by vol.)
30A	4.5	4.63	0.38	0.62	0.61
40A	6.5	6.84	0.39	0.61	0.64
50A(50A)	7.5(7.5)	7.84(7.84)	0.39	0.61	0.64
60A	8.5	8.18	0.41	0.59	0.69
70A	9.5	9.32	0.41	0.59	0.69
80A	10.5	10.47	0.41	0.59	0.69

Actual plastic viscosity*: mix plastic viscosity that is calculated using equation 4.6.

As mentioned above, a part of the river sand was replaced by an equivalent volume of the coarser fraction of limestone filler in the size range 125 μm - 2 mm. However, tests were also done on a mix of strength 50 MPa (shown in parenthesis in Tables 5.1 and 5.2) in which no replacement of the river sand fine aggregate was made in order to check whether this replacement made any difference to the flow characteristics of the SCC mix in the fresh state or its compressive strength in the hardened state.

5.3   Tests on fresh SCC

5.3.1   Flow-ability

Tests were conducted to determine the t_{500} and $t_{v-funnel}$ times of the fresh mixes. These are summarised in Table 5.3. The time taken by the fresh SCC mix to reach a 500 mm diameter spread in the slump cone flow (t_{500}) was determined from time sequencing a video recording of the test with an accuracy of a thousand of a second, while the time taken by the fresh SCC mix to flow out of the funnel (daylight appearing when viewed from above) was recorded as $t_{v-funnel}$ flow time (Figure 5.1). Within the chosen flow spread range of 650–750 mm, the t_{500} and $t_{v-funnel}$ varied between 0.50–1.92 s and 2.46–6.67 s,

respectively. Figures 5.2-5.4 show the horizontal spread of different grade SCC mixes. All test SCC mixes showed no signs of segregation or bleeding on thorough visual inspection.

Table 5.3: Flow-ability test results, t_{500} and $t_{v-funnel}$ of SCC mixes

Mix designation	Slump flow test		V–funnel test
	Spread, mm	t_{500}, s	$t_{v-funnel}$, s
30A	685	0.50	2.46
40A	730	0.64	2.53
50A(50A)	675(670)	1.17(1.10)	3.37(3.28)
60A	665	1.18	3.23
70A	700	1.42	5.46
80A	730	1.92	6.67

Figure 5.1: Recording V-funnel time (daylight appearing when viewed from above)

Figure 5.2: Horizontal spread of SCC mix: 30A (Left), 50A (Right)

Figure 5.3: Horizontal spread of SCC mix: 60A (Left), 80A (Right)

Figure 5.4: Horizontal spread of SCC mix (50A)

A comparison of the flow tests on 50 MPa mix, in which a part of the river sand fine aggregate was replaced by the coarser fraction of limestone filler with the same grade mixes but without the replacement (shown in parenthesis in Table 5.3), shows that the flow characteristics of the mixes are not significantly affected by this replacement. This is consistent with the small differences in the particle size distributions of the coarser fraction of limestone filler and river sand (Figure 5.5). Moreover, as the volume fractions (not the masses) of the fine aggregate (with or without replacement) in the mixes are the same (Tables 5.1 and 5.2), their plastic viscosity will be the same (see Eq. (4.6) in Chapter 4).
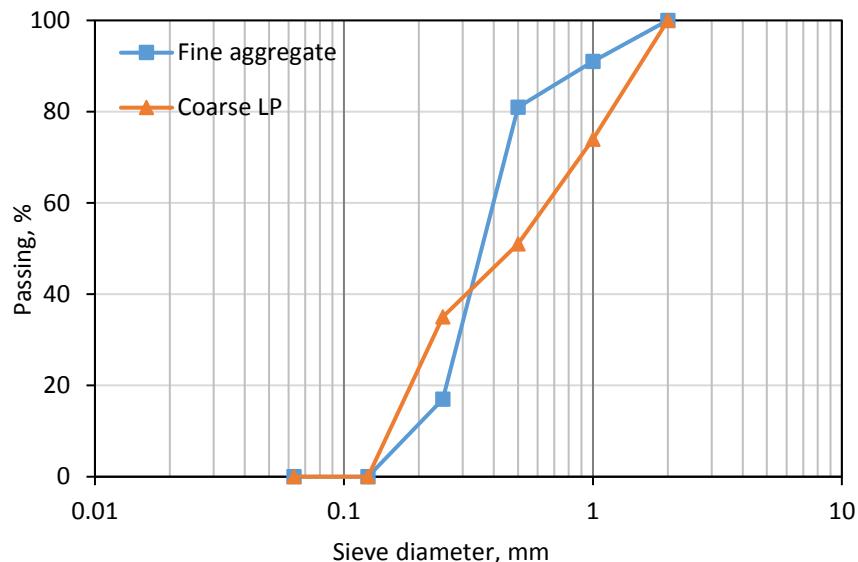
Figure 5.5: Particle size distribution curves for coarser fraction of limestone filler and fine aggregate

Figure 5.6 shows a plot of the flow time of all mixes and the corresponding water to powder (i.e. cement + ggbs + limestone powder < 125 µm) ratio (w/p). It is seen that a larger t_{500} requires a higher powder or lower water content. The w/p ratio has a considerable influence on both the fresh and hardened properties of SCC, with often its influence on the fresh properties limiting the selection of its value (Domone, 2006). It has been reported that a decrease in the water content and an increase in the amount of fine particles can increase cohesion and viscosity of the mix (Felekoğlu et al., 2007), resulting in a good distribution of the solid particles throughout the casting of SCC. However, mixes

with low water content require relatively high dosages of super–plasticiser, especially at low cm contents, to achieve the accepted requirements of SCC deformability (Khayat et al., 1999).
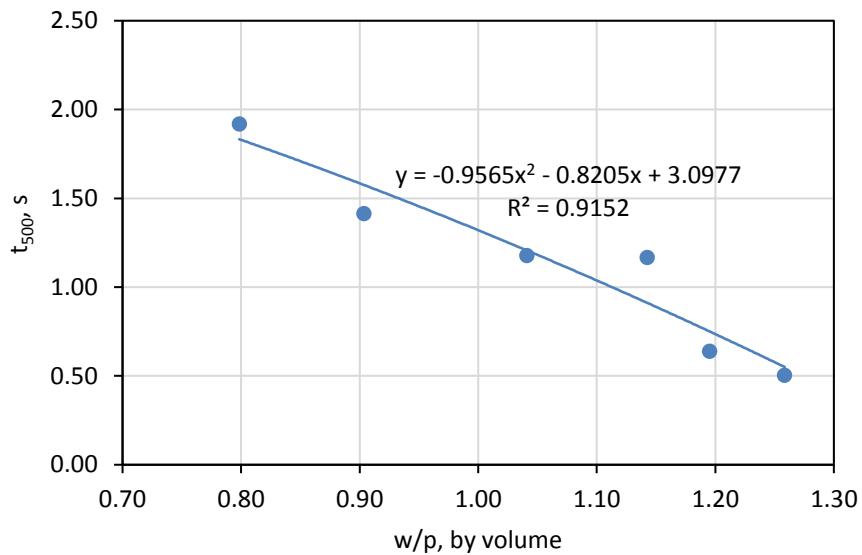
Figure 5.6: Relationship between flow time (t$_{500}$) and water to powder ratio

The time needed to reach 500 mm diameter spread is related to the plastic viscosity of the mix. This is clearly seen in Figure 5.7 for a given target flow spread. Regarding the plastic viscosity, it is worth mentioning that it is very difficult if not impossible to measure it accurately. It is well known (Banfill et al., 2001; Feys et al., 2007; Wallevik and Wallevik, 2011) that for one and the same mix, different types of rheometer give different values of Bingham parameters (plastic viscosity and yield stress). Therefore, the micromechanical procedure proposed by Ghanbari and Karihaloo (2009) which calculates the plastic viscosity of an SCC mix from the known plastic viscosity of the paste (which can be accurately measured with a viscometer) has been recommended and used in this chapter. This was already explained in Chapter 4 and indeed forms the basis of the proposed mix proportioning method.

It should also be mentioned that the yield stress is well correlated with the slump flow spread (Koehler and Fowler, 2007; Wallevick, 2003). That is why we have determined the target flow spread of our mixes within the range of 700±50 mm. It is implied that these mixes have nearly the same yield stress and thus make the plastic viscosity as the controlling parameter which we have correlated with t_{500} in Figure 5.7. The following statement from (Koehler and Fowler, 2007) supports this implicit assumption ''the plastic viscosity is often the main factor distinguishing the workability of one mix from another. Changes in plastic viscosity can directly reflect changes in materials or mixture proportions, making the t_{500} measurement particularly valuable for quality control''. Of course, a different choice of target plastic viscosity, say from the EFNARC (2005) will necessarily require different t_{500}.

The plastic viscosity has been plotted against $t_{v-funnel}$ and flow spread in Figure 5.8. It can be seen that the $t_{v-funnel}$ of mixes having the flow spread in the range of 665–730 mm increases with an increase in the mix plastic viscosity, despite an increase in the SP dosage. In other words, the flow time is dominated by the plastic viscosity rather than the SP dosage. This has also been observed by Nepomuceno et al. (2014) and Takada and Tangtermsirikul (2000).
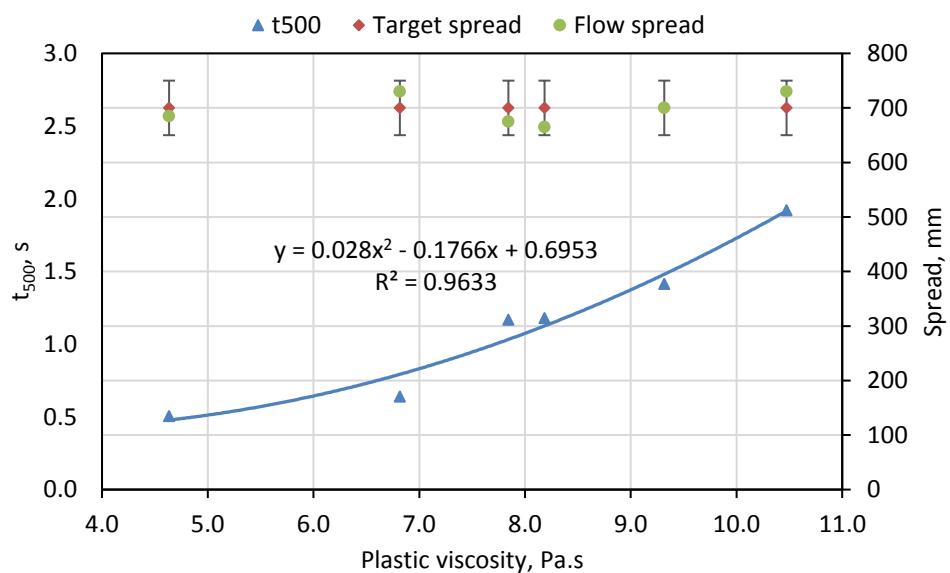
Figure 5.7: Relationship between plastic viscosity and t_{500} for target flow spread 700 ± 50 mm
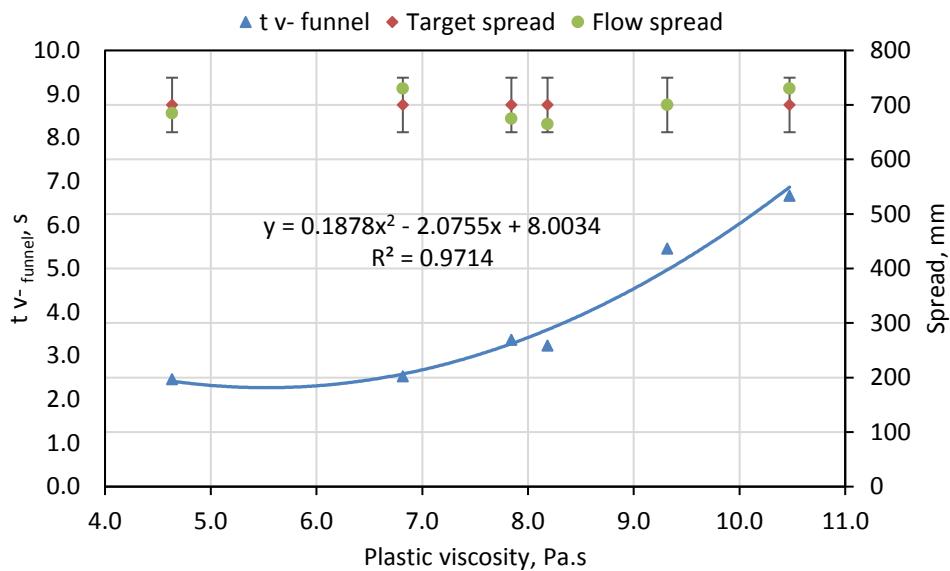
Figure 5.8: Relationship between plastic viscosity and $t_{v-funnel}$ time with a target flow spread (700±50 mm)

5.3.2 Passing and filling ability

All the above test mixes that satisfied the flow-ability criterion and showed no signs of segregation were subjected to the passing and filling ability test using the J–ring and L–box (BS EN 206-9, 2010; EFNARC, 2005) to ensure that they were able to pass through the narrow gaps that exist between reinforcing bars in real reinforced concrete structural elements. For this purpose, two types of J-ring test have been used: wide gaps (10 bars) and narrow gaps (16 bars) that are used for normal and congested reinforcement, respectively. The results of the latter are presented in Table 5.4 whereas the former are in Appendix C. There was a mix (60A which had a low flow spread, i.e. low dosage of SP) that had passed the flow-ability test but did not meet the passing ability criterion. In this instance, the SP dosage had to be increased (shown in square brackets in Table 5.1). The results indicated that (after the increase in SP) all mixes met the passing ability criterion and showed no blockage or signs of segregation (Figures 5.9 – 5.10). Again, the influence of the replacement of some river sand fine aggregate by the coarser fraction of limestone filler on the flow characteristics was minimal, as can be judged by comparing the entries for 50 MPa mixes without and within the parenthesis in Table 5.4. Figure 5.11 shows that t_{500j} time correlates well with the plastic viscosity for all the mixes.

Table 5.4: Passing ability test results, J–ring and L–box

Mix designation	J–ring flow test		L–box test		
	Spread, mm	t_{500j}, s	t_{200}, s	t_{400}, s	H_2/H_1 or BR
30A	650	0.69	0.47	1.08	0.91
40A	700	0.80	0.50	0.91	0.92
50A(50A)	640	1.41	0.67(0.62)	1.40(1.35)	0.86(0.88)
60A	665	1.48	0.77	1.48	0.89
70A	690	2.04	1.25	2.66	0.88
80A	700	2.80	1.45	3.10	0.93

Figure 5.9: Flow and passing ability of SCC mix: 30A (Left), 40A (Right)
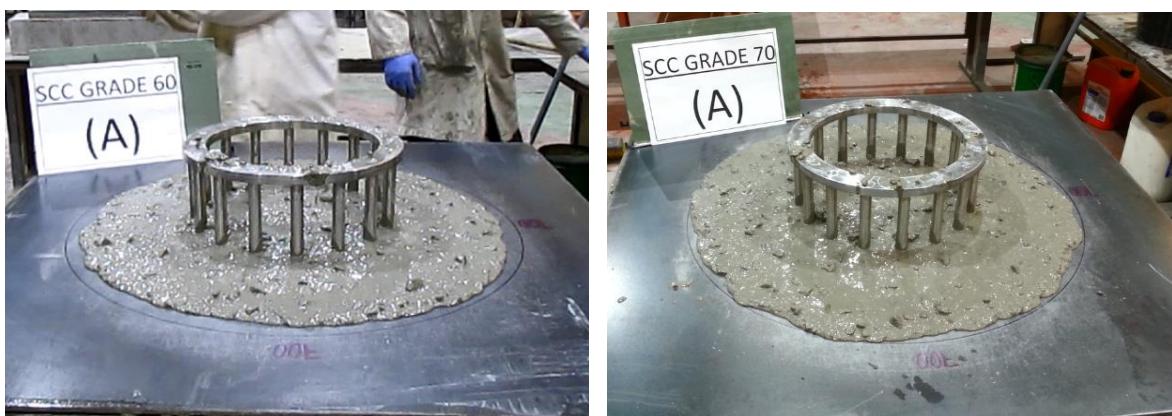
Figure 5.10: Flow and passing ability of SCC mix: 60A (Left), 70A (Right)

$$y = 0.0654x^2 - 0.6213x + 2.1456$$
$$R^2 = 0.9874$$
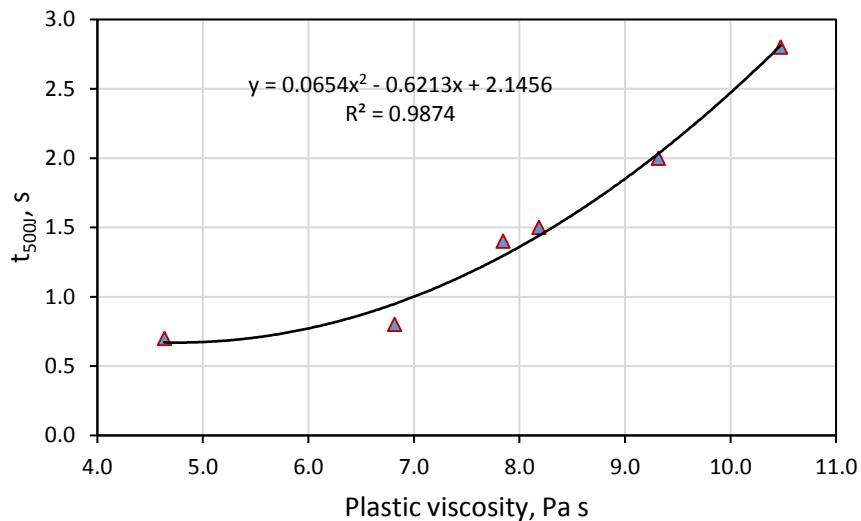
Figure 5.11: t_{500J} time versus plastic viscosity

The relationship between the parameters t_{500} of J-ring and slump flow of SCC was also taken into consideration in this study. The best-fit curve of t_{500} against the plastic viscosity is plotted graphically alongside t_{500J} in Figure 5.12. It was found that the difference between these times is more pronounced in the higher plastic viscosities (8-10.5 Pa s) than the lower ones. A possible explanation for this increase is that the mixes become sticky taking more time to pass through the obstacles of the J-ring.

$$y = 0.0654x^2 - 0.6213x + 2.1456$$
$$R^2 = 0.9874$$

$$y = 0.028x^2 - 0.1766x + 0.6953$$
$$R^2 = 0.9633$$
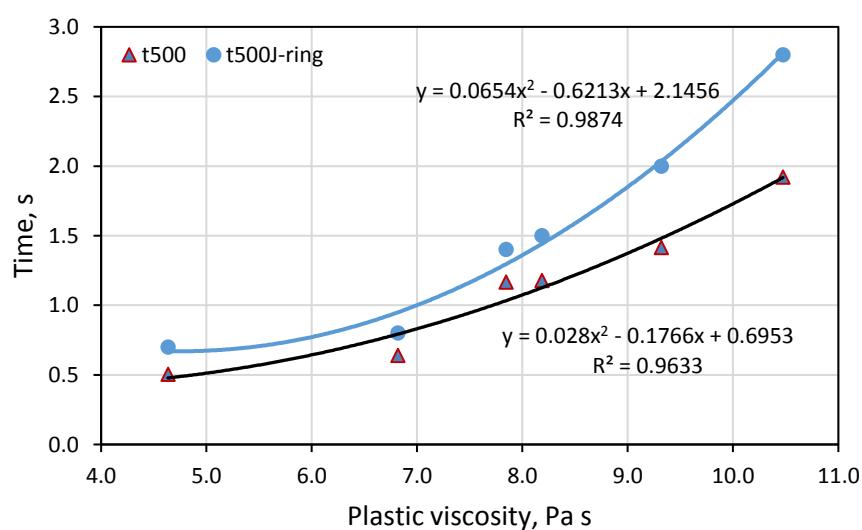
Figure 5.12: Plastic viscosity versus t_{500} and t_{500J}

According to the ASTM C 1621/ C 1621M (2008), the J-ring test can be used in combination with the slump flow test to assess the passing ability of SCC. If the difference between spread diameters ($D_{flow} - D_{J-ring}$) of the two tests is less than 25 mm then there is no visible blockage. If it is between 25 and 50 mm then there is minimal to noticeable blockage. Table 5.5 shows the difference from which it is clear that for all mixes there is minimal or no blockage.

Table 5.5: Difference between flow and J-ring spread diameter

Mix designation	D_{flow}, mm	D_{J-ring}, mm	$D_{flow} - D_{J-ring}$, mm
30A	685	650	35
40A	730	700	30
50A	675	640	35
60A	665	665	0
70A	700	690	10
80A	730	700	30

In order to test the ability of an SCC mix to fill the formwork containing reinforcement under its own weight, the L–box apparatus with two adjustable steel rods (each of diameter 12 mm) was used (12350-10, 2010; EFNARC, 2005). The times for the mix to reach 200 mm (t_{200}) and 400 mm (t_{400}) from the vertical leg as well as the blockage ratio (BR or H_2/H_1) were recorded. All mixes that had passed the J–ring test also passed the L–box test without any alteration in SP or mix ingredients (Figures 5.13–5.15). Figure 5.16 shows that t_{200} and t_{400} times correlate well with the plastic viscosity for all the mixes. The results also showed that no large aggregate particles had segregated or been blocked by the rods. Also, it can be seen (Table 5.4) that the mixes exhibited a blockage ratio (BR) of more than 0.80, which reflects good filling ability.

Therefore, from the flow and passing ability perspectives, all the test SCC mixes satisfied the required criteria for viscosity class 1 to qualify them as SCC in accordance with BS–EN 206–9 (2010).

Figure 5.13: Passing and filling of SCC mix: 30A (Left), 40A (Right)

Figure 5.14: Passing and filling of SCC mix: 60A (Left), 80A (Right)

Figure 5.15: Passing and filling of SCC mix (50A)
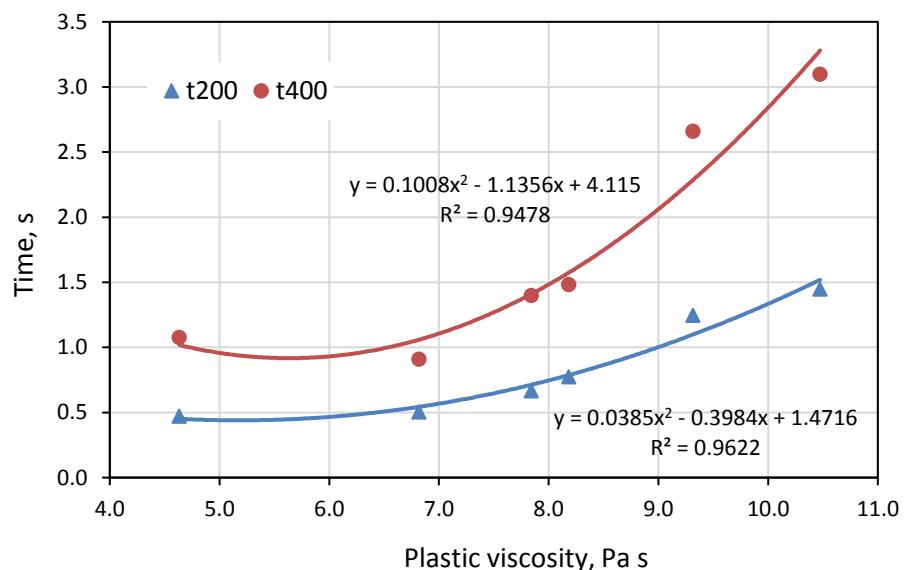
Figure 5.16: t_{200} and t_{400} times in L-box versus plastic viscosity

In Figures 5.7, 5.8, 5.11, 5.12 and 5.16, a bi-linear regression approximation was also explored. However, it was found in each case that the R^2 value is less than that shown in the respective figures.

5.4   Testing of hardened SCC

The accuracy of the proposed design method has been validated through compressive strength tests performed on 100 mm cube specimens (three per mix and age), cured in water at ambient temperature. The results are presented in Table 5.6 and Figure 5.17. The test was carried out at 7, 28 and 90 days of age. The results confirm the well–known trends against the w/cm ratio and confirmed the reliability of the proposed mix–design approach. The effect of the replacement of a part of the river sand fine aggregate by the coarser fraction of limestone powder is minimal also in the hardened state, as can be judged by the entries in the parenthesis in Table 5.6.

Table 5.6: Cube compressive strength test results for SCC mixes

Mix designation	Compressive strength, MPa		
	7 days	28 days	90 days
30A	24.3	37.2	45.7
40A	30.9	44.5	51.2
50A(50A)	35.6	50.9(50.1)	55.1
60A	43.2	62.7	72.6
70A	48.0	74.8	89.4
80A	56.5	80.9	91.4
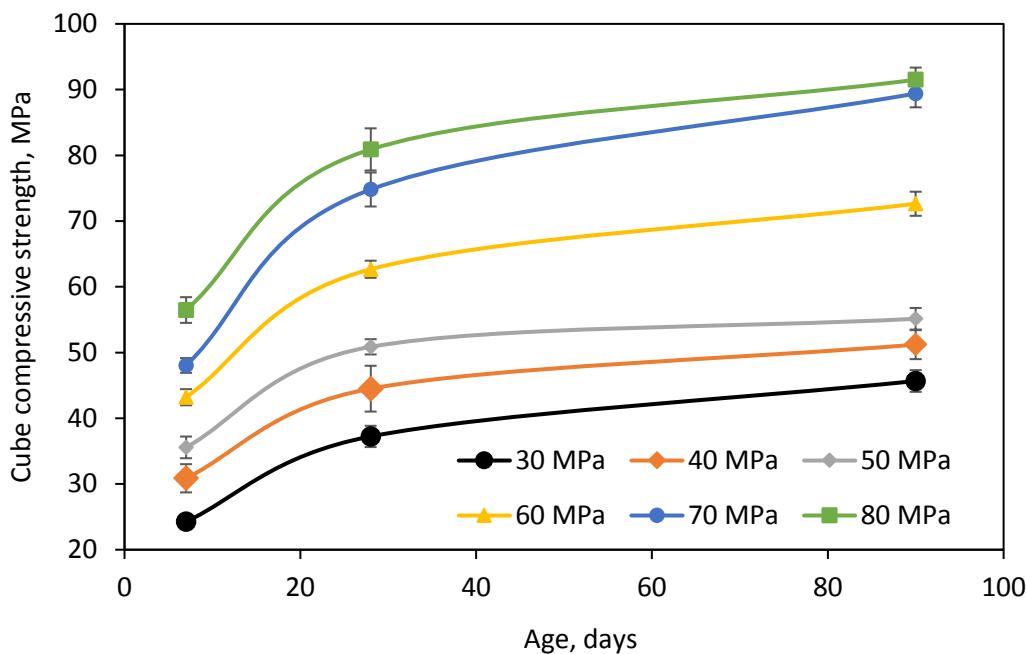
Figure 5.17: Gain of compressive strength with age

5.5 Concluding remarks

This chapter was concerned with the experimental validation of the mix design method proposed in Chapter 4. Several mixes proportioned with the method proposed in the previous chapter were prepared in the laboratory and found to meet the necessary self-compacting criteria and the target plastic viscosity and compressive strength, thus fully validating the proposed mix proportioning method.

It may however be necessary to increase the SP content in order to meet the passing and filling ability tests, but the content will still be in the range 0.4-0.6% of the mass of cementitious materials. It is worth emphasising that the plastic viscosity of the paste remains practically unaltered in this range; the SP content mostly affects the yield stress of the paste.

The coarser fraction of limestone filler (125 μm − 2 mm) can be used to replace an equivalent volume of river sand fine aggregate. Tests have shown that this replacement makes practically no difference to the properties of SCC in fresh and hardened tests. Such

a replacement is environmentally friendly and economic, thus enhancing the sustainability of the SCC mixes.

The proposed mix proportioning method is simple and leads to mix proportions that indeed are self-compacting concrete. It reduces considerably the extent of laboratory work, the testing time and the materials used.

Chapter 6

Influence of mix composition and strength on the fracture properties of SCC

6.1   Introduction

Self-compacting concrete (SCC) has undergone extensive investigations that have led to confidence in its fresh and hardened properties, yet its composition variations raise concerns as to its fracture behaviour. This chapter presents the results of an experimental study on fracture behaviour of SCC mixes differing by the coarse aggregate volume (CA), paste to solids ratio (p/s) and water to binder (or cementitious material (w/cm)) ratio. First the size-dependent fracture energy (G_f) has been determined using the RILEM work-of-fracture test on three point bend specimens of a single size, half of which contained a shallow starter notch (notch to depth ratio = 0.1), while the other half contained a deep notch (notch to depth ratio = 0.6). Then the specific size-independent fracture energy (G_F) was calculated using the simplified boundary effect formalism in which the variation in the fracture energy along the unbroken specimen ligament is approximated by a bilinear diagram. Finally, the bilinear approximation of the tension softening diagram (TSD) corresponding to G_F has been obtained using the non-linear hinge model.

The contents of this chapter have been published in the journal 'Construction and Building Materials' (see publication 6 in the list in Chapter 1).

6.2   Fracture behaviour of SCC

The fracture behaviour of concrete is significantly influenced by the properties of the interfacial transition zone (ITZ) (Akçaoğlu et al., 2004), which in turn are governed by the mix ingredients in vibrated concrete (VC) and self-compacting concrete (SCC), as well. In comparison with VC, SCC requires relatively high amounts of fine particles and paste, but low coarse aggregate content (Okamura and Ouchi, 2003; Okamura et al., 2000; Edamatsu et al., 1998; Su et al., 2001). Although SCC has passed from the research phase into real application, the differences in its composition from VC raise concerns about its fracture behaviour (Beygi et al., 2014a,b,c; Domone, 2006). The concern is primarily because a lower coarse aggregate content in an SCC mix relative to a VC mix of the same grade is likely to reduce its energy absorption capacity and thus its ductility. This needs to be addressed. Previous work (Beygi et al., 2014a,b,c; Nikbin et al., 2014b,c; Cifuentes and

Karihaloo, 2013; Beygi et al., 2013a; Rozière et al., 2007) on this topic was based on the size-dependent specific fracture energy, apart from the work of Cifuentes and Karihaloo (2013) who used the model of Hu and Wittmann (2000) and its simplified version proposed by Karihaloo et al. (2003).

It is the aim of the present chapter to investigate in detail the role of several composition parameters of SCC mixes in their fracture behaviour. In particular, the influence of coarse aggregate volume (CA), paste to solids (p/s) and water to binder (w/cm) ratios on the size-independent fracture energy (G_F) will be studied using the simplified boundary effect approach (SBE) suggested by Abdalla and Karihaloo (2003) and validated by Karihaloo et al. (2003). The corresponding bilinear approximation of the tension softening diagram will then be obtained using the procedure based on the non-linear hinge model proposed by Abdalla and Karihaloo (2004), and Murthy et al. (2013a).

6.3   Parameters describing the fracture behaviour of concrete

Specific fracture energy and the tension softening diagram of a concrete mix are the most important parameters describing its fracture behaviour. They form a basis for the evaluation of the load carrying capacity of cracked concrete structures (Karihaloo, 1995; Bazant and Planas, 1997). These parameters are explained below.

6.3.1   Specific fracture energy

According to RILEM recommendations (RILEM-50FMC, 1985), the specific fracture energy (or toughness) can be obtained by the work-of-fracture method requiring tests on notched three-point bend specimens of different sizes and notch to depth ratios.

It is however widely recognised (Abdalla and Karihaloo, 2003; Bažant, 1996; Bažant and Kazemi, 1991; Carpinteri and Chiaia, 1996; Hu and Wittmann, 1992; Mindess, 1984; Nallathambi et al., 1985) that the specific fracture energy of concrete obtained using the RILEM method is dependent on the size of the test specimen and the notch to depth ratio. To eliminate this size dependency, Guinea and co-workers (Guinea et al., 1992; Planas et al., 1992; Guinea et al., 1994) and Hu and Wittmann (2000) proposed methods

to correct the measured size-dependent specific fracture energy (G_f) in order to obtain a size-independent value (G_F). The methodology proposed by Guinea and co-workers (Guinea et al., 1992; Planas et al., 1992; Guinea et al., 1994) involves adding the non-measured work-of-fracture due to the curtailment of the tail of the load-central deflection (P-δ) curve recorded in the three-point bend test. On the other hand, the methodology of Hu and Wittmann (2000) is based on the observation that the local specific energy along the initially un-cracked specimen ligament varies during the crack propagation, the variation becomes more pronounced as the crack approaches the stress-free back face of the specimen, the so-called free boundary effect.

Abdalla and Karihaloo (2003) and Karihaloo et al. (2003) simplified the free boundary effect formalism of Hu and Wittmann (2000). They proposed and validated extensively a simplified method by which the size-independent fracture energy can be determined by testing only geometrically identical specimens of the same size, half of which contain a shallow starter notch (notch to depth ratio = 0.1), while the other half contain a deep notch (notch to depth ratio = 0.6). Their method significantly reduces the number of specimens to be tested and eliminates the need for using the least squares method to solve an over-determined system of simultaneous equations, as required in the Hu and Wittmann (2000) method.

6.3.2   Tension softening diagram (TSD)

Besides the size-independent fracture energy (G_F), the analysis of cracked concrete structures using the non-linear fictitious crack model (Hillerborg et al., 1976) requires the tension softening diagram, σ(w) of the concrete mix relating the residual stress transfer capability (σ) to the opening displacement (w) of the fictitious crack faces. As the determination of the tension softening diagram using the direct tension test is not a simple task (Karihaloo, 1995), it is often approximated by a bilinear relationship whose parameters are determined in an inverse manner by matching the experimental load-displacement curve of a notched three-point bend beam. For this an analytical model based on the concept of a non-linear hinge was proposed by Ulfkjær et al. (1995) and

Olesen (2001). In this model, the flexural response of a notched beam is obtained by allowing the fictitious crack to develop from the pre-existing notch in the central region of the beam where the bending moment is the largest. The width of this region, proportional to the beam depth, fixes the width of the non-linear hinge. Outside of this region, the material is assumed to behave in a linear elastic manner. Abdalla and Karihaloo (2004) and Murthy et al. (2013a) showed how the non-linear hinge model can be adapted to construct the bilinear tension softening diagram of a concrete mix corresponding to its size-independent specific fracture energy (G_F).

6.4   Theoretical background

The specific fracture energy (G_f), as defined by RILEM technical committee TC50, is the average energy given by dividing the total work of fracture by the projected fracture area (i.e. cross-section of initially un-cracked ligament) based on the load-displacement P-δ curve. Hence, for a specimen of depth W, thickness B and initial notch depth a (as schematically shown in Figure 6.1), the specific fracture energy (G_f) can be expressed as:

$$G_f = \frac{1}{(w-a)B} \int P d\delta \qquad\qquad (6.1)$$

The specimen weight can be neglected for the small specimens used in this study.

(Shallow notch)   (Deep notch)
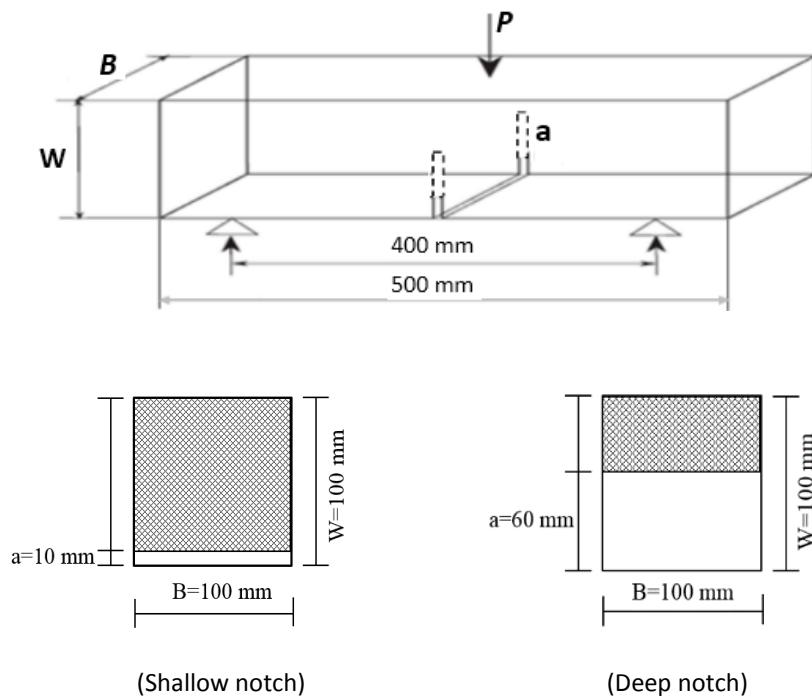
Figure 6.1: Schematic representation of the three-point bending test

The specific fracture energy (G_f) can also be determined using a local energy (g_f) concept described by Duan et al. (2003; 2007) as follows (see Figure 6.2):

$$G_f\left(\frac{a}{W}\right) = \frac{1}{w-a}\int_0^{w-a} g_f(x)dx \qquad (6.2)$$

Hu and Wittman (2000) proposed a bilinear approximation for the local fracture energy variation (g_f) along the crack path (Figure 6.2) with the intersection of the two asymptotes defining a transition ligament size (a_l). The latter, unlike the asymptotic value of specific fracture energy (G_F), varies with the material properties and specimen geometry.
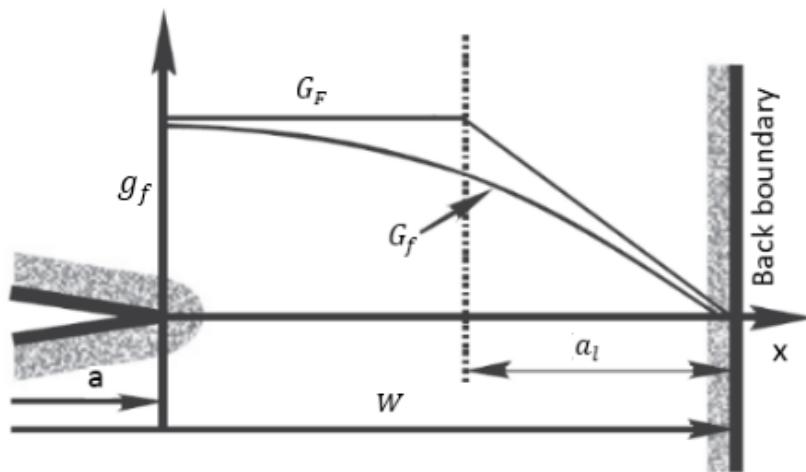
Figure 6.2: Bilinear local fracture energy $G_f\left(\frac{a}{W}\right)$ variation along the un-notched ligament of a notched specimen (After: Duan et al., 2003)

A relation between the measured size-dependent fracture energy (G_f), the transition length (a_l) and the size-independent fracture energy (G_F) can be obtained by substituting the bilinear approximation for the local fracture energy variation (Figure 6.2) into Eq. (6.2)

$$G_f\left(\frac{a}{W}\right) = \begin{cases} G_F\left[1 - \dfrac{\frac{a_l}{W}}{2(1-\frac{a}{W})}\right] & 1 - \dfrac{a}{W} > \dfrac{a_l}{W} \\[2em] G_F\left[\dfrac{(1-\frac{a}{W})}{2\frac{a_l}{W}}\right] & 1 - \dfrac{a}{W} \leq \dfrac{a_l}{W} \end{cases} \tag{6.3}$$

The values of G_F and a_l of a concrete mix are obtained once the mean size-dependent specific fracture energy (G_f) of the mix has been measured on specimens of identical sizes, half of which have a shallow starter notch (a/W = 0.1), while the other half have a deep starter notch (a/W = 0.6) by the RILEM work-of-fracture method using Eq. (6.1). Hu and Duan (2004) showed that although the measured values of G_f depend on W and a/W, the above procedure indeed leads to a G_F value that is essentially independent of the specimen size and relative notch depth.

In recent works, a trilinear approximation of the local fracture energy along the unbroken ligament was proposed by Muralidhara et al. (2010; 2011) and Karihaloo et al. (2013). As has been evidenced by acoustic emission data, the trilinear approximation is closer to how the local fracture energy varies as the crack grows from a notched specimen

(Muralidhara et al., 2010). The local fracture energy (G_f) first rises from the fictitious boundary (notch tip), then remains nearly constant G_F, before reducing again as the crack approaches the stress-free back face boundary, Figure 6.3.
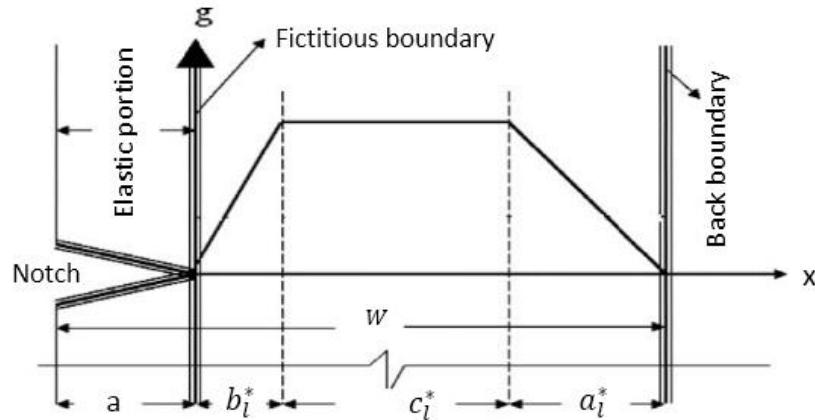
Figure 6.3: Trilinear approximation of local fracture energy, *g*$_f$ variation over the un-notched ligament length (After: Muralidhara et al., 2011)

The G_f and G_F relationship for the trilinear approximation is given in Eq. (6.4):

$$G_f\left(\frac{a}{W}\right) = \begin{cases} G_F\left[\dfrac{\frac{b_l^*}{W}}{2\left(1-\frac{a}{W}\right)}\right] & 1-\dfrac{a}{W} \leq \dfrac{b_l^*}{W} \\[3em] G_F\left[1-\dfrac{\left(\frac{a_l^*}{W}+\frac{b_l^*}{W}\right)}{2\left(1-\frac{a}{W}\right)}\right] & 1-\dfrac{a}{W} \geq \dfrac{a_l^*}{W} \end{cases} \qquad (6.4)$$

To obtain the values of G_F, a_l^* and b_l^* of a concrete mix, the G_f of specimens of identical sizes and a range (more than three) of the notch to depth ratios is first determined by the RILEM method. Then Eq. (6.4) is applied to the mean values of G_f different notch to depth ratios. This gives an over-determined system of equations which is solved by a least squares method to obtain the best estimation of G_F, a_l^* and b_l^*. It should be noted that the trilinear method proposed by Karihaloo et al. (2013) cannot be applied in the present study because the specimens have been tested with two notch to depth ratios only, as required by the bilinear model of Karihaloo et al. (2003). It is however known (Murthy et al., 2013b) that the bilinear and trilinear approximations give nearly the same values of the size-independent specific fracture energy (G_F).

6.5   Experimental programme

6.5.1   Materials

Locally available type II cement (CEM II/B-V 32.5R according to BS EN 197-1 (2011)) and ground granulated blast furnace slag (ggbs) with a specific gravity of 2.95 and 2.40, respectively were used. The super-plasticiser used was a poly-carboxylic ether-based type with specific gravity of 1.07. Crushed limestone coarse aggregate with a maximum size of 20 mm and a specific gravity of 2.80 was used, while the fine aggregate was river sand having a specific gravity of 2.65. Limestone powder as filler with maximum particle size of 125 μm was used (specific gravity 2.40). A part of the river sand was replaced by an equivalent volume of the coarser fraction of limestone filler in the size range 125 μm - 2 mm.

6.5.2   Mix design

A series of SCC mixes were designed according to the procedure described in Chapter 4 having 28-day nominal cube compressive strengths of 30, 60 and 80 MPa with w/cm ratios of 0.63, 0.47 and 0.35, respectively. The SCC mixes contained low paste to solid (p/s) ratio. They are designated A. They have been combined with mixes of medium p/s, designated B, that were studied by Alyhya (2016) and with mixes of high p/s, designated C, that were studied by Al-Rubaye (2016), in order to get a complete picture of the role of low, medium and high p/s ratios (as will be explained later). The compositions of all mixes are given in Table 6.1. In order to ensure that all mixes met the flow and passing ability criteria without segregation (SCC requirements), slump flow, J-ring, L-box and V-funnel tests were conducted (Table 6.2) according to BS EN 206-9 (2010) and EFNARC (2005).

Table 6.1: Mix proportions of test SCC mixes, kg/m³

Mix desig.	cm [a]		w	SP [b]	w/cm	SP/cm %	LP [c]	FA [d]		CA [e]	p/s by vol.
	cement	ggbs						FA**	FA ***		
30A*	240	80	201.6	1.4	0.63	0.44	109	164	579	924	0.61
30B*	240	80	201.6	1.6	0.63	0.50	156	234	530	840	0.67
30C*	240	80	201.6	2.3	0.63	0.72	194	291	504	756	0.72
60A	315	105	197.5	2.3	0.47	0.55	94	141	536	924	0.69
60B	315	105	197.5	2.4	0.47	0.57	125	188	528	840	0.72
60C	315	105	197.5	2.8	0.47	0.67	172	258	477	756	0.79
80A	367.5	122.5	171.5	2.8	0.35	0.57	94	141	536	924	0.69
80B	367.5	122.5	171.5	3.0	0.35	0.61	125	188	529	840	0.72
80C	367.5	122.5	171.5	3.5	0.35	0.71	172	258	478	756	0.79

*A, B and C indicate decrease in coarse aggregate and increase in paste volume for the same strength grade.

a: cementitious material, i.e. binder.

b: super-plasticiser.

c: limestone powder<125 μm.

d: fine aggregate<2 mm (Note: a part of the fine aggregate is the coarser fraction of the limestone powder, FA**125 μm -2 mm, whereas FA *** refers to natural river sand<2 mm).

e: coarse aggregate <20 mm.

Table 6.2: Flow and passing ability test results of SCC mixes

Mix designation	Slump flow		V-funnel	J–ring flow test		L–box test		
	Spread	t_{500}	$t_{v-funnel}$	Spread	t_{500J}	t_{200}	t_{400}	H_2 / H_1
	mm	s	s	mm	s	s	s	
30A	685	0.50	2.46	650	0.70	0.47	1.08	0.91
30B	665	0.88	2.47	635	1.04	0.57	1.11	0.84
30C	655	0.81	2.76	650	0.74	0.53	1.10	0.92
60A	665	1.18	3.23	665	1.48	0.77	1.48	0.89
60B	650	1.32	3.54	645	1.43	0.81	1.72	0.84
60C	655	1.40	4.04	630	1.60	0.81	1.65	0.87
80A	730	1.92	6.67	700	2.80	1.45	3.10	0.93
80B	750	2.06	7.34	730	2.70	1.62	3.20	0.90
80C	670	2.09	7.44	655	2.80	1.45	3.07	0.91

6.6   Specimen preparation and test procedure

From each of the nine mixes (Table 6.1) 12 beam specimens (Figure 6.1), three cubes (100 mm), and three cylinders (100 x 200 mm) were cast. The specimens were de-moulded after one day and cured in water at ambient temperature for 28 days. The cube compressive strength was measured according to BS EN 12390-3 (2009). Six of the beams were notched to a depth of 10 mm (notch to depth ratio a/W = 0.1) (Figure 6.4a), with a thin (2 mm) diamond saw while the remaining six were notched to a depth of 60 mm (a/W = 0.6) (Figure 6.4b). The split cylinder strength (f_{st}) and the modulus of elasticity (E) were measured on cylinders according to BS EN 12390-6 (2009) and BS 1881-121 (1983), respectively.

(a)　　　　　　　　　　　　　　　　　　(b)

Figure 6.4: (a) shallow notch to depth ratio (0.1), (b) deep notch to depth ratio (0.6)

As schematically shown in Figure 6.1, the tests for the determination of the fracture energy were performed according to the RILEM work-of-fracture method (RILEM-50FMC, 1985). The crack mouth opening displacement (CMOD) was used as the feedback control signal and the load-point deflection was measured simultaneously by means of a linearly variable displacement transducer (LVDT). The tests were performed in a stiff Dartec closed-loop universal testing machine with a maximum load capacity of 250 kN.

6.7　Results and discussion

Typical recorded load-deflection diagrams of three of the nine mixes are shown in Figure 6.5. The individual specimen curves for load-deflection and load-CMOD are given in Appendix D and Appendix E, respectively. The area under the load-deflection diagram was calculated from which the G_f(a,W) was determined using Eq. (6.1). Table 6.3 shows the results of the measured fracture energy G_f(a,W), with an indication of the mean value, standard deviation and the coefficient of variation (COV%).

Table 6.3: Measured fracture energy, G_f(a,W) for different SCC mixes from three point bending test (TPB)

Mix designation	W, mm	a/W	Mean [St. dev.] G_f(a,W), N/m	COV, %
30A	100	0.1	96.20 [8.90]	9.20
		0.6	53.50 [5.00]	9.30
30B	100	0.1	85.90 [7.70]	9.00
		0.6	53.00 [4.00]	7.60
30C	100	0.1	73.40 [7.30]	10.0
		0.6	52.30 [4.30]	8.20
60A	100	0.1	108.6 [11.6]	10.7
		0.6	65.80 [1.70]	2.60
60B	100	0.1	91.90 [5.70]	6.20
		0.6	56.50 [5.00]	8.85
60C	100	0.1	83.90 [9.60]	11.4
		0.6	51.90 [3.20]	6.10
80A	100	0.1	105.5 [5.50]	5.30
		0.6	58.50 [5.70]	9.80
80B	100	0.1	100.1 [9.90]	9.90
		0.6	57.00 [4.90]	8.60
80C	100	0.1	97.60 [11.0]	11.3
		0.6	57.70 [2.50]	4.30
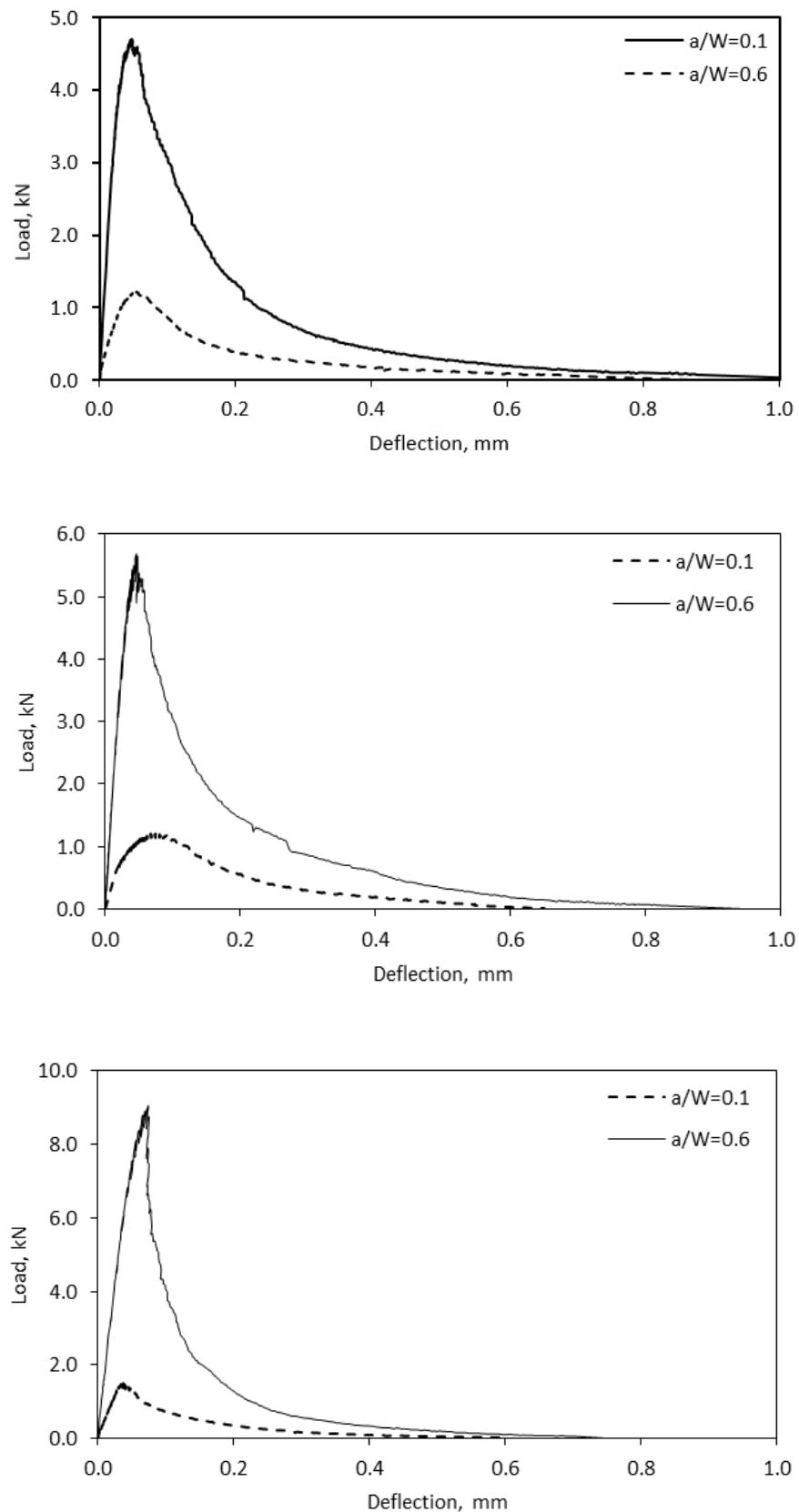
Figure 6.5: Typical load–displacement diagrams of two notched beams (out of twelve tested) from SCC mixes: 30A (top), 60A (middle), and 80A (bottom)

The specific size-independent fracture energy (G_F) and the transition ligament lengths (a_l) of all mixes are determined from $G_f(0.1)$ and $G_f(0.6)$ of Table 6.3 using the first of the two equalities in Eq. (6.3). In many mixes, however it transpired that the transition ligament length (a_l) so calculated violated the corresponding inequality for a/W = 0.6. In these cases the first of the two equalities was used only for a/W = 0.1, while the second equality was used for the deeper notch a/W = 0.6. The resulting values of G_F and a_l are reported in Table 6.4, together with the cube compressive strength (f_{cu}), split cylinder strength (f_{st}) and modulus of elasticity (E), measured according to the relevant British standards.

Table 6.4: Results of f_{cu}, f_{st}, E, G_F and a_l of test SCC mixes

Mix designation	f_{cu}, 28 days MPa	f_{st}, 28 days MPa	E, 28 days GPa	G_F N/m	a_l mm
30A	35.4	2.95	33.6	132.8	49.7
30B	37.0	3.04	32.7	112.3	42.4
30C	37.8	3.30	32.0	90.4	33.8
60A	60.5	3.40	36.7	143.2	43.6
60B	62.9	3.52	36.6	120.3	42.6
60C	65.2	3.65	34.5	109.7	42.3
80A	79.8	4.60	42.3	146.9	50.7
80B	81.6	5.00	40.8	136.5	47.9
80C	83.2	5.35	41.0	130.2	45.2

Within the range of coarse aggregate volume fraction (27-33%) investigated in this study, G_F increases with the increase of coarse aggregate fraction as is clear from Table 6.4 and Figure 6.6 because of the increase in the energy dissipation mechanisms (micro-cracking, crack branching, aggregate interlock) in much the same manner as in VC (Karihaloo, 1995; Akcay et al., 2012; Prokopski and Langier, 2000). This observation is in agreement with previous research on SCC (Beygi et al., 2014c; Nikbin et al., 2014b).

Moreover, it can be seen from Figure 6.6 that the increase in G_F with the coarse aggregate volume fraction is less pronounced in the high strength mix (grade 80) than in mix grades 30 and 60. This is may be attributed to the fact that the ITZ (Beygi et al., 2014b) in grade 80 mixes is much denser and therefore more susceptible to cracking because it contains a higher proportion of cementitious materials, as can be seen in Table 6.1.
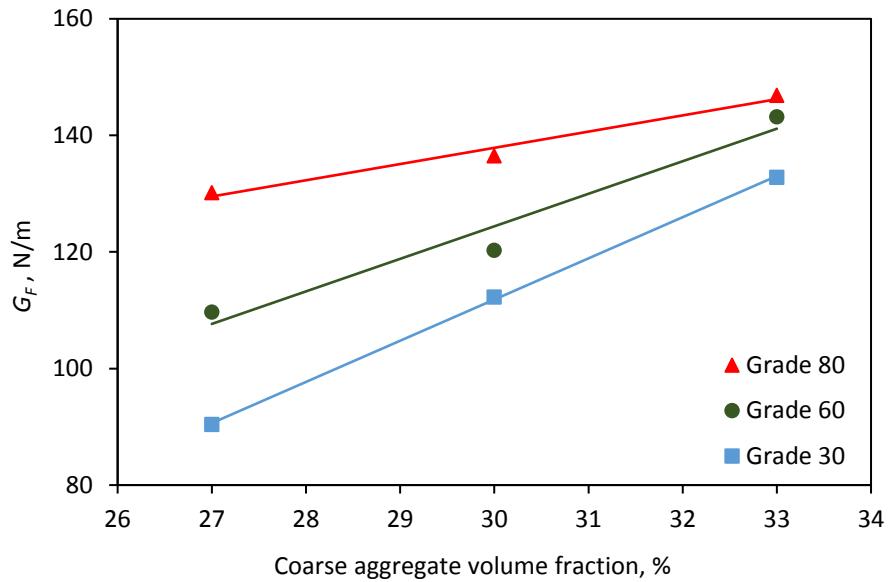
Figure 6.6: Variation of G_F of SCC mixes of different grades with coarse aggregate volume fraction

An increase in the paste to solids (p/s) ratio in all mix grades, as expected, leads to a slight increase in the cube compressive strength (f_{cu}) but a noticeable decrease in G_F, as shown in Figure 6.7.
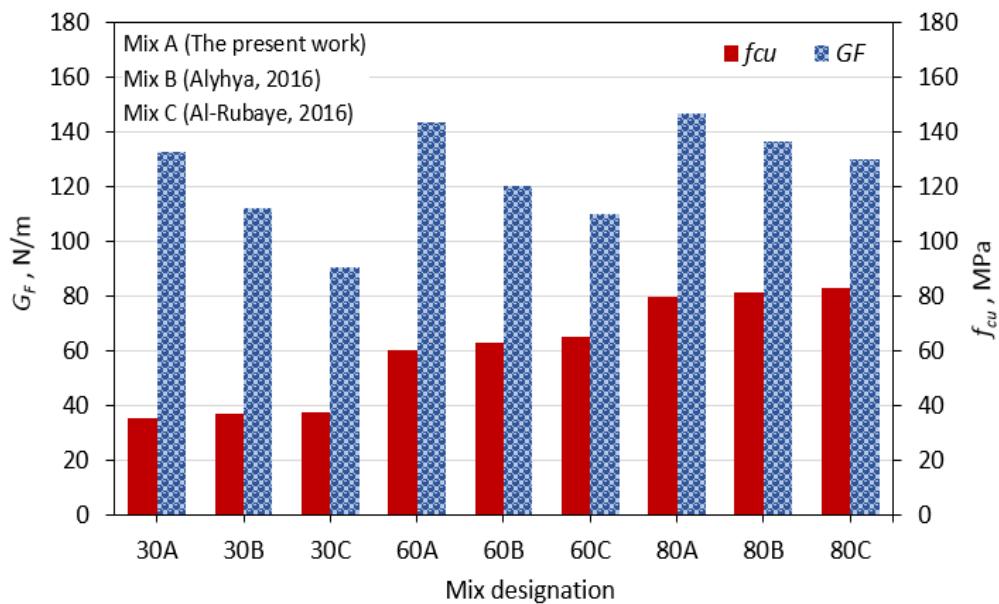
Figure 6.7: Variation of the G_F and f_{cu} with different p/s ratios.

As expected, G_F decreases with increasing water to binder *(w/cm)* ratio, in much the same manner as in VC (Prokopski and Langier, 2000; Nallathambi et al., 1984) as shown in Figure 6.8. This result is consistent with the recent study on normal strength self-compacting concrete conducted by Beygi et al. (2013a) who found that fracture energy decreases by 38% as w/cm ratio is increased from 0.4 to 0.7. G_F of high strength self-compacting concrete (f_{cu} ~ 100 MPa), on the other hand has been reported by Cifuentes and Karihaloo (2013) to be just 90 N/m for w/cm = 0.23. This is a consequence of the densification of ITZ as a result of using a fairly high volume fraction of micro-silica.
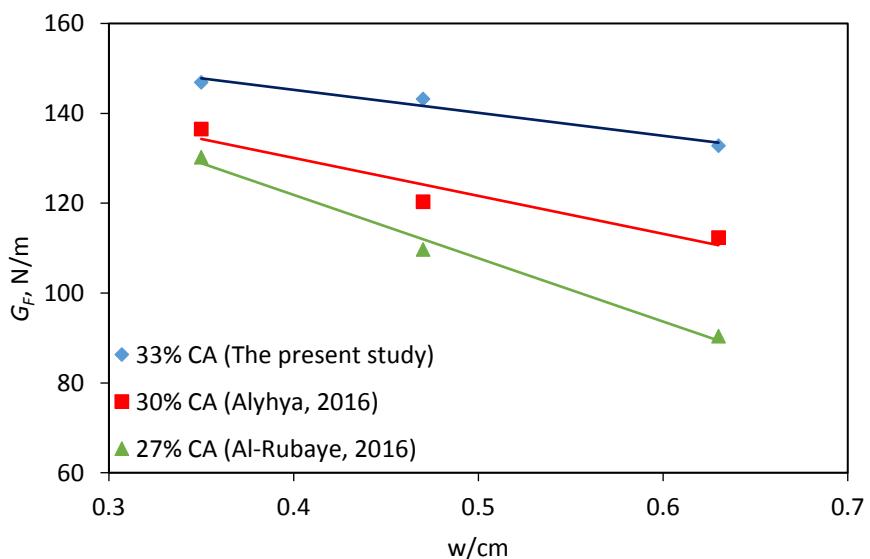
Figure 6.8: Variation in G_F with w/cm ratio for different coarse aggregate (CA) volume fractions

6.8   Bilinear tension softening diagram

To complete the determination of the fracture properties of the SCC mixes, we now outline briefly an inverse procedure based on the non-linear hinge concept for identifying the parameters of the bilinear tension softening diagrams of the mixes corresponding to their above size-independent values of the specific fracture energy (G_F). The details of the procedure may be found in (Abdalla and Karihaloo, 2004; Murthy et al., 2013a). It should be mentioned that the popularity of the bilinear approximation of the tension softening diagram (Figure 6.9) stems from the fact that it captures the two major mechanisms responsible for the observed tension softening in a concrete mix, namely micro-cracking and frictional aggregate interlock. The initial linear branch of the bilinear diagram which is steep is a consequence of the micro-cracking, whereas the second linear branch which is shallow is a result of the frictional aggregate interlock.
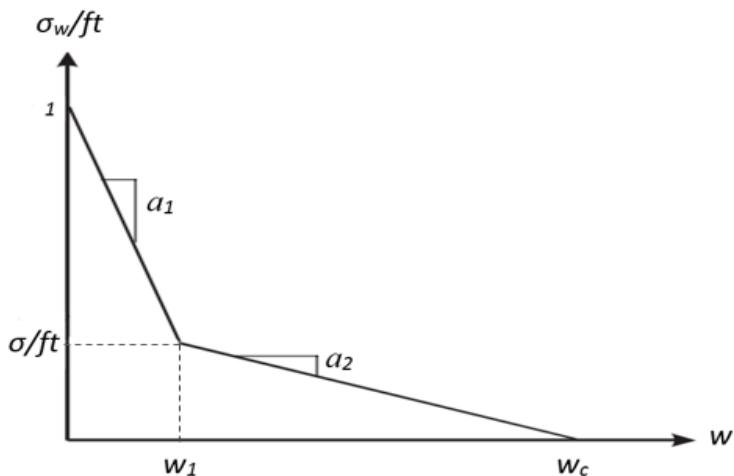
Figure 6.9: Bilinear softening diagram

In the non-linear hinge model of a pre-notched beam, a part of the beam on either side of the notch is isolated as a short beam segment subjected to a bending moment and a normal force. The growth of the real crack and associated fictitious crack representing the fracture process zone is viewed as a local change in the overall stress and strain fields in this isolated beam segment.

The constitutive relationship inside the hinge segment depends on the position of the fictitious crack along the depth of the beam. The axial load and bending moment are related to the hinge rotation in four phases depending on the crack propagation. Phase 0 represents the elastic state when no fictitious crack has formed ahead of the pre-existing notch. Phases I, II and III represent different stages of crack propagation. In phase I, the fictitious crack ahead of the notch is such that the maximum crack opening is less than w_1 corresponding to the knee in the bilinear diagram. In phase II, a part of the fictitious crack of length longer than d has a width in excess of w_1, but in the remaining part it is less than w_1. In phase III, a part of the fictitious crack has opened more than w_c and thus become traction-free, while the opening of the remaining part is still less than w_c or even w_1.

Analytical expressions relating the hinge rotation to the bending moment and crack length in each phase, and in turn to the applied central load on the beam and crack mouth opening displacement (CMOD) are given in Abdalla and Karihaloo (2004). The expressions for CMOD and central load are used to minimise the sum of squares of the error between the theoretical and experimental values of the load with respect to the three unknown parameters of the bilinear tension softening diagram (Figure 6.9). The accuracy of this minimization procedure depends on the total number of observations from the recorded load-CMOD diagram used in this procedure and the allowable error (<3%). For this purpose, a MATLAB program was written and is given in Appendix F. The load-CMOD curves generated by the hinge model and average experimental load-CMOD curves are shown in Figure 6.10.
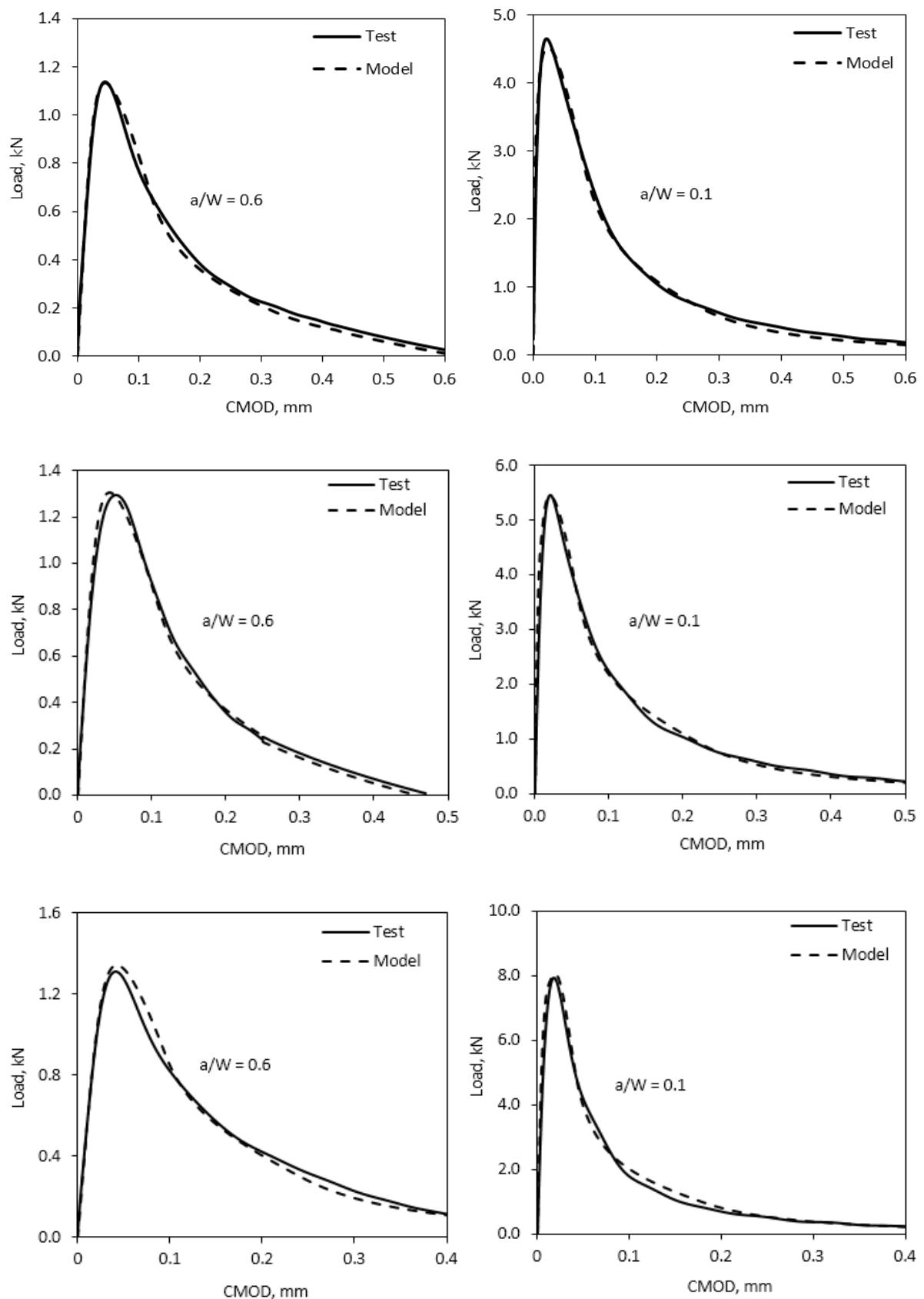
Figure 6.10: Load-CMOD curves generated by the hinge model and average experimental load-CMOD curves: 30A (top), 60A (middle), and 80A (bottom)

As the load-CMOD diagrams are recorded on tests on beams with a notch to depth ratio of 0.1 or 0.6, the three unknown parameters of the bilinear tension softening diagram obtained from the above minimization procedure correspond not to the G_F of the SCC mix but to its size-dependent $G_f(0.1)$ and $G_f(0.6)$. These pairs of three parameters need therefore to be appropriately scaled to reflect the size-independent G_F of the mix. The scaling procedure is described in Abdalla and Karihaloo (2004).

The bilinear tension softening diagrams of all nine SCC mixes corresponding to their G_F are shown in Figure 6.11. The three parameters describing the shape of the bilinear diagram, together with the direct tensile strength (f_{ct}) and the elastic modulus (E) of all SCC mixes are given in Table 6.5. The slope of the initial part of the bilinear softening curve increases with the increasing the p/s ratio, but the influence of p/s decreases as the f_{cu} of the mix increases. In addition, the critical crack opening (w_c) is dominated by the coarse aggregate volume in the mix and the mix grade. The larger the coarse aggregate volume the larger is the critical crack opening (w_c). However, the higher the mix grade the lower is the critical crack opening (w_c) (Figure 6.11).

Table 6.5: Parameters of the bilinear softening diagram corresponding to G_F

Mix Designation	a_1 mm^{-1}	a_2 mm^{-1}	w_1 mm	w_c mm	$\frac{\sigma}{f_t}$	G_F N/m	E GPa	l_{ch} mm
30A	10.07	1.12	0.078	0.272	0.218	132.8	33.6	1377
30B	13.21	1.05	0.060	0.254	0.203	112.3	32.7	976
30C	18.76	1.20	0.043	0.198	0.186	90.4	32.0	519
60A	10.97	1.14	0.073	0.251	0.203	143.2	36.7	1057
60B	13.17	1.25	0.062	0.213	0.189	120.3	36.6	771
60C	15.38	1.28	0.053	0.198	0.185	109.7	34.5	497
80A	16.19	1.18	0.048	0.238	0.225	146.9	42.3	647
80B	18.51	1.39	0.043	0.194	0.211	136.5	40.8	380
80C	19.75	1.38	0.041	0.177	0.188	130.2	41.0	289
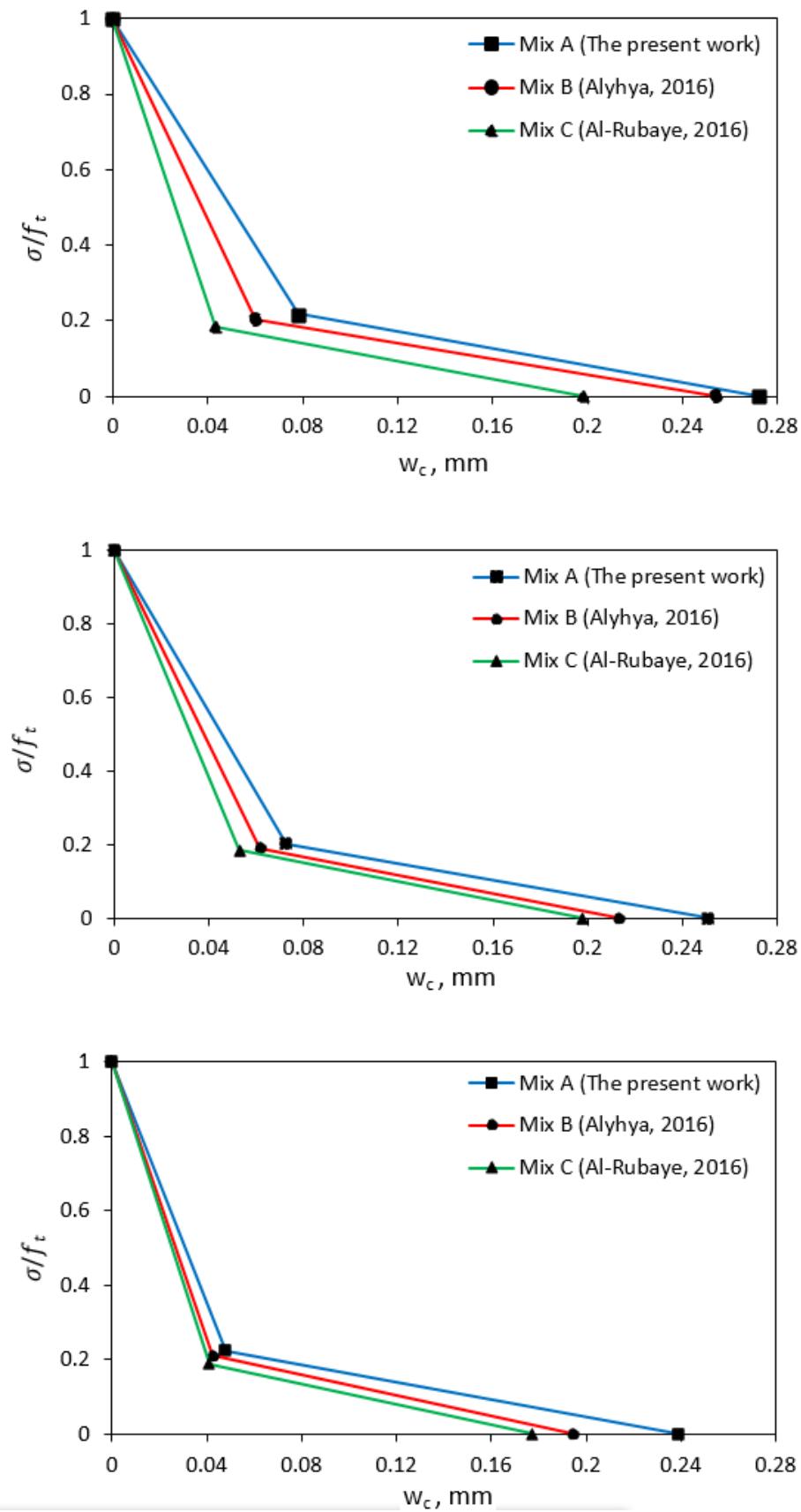
Figure 6.11: The normalised bilinear stress-crack opening relationship for SCC mixes corresponding to their G_F

6.9   Direct and indirect tensile strengths and characteristic length of test SCC mixes

It is well documented that the direct tensile strength (f_{ct}) is approximately two thirds of the indirect tensile strength (f_{st}) for VC (Neville, 1996). Although the literature is rich in reporting on SCC, the effect of p/s ratio and mix grade on tensile strength is still not fully addressed. The relationship between the direct tensile strength (determined by the inverse analysis using the non-linear hinge model) and splitting strengths (f_{ct}/f_{st}) of SCC mixes of different p/s ratio and mix grade are summarised in Table 6.6 and Figure 6.12. It is found that f_{ct}/f_{st} is dominated by the p/s in the mix and the mix grade: it increases with both an increase in p/s and mix grade. This might provide a better understanding of the effect of p/s on the tensile strength of SCC and a useful guide for determining the f_{ct} from the f_{st} in SCC mixes. Note that the ratio (f_{ct}/f_{st}) is slightly different from the conventional 0.65 (Neville, 1996). It depends on the p/s ratio and strength grade (Table 6.6).

Table 6.6: Relation between f_{ct} and f_{st} of test SCC mixes

Mix Designation	f_{ct} MPa	f_{st} MPa	$\dfrac{f_{ct}}{f_{st}}$	Mean $\dfrac{f_{ct}}{f_{st}}$
30A	1.80	2.95	0.61	
30B	1.94	3.04	0.64	0.66
30C	2.36	3.30	0.72	
60A	2.23	3.40	0.66	
60B	2.39	3.52	0.68	0.70
60C	2.76	3.65	0.75	
80A	3.10	4.60	0.67	
80B	3.83	5.00	0.77	0.75
80C	4.30	5.35	0.80	
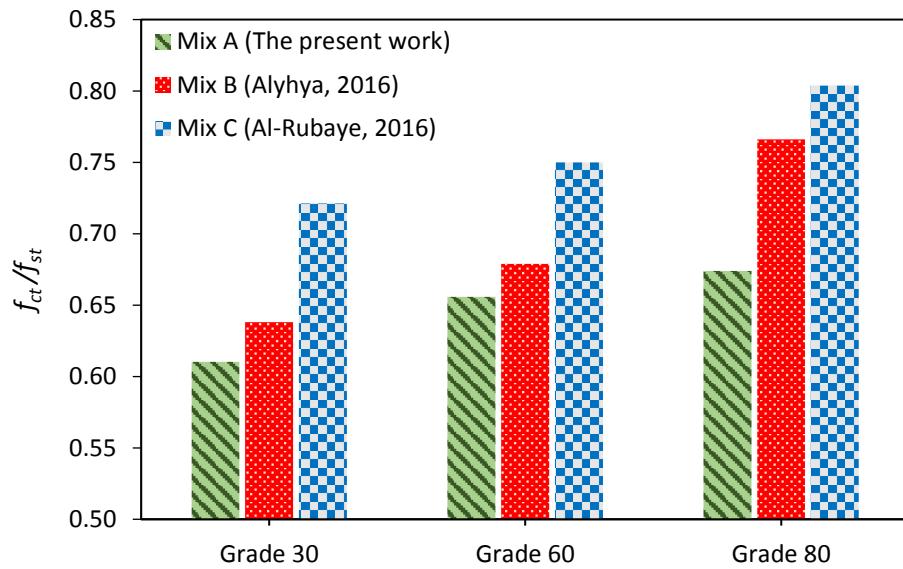
Figure 6.12: Direct (*f_{ct}*) and indirect (*f_{st}*) tensile strengths of different SCC mixes

Also given in Table 6.5 is the characteristic length (l_{ch}) of each mix calculated using the relation (Cifuentes and Karihaloo, 2013):

$$l_{ch} = \frac{E\,G_F}{f_{ct}^2}$$
(6.5)

The characteristic length (l_{ch}) represents the ductility of a mix; the larger the characteristic length, the more ductile the mix. l_{ch} is dominated by the coarse aggregate volume fraction and it decreases with increasing strength grade (Figure 6.13).
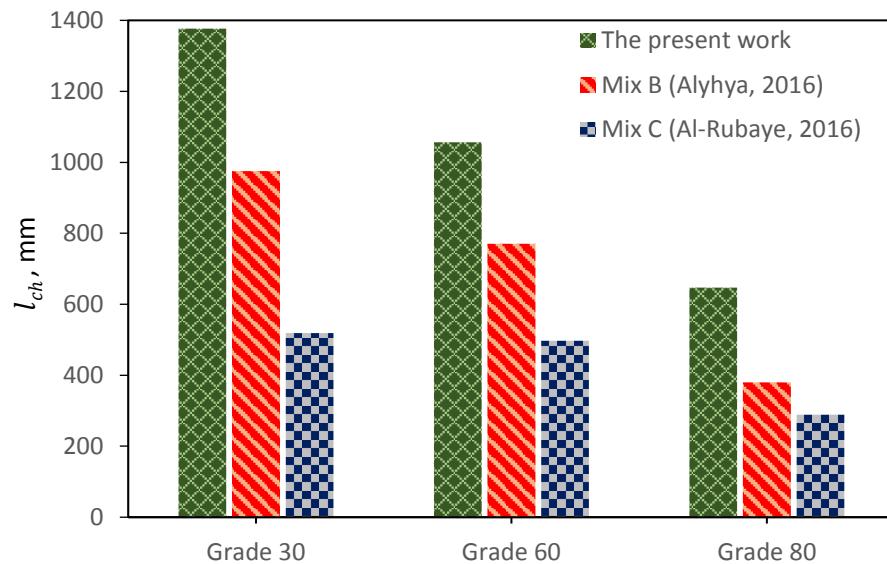
Figure 6.13: Characteristic length (l_{ch}) of different test SCC mixes

6.10   Concluding remarks

The results of an experimental study on fracture behaviour of SCC mixes differing by the coarse aggregate volume, paste to solids ratio and water to binder ratio were presented in this chapter. The bilinear approximation of the tension softening diagram corresponding to G_F has also been obtained using the non-linear hinge model. The results confirm the dependency of the RILEM fracture energy on the notch depth.

The specific fracture energy (G_F) increases with an increase in the coarse aggregate volume fraction, irrespective of the SCC mix grade, although the increase is less pronounced in higher strength mix (grade 80) than in grades 30 and 60 of SCC.

Within the same nominal strength grade, an increase in the paste to solids (p/s) ratio results in a marginal increase in the strength itself, but a noticeable decrease in G_F. It was found also that an increase in the w/cm ratio reduces G_F. The decrease becomes more pronounced with decreasing coarse aggregate volume fraction.

The critical crack opening (w_c) is dominated by the coarse aggregate volume in the mix and the mix grade. The larger the coarse aggregate volume (or the smaller the paste to solids ratio) the larger is the critical crack opening (w_c). However, the higher the mix grade the lower is the critical crack opening (w_c). The characteristic length (l_{ch}) is dominated by the coarse aggregate volume fraction and it decreases with increasing strength grade.

Chapter 7

Simulation of SCC flow in the J-ring test using smooth particle hydrodynamics (SPH)

7.1   Introduction

With the recent tendency towards the use of computer modelling in solving complex engineering problems, its application in concrete technology is in demand and increasingly becoming an accepted tool. Owing to the requirement for highly durable concrete structures, self-compacting concrete (SCC) with its unique characteristics (flow-ability, passing ability and stability) has been developed, and is increasingly replacing vibrated concrete (VC) in different structural applications. SCC, which is characterised in its fresh state by high flow-ability and rheological stability, has excellent applicability for elements with complicated shapes and congested reinforcement. It has rationalised the construction process by offering several economic and technical advantages over VC.

Since the main characteristic of SCC is its flow-ability, its fresh property cannot be fully comprehended without understanding its rheology. The quality control and accurate prediction of the SCC rheology is crucial for the success of its production. The accurate prediction of the SCC flowing behaviour is not a simple task, particularly in the presence of heavy reinforcement, complex formwork shapes and large size of aggregate. In this regard, an indispensable and inexpensive approach offering considerable potential is the numerical simulation of SCC flow (Gram and Silfwerbrand, 2011). This approach will deepen the understanding of the SCC mix flow behaviour and evaluate its ability to meet the necessary self-compacting criteria of passing ability and segregation resistance (i.e. homogeneous distribution of coarse particles in the matrix).

From a computational point of view, choosing the right strategy for the simulation is an important issue, and several approaches have been tried to simulate the flow (Wu and Shu, 2010; Švec et al., 2012; Baaijens, 2001). Of these approaches, the one offering considerable potential is the smooth particle hydrodynamics (SPH). Identifying SCC as a homogeneous fluid that consists of particles of different sizes and shapes, SPH (as a mesh-free particle method) is an ideal computational method to represent its rheological behaviour with an acceptable level of accuracy. This methodology can also assist in proportioning SCC mixes, thus improving on the traditional trial and error SCC mix design (Karihaloo and Ghanbari, 2012; Deeb and Karihaloo, 2013). It has also been used and proved to be efficient and accurate in modelling the flow and monitoring the movement of large aggregates and/or short steel fibres of SCC in the cone slump flow and L-box tests

(Deeb et al., 2014a,b,c). The SPH simulation methodology also provides a useful tool for predicting the yield stress (τ_y) of SCC mixes accurately in an inverse manner from the flow spread (Badry et al., 2016). This is particularly relevant to the characterisation of an SCC mix because the measurement of τ_y by rheometers is inconsistent and fraught with inaccuracies.

The aim of this chapter is to extend the SPH approach to simulating the flow of SCC in the J-ring test. This methodology will provide a thorough understanding of whether or not an SCC mix can satisfy the self-compactibility criterion of passing ability through narrow gaps in reinforcement besides the flow-ability criterion. The capabilities of the SPH methodology will be validated, in terms of flow pattern, time to reach 500 mm flow and blockage assessment, by comparing the results of the numerical simulations with actual J-ring tests carried out in the laboratory on a range of SCC mixes. The distribution of large coarse aggregates in the mixes will also be tracked during the simulation in order to check whether or not they are homogeneously distributed after the flow has stopped. For this the distribution of large coarse aggregates in the mix flow pancake after it has stopped to flow will be examined along two diametrical planes, in four quadrants and in three concentric circular regions. Along all these cut sections the distribution should be nearly the same, if the large aggregates are indeed uniformly distributed.

The contents of this chapter have been published in the journal 'Cement and Concrete Research' (see publication 1 in the list in Chapter 1).

7.2   Development of the mixes

An extensive laboratory study was conducted to produce different low and moderate strength SCC mixes, with nominal 28-day cube compressive strengths of 30, 40, 50, 60, 70 and 80 MPa. These mixes were designed according to the rational mix design method proposed in (Abo Dhaheer et al., 2016a,b). The compositions of all mixes are given in Chapter 5 (Table 5.1). In order to ensure that all mixes met the flowing and passing ability criteria without segregation (SCC requirements), slump flow, J-ring, L-box and V-funnel tests were conducted (see Tables 5.3 – 5.5 in Chapter 5) according to BS EN 206-9 (2010) and EFNARC (2005).

7.3   Numerical modelling

Fresh SCC is a non–Newtonian fluid that can be described by a Bingham–type constitutive relation between the shear stress and shear strain rate. This equation is bi-linear with a kink at zero shear strain rate. From a practical computational perspective, it is expedient to approximate it by a smooth continuous function

$$\tau = \eta\dot{\gamma} + \tau_y\left(1 - e^{-m\dot{\gamma}}\right)$$
(7.1)

where m is a very large number (e.g. m = 10^5). It can be seen from Figure 7.1 that the continuous function in Equation (7.1) approaches the bi-linear function for large m. Here, τ , η , $\dot{\gamma}$ and τ_y represent shear stress, mix plastic viscosity, shear strain rate and mix yield stress, respectively.
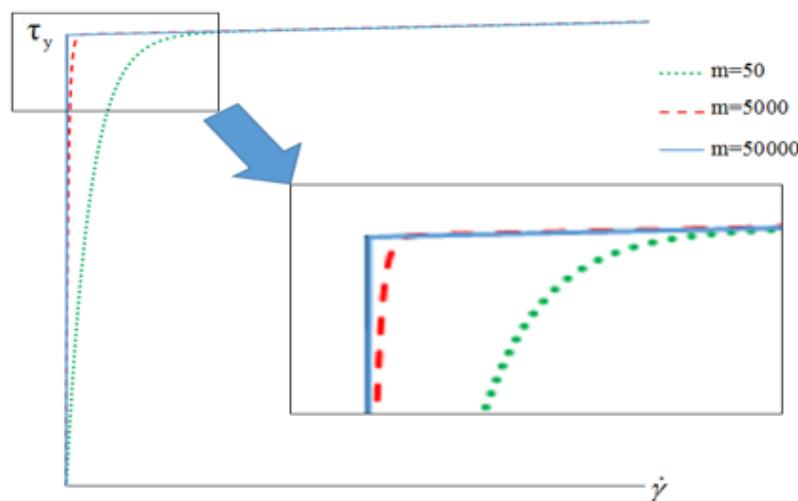
Figure 7.1: A bi-linear Bingham fluid constitutive model replaced by the continuous function

The Bingham-type constitutive model of the mix (Eq. 7.1) is coupled with the Lagrangian continuity equation (Eq. 7.2) and momentum conservation equation (Eq. 7.3) to model the flow of the SCC mix:

$$\frac{1}{\rho}\frac{D\rho}{Dt} + \nabla.\mathbf{v} = 0$$
(7.2)

$$\frac{D\mathbf{v}}{Dt} = -\frac{1}{\rho}\nabla P + \frac{1}{\rho}\nabla.\boldsymbol{\tau} + g \tag{7.3}$$

where ρ, t, $\mathbf{v}$, P and g represent the fluid particle density, time, particle velocity, pressure and gravitational acceleration, respectively.

A projection method based on the predictor-corrector time stepping scheme (Koshizuka et al., 1998; Chorin, 1968; Cummins and Rudman, 1999) is used to track the flow. In the prediction step the momentum conservation equation (Eq. 7.3) is explicitly integrated in time without enforcing incompressibility, i.e. only the viscous stress and gravity terms are considered in Eq. 7.3, and an intermediate particle velocity $\mathbf{v}_{n+1}^{*}$ is obtained as:

$$\mathbf{v}_{n+1}^{*} = \mathbf{v}_{n} + \left(g + \frac{1}{\rho}\nabla.\boldsymbol{\tau} \right)\Delta t \tag{7.4}$$

In the correction step the ignored pressure term in Eq. 7.3 is considered:

$$\frac{\mathbf{v}_{n+1} - \mathbf{v}_{n+1}^{*}}{\Delta t} = -\left(\frac{1}{\rho}\nabla P_{n+1} \right) \tag{7.5}$$

where $\mathbf{v}_{n+1}$ is the corrected particle velocity at the time step n+1. The solution of Eq. 7.5 requires the pressure P_{n+1}. This is obtained by enforcing the incompressibility condition. For a flow without a change in density, the incompressibility condition follows from the continuity equation (Eq. 7.2):

$$\nabla.\mathbf{v}_{n+1} = 0 \tag{7.6}$$

Hence the intermediate velocity can be projected on the divergence-free space by writing the divergence of Eq. 7.5, using Eq. 7.6, as:

$$\nabla.\left(\frac{1}{\rho}\nabla P_{n+1} \right) = \frac{\nabla.\mathbf{v}_{n+1}^{*}}{\Delta t} \tag{7.7}$$

As the density of particles remains constant in this simulations, Eq. 7.7 can be rewritten as:

$$\nabla^2 P_{n+1} = \frac{\rho}{\Delta t}\nabla.\mathbf{v}_{n+1}^{*} \tag{7.8}$$

where ∇^2 is the Laplacian. Once the Poisson equation (Eq. 7.8) has been solved to calculate the pressure, the particle velocity is updated by Eq. 7.5 so that the instantaneous particle position can be updated as:

$$\mathbf{x}_{n+1} = \mathbf{x}_{n} + \mathbf{v}_{n+1}\Delta t \tag{7.9}$$

7.4   Boundary conditions

Two types of boundary conditions need to be considered in the simulation of the J-ring test when solving the continuity and momentum conservation equations. These are: (1) the pressure on the free surface vanishes, and (2) the normal component of the particle velocity and the pressure gradient vanish at the wall of the cone, at the J-ring bars and on the bottom plate, as shown in Figure. 7.2a. The zero pressure gradient is used only for solving the second-order pressure Poisson equation (7.8).
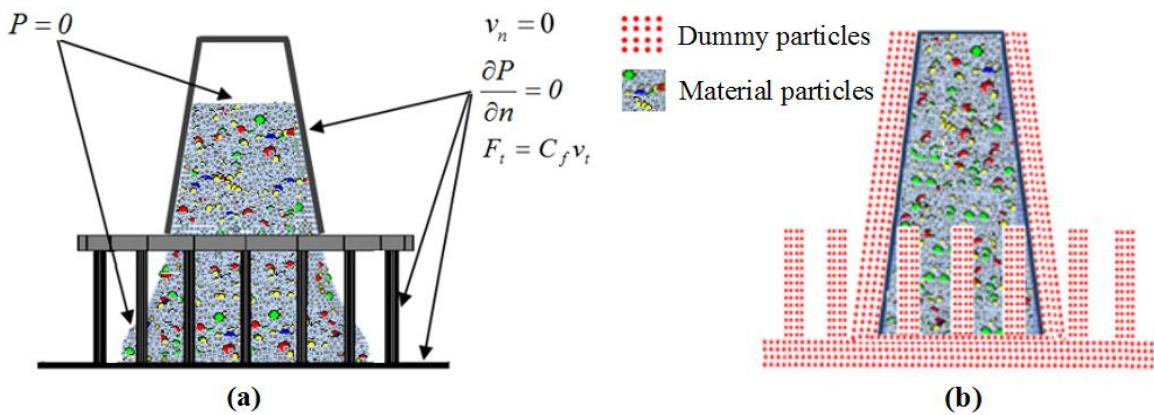
Figure 7.2: (a) boundary conditions, (b) dummy particles for enforcing boundary conditions

In the simulations, the technique based on arrays of rigid dummy particles was used to implement the boundary conditions on the cone wall, J-ring bars and base plate, as shown in Figure. 7.2b. For realistic simulations, the friction between the SCC mix and the contacting surfaces needs to be taken into consideration, as this contributes a force that resists the flow. The coefficients of kinematic friction (C_f) between the mix and the steel base plate and the J-ring bars are 0.55 and 0.48 N s/m, respectively. The former was determined previously (Deeb et al., 2014b) by matching the t_{500} (the time when the mix spread reaches 500 mm) in slump cone test conducted in the same laboratory with the simulated results. The latter was chosen by matching the t_{500J} in the J-ring test with the simulated results of Mix50 in the present study (Table 7.1). These calibrated coefficients of kinematic friction were then held unchanged for all other five mixes simulated in this study.

Table 7. 1: Simulation trials on Mix50 to determine the coefficients of kinematic friction (C_f) between the mix and the steel of J-ring bars

Mix designation	Plastic viscosity, Pa s	Yield stress, Pa	Trial C_f	t_{500J} experimental, s	t_{500J} simulated, s
			0.44		1.3
Mix50A	7.84	180	0.46	1.4	1.3
			0.48		1.4

7.5   Treatment of particles in the simulated mixes

The volume of the mix in the cone, 5.498×10^6 mm^3, was simulated by 23,581 particles. If all particles possess the same density as the viscous homogeneous continuum, the number of particles used gives a resolution of 233.15 mm^3 per particle. This resolution will be rather different if the particles possess different densities, and therefore, the large aggregates that can be distinguished from the homogeneous mass must have a volume exceeding this minimum. That is why only the aggregates of size 8 mm and above could be treated as discrete identities.

The simulated particles were generated randomly. Particles representing the mortar as well as the coarse aggregates form a homogeneous mass and possess the same continuum properties except for their assigned volumes. The masses of the SPH particles representing different coarse aggregate size particles in the mix were calculated according to their respective volume fractions in the mix. The volume fractions of coarse aggregates in different size ranges (g ≥ 20, 16 ≤ g < 20, 12 ≤ g < 16 and 8 ≤ g < 12 mm) were calculated (Table 7.2) by performing sieve analysis within a given aggregate test sample. For the purpose of modelling, each aggregate size range was replaced by a representative aggregate size, as illustrated in Table 7.2. Also given in Table 7.2 is the assigned volume (V_a) for each particle size, which appears in the discrete form of SPH equations is equal to the ratio of its actual mass to the density of the continuum. The calculation of the assigned volumes of particles corresponding to their size range (g) in the 3D simulation of J-ring test is presented in the following section.

7.6   Calculating the assigned volumes of SCC particles

Step 1: Determination of the mortar density

The volume fraction of mortar (i.e. cm + ggbs + water + LP + FA + SP + CA < 8 mm) is first calculated as:

Volume fraction of mortar = total volume − volume fractions of CA (≥ 8mm)

Volume fraction of mortar = $1.0 - 0.0156 - 0.0882 - 0.0509 - 0.0969$
$$= 0.7484 \text{ m}^3$$

Using the rule of mixtures, the density of mortar can be determined as:

$$\text{Mix density} = \sum \begin{array}{l} \text{volume fraction of CA } (\geq 8\text{mm}) \times \text{CA density} \\ +\text{mortar volume fraction} \times \text{mortar density} \end{array}$$

$$2374.3 = (0.0156 + 0.0882 + 0.0509 + 0.0969) \times 2800$$

$$+ 0.7484 \times \text{mortar density}$$

Mortar density $= 2231 \text{ kg/m}^3$

Step 2: Determination of number of particles (Np) of each size range (g)

$$\text{Np (g)} = \frac{\text{volume fraction of each size range} \times \text{cone volume}}{\text{volume of one representative particle}}$$

$$\text{Np (g} \geq 20) \qquad = \frac{0.0156 \times 5498000}{4190.5} = 20$$

$$\text{Np } (16 \leq \text{g} < 20) = \frac{0.0882 \times 5498000}{3054.9} = 159$$

$$\text{Np } (12 \leq \text{g} < 16) = \frac{0.0509 \times 5498000}{1437.3} = 195$$

$$\text{Np } (8 \leq \text{g} < 12) \quad = \frac{0.0969 \times 5498000}{523.8} = 1017$$

$$\text{Np (g} < 8) \qquad = 23581 - (20 + 159 + 195 + 1017) = 22190$$

Step 3: Determination of volume of each representative mortar particle ($g < 8$)

Volume of mortar in the cone = mortar volume fraction× cone volume

$$= 0.7484 \times 5498000 = 4114703 \text{ mm}^3$$

Volume of each mortar particle $(g < 8) = \dfrac{\text{volume of mortar in the cone}}{Np(g < 8)}$

$$= \frac{4114703}{22191} = 185.422 \text{ mm}^3$$

Step 4: Determination of the assigned volume (Va) of each size range (g)

Assigned volume per particle (Va) $= \dfrac{\text{actual volume of particle} \times \text{actual density}}{\text{density of continuum}}$

Va $(g \geq 20)$ $\qquad = \dfrac{4190.5 \times 2800}{2374.3} = 4941.8 \text{ mm}^3$

Va $(16 \leq g < 20) = \dfrac{3054.9 \times 2800}{2374.3} = 3602.6 \text{ mm}^3$

Va $(12 \leq g < 16) = \dfrac{1437.3 \times 2800}{2374.3} = 1695.0 \text{ mm}^3$

Va $(8 \leq g < 12) \quad = \dfrac{523.8 \times 2800}{2374.3} = 617.7 \text{ mm}^3$

Va $(< 8) \qquad = \dfrac{185.422 \times 2231}{2374.3} = 174.2 \text{ mm}^3$

Table 7. 2: Volume fractions and assigned volumes of particles corresponding to their size range (g) in the 3D simulation of J-ring test

Mix particles	Particle range, mm	Representative particle diameter, mm	Density kg/m^3	Volume fraction, %	3D J-ring test	
					Number of particles	Assigned volume per particle, mm^3
Aggregate particles	g ≥ 20	20	2800	1.56	20	4941.8
	16 ≤ g <20	18	2800	8.82	159	3602.6
	12 ≤ g < 16	14	2800	5.09	195	1695.0
	8 ≤ g < 12	10	2800	9.69	1017	617.7
Mortar particles	g < 8		2231	74.84	22190	174.2
Total			2374.3	100	23581	

Throughout the simulation, particles representing the coarse aggregates based on their assigned volumes were tagged (Figure 7.3) in order to monitor their velocity vectors and positions.
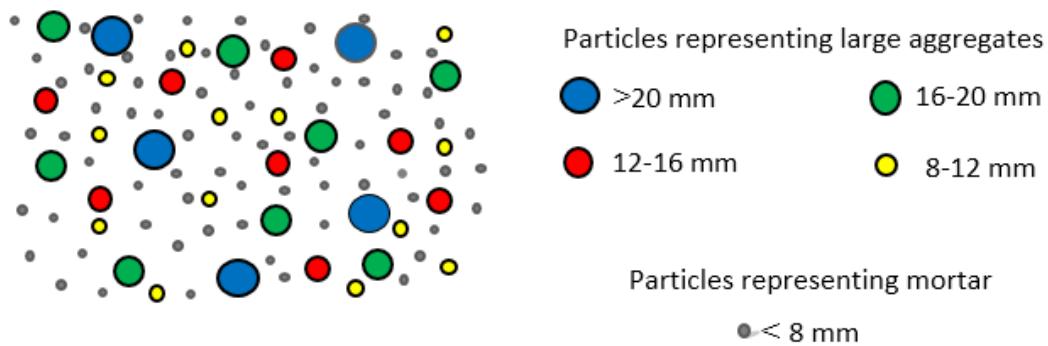
Figure 7.3 : Schematic sketch of particle representation in the simulated mixes (After: Deeb et al., 2014a)

7.7   Simulation results

To investigate how efficient the SPH is to predict the flow of SCC mixes through gaps in the reinforcing bars, different SCC mixes were three-dimensionally simulated in the J-ring apparatus. The rheological parameters (plastic viscosity and yield stress) of each of these mixes have been determined. The plastic viscosity of a mix was calculated using the micromechanical procedure described in (Ghanbari and Karihaloo, 2009), based on the plastic viscosity of the paste (i.e. cement, ggbs, water, super-plasticiser and entrapped air). The latter was estimated from viscometer measurements of similar pastes reported in the literature (Sun et al., 2006; Nehdi and Rahman, 2004). The results are given in Table 7.3. The yield stress (τ_y) was predicted in an inverse manner using the SPH simulation of slump flow test (Badry et al., 2016). Over the wide range of SCC mixes (30 – 80 MPa) simulated, it has been found (Badry et al., 2016) that the τ_y varies only marginally from 175 to 190 Pa. Therefore, the same range was used for τ_y of the mixes in the present study (Table 7.3).

The simulation and experimental results for t$_{500J}$ and spread of all mixes are shown in Table 7.3. It is noted that the results are in very good agreement. It will be recalled that only mix 50MPa was used to calibrate the coefficient of kinematic friction (C_f) between the mix and bars, which was then held unchanged for the simulations of all the remaining five mixes. The simulation results of SCC mixes will be discussed below in terms of flow pattern and t$_{500J}$, passing ability, and segregation resistance. In this study, it is worth mentioning that the simulation has been performed on a narrow spacing bar J-ring test (with 16 bars; this is the current British standard (BS EN 12350-12, 2010)) and a wide one (with 10 bars; this was the earlier European standard, now superseded) to simulate the SCC flow in congested and normal reinforcement, respectively. The former will be reported in this chapter, whereas the latter is described in Appendix G.

Table 7. 3: Simulation and experimental results for SCC mixes

Mix Designation	Plastic viscosity, Pa s	Yield stress, Pa	t_{500J}, s		Spread diameter, mm	
			experimental	simulated	experimental	simulated
30	4.63	175	0.7	0.7	650	640
40	6.84	175	0.8	0.9	700	680
50	7.84	180	1.4	1.4	640	640
60	8.18	175	1.5	1.6	665	655
70	9.32	180	2.0	2.0	690	695
80	10.47	190	2.8	2.7	700	700

7.7.1   Mix flow pattern and t_{500J}

The experimental and simulated flow patterns of selected SCC mix (Mix60) at different times during the flow are shown in Figures 7.4 – 7.6. The experimental and simulated flow patterns of all the remaining five mixes are shown in Appendix G. The simulations are found to be well correlated with the experimental results. From Figure 7.4 it can be noticed that the shape and the free surface profile of the simulated mix around the J-ring bars is similar to that observed in the test. The spread at 500 mm diameter also looks very similar to that observed in the laboratory test (Figure 7.5). The final spread of the simulated mix has the same smooth "pancake" appearance as in the laboratory test (Figure 7.6). Moreover, it can be observed (Table 7.3) that SPH can predict very well the time needed for flow to reach the spread at 500 mm diameter (t_{500J}) for all the test mixes.
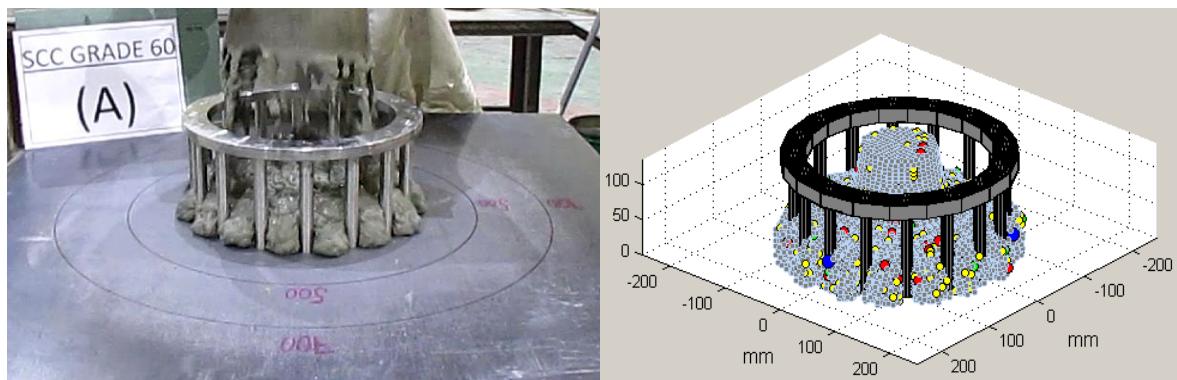
Figure 7.4: Flow pattern of SCC Mix60 just after passing through the gaps in J-ring bars (at 0.5 s)
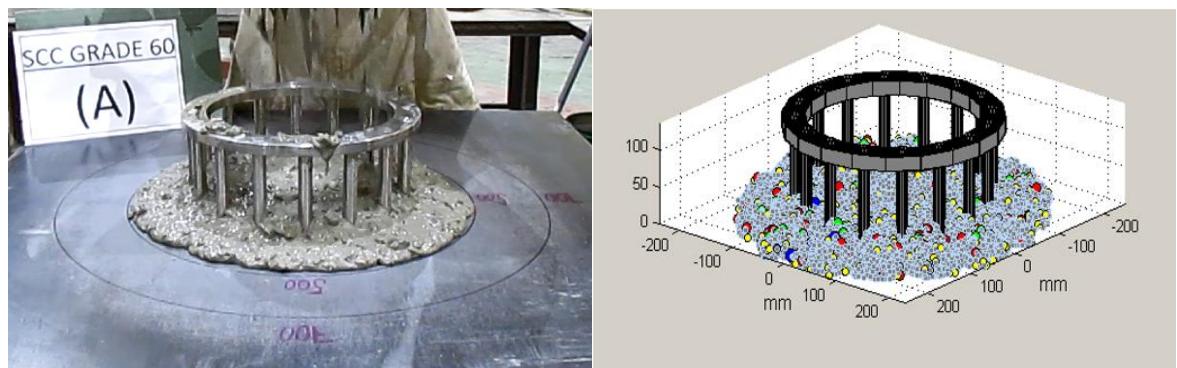
Figure 7.5: Flow pattern of SCC Mix60 at t$_{500J}$ (at 1.5 s)
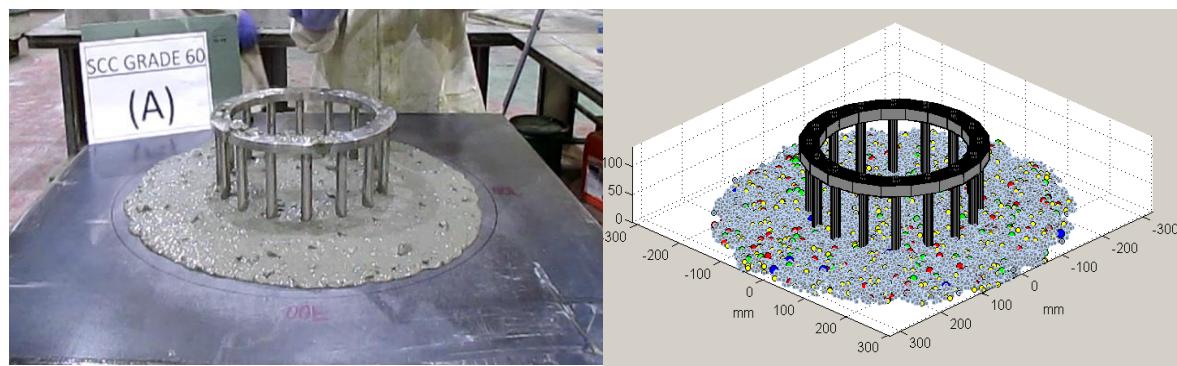
Figure 7.6: Flow pattern of SCC Mix60 after it has stopped (at 11.0 s)

7.7.2   Passing ability

With the reference to the passing ability criterion, SCC should have the ability to flow and pass through congested reinforcement and narrow openings while maintaining adequate suspension and distribution of coarse particles in the matrix. This means that arching near obstacles and blockage during flow have to be avoided. In this simulation, the SCC passing ability can be judged in terms of the height difference between the concrete inside and outside the steel bars of the J-ring according to BS EN12350-12 (2010). Taking the acceptance criterion of SCC passing ability that the height difference is ≤ 10 mm (BS EN 206-9, 2010), it is clear from Table 7.4 that all the six simulated mixes did flow through the gaps in the J-ring without blockage, as indeed they did in the laboratory tests.

Table 7. 4: Height difference between the concrete inside and outside the steel bars of the J-ring test

Mix Designation	Height difference, mm	
	experimental	simulated
30A	10	10
40A	7	8
50A	10	9
60A	9	7
70A	7	7
80A	7	5

7.7.3   Assessment of segregation resistance

The numerical simulation of flow, as shown above, is a powerful tool for understanding the rheological behaviour of SCC mixes in terms of flow pattern, t_{500J}, the flow spread and passing ability (i.e. no blockage). It can also be used for assessing the segregation resistance of the SCC mix through an assessment of the coarse aggregate distribution in the "pancake" after it has stopped to flow. For this, the distribution of coarse aggregates in the SCC mixes will be evaluated along three different cut sections: (1) in three concentric circular regions of the "pancake", (2) in four quadrants and (3) along two orthogonal diameters.

In concentric regions approach the coarse aggregate distribution in the mix "pancake" has been evaluated, following an approach proposed by Tregger et al. (2012) for experimental slump flow "pancake". Their assessment procedure is based on the concentration of aggregates in concentric rings, irrespective of whether this concentration is made up of aggregates of one or several size ranges. However, if the concentration of aggregates is the same in all the rings, there is no guarantee that the distribution of aggregates of different size ranges is the same. It is the distribution of coarse aggregates of different size ranges that determines whether or not there is segregation in the mix. Therefore, the approach proposed in (Tregger et al., 2012) has been applied here to the SCC coarse aggregate distribution rather than its concentration in the simulated J-ring "pancake". The distribution has been determined in three concentric circular regions: inside the J-ring (Figure 7.7A), between the outer edge of J-ring bars and a diameter of 500 mm spread (Figure 7.7B), and finally between the diameter of 500 mm and the final spread of the mix (Figure 7.7C). From Figure 7.8 it can be seen that the coarse aggregates in the three concentric circular regions are evenly distributed throughout the matrix.
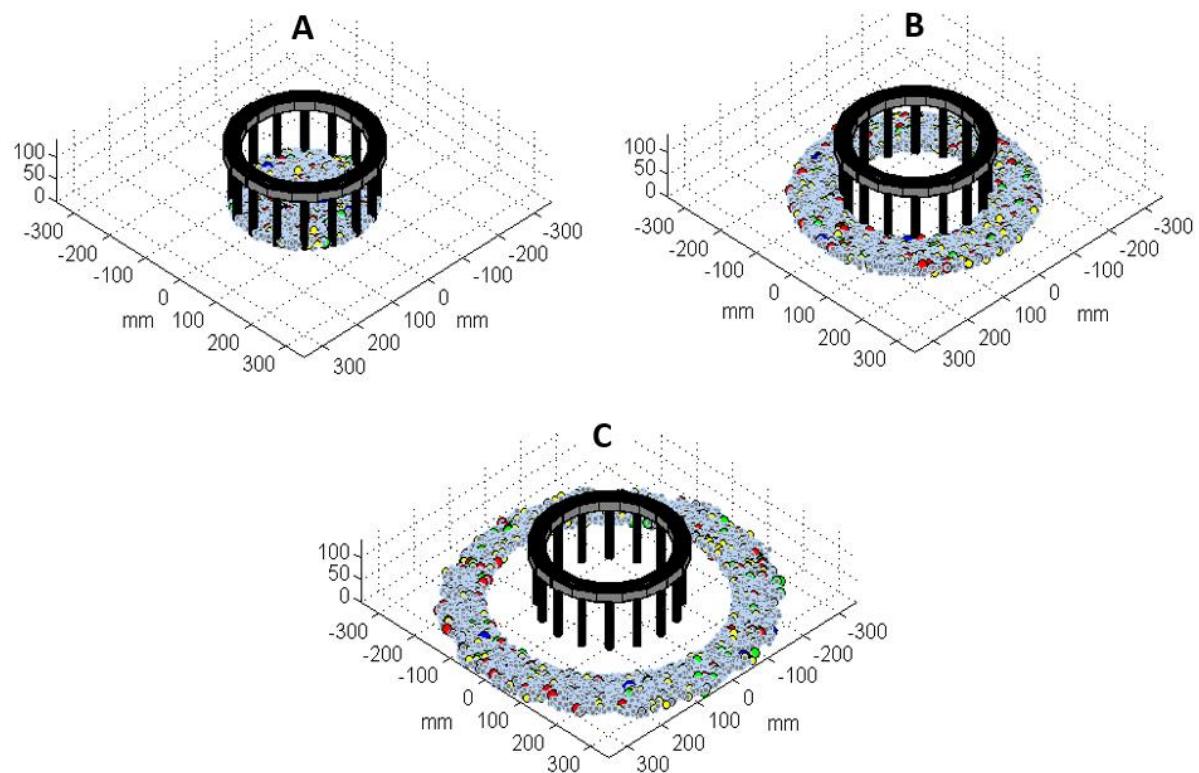
Figure 7.7 : Coarse aggregate distributions in the three concentric circular regions
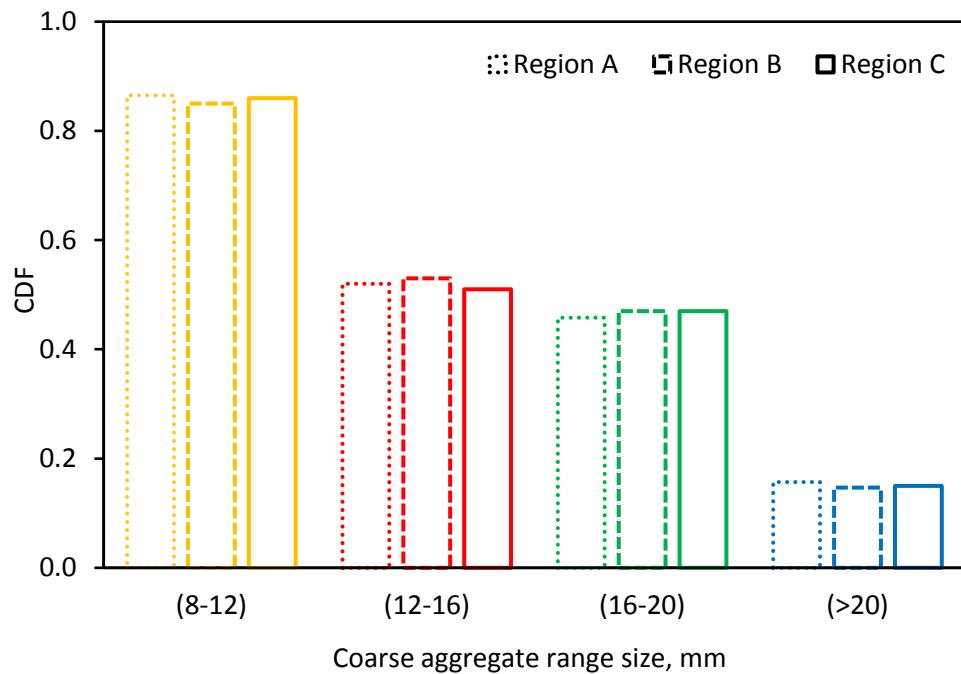
Figure 7.8: The three concentric circular regions to evaluate the distribution of coarse aggregates in the J-ring "pancake"

The distributions of coarse aggregates in the SCC mix ''pancake'' were also calculated after splitting the "pancake" into four quadrants (Figure 7.9). In each quadrant, the distribution was quantified by counting the number of coarse aggregate particles in each size range. It can be seen from Figure 7.10 that the larger aggregates (≥ 8 mm) are almost identically distributed in the four quadrants, providing further confirmation of the segregation resistance of the mix. Thus, SPH allows tagging of the large aggregate particles in order to track their locations during the flow and after it has stopped.
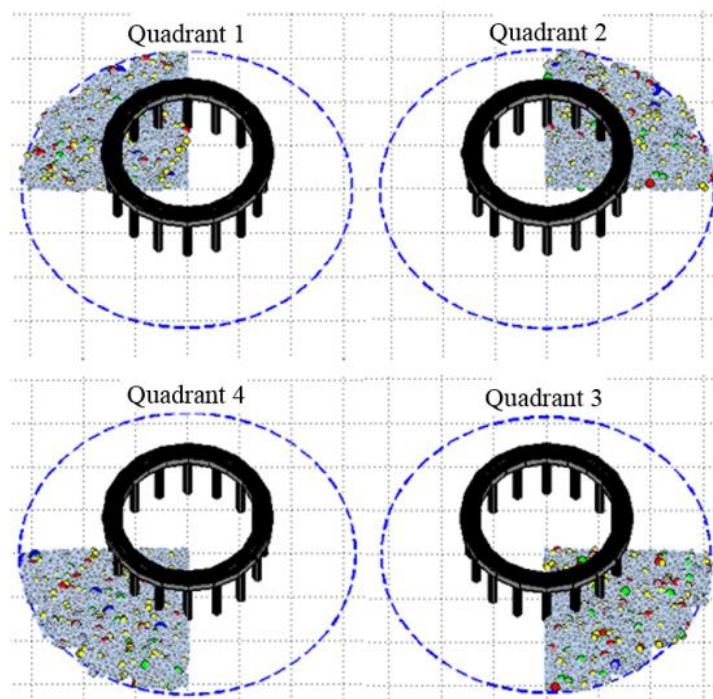
Figure 7.9: Four quadrants of Mix50 "pancake" to determine the aggregate distribution
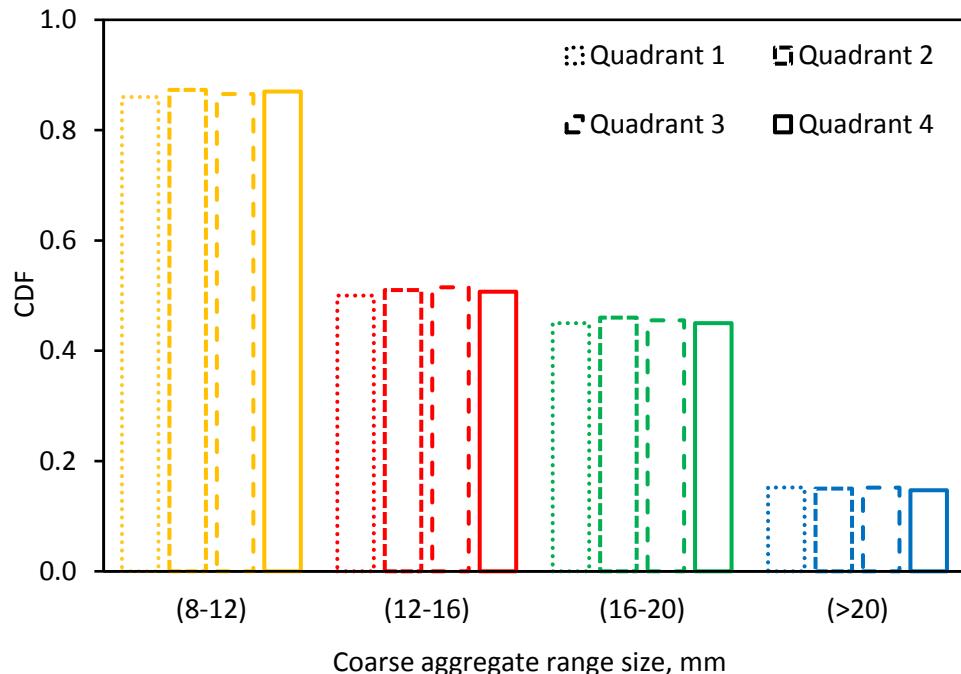
Figure 7.10: Coarse aggregate distributions in the four quadrants

The coarse aggregates along the two diametrical sections (AA and BB in Figure 7.11) were investigated by performing a statistical analysis on the coarse aggregates exposed in these sections (Figure 7.12) using the Weibull cumulative distribution function (CDF). Figure 7.13 confirms that the distributions of the coarse aggregate particles of different size ranges are nearly the same along the cut diameters. This attests to the homogeneity of flow, i.e. to no segregation during the flow. Therefore, the numerical methodology (SPH) can capture the flow behaviour of SCC mixes and provide insight into the distribution of large aggregates during the flow.
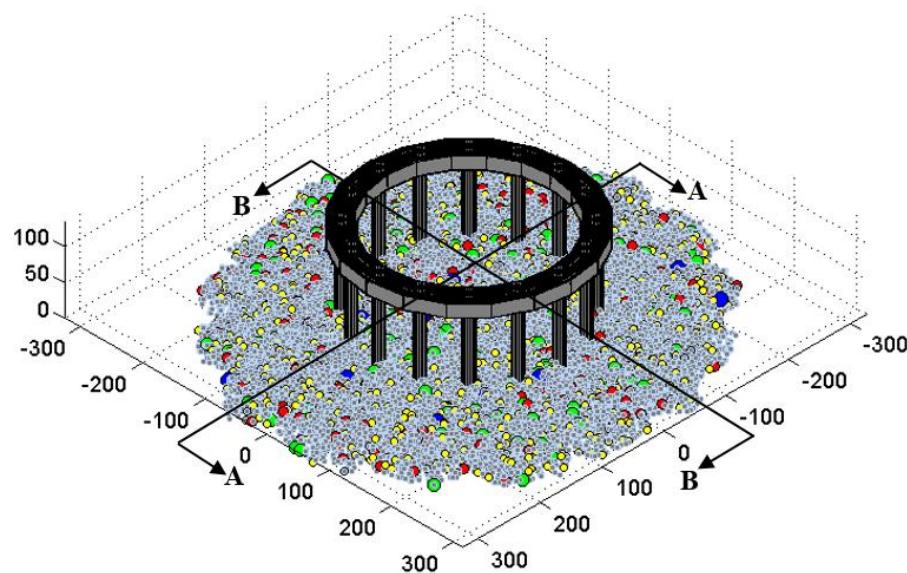
Figure 7.11: Flow pattern of SCC (Mix30) showing the large aggregates
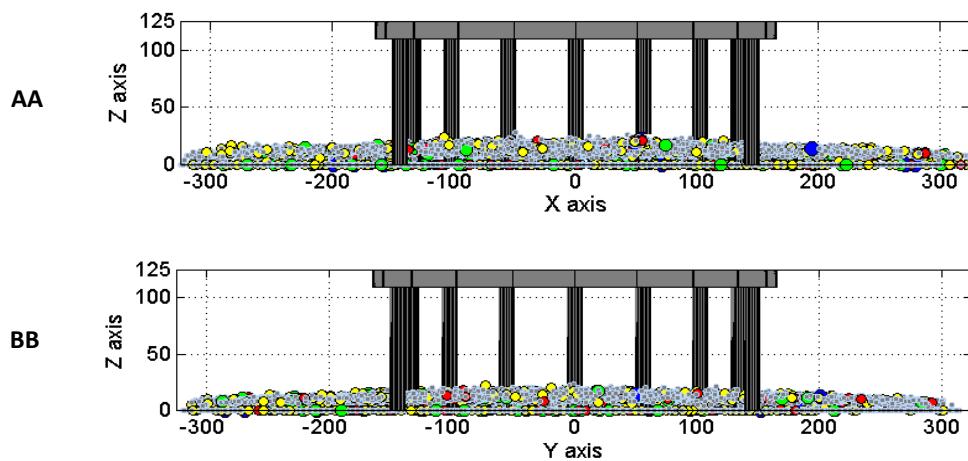
Figure 7.12: Coarse aggregate distributions along diametrical cross-sections (AA and BB) of Mix30 "pancake"
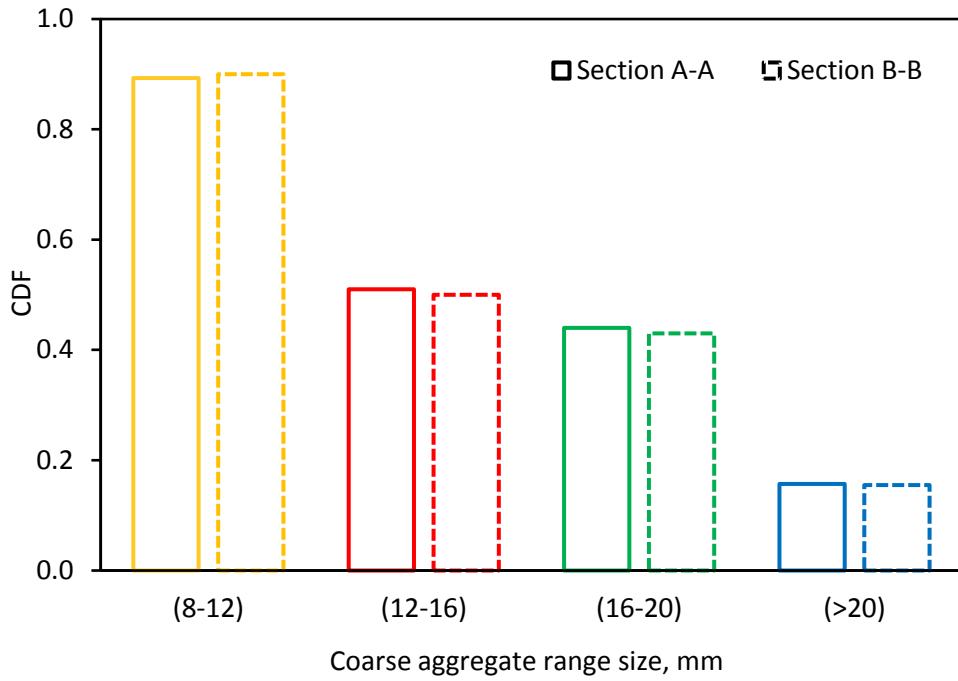
Figure 7.13: Coarse aggregate distributions along the diametrical cross-sections

7.8   Remarks on simulation time

In the above numerical strategy, the SCC incompressibility has been imposed exactly through the pressure Poisson equation (7.8). This is found to be very time-consuming. An alternative strategy that is very popular in many applications was therefore also tried. In this strategy the incompressibility condition is imposed approximately through the so-called weakly or quasi-compressible SPH (Monaghan, 1994). It leads to the replacement of the real incompressible fluid by an artificial quasi-compressible fluid having a small, user-defined, fluctuation in the density. However, it requires a much smaller time step in order to keep the density fluctuation down to 1% (Lee et al., 2008). The weakly incompressible SPH strategy was implemented on one SCC mix (Mix50) in order to check whether or not it leads to a significant reduction in the simulation time in comparison with the method used above. The simulations (in 10-bar J-ring test), for both weakly-compressible SPH (WCSPH) and incompressible SPH (ISPH), were simultaneously run on STONE PC-1210 workstation (3.60 GHz, Intel(R) Core(TM) i7-4790 CPU). It was found that the time taken to simulate the flow for 10 s in WCSPH approximation was actually longer

than that in ISPH, 98 h against 65 h. This is no doubt a result of the fact that the time step in implicit WCSPH scheme had to be very small to avoid numerical instability (Lee et al., 2008).

7.9   Concluding remarks

Smooth particle hydrodynamics (SPH), with its adaptability, simplicity and Lagrangian nature, is more attractive approach to deal with the heterogeneous flow. In the field of SCC, it has high potential for greater acceptance and wider applications such as, mix proportioning, predicting the rheological parameters, modelling the flow and monitoring the movement of large aggregates and/or short steel fibres in the cone slump flow and L-box tests. In this chapter, the goal was to extend the SPH approach to simulating the flow of SCC through gaps in reinforcing bars using the J-ring test. In this test the capabilities of SPH methodology were validated by comparing the experimental and simulations results of different SCC mixes. The comparison showed that the simulations were in very good agreement with experimental results for all six mixes. The free surface profiles around the J-ring bars, the spread at 500 mm diameter and the final flow pattern are all captured accurately by SPH.

In this simulation, the SCC passing ability was judged in terms of the height difference between the concrete inside and outside the steel bars of the J-ring. The results showed that all the six simulated mixes did flow through the gaps in the J-ring without blockage, as indeed they did in the laboratory tests. In term of segregation resistance aassessment, SPH allows tagging of the large aggregate particles in order to track their locations during the flow and after it has stopped. This allows the distribution of large aggregates in the mixes to be examined in order to ensure that they have not segregated from the mortar. The SPH simulation methodology can indeed replace the time-consuming laboratory J-ring test, thereby saving time, effort and materials.

Regarding the numerical solution strategies used in SPH, it is revealed that there is no advantage to be gained in terms of simulation time by approximating the truly incompressible SCC by a weakly incompressible SCC at least on the computational platform used in this study.

Chapter 8

Conclusions and recommendations for further study

8.1   Conclusions

From the main achievements of the research work embodied in this thesis, the following conclusions can be drawn:

❖ Self-compacting concrete (SCC) has undergone extensive investigations that have led to confidence in its fresh and hardened properties. Nevertheless, its mix proportioning methods have not kept pace with their production techniques. An easy-to-use rational method for designing an SCC mix based on the desired target plastic viscosity and compressive strength of the mix was developed in the present study. The systematic steps taken to develop this rational method were described in Chapter 4. It is based on the micromechanical procedure that has recently been developed to determine the SCC mix plastic viscosity. It should not be forgotten that the developed micromechanical procedure has enriched this research work far beyond the scope of its original intended use for the determination of SCC mix plastic viscosity; it forms the backbone of this rational mix design method. The simplicity and usefulness of this mix proportioning method are enhanced by the provision of design charts as a guide for mix proportioning. The characteristic cube strength of mixes varied between 30 and 80 MPa at 28 days age, and the target plastic viscosity between 3 and 15 Pa s: the upper bound of all mix grades was 15 Pa s, whereas the lower bound varied between 3 – 8 Pa s in mix grade range 30 – 80 MPa.

❖ The experimental work attesting the validity of the proposed mix design procedure was performed via a series of SCC mixes in both fresh and hardened states (Chapter 5). The test mixes were found to meet the necessary self-compacting and the compressive strength criteria, thus fully validating the proposed mix proportioning method. Therefore, this method reduces considerably the extent of laboratory work, the testing time and the materials used. Enhancing the sustainability of the designed SCC mixes, the coarser fraction of limestone filler was successfully used to replace an equivalent volume of river sand fine aggregate. Such a replacement is environmentally friendly and economic.

❖ Although SCC has left his early stage of laboratory studies and has now become an industrial product, the differences in its composition from VC sill raise concerns about its fracture behaviour. The concern is primarily because a lower coarse aggregate

content in an SCC mix relative to a VC mix of the same grade is likely to reduce its energy absorption capacity and thus its ductility. In this study, the role of several composition parameters of SCC mixes (coarse aggregate (CA) volume, paste to solids ratio (p/s) and water to binder ratio (w/cm)) in their fracture behaviour was investigated (Chapter 6). The results showed that the specific fracture energy (G_F) increases with an increase in the CA volume fraction, irrespective of the SCC mix grade, although the increase is less pronounced in higher strength than in low strength SCC mixes. Within the same nominal strength grade, an increase in the p/s results in a marginal increase in the strength itself, but a noticeable decrease in G_F. Besides that, an increase in the w/cm ratio reduces G_F. The decrease becomes more pronounced with decreasing CA volume fraction.

❖ The critical crack opening (w_c) of the test notched beams is dominated by the CA volume in the mix and the mix grade. The larger the CA volume (or the smaller the p/s) the larger is the critical crack opening (w_c). However, the higher the mix grade the lower is the w_c. As in w_c, the same tendency was found in the characteristic length (l_{ch}), which is also dominated by the CA volume fraction and strength grade. Also investigated in this study is the relationship between the direct tensile strength (determined by the inverse analysis using the non-linear hinge model) and splitting strength (f_{ct}/f_{st}) of SCC mixes of different p/s ratio and mix grade. It is found that f_{ct}/f_{st} is dominated by the p/s in the mix and the mix grade: it increases with both an increase in p/s and mix grade.

❖ An incompressible mesh-less smooth particle hydrodynamics (SPH) methodology has been implemented to simulate the flow of SCC through gaps in reinforcing bars using the J-ring test. A suitable Bingham-type constitutive model has been coupled with the Lagrangian momentum and continuity equations to simulate the flow. The capabilities of SPH methodology were validated by comparing the experimental and simulations results of different SCC mixes (Chapter 7). The comparison showed that the simulations were in very good agreement with experimental results for all the test mixes. The free surface profiles around the J-ring bars, the spread at 500 mm diameter and the final flow pattern are all captured accurately by SPH.

❖ The results also showed that all the simulated mixes did flow through the gaps in the J-ring without blockage, as indeed they did in the laboratory tests. In terms of segregation assessment, SPH allows tagging of the large aggregate particles in order to track their locations during the flow and after it has stopped. This allows the distribution of large aggregates in the mixes to be examined in order to ensure that they have not segregated from the mortar. The SPH simulation methodology can indeed replace the time-consuming laboratory J-ring test, thereby saving time, effort and materials.

❖ With respect to the numerical solution strategies used in SPH, it was revealed that there is no advantage to be gained in terms of simulation time by approximating the truly incompressible SCC by a weakly incompressible SCC at least on the computational platform used in this study.

8.2   Recommendations for further study

The development of SCC has revolutionised construction processes by offering superior economic and technical advantages over VC. Being one of the future environmentally-friendly materials for buildings and different construction applications, further research in SCC is worthwhile, and the following areas are recommended for future study:

❖ It would be interesting to construct design charts for proportioning SCC mixes whose plastic viscosity is below the lower limit of 3 Pa s and above the upper limit of 15 Pa s. The former could be achieved by adding a high level of cement replacement materials (e.g. ggbs) and/or high dosage of super-plasticisers. The latter, however, could be attained by adding a viscosity modifying agent (VMA).

❖ All the design charts of the proposed mix design procedure, reported in Chapter 4, were developed for proportioning SCC mixes without fibres, and with the characteristic cube strength between 30 and 80 MPa. The procedure can, of course, be generalised, and the design charts be enriched if steel fibres are used and the range of characteristic cube strengths is extended.

❖ It would be advisable to investigate the role of compositional parameters (p/s, CA volume and w/cm) of SCC mixes, with or without steel fibres, in their fracture behaviour using lightweight aggregate instead of normal aggregate. This could give a clearer picture of the fracture behaviour of the lightweight concrete in terms of specific fracture energy, the critical crack opening and the mix ductility.

❖ To exploit the full potential of SPH approach, the flow of SCC mixes and monitoring of their coarse aggregate is worthwhile to be simulated into practical size formworks with the presence of different sizes and densities of reinforcement. To gain this advantage, it is, however, necessary to accelerate the SPH simulation process, as time taken to simulate the flow will be longer than that in the standard tests.

References

Abdalla, H.M. and Karihaloo, B.L. (2003). Determination of size-independent specific fracture energy of concrete from three-point bend and wedge splitting tests. Magazine of Concrete Research, 55(2), pp. 133–141.

Abdalla, H.M. and Karihaloo, B.L. (2004). A method for constructing the bilinear tension softening diagram of concrete corresponding to its true fracture energy. Magazine of Concrete Research, 56(10), pp. 597–604.

Abo Dhaheer, M.S., Al-Rubaye, M.M., Alyhya, W.S., Karihaloo, B.L. and Kulasegaram, S. (2016a). Proportioning of self-compacting concrete mixes based on target plastic viscosity and compressive strength: experimental validation. Journal of Sustainable Cement-Based Materials, 5(4), pp. 217–232.

Abo Dhaheer, M.S., Al-Rubaye, M.M., Alyhya, W.S., Karihaloo, B.L. and Kulasegaram, S. (2016b). Proportioning of self–compacting concrete mixes based on target plastic viscosity and compressive strength: mix design procedure. Journal of Sustainable Cement-Based Materials, 5(4), pp. 199–216.

ACI Committee 211. (1991). Standard practice for selecting proportions for normal, heavy weight and mass concrete. Manual of Concrete Practice (reapproved), pp. 1–38.

Akçaoğlu, T., Tokyay, M. and Çelik, T. (2004). Effect of coarse aggregate size and matrix quality on ITZ and failure behavior of concrete under uniaxial compression. Cement and Concrete Composites, 26, pp. 633–638.

Akcay, B., Agar-Ozbek, A.S., Bayramov, F., Atahan, H.N., Sengul, C. and Tasdemir, M.A. (2012). Interpretation of aggregate volume fraction effects on fracture behavior of concrete. Construction and Building Materials, 28(1), pp. 437–443.

Al-Rubaye, M.M. 2016. Self-compacting concrete: design, properties and simulation of the flow characteristics in the L-box. PhD thesis, School of Engineering, Cardiff University, UK.

Alyhya, W.S. 2016. Self-compacting concrete: mix proportioning, properties and its flow simulation in the V-funnel. PhD thesis, School of Engineering, Cardiff University, UK.

Amini, Y., Emdad, H. and Farid, M. (2011). A new model to solve fluidhypo-elastic solid interaction using the smoothed particle hydrodynamics (SPH) method. European Journal of Mechanics, B/Fluids 30(2), pp. 184–194.

Assaad, J., Khayat, K., Mesbah, H. (2003). Assessment of the thixotropy of flowable and self-consolidating concrete. ACI Materials Journal, 100(2), pp. 99–107.

ASTM C1621/C1621M. 2008. Standard test method for passing ability of self-consolidating concrete by J-ring.

Baaijens, F.P.T. (2001). A fictitious domain/mortar element method for fluid-structure interaction. International journal of numerical methods in fluids, 35, pp. 743–761.

Badry, F., Kulasegaram, S. and Karihaloo, B.L. (2016). Estimation of the yield stress and distribution of large aggregates from slump flow test of self-compacting concrete mixes using smooth particle hydrodynamics simulation. Journal of Sustainable Cement-Based Materials, 5(3), pp. 117–134.

Badry, F.F. (2015). Experimental and numerical studies in self-compacting concrete. PhD thesis, School of Engineering, Cardiff Unversity, UK.

Banfill, P., Beaupr, D., Chapdelaine, F., de Larrard, F., Domone, P., Nachbaur, L. (2000). Comparison of concrete rheometers: International tests at LCPC. Ferraris, C. F. and Brower, L. E. ed. National Institute of Standards and Technology, Nantes, France.

Banfill, P.F. (2006). Rheology of fresh cement and concrete. Rheology Reviews, pp. 61–130.

BASF. (2014). MasterGlenium ACE 499: High range water reducing admixture for concrete.

Bažant, Z.P. (1984). Size effect in blunt fracture: concrete, rock, metal. ASCE Journal of Engineering Mechanics, 110, pp. 518-535.

Bažant, Z.P. (1996). Analysis of work-of-fracture method for measuring fracture energy of concrete. Journal of Engineering Mechanics 122, pp. 138–144.

Bažant, Z.P. and Kazemi, M.T. (1991). Size dependence of concrete fracture energy determined by RILEM work-of-fracture method. International Journal of Fracture, 51(2), pp. 121–138.

Bažant, Z.P. and Planas, J. (1997). Fracture and size effect in concrete and other quasi-brittle materials. UK: CRC Press.

Becker, M., Teschner, M. (2007). Weakly compressible SPH for free surface flows. San Diego, Eurographics/ ACM SIGGRAPH Symposium on Computer Animation, pp. 1-8.

Beygi, M., Kazemi, M.T., Amiri, J. V., Nikbin, I.M., Rabbanifar, S. and Rahmani, E. (2014a). Evaluation of the effect of maximum aggregate size on fracture behavior of self compacting concrete. Construction and Building Materials, 55, pp. 202–211.

Beygi, M., Kazemi, M.T., Nikbin, I.M. and Amiri, V.J. (2013a). The effect of water to cement ratio on fracture parameters and brittleness of self-compacting concrete. Materials and Design, 50, pp. 267–276.

Beygi, M., Kazemi, M.T., Nikbin, I.M. and Amiri, V.J. (2014b). The effect of aging on the fracture characteristics and ductility of self-compacting concrete. Materials and Design, 55, pp. 937–948.

Beygi, M., Kazemi, M.T., Nikbin, I.M., Amiri, V.J., Rabbanifar, S. and Rahmani, E. (2014c). The influence of coarse aggregate size and volume on the fracture behavior and brittleness of self-compacting concrete. Cement and Concrete Research, 66, pp. 75–90.

Beygi, M.H., Berenjian, J., Lotfi Omran, O., Sadeghi Nik, A. and Nikbin, I.M. (2013b). An experimental survey on combined effects of fibers and nanosilica on the mechanical, rheological, and durability properties of self-compacting concrete. Materials and Design, 50, pp. 1019–1029.

Bonet, J., Kulasegaram, S., (2000). Correction and stabilization of smooth particle hydrodynamic methods with application in metal forming simulations. International Journal of Numerical Methods in Engineering, 47(6), pp. 1189-1214.

Bonet, J., Lok, T. S. L., (1999). Variational and momentum aspects of smooth particle hydrodynamics formulations. Computer Method in Applied Mechanics and Engineering, 180(1-2), pp. 97-115.

Bosiljkov, V.B. (2003). SCC mixes with poorly graded aggregate and high volume of limestone filler. Cement and Concrete Research, 33(9), pp. 1279–1286.

Boukendakdji, O., Kadri, E. and Kenai, S. (2012). Effects of granulated blast furnace slag and super-plasticizer type on the fresh properties and compressive strength of self-compacting concrete. Cement and Concrete Composites, 34(4), pp. 583–590.

Brouwers, H. J. H., Radix, H. J. (2005). Self-Compacting Concrete: Theoretical and experimental study. Cement and Concrete Research, 35 (11), pp. 2116–2136.

BS 1881. (1983). Part 121. Method for determination of static modulus of elasticity in compression. British Standards publication.

BS EN 12350-10. (2010). Testing fresh concrete, Part 10: Self-compacting concrete - L-box test. British Standards publication.

BS EN 12350-8. (2010). Testing fresh concrete, Part 8: Self-compacting concrete - Slump flow test. British Standards publication.

BS EN 12350-9. (2010). Testing fresh concrete, Part 9: Self-compacting concrete - V-funnel test. British Standards publication.

BS EN 12350-12. (2010). Testing fresh concrete, Part 9: Self-compacting concrete - J- ring test. British Standards publication.

BS EN 12390. (2009). Part 3. Testing hardened concrete: Compressive strength of test specimens. British Standards publication.

BS EN 12390. (2009). Part 6. Testing hardened concrete: Tensile splitting strength of test specimens. British Standards publication.

BS EN 197. (2011). Part 1. Cement: Composition, specifications and conformity criteria for common cements. British Standards publication.

BS EN 206-9. (2010). Additional Rules for Self-compacting concrete (SCC). British Standards publication.

Bui, V.K., Akkaya, Y. and Shah, S.P. (2002). Rheological model for self-consolidating concrete. ACI Materials Journal, 99(6), pp. 549–559.

Carpinteri, A. and Brighenti, R. (2010). Fracture behaviour of plain and fiber-reinforced concrete with different water content under mixed mode loading. Materials and Design, 31(4), pp. 2032–2042.

Carpinteri, A. and Chiaia, B. (1996). Size effects on concrete fracture energy: dimensional transition from order to disorder. Materials and Structures, 29(5), pp. 259–266.

Chidiac, S.E. and Mahmoodzadeh, F. (2009). Plastic viscosity of fresh concrete- A critical review of predictions methods. Cement and Concrete Composites, 31(8), pp. 535–544.

Choi, Y.W., Kim, Y.J., Shin, H.C. and Moon, H.U. (2006). An experimental research on the fluidity and mechanical properties of high-strength lightweight self-compacting concrete. Cement and Concrete Research, 36(9), pp. 1595–1602.

Chorin, A.J. (1968). Numerical solution of the Navier-Stokes equations. Mathematics of Computation, 22(104), pp. 745–762.

Cifuentes, H. and Karihaloo, B.L. (2013). Determination of size-independent specific fracture energy of normal and high strength self-compacting concrete from wedge splitting tests. Construction and Building Materials, 48(2), pp. 548–553.

Collepardi, M., Collepardi, S. and Troli, R. (2007). Properties of SCC and flowing concrete. In: Kraus, R. N., Naik, T. R. and Pouya, P. ed. Proceeding International Conference: Sustainable Construction Materials and Technologies. Coventry, UK: Special papers proceedings, UW Milwaukee CBU, pp. 25–31.

Corinaldesi, V. and Moriconi, G. (2004). Durable fiber reinforced self-compacting concrete. Cement and Concrete Research, 34(2), pp. 249–254.

Craeye, B., Itterbeeck, P.V., Desnerck, P., Boel, V. and De Schutter, G. (2014). Modulus of elasticity and tensile strength of self-compacting concrete: survey of experimental data and structural design codes. Cement and Concrete Composites, 54, pp. 53–61.

Cummins, S.J. and Rudman, M. (1999). An SPH projection method. Journal of Computational Physics, 152(2), pp. 584–607.

de Kruif, C.G., Van Iersel, E.M.F., Vrij, A. and Russel W. B. (1985). Hard sphere colloidal dispersions: Viscosity as a function of shear rate and volume fraction. The Journal of Chemical Physics, 83(9), pp. 4717–4725.

Deeb, R. (2013). Flow of self-compacting concrete. PhD thesis, School of Engineering, Cardiff University, UK.

Deeb, R. and Karihaloo, B.L. (2013). Mix proportioning of self-compacting normal and high-strength concretes. Magazine of Concrete Research, 65(9), pp. 546–556.

Deeb, R., Karihaloo, B.L., Kulasegaram, S. (2014a). Reorientation of short steel fibres during the flow of self-compacting concrete mix and determination of the fibre orientation factor. Cement and Concrete Research, 56, pp. 112–120.

Deeb, R., Kulasegaram, S. and Karihaloo, B.L. (2014b). 3D modelling of the flow of self-compacting concrete with or without steel fibres. Part I: slump flow test. Computational Particle Mechanics, 1, pp. 373–389.

Deeb, R., Kulasegaram, S. and Karihaloo, B.L. (2014c). 3D modelling of the flow of self-compacting concrete with or without steel fibres. Part II: L-box test and the assessment of fibre reorientation during the flow. Computational Particle Mechanics, 1, pp. 391–408.

Desnerck, P., Boel, V., Craeye, B. and Itterbeeck, P.V. (2014). Mechanical properties of self-compacting concrete. In: K. H. Khayat and G. De Schutter ed. Self-Compacting Concrete - State-of-the-Art Report of RILEM. RILEM Publications SARL, pp. 15–72.

Dinakar, P., Babu, K.G. and Santhanam, M. (2008). Durability properties of high volume fly ash self compacting concretes. Cement and Concrete Composites, 30(10), pp. 880–886.

Dinakar, P., Reddy, M.K. and Sharma, M. (2013a). Behaviour of self-compacting concrete using Portland pozzolana cement with different levels of fly ash. Materials and Design, 46, pp. 609–616.

Dinakar, P., Sethy, K.P. and Sahoo, U.C. (2013b). Design of self-compacting concrete with ground granulated blast furnace slag. Materials and Design, 43, pp. 161–169.

Domone, P.L. (2000). Mix design. In: Å. Skarendahl and Ö Petersson ed. Self-Compacting Concrete - State-of-the-Art Report of RILEM TC 174-SCC. RILEM Publications SARL, France, pp. 49–65.

Domone, P.L. (2003). Fresh concrete: Advanced concrete technology. In: J. Newman, B. S. Choo ed. Elsevier Ltd.

Domone, P.L. (2006). Self-compacting concrete: An analysis of 11 years of case studies. Cement and Concrete Composites, 28(2), pp. 197–208.

Domone, P.L. (2007). A review of the hardened mechanical properties of self-compacting concrete. Cement and Concrete Composites, 29(1), pp. 1–12.

Domone, P.L. and Illston, J. (2010). Construction materials: Their nature and behaviour. New York, USA: Spon Press.

Dransfield, J. (2003). Admixtures for concrete, mortar, and grout. In: Newman, J. and Choo, B. S. ed. In Advanced Concrete Technology. USA: Elsevier Ltd.

Duan, K., Hu, X. and Wittmann, F.H. (2003). Boundary effect on concrete fracture and non-constant fracture energy distribution. Engineering Fracture Mechanics, 70(16), pp. 2257–2268.

Duan, K., Hu, X. and Wittmann, F.H. (2007). Size effect on specific fracture energy of concrete. Engineering Fracture Mechanics, 74, pp. 87–96.

Edamatsu, Y., Nishida, N. and Ouchi, M. (1998). A rational mix design method for self-compacting concrete interaction between coarse aggregate and mortar particles. In: Å. Skarendahl and Ö. Pettersson ed. 1st International RILEM Symposium on Self-Compacting

Concrete. RILEM Publications SARL, Stockholm, Sweden, pp. 309–320.EFNARC Guidelines. 2002. Specification and Guidelines for Self-Compacting Concrete. p. 32.

EFNARC Guidelines. (2005). The European Guidelines for Self-Compacting Concrete; Specification, Production and Use. p. 63.

Felekoğlu, B., Türkel, S. and Baradan, B. (2007). Effect of water/cement ratio on the fresh and hardened properties of self-compacting concrete. Building and Environment, 42(4), pp. 1795–1802.

Ferrara, L., Park, Y.D. and Shah, S.P. (2007). A method for mix-design of fiber-reinforced self-compacting concrete. Cement and Concrete Research, 37(6), pp. 957–971.

Ferraris, C.F. (1999). Measurement of the rheological properties of high performance concrete: State of the art report. Journal of Research of the National Institute of Standards and Technology, 104(5), pp. 461–478.

Feys, D., Heirman, G., Schutter, G. De, Verhoeven, R., Vandewalle, L. and Gemert, D. Van (2007). Comparison of two concrete rheometers for shear thickening behaviour of SCC. In: G. De Schutter and V. Boel ed. 5th International RILEM Symposium on Self-Compacting Concrete. RILEM Publications SARL, Ghent, Belgium, pp. 365–370.

Figueiras, H., Nunes, S., Coutinho, J.S. and Andrade, C. (2014). Linking fresh and durability properties of paste to SCC mortar. Cement and Concrete Composites, 45, pp. 209–226.

Ghanbari, A. and Karihaloo, B.L. (2009). Prediction of the plastic viscosity of self-compacting steel fibre reinforced concrete. Cement and Concrete Research, 39(12), pp. 1209–1216.

Ghanbari, A. (2011). Self-compacting high and ultra-high performance concretes. PhD thesis, School of Engineering, Cardiff University, UK.

Ghazi, F.K. and AlJadiri, R.S. (2010). New method for proportioning self-consolidating concrete based on compressive strength requirements. ACI Material Journal, 107(5), pp. 490-497.

Gingold, R.A. and Monaghan, J.J. (1977). Smoothed particle hydrodynamics: theory and application to non-spherical stars. Monthly Notices of the Royal Astronomical Society, 181(3), pp. 375–389.

Goodier, C.I. (2003). Development of self-compacting concrete. In: Proceedings of the ICE-Structures and Buildings, 156(4), pp. 405–414.

Gram, A. and Silfwerbrand, J. (2011). Numerical simulation of fresh SCC flow: applications. Materials and Structures, 44(4), pp. 805–813.

Guinea, G.V., Planas, J. and Elices, M. (1992). Measurement of the fracture energy using three-point bend tests: Part 1-Influence of experimental procedures. Materials and Structures, 25(4), pp. 212–218.

Guinea, G.V., Planas, J. and Elices, M. (1994). A general bilinear fit for the softening curve of concrete. Materials and Structures, 27(2), pp. 99–105.

Heirman, G., Hendrickx, R., Vandewalle, L., Van Gemert, D., Feys, D., De Schutter, G. (2009). Integration approach of the Couette inverse problem of powder type self-compacting concrete in a wide-gap concentric cylinder rheometer: Part II. Influence of mineral additions and chemical admixtures on the shear thickening flow behaviour. Cement and Concrete Research 39(3), pp. 171–181.

Heirman, G., Vandewalle, L., Van Gemert, D., Wallevik, Ó. (2008). Integration approach of the Couette inverse problem of powder type self-compacting concrete in a wide-gap concentric cylinder rheometer. Journal of Non-Newtonian Fluid Mechanics,150(2/3), pp. 93-103.

Hillerborg, A., Modeer, M. and Petersson, P.E. (1976). Analysis of crack formation and crack growth in concrete by means of fracture mechanics and finite elements. Cement and Concrete Research, 6, pp. 773–782.

Hoffmann, C. and Leemann, A. (2005). Properties of self-compacting and conventional concrete – differences and similarities. Magazine of Concrete Research, 57(6), pp. 315–319.

Hu, X. and Duan, K. (2004). Influence of fracture process zone height on fracture energy of concrete. Cement and Concrete Research, 34(8), pp. 1321–1330.

Hu, X. and Wittmann, F. (1992). Fracture energy and fracture process zone. Materials and Structures, 25(6), pp. 319–326.

Hu, X. and Wittmann, F. (2000). Size effect on toughness induced by crack close to free surface. Engineering Fracture Mechanics, 65, pp. 209–221.

Karihaloo, B.L. (1995). Fracture Mechanics and Structural Concrete. UK: Addison Wesley Longman.

Karihaloo, B.L. and Ghanbari, A. (2012). Mix proportioning of self-compacting high and ultra high performance concretes with and without steel fibres. Magazine of Concrete Research, 64(12), pp. 1089–1100.

Karihaloo, B.L., Abdalla, H.M. and Imjai, T. (2003). A simple method for determining the true specific fracture energy of concrete. Magazine of Concrete Research, 55(5), pp. 471–481.

Karihaloo, B.L., Murthy, A.R. and Iyer, N.R. (2013). Determination of size-independent specific fracture energy of concrete mixes by the tri-linear model. Cement and Concrete Research, 49, pp. 82–88.

Kasemchaisiri, R. and Tangtermsirikul, S. (2008). Deformability prediction model for self-compacting concrete. Magazine of Concrete Research, 60(2), pp. 93–108.

Khaloo, A., Raisi, E.M., Hosseini, P. and Tahsiri, H. (2014). Mechanical performance of self-compacting concrete reinforced with steel fibers. Construction and Building Materials, 51, pp. 179–186.

Khayat, K.H. (1998). Use of viscosity modifying admixture to reduce top-bar effect of anchored bars cast with fluid concrete. ACI Materials Journal 95(2), pp. 158–167.

Khayat, K.H. (1999). Workability, testing, and performance of self-consolidating concrete. ACI Materials Journal, 96(3), pp. 346–353.

Khayat, K.H. (2000). Optimization and performance of air-entrained, self-consolidating concrete. ACI Structural Journal, 97(5), pp. 526–535.

Khayat, K.H., Ghezal, A. and Hadriche, M.S. (1999). Factorial design model for proportioning self-consolidating concrete. Materials and Structures, 32(9), pp. 679–686.

Khayat, K.H., Hu, C. and Monty, H. (1999). Stability of self-consolidating concrete, advantages, and potential applications. In: Å. Skarendahl and Ö. Pettersson ed. 1st International RILEM Symposium on Self-Compacting Concrete. RILEM Publications SARL, Stockholm, Sweden, pp. 143–152.

Kim, J.H., Noemi, N. and Shah, S.P. (2012). Effect of powder materials on the rheology and formwork pressure of self-consolidating concrete. Cement and Concrete Composites, 34(6), pp. 746–753.

Koehler, E.P. and Fowler, D.W. (2007). Aggregates in self- consolidating concrete. International Center for Aggregates Research (ICAR), The University of Texas, Austin, USA.

Koshizuka, S., Nobe, A. and Oka, Y. (1998). Numerical analysis of breaking waves using the moving particle semi-implicit method. International Journal for Numerical Methods in Fluids, 26(7), pp. 751–769.

Krieger, I.M. and Dougherty, T.J. (1959). A mechanism for Non-Newtonian flow in suspensions of rigid spheres. Transactions of The Society of Rheology, 3, pp. 137–152.

Kulasegaram, S. and Karihaloo, B.L. (2013). Fibre-reinforced, self-compacting concrete flow modelled by smooth particle hydrodynamics. Proceedings of the Institution of Civil Engineers (ICE) - Engineering and Computational Mechanics 166(1), pp. 22–31.

Kulasegaram, S., Karihaloo, B.L. and Ghanbari, A. (2011). Modelling the flow of self-compacting concrete. International Journal for Numerical and Analytical Methods in Geomechanics, 35(6), pp. 713–723.

Lachemi, M., Hossain, K., Lambros, V., Bouzoubaa, N., (2003). Development of cost effective self-consolidating concrete incorporating fly ash, slag cement, or viscosity-modifying admixtures. ACI Materials Journal, 100(5), pp. 419-425.

Lee, E.S., Moulinec, C., Xu, R., Violeau, D., Laurence, D. and Stansby, P. (2008). Comparisons of weakly compressible and truly incompressible algorithms for the SPH mesh free particle method. Journal of Computational Physics, 227(18), pp. 8417–8436.

Li, L.G. and Kwan, a. K.H. (2011). Mortar design based on water film thickness. Construction and Building Materials, 25(5), pp. 2381–2390.

Li, L.G. and Kwan, A.K.H. (2013). Concrete mix design based on water film thickness and paste film thickness. Cement and Concrete Composites, 39, pp. 33–42.

Liu, G.R. and Liu, M.B. (2003). Smoothed Particle Hydrodynamics - A meshfree particle method. Singapore: World Scientific Publishing Co. Pte. Ltd,.

Lucy, L.B. (1977). A numerical approach to the testing of the fission hypothesis. The astronomical journal, 82(12), pp. 1013–1024.

Mindess, S. (1984). The effect of specimen size on the fracture energy of concrete. Cement and concrete Research, 14(3), pp. 431–436.

Monaghan, J.J. (1994). Simulating free surface flows with SPH. Journal of Computational Physics, 110(2), pp. 399–406.

Muralidhara, S., Prasad, B.K.R., Eskandari, H. and Karihaloo, B.L. (2010). Fracture process zone size and true fracture energy of concrete using acoustic emission. Construction and Building Materials, 24(4), pp. 479–486.

Muralidhara, S., Prasad, B.K.R., Karihaloo, B.L. and Singh, R.K. (2011). Size-independent fracture energy in plain concrete beams using tri-linear model. Construction and Building Materials, 25(7), pp. 3051–3058.

Murthy, A.R., Karihaloo, B.L., Iyer, N.R. and Prasad, B.K.R. (2013). Determination of size-independent specific fracture energy of concrete mixes by two methods. Cement and Concrete Research, 50, pp. 19–25.

Murthy, A.R., Karihaloo, B.L., Iyer, N.R. and Prasad, R.B.K. (2013a). Bilinear tension softening diagrams of concrete mixes corresponding to their size-independent specific fracture energy. Construction and Building Materials, 47, pp. 1160–1166.

Nallathambi, P., Karihaloo, B.L. and Heaton, B.S. (1984). Effect of specimen and crack sizes, water/cement ratio and coarse aggregate texture upon fracture toughness of concrete. Magazine of Concrete Research, 36(129), pp. 227–236.

Nallathambi, P., Karihaloo, B.L. and Heaton, B.S. (1985). Various size effects in fracture of concrete. Cement and Concrete Research, 15(1), pp. 117–126.

Nanthagopalan, P. and Santhanam, M. (2009). Experimental investigations on the influence of paste composition and content on the properties of self-compacting concrete. Construction and Building Materials, 23(11), pp. 3443–3449.

Nehdi, M. and Rahman, M. A. (2004). Estimating rheological properties of cement pastes using various rheological models for different test geometry, gap and surface friction. Cement and Concrete Research, 34(11), pp. 1993–2007.

Nepomuceno, M., Oliveira, L. and Lopes, S.M.R. (2012). Methodology for mix design of the mortar phase of self-compacting concrete using different mineral additions in binary blends of powders. Construction and Building Materials, 26(1), pp. 317–326.

Neville, A.M. (1995). Properties of concrete. 4th ed. UK: Longman Scientific Group Ltd.

Nikbin, I.M., Beygi, M.H.A., Kazemi, M.T., Amiri, J. V., Rabbanifar, S., Rahmani, E. (2014a). A comprehensive investigation into the effect of water to cement ratio and powder content on mechanical properties of self-compacting concrete. Construction and Building Materials, 57, pp. 69–80.

Nikbin, I.M., Beygi, M.H.A., Kazemi, M.T., Amiri, J. V., Rahmani, E., Rabbanifar, S. (2014c). A comprehensive investigation into the effect of aging and coarse aggregate size and volume on mechanical properties of self-compacting concrete. Construction and Building Materials 59, pp. 199–210.

Nikbin, I.M., Beygi, M.H.A., Kazemi, M.T., Amiri, J. V., Rahmani, E., Rabbanifar, S. (2014b). Effect of coarse aggregate volume on fracture behavior of self-compacting concrete. Construction and Building Materials 52, pp. 137–145.

Noguchi, T., Oh, S.G. and Tomosawa, F. (1999). Rheological approach to passing ability between reinforcing bars of self-compacting concrete. In: Å. Skarendahl and Ö. Petersson ed. 1st International RILEM Symposium on Self-Compacting Concrete. RILEM Publications SARL, Stockholm, Sweden, pp. 59–70.

Nunes, S. l., Oliveira, P.M., Coutinho, J.S. and Figueiras, J. (2009). Interaction diagrams to assess SCC mortars for different cement types. Construction and Building Materials, 23(3), pp. 1401–1412.

Nuruddin, M.F., Chang, K.Y. and Azmee, N.M. (2014). Workability and compressive strength of ductile self-compacting concrete (DSCC) with various cement replacement materials. Construction and Building Materials, 55, pp. 153–157.

Obla, K. H., Thomas, M., Shashiprakash, S. G., Perebatova, O., (2003). Properties of concrete containing ultra-fine fly ash. ACI Materials Journal, 100(5), pp. 426-433.

Okamura, H. and Ouchi, M. (2003). Self-compacting concrete. Journal of advanced concrete technology, 1(1), pp. 5–15.

Okamura, H., Ozawa, K. and Ouchi, M. (2000). Self-compacting concrete. Structural Concrete, 1(1), pp. 3–17.

Okumara, H. and Ouchi, M. (1999). Self-compacting concrete development, present use and future. In: Å. Skarendahl and Ö. Petersson ed. 1st International RILEM Symposium on Self-Compacting Concrete. RILEM Publications SARL, Stockholm, Sweden, pp. 3–14.

Olesen, J.F. (2001). Fictitious crack propagation in fiber-reinforced concrete beams. Journal of Engineering Mechanics, 127, pp. 272–280.

Omran, A. and Khayat, K. (2016). Models to predict form pressure exerted by SCC – results of six field campaigns. In: 8th International RILEM Symposium on Self-Compacting Concrete, Washington DC, USA, pp. 599–612.

Ouchi, M., Hinino, M., Ozawa, K. and Okamura, H. (1998). A rational mix design method for mortar in self-compacting concrete. In: Proceedings of the Sixth East Asia-Pacific Conference on Structural Engineering and Construction. Taipei, Taiwan, pp. 1307–1312.

Pamnani, N.J. (2014). Effect of curing techniques on mechanical properties of self-compacting concrete. PhD thesis, Sardar Patel University, India.

Panesar, D.K. and Shindman, B. (2011). Elastic properties of self-consolidating concrete. Construction and Building Materials, 25(8), pp. 3334–3344.

Parra, C., Valcuende, M. and Gómez, F. (2011). Splitting tensile strength and modulus of elasticity of self-compacting concrete. Construction and Building Materials, 25(1), pp. 201–207.

Patzák, B. and Bittnar, Z. (2009). Modeling of fresh concrete flow. Computers and Structures, 87, pp. 962–969.

Persson, B. (2001). A comparison between mechanical propel-ties of self-compacting concrete and the corresponding properties of normal concrete. Cement and Concrete Research, 31(2), pp. 193–198.

Petersson, Ö. and Billberg, P. (1999). Investigation on blocking of self- compacting concrete with different maximum aggregate size and use of viscosity agent instead filler. In: Å. Skarendahl and Ö. Petersson ed. 1st International RILEM Symposium on Self-Compacting Concrete. RILEM Publications SARL, Stockholm, Sweden, pp. 333–344.

Petit, J.Y., Wirquin, E., Vanhove, Y. and Khayat, K. (2007). Yield stress and viscosity equations for mortars and self-consolidating concrete. Cement and Concrete Research, 37(5), pp. 655–670.

Pettitt, A.R. (2014). Constructing a map of the Galaxy from numerical simulations and synthetic observations. PhD thesis, University of Exeter, UK.

Planas, J., Elices, M. and Guinea, G.V. (1992). Measurement of the fracture energy using three-point bend tests: Part 2-Influence of bulk energy dissipation. Materials and Structures, 25(5), pp. 305–312.

Prokopski, G. and Langier, B. (2000). Effect of water/cement ratio and silica fume addition on the fracture toughness and morphology of fractured surfaces of gravel concretes. Cement and Concrete Research, 30(9), pp. 1427–1433.

Rabehi, M., Mezghiche, B. and Guettala, S. (2013). Correlation between initial absorption of the cover concrete, the compressive strength and carbonation depth. Construction and Building Materials, 45, pp. 123–129.

RILEM State-of-the-Art Reports. (2014). Simulation of fresh concrete flow. Roussel, N. and Gram, A. ed. Netherlands: Springer Ltd.

RILEM State-of-the-Art Reports TC174. (2000). Self-compacting concrete. Å. Skarendahl and Ö. Petersson ed. France: RILEM Publications SARL.

RILEM TCS50. (1985). Determination of the fracture energy of mortar and concrete by means of three-point bend tests on notched beams. Materials and Structures, 18(106), pp. 285–290.

Roussel, N. (2006b). A theoretical frame to study stability of fresh concrete. Materials and Structures, 39(1), pp. 81–91.

Roussel, N. (2006a). Correlation between yield stress and slump: comparison between numerical simulations and concrete rheometers results. Materials and Structures, 39(4), pp. 501–509.

Roussel, N. (2007). Rheology of fresh concrete: from measurements to predictions of casting processes. Materials and Structures, 40(10), pp. 1001–1012.

Roussel, N., Geiker, M.R., Dufour, F., Thrane, L.N. and Szabo, P. (2007). Computational modeling of concrete flow: General overview. Cement and Concrete Research, 37(9), pp. 1298–1307.

Roussel, N., Lemaitre, A., Flatt, R.J. and Coussot, P. (2010). Steady state flow of cement suspensions: A micromechanical state of the art. Cement and Concrete Research, 40(1), pp. 77–84.

Roussel, N., Nguyen, T.L.H., Yazoghli, O. and Coussot, P. (2009). Passing ability of fresh concrete: A probabilistic approach. Cement and Concrete Research, 39(3), pp. 227–232.

Rozière, E., Granger, S., Turcry, P. and Loukili, A. (2007). Influence of paste volume on shrinkage cracking and fracture properties of self-compacting concrete. Cement and Concrete Composites, 29(8), pp. 626–636.

Saak, A.W., Jennings, H.M. and Shah, S.P. (2001). New methodology for designing self-compacting concrete. ACI Materials Journal 98(6), pp. 429–439.

Shao, S. and Lo, E.Y.M. (2003). Incompressible SPH method for simulating Newtonian and non-Newtonian flows with a free surface. Advances in Water Resources, 26(7), pp. 787–800.

Shi, C., Wu, Z., Lv, K. and Wu, L. (2015). A review on mixture design methods for self-compacting concrete. Construction and Building Materials, 84, pp. 387–398.

Siddique, R., Khan, M. I. (2011). Supplementary Cementing Materials: Silica Fume. Engineering Materials, Ch:2. Springer-Verlag Berlin Heidelberg, , pp. 67-119.

Sonebi, M., Svermova, L. and Bartos, P.J.M. (2004). Factorial design of cement slurries containing limestone powder for self-consolidating slurry-infiltrated fiber concrete. ACI Material Journal, pp. 136–145.

Su, N. and Miao, B. (2003). A new method for the mix design of medium strength flowing concrete with low cement content. Cement and Concrete Composites, 25(2), pp. 215–222.

Su, N., Hsu, K.-C. and Chai, H.-W. (2001). A simple mix design method for self-compacting concrete. Cement and Concrete Research, 31(12), pp. 1799–1807.

Sun, Z., Voigt, T. and Shah, S.P. (2006). Rheometric and ultrasonic investigations of viscoelastic properties of fresh Portland cement pastes. Cement and Concrete Research, 36(2), pp. 278–287.

Švec, O., Skoček, J., Stang, H., Geiker, M.R. and Roussel, N. (2012). Free surface flow of a suspension of rigid particles in a non-Newtonian fluid: A lattice Boltzmann approach. Journal of Non-Newtonian Fluid Mechanics, 179-180, pp. 32–42.

Tada, H., Paris, P.C. and Irwin, G.R. (1985). The stress analysis of cracks handbook. 3rd ed. ASME Press.

Takada K. and Tangtermsirikul S. (2000). Self-compacting concrete: Testing of fresh concrete IV. In: Å. Skarendahl and Ö Petersson ed. RILEM State-of-the-Art Report TC174. RILEM Publications SARL, France, pp. 25–39.

Takeda, H., Miyama, S.M. and Sekiya, M. (1994). Numerical simulation of viscous flow by smoothed particle hydrodynamics. Progress of Theoretical Physics 92(5), pp. 939–960.

Tattersall, G.H. (2003). Workability and Quality Control of Concrete. UK: E and FN Spon Ltd.

Topçu, I.B. and Uğurlu, A. (2003). Effect of the use of mineral filler on the properties of concrete. Cement and Concrete Research, 33(7), pp. 1071–1075.

Tregger, N., Ferrara, L. and Shah, S. P. (2007). Empirical relationships between viscosity and flow time measurements from mini-slump tests for cement pastes formulated from SCC, Proceedings of the 5th International RILEM Symposium-SCC, pp. 273-278, Ghent, Belgium.

Tregger, N., Gregori, A., Ferrara, L. and Shah, S. (2012). Correlating dynamic segregation of self-consolidating concrete to the slump-flow test. Construction and Building Materials, 28(1), pp. 499–505.

Ulfkjær, J.P., Krenk, S. and Brincker, R. (1995). Analytical model for fictitious crack Propagation in concrete beams. Journal of Engineering Mechanics, 121(1), pp. 7–15.

Vasilić, K. (2015). A numerical model for self-compacting concrete flow through reinforced sections: A porous medium analogy. PhD thesis, Faculty of Civil Engineering, The Technical University of Dresden, Berlin, Germany.

Vasilić, K., Roussel, N., Meng, B., Kühne, H. C. (2010). Computational modeling of SCC flow through reinforced sections in self-compacting concrete (SCC). Canada, In: Proceedings of the 2010 International RILEM Symposium on Self-Compacting Concrete. Design, production and placement of self-consolidating concrete eds. Khayat, K. H. and Feys, D., pp. 187-195.

Vesenjak, M. and Ren, Z. (2007). Application aspects of the meshless SPH method. Journal of the Serbian Society for Computational Mechanics, 1(1), pp. 74–86.

Vilanova, A., Gomez, J.F. and Landsberger, G.A. (2011). Evaluation of the mechanical properties of self-compacting concrete using current estimating models estimating the modulus of elasticity, tensile strength, and modulus of rupture of self-compacting concrete. Construction and Building Materials, 25, pp. 3417–26.

Wallevick, J.E. (2003). Rheology of particle suspension: fresh concrete, mortar and cement paste with various types of lignosulfates. Department of Structural Engineeringh, The Norwegian University of Science and Technology (NTNU), Norway.

Wallevik, O.H. and Wallevik, J.E. (2011). Rheology as a tool in concrete science: The use of rheographs and workability boxes. Cement and Concrete Research, 41(12), pp. 1279–1288.

Wu, J. and Shu, C. (2010). An improved immersed boundary-lattice Boltzmann method for simulating three-dimensional incompressible flows. Journal of Computational Physics, 229, pp. 5022–5042.

Wu, Q. and An, X. (2014). Development of a mix design method for SCC based on the rheological characteristics of paste. Construction and Building Materials, 53, pp. 642–651.

Yahia, A., Tanimura, M. and Shimoyama, Y. (2005). Rheological properties of highly flowable mortar containing limestone filler-effect of powder content and w/c ratio. Cement and Concrete Research, 35(3), pp. 532–539.

Ye, G., Liu, X., De Schutter, G., Poppe, a. M. and Taerwe, L. (2007). Influence of limestone powder used as filler in SCC on hydration and microstructure of cement pastes. Cement and Concrete Composites, 29(2), pp. 94–102.

Zerbino, R., Barragán, B., Garcia, T., Agulló, L. and Gettu, R. (2009). Workability tests and rheological parameters in self-compacting concrete. Materials and Structures, 42(7), pp. 947–960.

Zhu, W. and Gibbs, J.C. (2005). Use of different limestone and chalk powders in self-compacting concrete. Cement and Concrete Research, 35, pp. 1457–1462.

Appendix A

A MATLAB program for designing SCC mixes

```
************************************************************************
%                         CARDIFF UNIVERSITY
%
%                       SCHOOL OF ENGINEERING
%
% A MATLAB program for designing Self-Compacting Concrete mixes
% according to their target plastic viscosity and compressive strength
%***********************************************************************
%    List of variables
%    Name            Description
%    -----           ------------
%    WCM             Water to cementitious materials (binder) ratio
%    PV              Paste viscosity (values based on w/cm and sp dosage)
%    TMV             Target mix viscosity
%    Z, U and X      Random names are used to solve equations
%    t1, t2 and t3   Factors are chosen arbitrarily such that t1*t2*t3=1
%    H               Unity factor (H=t1*t2*t3)
%    CM              Cementitious materials
%    WTR             Water content (kg)
%    CEM             Cement content (kg)
%    GG              Cement replacement materials (kg) e.g. GGBS
%    SP              Superplasticizer dosage (kg)
%    VPS             Volume of paste per cubic meter
%    FLP             Volume fraction of filler (materials < 125µm)
%    FS              Volume fraction of fine aggregate
%    FG              Volume fraction of coarse aggregate
%    WLP             Mass of filler
%    WS              Mass of fine aggregate
%    WG              Mass of coarse aggregate
%    VLP             Volume of filler per cubic meter
%    VS              Volume of fine aggregate per cubic meter
%    VG              Volume of coarse aggregate per cubic meter
%    TV              Total volume of the mix (m³)
%    PSRATIO         Paste to solid ratio
%    FFLP            A factor larger than unity that predicts the
%                    increase in the plastic viscosity induced by
%                    addition of filler
%    FFS             A factor larger than unity that predicts the
%                    increase in the plastic viscosity induced by
%                    addition of fine aggregate
%    FFG             A factor larger than unity that predicts the
```

```
%                  increase in the plastic viscosity induced by
%                  addition of coarse aggregate
%   AMV            Actual mix plastic viscosity calculated by
%                  micromechanical procedure
%   ERR            Percentage difference between target (TMV) and
%                  actual mix viscosity (AMV)
%   PWDR           Powder content (Any materials <=125µm i.e.
%                  (cementitious materials and filler))
%   WTPR           Water to powder ratio
%   FIRSTLINE      Normalized cementitious materials content
%   SECONDLINE     Normalized cementitious materials and filler
%                  contents
%   THIRDLINE       Normalized cementitious materials, filler and fine
%                   aggregate contents
%   FOURTHLINE      Normalized cementitious materials, filler, fine
%                    aggregate and coarse aggregate contents


%*****************************************************************
%*****************************************************************


clear
clc
% Input the water to binder (cementitious materials) ratio from Eq. 4.1
WCM=0.63;
% Input the paste viscosity from Table 4.1
PV=0.11;
%*****************************************************************

s=0;
p=0;
for TMV=3.0:0.05:15
Z=0.524^ (-1.9)*0.63^ (-1.9)*0.74^ (-1.9);
U= (Z*TMV/PV) ^ (-1/1.9);
X=U^ (1/3) ;
t1=0.424/X ;
t2=0.53/X ;
t3=0.64/X ;
a=linspace (0, t1, 200) ;
b=linspace (0, t2, 200) ;
c=linspace (0, t3, 200) ;
```

```
for i= 1:200
for j= 1:200
for k= 1:200


H=a (i)*b (j)*c (k);
if (H<=1.0001 && H>=0.9999)
s=s+1;
% input the cementitious materials contents limits
for CM=230:5:350
WTR(s) =CM*WCM;
CEM(s) =0.75*CM;
GG(s) =0.25*CM;
SP(s) =0.0065*CM;
VPS(s) =CEM(s)/2950+GG(s)/2400+WTR(s)/1000+SP(s)/1070+0.02;


FLP(s) =0.524-a(i)*X;
FS(s) =0.63-b(j)*X;
FG(s) =0.74-c(k)*X;
WLP(s) =2400*FLP(s)*VPS(s)/ (1-FLP(s));
WS(s) =2650*FS(s)*(VPS(s) + (WLP(s)/2400))/ (1-FS(s));
WG(s) =2800*FG(s)*(VPS(s) + (WLP(s)/2400) + (WS(s)/2650))/ (1-FG(s));


VLP(s) =WLP(s)/2400;
VS(s) =WS(s)/2650;
VG(s) =WG(s)/2800;
TV(s) =VLP(s) +VS(s) +VG(s) +VPS(s)-0.02;


WCEMnew(s) =CEM(s)*0.98/TV(s);
WGGnew(s) =GG(s)*0.98/TV(s);
WWTRnew(s) =WTR(s)*0.98/TV(s);
WSPnew(s) =SP(s)*0.98/TV(s);
WLPnew(s) =WLP(s)*0.98/TV(s);
WSnew(s) =WS(s)*0.98/TV(s);
WGnew(s) =WG(s)*0.98/TV(s);
VCEMnew(s) =WCEMnew(s)/2950;
VGGnew(s) =WGGnew(s)/2400;
VWTRnew(s) =WWTRnew(s)/1000;
VSPnew(s) =WSPnew(s)/1070;
VLPnew(s) =WLPnew(s)/2400;
VSnew(s) =WSnew(s)/2650;
```

```
VGnew(s) =WGnew(s)/2800;
TVnew(s) =VCEMnew(s) +VGGnew(s) +VWTRnew(s) +VSPnew(s)
+VLPnew(s)+VSnew(s) +VGnew(s) +0.02;


 WCMnew(s) =WCEMnew(s) +WGGnew(s);
 STAG(s) =VSnew(s)/ (VSnew(s) +VGnew(s))*100;
 GTAG(s) =VGnew(s)/ (VSnew(s) +VGnew(s))*100;
 VPSnew(s) =VCEMnew(s) +VGGnew(s) +VWTRnew(s) +VSPnew(s) +0.02;
 PSRATIO(s) = (VPSnew(s) +VLPnew(s))/ (VSnew(s) +VGnew(s));
 FLPnew(s) =VLPnew(s)/ (VLPnew(s) +VPSnew(s));
 FSnew(s) =VSnew(s)/ (VSnew(s) +VLPnew(s) +VPSnew(s));
 FGnew(s) =VGnew(s)/ (VGnew(s) +VSnew(s) +VLPnew(s) +VPSnew(s));
 FFLP(s) = (1-FLPnew(s)/0.524) ^ (-1.9);
 FFS(s) = (1-FSnew(s)/0.63) ^ (-1.9);
 FFG(s) = (1-FGnew(s)/0.74) ^ (-1.9);
 AMV(s) =PV*FFLP(s)*FFS(s)*FFG(s);
 ERR(s) = (AMV(s)-TMV)/TMV*100;
 PWDR=WCMnew(s) +WLPnew(s);
 WTPR(s) =VWTRnew(s)/ (VLPnew(s) +VCEMnew(s) +VGGnew(s))*100;



            A=TVnew(s);
            B=WLPnew(s);
            C=WSnew(s);
            D=WGnew(s);
            E=STAG(s);
            F=GTAG(s);
            G=PSRATIO(s);
            I=AMV(s);
            L=ERR(s);
            J=WTPR(s);
            K=WCMnew(s);
            R=WSPnew(s);
            WCMRnew(s) =WWTRnew(s)/WCMnew(s);
            EEE=WCMRnew(s);
            WWTR=WWTRnew(s);


 % Check the typical range of SCC mix compositions according to EFNARC
         if (PWDR>=380 && PWDR<=600)
         if (WWTR>=150 && WWTR<=210)
```

```
        if (D>=750 && D<=1000)
        if (J>=85 && J<=130)
        if (E>=48 && E<=55)
% Check the percentage difference between (TMV) and (AMV)
        if (L>=-5 && L<=5)


                p=p+1;
                AA (p) =K/I;
                BB (p) = (K+B)/I;
                CC (p) = (K+B+C)/I;
                DD (p) = (K+B+C+D)/I;
                EE (p) =C/I;
                FF (p) =D/I;
                RR (p) =B/I;
                TT (p) =(C+D)/I;
                StoTOTAL (p) =E/I;
                SANDplusLP (p) = (B+C)/I;
                CMplusSAND (p) = (K+C)/I;


                AAA=AA (p);
                BBB=BB (p);
                CCC=CC (p);
                DDD=DD (p);


                GGG=EE (p);
                FFF=FF (p);
                RRR=RR (p);
                TTT=TT (p);
                STST=StoTOTAL (p);
                SLP=SANDplusLP (p);
                CMSAND=CMplusSAND (p);


                TotalVolume (p) =A;
                Limestone (p) =B;
                Sand (p) =C;
                CoarseAGG (p) =D;
                StoTAG (p) =E;
                GtoTAG (p) =F;
                PtoSRATIO (p) =G;
                Viscosity (p) =I;
```

```
                        ERROR (p) =L;
                        SUPER (p) =R;
                        WATER (p) =WWTR;
                        CMmaterials (p) =K;
                        WtoPRatio (p) =J;
                        FIRSTLINE (p) =AAA;
                        SECONDLINE (p) =BBB;
                        THIRDLINE (p) =CCC;
                        FOURTHLINE (p) =DDD;


                        WATERtoCM (p) =EEE;
                        SANDtoVISCOSITY (p) =GGG;
                        GRAVELtoVISCOSITY (p) =FFF;
                        LIMEtoVISCOSITY (p) =RRR;
                        CAplusFA (p) =TTT;
                        StoTOTALAGG (p) =STST;
                        LPplusLSAND (p) =SLP;
                        CMandSAND (p) =CMSAND;


                end
                end
                end
                end
                end
                end
        end
        end
        end
        end
        end
        end
 ****************************************************************
% print the results in order to plot the graphs
GtoTAG = round (GtoTAG);
Limestone = round (Limestone);
Sand = round (Sand);
CoarseAGG = round (CoarseAGG);
StoTAG = round (StoTAG);
TotalVolume = round (TotalVolume*1000)/1000;
ERR = round (ERR);
```

```matlab
PSRATIO = round (PSRATIO);


%*****************************************************************


% desired parameters to be printed in the output sheet

myMatrix =
[CMmaterials;Limestone;Sand;CoarseAGG;WATER;SUPER;TotalVolume;WATERtoCM;W
toPRatio;StoTAG;GtoTAG;PtoSRATIO;ERROR;Viscosity;FIRSTLINE;SECONDLINE;THI
RDLINE;FOURTHLINE]';


HeaderNames='CMmaterials,Limestone,Sand,CoarseAGG,WATER,SUPER,TotalVolume
,WATERtoCM,WtoPRatio,StoTAG,GtoTAG,PtoSRATIO,ERROR,Viscosity,FIRSTLINE,SE
CONDLINE,THIRDLINE,FOURTHLINE';
%*****************************************************************


% preferable output sheet name printed here (change the underline text)

fileName ='choose output file name here.csv';
outid = fopen (fileName, 'w+');
fprintf (outid, '%s', HeaderNames);
fclose (outid);

dlmwrite(fileName,myMatrix,'roffset',1,'-append', 'precision', 4);
% you may need to increase precision to allow all digits to be saved
disp (strcat ('Generated report ''', fileName,''''))
%*****************************************************************
```

Appendix B

Typical SCC mixes of different strength grades, plastic viscosities and paste/solid ratios designed using the proposed mix design method

Table B.1: Mix constituents (kg/m³) for mixes grade 30

Mix No.	cm Cem.	cm ggbs	Water	SP	w/cm	LP	FA	CA	Paste Vol.	Solid Vol.	p/s ratio	η_{mix} Pa s
1	260.5	86.8	218.8	2.4	0.63	235	696	769	0.46	0.54	0.86	3.60
2	254.2	84.7	213.5	2.4	0.63	217	704	804	0.45	0.55	0.81	3.88
3	253.5	84.5	212.9	2.4	0.63	250	700	773	0.46	0.54	0.85	4.06
4	252.2	84.1	211.8	2.4	0.63	173	809	752	0.43	0.57	0.74	4.28
5	243.3	81.1	204.4	2.3	0.63	187	741	841	0.42	0.58	0.72	4.59
6	241.3	80.4	202.6	2.3	0.63	188	744	844	0.42	0.58	0.72	4.75
7	240.4	80.1	201.9	2.2	0.63	202	767	807	0.42	0.58	0.73	4.99
8	240.0	80.0	201.6	2.2	0.63	271	728	769	0.45	0.55	0.82	5.23
9	233.7	77.9	196.3	2.2	0.63	177	766	862	0.40	0.60	0.68	5.45
10	231.4	77.1	194.3	2.2	0.63	189	764	859	0.40	0.60	0.68	5.70
11	230.9	77.0	193.9	2.2	0.63	233	784	788	0.42	0.58	0.73	6.12
12	226.8	75.6	190.5	2.1	0.63	239	758	823	0.42	0.58	0.72	6.41
13	223.4	74.5	187.6	2.1	0.63	224	753	859	0.41	0.59	0.69	6.65
14	227.3	75.8	190.9	2.1	0.63	211	840	768	0.41	0.59	0.69	6.83
15	226.1	75.4	190.0	2.1	0.63	198	859	767	0.40	0.60	0.67	7.09
16	220.2	73.4	185.0	2.1	0.63	206	801	841	0.40	0.60	0.66	7.32
17	218.9	73.0	183.9	2.0	0.63	156	826	878	0.37	0.63	0.60	7.57
18	218.6	72.9	183.6	2.0	0.63	163	840	856	0.38	0.62	0.61	7.80
19	220.4	73.5	185.1	2.1	0.63	189	872	785	0.39	0.61	0.64	8.00
20	215.8	71.9	181.3	2.0	0.63	171	840	857	0.38	0.62	0.60	8.25
21	214.1	71.4	179.8	2.0	0.63	246	796	821	0.41	0.59	0.68	8.49
22	213.8	71.3	179.6	2.0	0.63	257	803	803	0.41	0.59	0.70	8.73
23	212.6	70.9	178.5	2.0	0.63	172	846	862	0.37	0.63	0.59	8.87
24	211.1	70.4	177.3	2.0	0.63	155	837	896	0.36	0.64	0.57	8.99

25	208.8	69.6	175.4	1.9	0.63	242	783	859	0.40	0.60	0.66	9.19
26	210.8	70.3	177.0	2.0	0.63	186	858	839	0.38	0.62	0.60	9.42
27	212.3	70.8	178.3	2.0	0.63	206	877	790	0.39	0.61	0.63	9.50
28	207.4	69.1	174.2	1.9	0.63	157	847	897	0.36	0.64	0.56	9.85
29	205.4	68.5	172.6	1.9	0.63	247	804	844	0.40	0.60	0.65	10.15
30	204.8	68.3	172.0	1.9	0.63	171	840	899	0.36	0.64	0.57	10.27
31	203.2	67.7	170.7	1.9	0.63	161	827	929	0.36	0.64	0.55	10.38
32	200.6	66.9	168.5	1.9	0.63	233	788	895	0.38	0.62	0.62	10.77
33	208.4	69.5	175.1	1.9	0.63	153	918	823	0.36	0.64	0.56	11.08
34	204.1	68.0	171.4	1.9	0.63	186	880	841	0.37	0.63	0.58	11.22
35	204.3	68.1	171.6	1.9	0.63	145	891	876	0.35	0.65	0.54	11.50
36	198.3	66.1	166.6	1.9	0.63	167	837	929	0.35	0.65	0.54	11.72
37	198.7	66.2	166.9	1.9	0.63	234	830	857	0.38	0.62	0.61	11.93
38	196.5	65.5	165.1	1.8	0.63	167	840	933	0.35	0.65	0.54	12.26
39	194.4	64.8	163.3	1.8	0.63	227	800	913	0.37	0.63	0.59	12.39
40	200.0	66.7	168.0	1.9	0.63	243	883	786	0.39	0.61	0.63	12.73
41	193.4	64.5	162.4	1.8	0.63	218	816	910	0.37	0.63	0.58	12.89
42	192.5	64.2	161.6	1.8	0.63	218	818	912	0.37	0.63	0.58	13.19
43	193.7	64.6	162.8	1.8	0.63	155	849	948	0.34	0.66	0.52	13.30
44	194.9	65.0	163.8	1.8	0.63	204	873	861	0.36	0.64	0.57	13.61
45	198.8	66.3	167.0	1.9	0.63	176	927	822	0.36	0.64	0.55	13.85
46	193.7	64.6	162.7	1.8	0.63	160	876	913	0.34	0.66	0.52	14.07
47	196.7	65.6	165.2	1.8	0.63	175	919	840	0.35	0.65	0.55	14.33
48	192.4	64.1	161.6	1.8	0.63	160	878	916	0.34	0.66	0.52	14.59
49	191.6	63.9	160.9	1.8	0.63	178	878	898	0.35	0.65	0.53	14.78
50	190.6	63.5	160.1	1.8	0.63	145	869	950	0.33	0.67	0.50	15.08

Table B.2: Mix constituents (kg/m³) for mixes grade 40

| Mix No. | cm | | Water | SP | w/cm | LP | FA | CA | Paste Vol. | Solid Vol. | p/s ratio | η_{mix} Pa s |
	Cem.	ggbs										
1	289.4	96.5	220	2.7	0.57	164	706	798	0.45	0.55	0.81	4.78
2	287.0	95.7	218.1	2.7	0.57	165	710	802	0.45	0.55	0.80	4.94
3	287.3	95.8	218.3	2.7	0.57	136	765	776	0.43	0.57	0.77	5.12
4	284.0	94.7	215.8	2.7	0.57	208	720	751	0.46	0.54	0.85	5.36
5	282.1	94.0	214.4	2.6	0.57	138	773	784	0.43	0.57	0.75	5.52
6	279.5	93.2	212.4	2.6	0.57	210	727	758	0.46	0.54	0.84	5.72
7	275.1	91.7	209.1	2.6	0.57	150	748	821	0.42	0.58	0.74	5.92
8	275.1	91.7	209.1	2.6	0.57	213	739	757	0.45	0.55	0.82	6.14
9	271.2	90.4	206.1	2.5	0.57	194	732	799	0.44	0.56	0.78	6.32
10	273.0	91.0	207.5	2.5	0.57	123	828	774	0.41	0.59	0.70	6.62
11	269.4	89.8	204.7	2.5	0.57	110	810	821	0.40	0.60	0.67	6.80
12	267.5	89.2	203.3	2.5	0.57	159	805	777	0.42	0.58	0.72	7.02
13	265.3	88.4	201.6	2.5	0.57	237	742	760	0.45	0.55	0.81	7.21
14	261.5	87.2	198.8	2.4	0.57	231	722	801	0.44	0.56	0.79	7.40
15	259.7	86.6	197.4	2.4	0.57	93	790	897	0.38	0.62	0.62	7.63
16	257.0	85.7	195.3	2.4	0.57	217	735	820	0.43	0.57	0.75	7.88
17	259.2	86.4	197	2.4	0.57	242	762	754	0.44	0.56	0.80	8.05
18	260.6	86.9	198	2.4	0.57	131	857	778	0.40	0.60	0.66	8.27
19	256.7	85.6	195	2.4	0.57	107	830	848	0.38	0.62	0.62	8.46
20	253.0	84.3	192.3	2.4	0.57	250	732	798	0.44	0.56	0.78	8.66
21	253.4	84.5	192.6	2.4	0.57	100	830	868	0.38	0.62	0.60	8.92
22	251.3	83.8	191	2.3	0.57	220	791	776	0.42	0.58	0.74	9.13
23	247.6	82.5	188.2	2.3	0.57	108	798	912	0.37	0.63	0.59	9.31
24	251.6	83.9	191.2	2.3	0.57	104	852	845	0.38	0.62	0.60	9.49

25	254.9	85.0	193.7	2.4	0.57	107	899	781	0.38	0.62	0.62	9.74
26	243.9	81.3	185.4	2.3	0.57	187	789	843	0.40	0.60	0.67	9.95
27	247.1	82.4	187.8	2.3	0.57	156	851	803	0.39	0.61	0.65	10.16
28	242.1	80.7	184	2.3	0.57	152	808	870	0.38	0.62	0.62	10.34
29	239.0	79.7	181.7	2.2	0.57	166	784	890	0.39	0.61	0.63	10.57
30	247.5	82.5	188.1	2.3	0.57	107	886	821	0.37	0.63	0.59	10.76
31	239.7	79.9	182.2	2.2	0.57	110	822	912	0.36	0.64	0.57	11.01
32	240.4	80.1	182.7	2.2	0.57	235	808	780	0.42	0.58	0.71	11.24
33	236.5	78.8	179.7	2.2	0.57	130	810	912	0.37	0.63	0.58	11.39
34	240.5	80.2	182.7	2.2	0.57	140	867	827	0.38	0.62	0.61	11.64
35	236.2	78.7	179.5	2.2	0.57	111	827	918	0.36	0.64	0.56	11.83
36	235.1	78.4	178.7	2.2	0.57	148	834	871	0.37	0.63	0.60	12.09
37	232.7	77.6	176.8	2.2	0.57	131	816	919	0.36	0.64	0.57	12.27
38	237.7	79.2	180.6	2.2	0.57	125	876	844	0.37	0.63	0.58	12.47
39	234.4	78.1	178.2	2.2	0.57	135	854	867	0.37	0.63	0.58	12.69
40	236.2	78.7	179.5	2.2	0.57	183	882	777	0.39	0.61	0.64	12.88
41	231.6	77.2	176	2.2	0.57	133	844	890	0.36	0.64	0.57	13.12
42	239.8	79.9	182.3	2.2	0.57	84	914	845	0.35	0.65	0.55	13.34
43	233.7	77.9	177.6	2.2	0.57	183	886	780	0.39	0.61	0.63	13.55
44	230.9	77.0	175.4	2.2	0.57	118	860	894	0.36	0.64	0.55	13.76
45	238.1	79.4	180.9	2.2	0.57	84	917	847	0.35	0.65	0.54	13.88
46	226.4	75.5	172	2.1	0.57	140	833	911	0.36	0.64	0.56	14.16
47	234.0	78.0	177.8	2.2	0.57	123	912	822	0.36	0.64	0.57	14.31
48	231.8	77.3	176.2	2.2	0.57	107	892	869	0.35	0.65	0.55	14.52
49	224.4	74.8	170.5	2.1	0.57	141	836	915	0.36	0.64	0.56	14.75
50	225.3	75.1	171.2	2.1	0.57	177	856	848	0.37	0.63	0.60	15.02

Table B.3: Mix constituents (kg/m³) for mixes grade 50

Mix No.	cm		Water	SP	w/cm	LP	FA	CA	Paste Vol.	Solid Vol.	p/s ratio	η_{mix} Pa s
	Cem.	ggbs										
1	311.2	103.7	219.9	2.9	0.53	139	709	795	0.45	0.55	0.81	5.45
2	309.6	103.2	218.8	2.9	0.53	125	727	798	0.44	0.56	0.79	5.60
3	306.8	102.3	216.8	2.9	0.53	126	730	803	0.44	0.56	0.78	5.81
4	304.6	101.5	215.3	2.8	0.53	153	712	798	0.45	0.55	0.81	5.94
5	302.5	100.8	213.8	2.8	0.53	100	805	768	0.42	0.58	0.73	6.57
6	300.8	100.3	212.6	2.8	0.53	130	794	750	0.43	0.57	0.76	6.67
7	300.4	100.1	212.3	2.8	0.53	100	808	771	0.42	0.58	0.72	6.77
8	294.7	98.2	208.2	2.8	0.53	179	737	774	0.45	0.55	0.80	6.96
9	292.6	97.5	206.8	2.7	0.53	113	839	750	0.42	0.58	0.71	7.77
10	285.8	95.3	201.9	2.7	0.53	186	737	795	0.44	0.56	0.78	7.82
11	291.8	97.3	206.2	2.7	0.53	113	840	751	0.41	0.59	0.71	7.86
12	285.1	95.0	201.5	2.7	0.53	143	784	798	0.42	0.58	0.72	8.08
13	281.8	93.9	199.1	2.6	0.53	106	765	872	0.40	0.60	0.67	8.17
14	285.8	95.3	201.9	2.7	0.53	97	831	801	0.40	0.60	0.67	8.42
15	278.7	92.9	197.0	2.6	0.53	107	769	877	0.40	0.60	0.66	8.56
16	277.1	92.4	195.8	2.6	0.53	107	771	880	0.39	0.61	0.65	8.77
17	278.3	92.8	196.7	2.6	0.53	200	766	773	0.43	0.57	0.77	8.96
18	276.8	92.3	195.6	2.6	0.53	105	805	848	0.39	0.61	0.65	9.20
19	273.3	91.1	193.1	2.6	0.53	111	782	877	0.39	0.61	0.64	9.38
20	275.7	91.9	194.8	2.6	0.53	111	828	821	0.39	0.61	0.65	9.65
21	272.9	91.0	192.8	2.5	0.53	106	811	854	0.39	0.61	0.64	9.80
22	270.8	90.3	191.3	2.5	0.53	181	786	800	0.42	0.58	0.72	10.00
23	267.4	89.1	189.0	2.5	0.53	155	778	850	0.40	0.60	0.68	10.25
24	268.1	89.4	189.4	2.5	0.53	181	790	804	0.41	0.59	0.71	10.44
25	267.5	89.2	189.1	2.5	0.53	120	818	847	0.39	0.61	0.64	10.70

26	264.7	88.2	187.1	2.5	0.53	101	798	901	0.38	0.62	0.61	10.86
27	265.4	88.5	187.5	2.5	0.53	121	821	851	0.39	0.61	0.63	11.11
28	264.8	88.3	187.1	2.5	0.53	218	785	777	0.43	0.57	0.74	11.21
29	263.7	87.9	186.4	2.5	0.53	121	824	853	0.38	0.62	0.62	11.41
30	260.9	87.0	184.4	2.4	0.53	102	803	907	0.37	0.63	0.59	11.59
31	262.1	87.4	185.2	2.4	0.53	122	826	856	0.38	0.62	0.62	11.75
32	264.3	88.1	186.7	2.5	0.53	153	866	770	0.40	0.60	0.66	12.07
33	256.7	85.6	181.3	2.4	0.53	149	795	875	0.39	0.61	0.63	12.25
34	259.2	86.4	183.2	2.4	0.53	130	833	848	0.38	0.62	0.62	12.40
35	257.5	85.8	181.9	2.4	0.53	118	825	877	0.38	0.62	0.60	12.60
36	262.9	87.6	185.8	2.5	0.53	113	886	799	0.38	0.62	0.61	12.81
37	255.7	85.2	180.7	2.4	0.53	118	827	880	0.37	0.63	0.60	13.01
38	258.2	86.1	182.4	2.4	0.53	93	851	876	0.37	0.63	0.58	13.13
39	254.3	84.8	179.7	2.4	0.53	182	815	822	0.40	0.60	0.66	13.23
40	251.2	83.7	177.5	2.3	0.53	140	798	901	0.38	0.62	0.61	13.36
41	252.1	84.0	178.1	2.4	0.53	211	788	824	0.41	0.59	0.69	13.50
42	253.7	84.6	179.2	2.4	0.53	191	829	799	0.40	0.60	0.67	13.69
43	251.8	83.9	177.9	2.4	0.53	114	825	900	0.37	0.63	0.58	13.80
44	249.0	83.0	175.9	2.3	0.53	172	794	874	0.39	0.61	0.63	13.90
45	254.0	84.7	179.5	2.4	0.53	191	854	773	0.40	0.60	0.67	14.07
46	247.7	82.6	175.0	2.3	0.53	172	796	876	0.39	0.61	0.63	14.23
47	248.9	83.0	175.9	2.3	0.53	115	829	905	0.36	0.64	0.57	14.57
48	253.1	84.4	178.9	2.4	0.53	87	870	880	0.36	0.64	0.56	14.84
49	247.9	82.6	175.2	2.3	0.53	175	837	829	0.39	0.61	0.63	15.04
50	251.3	83.8	177.6	2.3	0.53	92	870	880	0.36	0.64	0.56	15.23

Table B.4: Mix constituents (kg/m³) for mixes grade 60

Mix No.	cm		Water	SP	w/cm	LP	FA	CA	Paste Vol.	Solid Vol.	p/s ratio	η_{mix} Pa s
	Cem.	ggbs										
1	346.80	115.60	217.30	3.24	0.47	124	718	762	0.46	0.54	0.84	6.01
2	338.40	112.80	212.00	3.16	0.47	137	715	776	0.45	0.55	0.83	6.57
3	336.08	112.03	210.60	3.14	0.47	137	718	780	0.45	0.55	0.82	6.75
4	334.20	111.40	209.40	3.12	0.47	115	731	798	0.44	0.56	0.78	6.89
5	334.50	111.50	209.60	3.12	0.47	135	728	777	0.45	0.55	0.81	6.91
6	332.40	110.80	208.30	3.10	0.47	109	723	820	0.43	0.57	0.77	6.96
7	332.85	110.95	208.60	3.11	0.47	116	733	800	0.44	0.56	0.78	7.01
8	330.68	110.23	207.20	3.09	0.47	136	733	782	0.44	0.56	0.80	7.24
9	327.60	109.20	205.30	3.06	0.47	145	718	797	0.44	0.56	0.80	7.41
10	325.43	108.48	204.00	3.04	0.47	133	734	801	0.44	0.56	0.78	7.65
11	322.43	107.48	202.00	3.01	0.47	146	725	805	0.44	0.56	0.78	7.90
12	320.78	106.93	201.00	2.99	0.47	147	727	807	0.44	0.56	0.78	8.06
13	320.40	106.80	200.80	2.99	0.47	149	733	799	0.44	0.56	0.78	8.15
14	321.53	107.18	201.50	3.00	0.47	162	760	752	0.44	0.56	0.80	8.32
15	320.33	106.78	200.80	2.99	0.47	162	762	754	0.44	0.56	0.80	8.45
16	316.43	105.48	198.30	2.95	0.47	150	738	805	0.43	0.57	0.77	8.57
17	314.03	104.68	196.80	2.93	0.47	158	722	820	0.43	0.57	0.77	8.71
18	318.83	106.28	199.80	2.98	0.47	110	803	775	0.42	0.58	0.72	8.81
19	311.40	103.80	195.10	2.91	0.47	159	726	823	0.43	0.57	0.76	9.01
20	314.10	104.70	196.80	2.93	0.47	161	778	757	0.44	0.56	0.77	9.23
21	308.55	102.85	193.40	2.88	0.47	162	734	819	0.43	0.57	0.76	9.41
22	312.15	104.05	195.60	2.91	0.47	151	799	752	0.43	0.57	0.75	9.61
23	304.58	101.53	190.90	2.84	0.47	148	739	843	0.42	0.58	0.72	9.84
24	309.08	103.03	193.70	2.89	0.47	132	806	777	0.42	0.58	0.72	9.97

25	303.30	101.10	190.10	2.83	0.47	163	741	827	0.43	0.58	0.74	10.10
26	308.25	102.75	193.20	2.88	0.47	140	818	758	0.42	0.58	0.73	10.25
27	305.18	101.73	191.20	2.85	0.47	148	803	775	0.42	0.58	0.73	10.48
28	298.28	99.43	186.90	2.78	0.47	154	745	849	0.42	0.58	0.71	10.72
29	299.70	99.90	187.80	2.80	0.47	142	777	825	0.41	0.59	0.70	10.86
30	298.95	99.65	187.30	2.79	0.47	176	768	797	0.43	0.57	0.74	11.04
31	296.03	98.68	185.50	2.76	0.47	195	735	820	0.43	0.57	0.75	11.21
32	299.40	99.80	187.60	2.79	0.47	149	811	782	0.41	0.59	0.71	11.37
33	299.03	99.68	187.40	2.79	0.47	100	827	824	0.39	0.61	0.65	11.60
34	294.38	98.13	184.50	2.75	0.47	108	792	866	0.39	0.61	0.64	11.75
35	299.85	99.95	187.90	2.80	0.47	115	854	775	0.40	0.60	0.67	11.92
36	291.30	97.10	182.50	2.72	0.47	102	784	890	0.39	0.61	0.63	12.12
37	297.75	99.25	186.60	2.78	0.47	116	857	778	0.40	0.60	0.66	12.30
38	289.43	96.48	181.40	2.70	0.47	102	787	893	0.38	0.62	0.62	12.48
39	287.63	95.88	180.20	2.69	0.47	161	769	849	0.41	0.59	0.69	12.66
40	295.20	98.40	185.00	2.76	0.47	116	861	781	0.40	0.60	0.66	12.81
41	288.60	96.20	180.90	2.69	0.47	146	810	820	0.40	0.60	0.67	13.07
42	289.95	96.65	181.70	2.71	0.47	141	832	798	0.40	0.60	0.67	13.21
43	287.03	95.68	179.90	2.68	0.47	147	812	822	0.40	0.60	0.67	13.38
44	288.30	96.10	180.60	2.69	0.47	141	835	800	0.40	0.60	0.66	13.56
45	286.88	95.63	179.80	2.68	0.47	94	829	866	0.38	0.62	0.61	13.74
46	287.48	95.83	180.20	2.68	0.47	158	842	776	0.41	0.59	0.68	13.90
47	288.23	96.08	180.60	2.69	0.47	90	851	844	0.38	0.62	0.61	13.99
48	285.60	95.20	179.00	2.67	0.47	163	842	776	0.41	0.59	0.68	14.28
49	280.05	93.35	175.50	2.61	0.47	162	792	847	0.40	0.60	0.66	14.43
50	284.10	94.70	178.00	2.65	0.47	164	844	778	0.40	0.60	0.68	14.62

Table B.5: Mix constituents (kg/m³) for mixes grade 70

Mix No.	cm Cem.	ggbs	Water	SP	w/cm	LP	FA	CA	Paste Vol.	Solid Vol.	p/s ratio	η_{mix} Pa s
1	376.73	125.58	200.90	3.52	0.40	127	698	784	0.46	0.54	0.84	7.06
2	374.03	124.68	199.50	3.49	0.40	151	690	773	0.46	0.54	0.86	7.29
3	372.00	124.00	198.40	3.47	0.40	128	704	791	0.45	0.55	0.82	7.41
4	368.48	122.83	196.50	3.44	0.40	130	718	784	0.45	0.55	0.81	7.77
5	364.13	121.38	194.20	3.40	0.40	131	724	790	0.44	0.56	0.80	8.14
6	367.58	122.53	196.00	3.43	0.40	110	775	750	0.44	0.56	0.78	8.21
7	362.18	120.73	193.20	3.38	0.40	131	726	792	0.44	0.56	0.80	8.31
8	365.48	121.83	194.90	3.41	0.40	110	778	753	0.44	0.56	0.78	8.40
9	362.18	120.73	193.10	3.38	0.40	161	733	750	0.46	0.54	0.84	8.51
10	361.13	120.38	192.60	3.37	0.40	108	761	786	0.43	0.57	0.76	8.61
11	360.98	120.33	192.50	3.37	0.40	130	768	753	0.44	0.56	0.79	8.75
12	358.88	119.63	191.40	3.35	0.40	108	763	789	0.43	0.57	0.76	8.83
13	357.90	119.30	190.90	3.34	0.40	108	765	790	0.43	0.57	0.75	8.93
14	353.70	117.90	188.70	3.30	0.40	130	742	801	0.43	0.57	0.77	9.17
15	353.48	117.83	188.50	3.30	0.40	140	765	765	0.44	0.56	0.78	9.46
16	350.33	116.78	186.90	3.27	0.40	130	746	806	0.43	0.57	0.76	9.53
17	352.05	117.35	187.80	3.29	0.40	140	767	767	0.44	0.56	0.77	9.62
18	348.00	116.00	185.60	3.25	0.40	131	749	809	0.43	0.57	0.75	9.80
19	348.83	116.28	186.10	3.26	0.40	141	771	771	0.43	0.57	0.77	9.98
20	347.78	115.93	185.50	3.25	0.40	141	772	773	0.43	0.57	0.76	10.11
21	339.00	113.00	180.80	3.16	0.40	139	738	837	0.42	0.58	0.73	10.69
22	337.35	112.45	179.90	3.15	0.40	139	739	839	0.42	0.58	0.73	10.90
23	335.63	111.88	179.00	3.13	0.40	140	741	841	0.42	0.58	0.72	11.13
24	334.05	111.35	178.20	3.12	0.40	140	743	844	0.42	0.58	0.72	11.35

25	335.63	111.88	179.00	3.13	0.40	148	771	801	0.42	0.58	0.73	11.53
26	337.80	112.60	180.10	3.15	0.40	124	809	783	0.42	0.58	0.71	11.67
27	332.03	110.68	177.10	3.10	0.40	137	758	838	0.41	0.59	0.71	11.78
28	336.38	112.13	179.40	3.14	0.40	124	811	785	0.41	0.59	0.71	11.88
29	330.53	110.18	176.30	3.09	0.40	137	760	840	0.41	0.59	0.70	11.99
30	336.60	112.20	179.50	3.14	0.40	124	828	766	0.41	0.59	0.71	12.11
31	333.90	111.30	178.10	3.12	0.40	125	814	788	0.41	0.59	0.70	12.27
32	330.08	110.03	176.00	3.08	0.40	149	778	808	0.42	0.58	0.72	12.37
33	334.05	111.35	178.20	3.12	0.40	124	831	769	0.41	0.59	0.70	12.52
34	331.88	110.63	177.00	3.10	0.40	127	820	784	0.41	0.59	0.70	12.66
35	328.50	109.50	175.20	3.07	0.40	93	799	855	0.39	0.61	0.65	12.80
36	331.20	110.40	176.60	3.09	0.40	125	835	773	0.41	0.59	0.69	13.01
37	324.23	108.08	172.90	3.03	0.40	138	778	838	0.41	0.59	0.69	13.16
38	328.05	109.35	175.00	3.06	0.40	128	825	789	0.41	0.59	0.69	13.32
39	322.58	107.53	172.00	3.01	0.40	139	780	840	0.41	0.59	0.68	13.45
40	325.20	108.40	173.50	3.04	0.40	146	814	788	0.41	0.59	0.70	13.63
41	319.43	106.48	170.30	2.98	0.40	122	773	874	0.40	0.60	0.66	13.81
42	323.85	107.95	172.70	3.02	0.40	146	815	789	0.41	0.59	0.70	13.89
43	321.23	107.08	171.30	3.00	0.40	139	798	823	0.40	0.60	0.68	14.00
44	317.78	105.93	169.50	2.97	0.40	123	775	876	0.39	0.61	0.65	14.11
45	322.43	107.48	171.90	3.01	0.40	114	825	820	0.40	0.60	0.65	14.25
46	328.50	109.50	175.20	3.07	0.40	98	878	766	0.40	0.61	0.65	14.34
47	315.98	105.33	168.50	2.95	0.40	123	777	879	0.39	0.61	0.65	14.45
48	317.85	105.95	169.50	2.97	0.40	143	800	825	0.40	0.60	0.68	14.62
49	315.08	105.03	168.00	2.94	0.40	100	789	896	0.38	0.62	0.62	14.84
50	325.35	108.45	173.50	3.04	0.40	98	883	770	0.39	0.61	0.64	15.01

Table B.6: Mix constituents (kg/m³) for mixes grade 80

Mix No.	cm Cem.	ggbs	Water	SP	w/cm	LP	FA	CA	Paste Vol.	Solid Vol.	p/s ratio	η_{mix} Pa s
1	396.83	132.28	185.20	3.70	0.35	116	689	824	0.45	0.55	0.80	8.01
2	398.63	132.88	186.00	3.72	0.35	116	720	786	0.45	0.55	0.81	8.10
3	400.13	133.38	186.70	3.74	0.35	114	749	755	0.45	0.55	0.81	8.20
4	394.43	131.48	184.10	3.68	0.35	117	725	791	0.44	0.56	0.80	8.45
5	389.48	129.83	181.70	3.63	0.35	114	692	842	0.44	0.56	0.78	8.57
6	391.65	130.55	182.80	3.66	0.35	104	734	804	0.44	0.56	0.77	8.69
7	386.55	128.85	180.40	3.61	0.35	115	696	846	0.44	0.56	0.77	8.82
8	384.83	128.28	179.60	3.59	0.35	112	693	857	0.43	0.57	0.76	8.93
9	387.68	129.23	180.90	3.62	0.35	105	739	809	0.43	0.57	0.76	9.06
10	382.43	127.48	178.50	3.57	0.35	112	696	860	0.43	0.57	0.76	9.15
11	388.95	129.65	181.50	3.63	0.35	113	767	767	0.44	0.56	0.78	9.23
12	378.90	126.30	176.80	3.54	0.35	115	687	875	0.43	0.57	0.75	9.39
13	386.25	128.75	180.30	3.61	0.35	114	770	770	0.43	0.57	0.77	9.49
14	376.65	125.55	175.80	3.52	0.35	116	689	878	0.43	0.57	0.74	9.61
15	383.03	127.68	178.70	3.58	0.35	107	771	785	0.43	0.57	0.75	9.78
16	374.55	124.85	174.80	3.50	0.35	114	697	876	0.42	0.58	0.74	9.87
17	373.35	124.45	174.20	3.48	0.35	115	699	878	0.42	0.58	0.73	10.00
18	377.63	125.88	176.20	3.53	0.35	101	757	822	0.42	0.58	0.73	10.13
19	378.08	126.03	176.40	3.53	0.35	108	776	791	0.42	0.58	0.74	10.32
20	374.78	124.93	174.90	3.51	0.35	101	760	825	0.42	0.58	0.72	10.45
21	373.28	124.43	174.20	3.45	0.35	105	760	825	0.42	0.58	0.72	10.61
22	376.35	125.45	175.60	3.48	0.35	114	797	766	0.43	0.57	0.74	10.76
23	369.38	123.13	172.40	3.49	0.35	103	742	857	0.41	0.59	0.71	10.81
24	374.40	124.80	174.70	3.43	0.35	115	799	769	0.42	0.58	0.74	11.00
25	367.20	122.40	171.40	3.42	0.35	98	752	857	0.41	0.59	0.69	11.16

26	366.23	122.08	170.90	3.40	0.35	111	758	838	0.41	0.59	0.71	11.37
27	364.65	121.55	170.20	3.43	0.35	98	755	861	0.41	0.59	0.69	11.49
28	368.03	122.68	171.70	3.38	0.35	113	802	786	0.42	0.58	0.71	11.75
29	361.73	120.58	168.80	3.40	0.35	99	759	864	0.41	0.60	0.68	11.89
30	364.20	121.40	170.00	3.33	0.35	97	796	821	0.41	0.59	0.69	12.11
31	357.30	119.10	166.70	3.39	0.35	95	747	892	0.40	0.60	0.66	12.27
32	363.23	121.08	169.50	3.32	0.35	102	806	806	0.41	0.59	0.69	12.40
33	355.28	118.43	165.80	3.37	0.35	95	749	895	0.40	0.60	0.66	12.57
34	361.20	120.40	168.50	3.34	0.35	103	809	808	0.41	0.59	0.68	12.71
35	357.53	119.18	166.80	3.29	0.35	104	788	838	0.40	0.60	0.68	12.87
36	352.35	117.45	164.40	3.32	0.35	96	753	899	0.39	0.61	0.65	13.02
37	355.58	118.53	165.90	3.35	0.35	104	790	841	0.40	0.60	0.67	13.18
38	359.18	119.73	167.60	3.33	0.35	109	830	784	0.41	0.59	0.69	13.34
39	357.30	119.10	166.70	3.23	0.35	104	823	802	0.40	0.60	0.68	13.49
40	345.98	115.33	161.50	3.27	0.35	101	734	930	0.39	0.61	0.64	13.64
41	350.48	116.83	163.60	3.21	0.35	108	783	858	0.40	0.60	0.66	13.79
42	344.18	114.73	160.60	3.30	0.35	102	736	932	0.39	0.61	0.64	13.94
43	353.63	117.88	165.00	3.27	0.35	105	827	806	0.40	0.60	0.67	14.13
44	350.48	116.83	163.60	3.32	0.35	98	810	840	0.39	0.61	0.65	14.29
45	355.80	118.60	166.00	3.18	0.35	100	862	769	0.40	0.60	0.67	14.48
46	340.95	113.65	159.10	3.25	0.35	97	747	934	0.38	0.62	0.62	14.64
47	347.70	115.90	162.30	3.31	0.35	99	813	844	0.39	0.61	0.64	14.81
48	354.30	118.10	165.30	3.21	0.35	95	872	769	0.40	0.60	0.66	14.96
49	343.80	114.60	160.50	3.18	0.35	93	797	878	0.39	0.61	0.63	15.13
50	340.88	113.63	159.10	3.11	0.35	91	777	910	0.38	0.62	0.62	15.24

Appendix C

Passing-ability test results of wide bar spacing (10 bars) J-ring apparatus

Table C.1: t$_{500J}$ and difference between flow and J-ring spread diameter

Mix designation	t$_{500j}$, s	D $_{flow}$, mm	D $_{J-ring}$, mm	D $_{flow}$ – D $_{J-ring}$, mm
30A	0.60	685	665	20
40A	0.74	730	710	20
50A(50A)	1.40(1.31)	675(670)	660(650)	15(20)
60A	1.48	665	640	25
70A	1.79	700	700	0
80A	2.43	730	705	25

Figure C.1: Flow and passing ability of SCC mix: 30A (Left), 50A (Right)
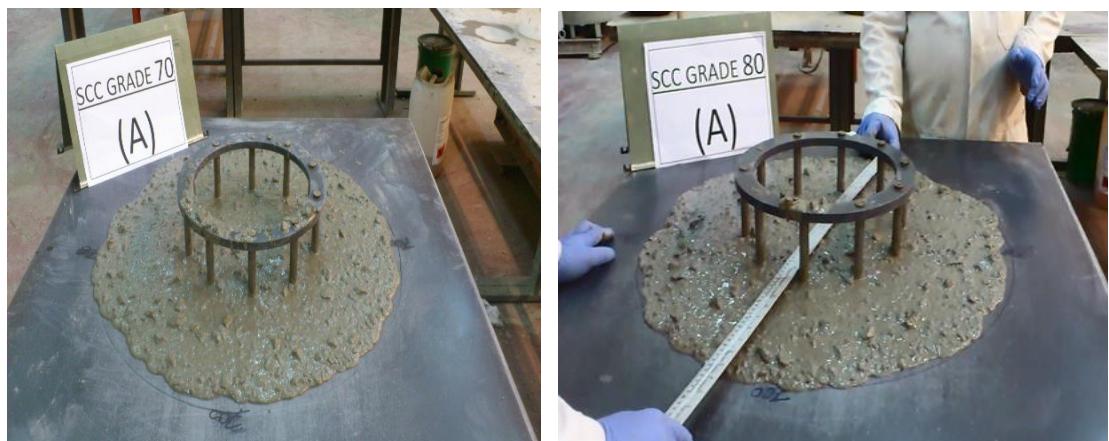
Figure C.2: Flow and passing ability of SCC mix: 70A (Left), 80A (Right)

Figure C.3: Flow and passing ability of SCC mix (50A)
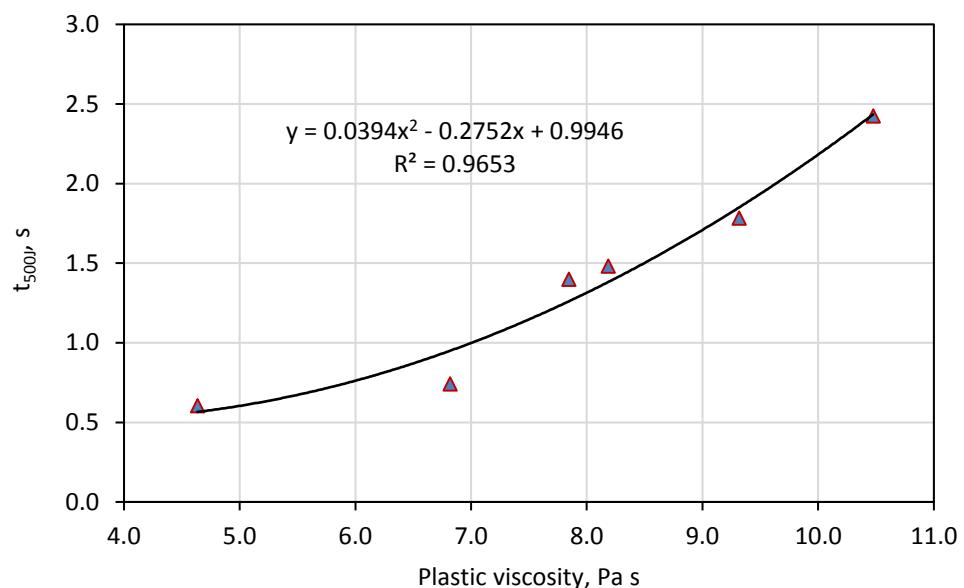
Figure C.4: t$_{500J}$ time versus plastic viscosity
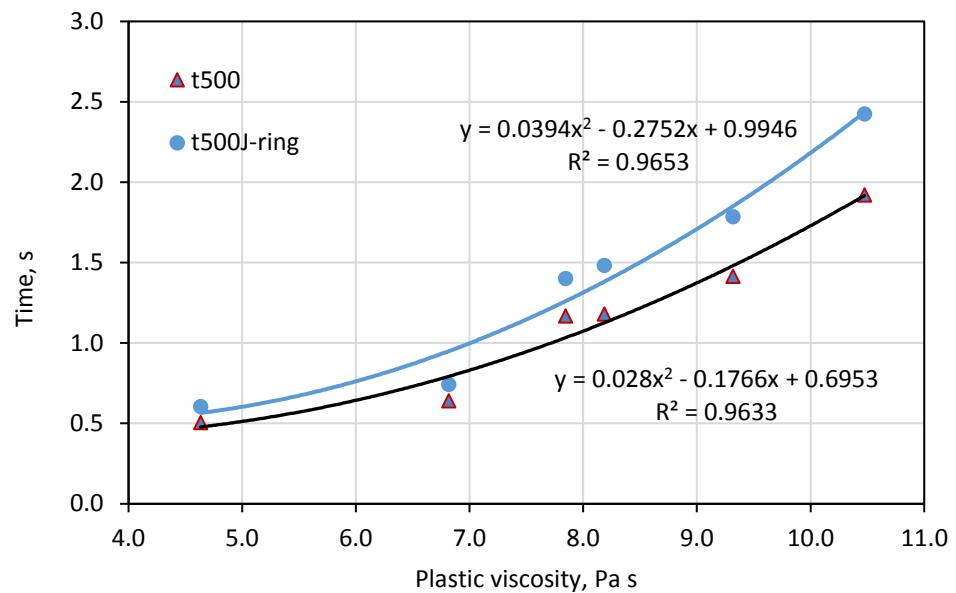
Figure C.5: Plastic viscosity versus t₅₀₀ and t₅₀₀J

Appendix D

Experimental load-deflection diagrams for deep and shallow notched specimens of SCC subjected to TPB test
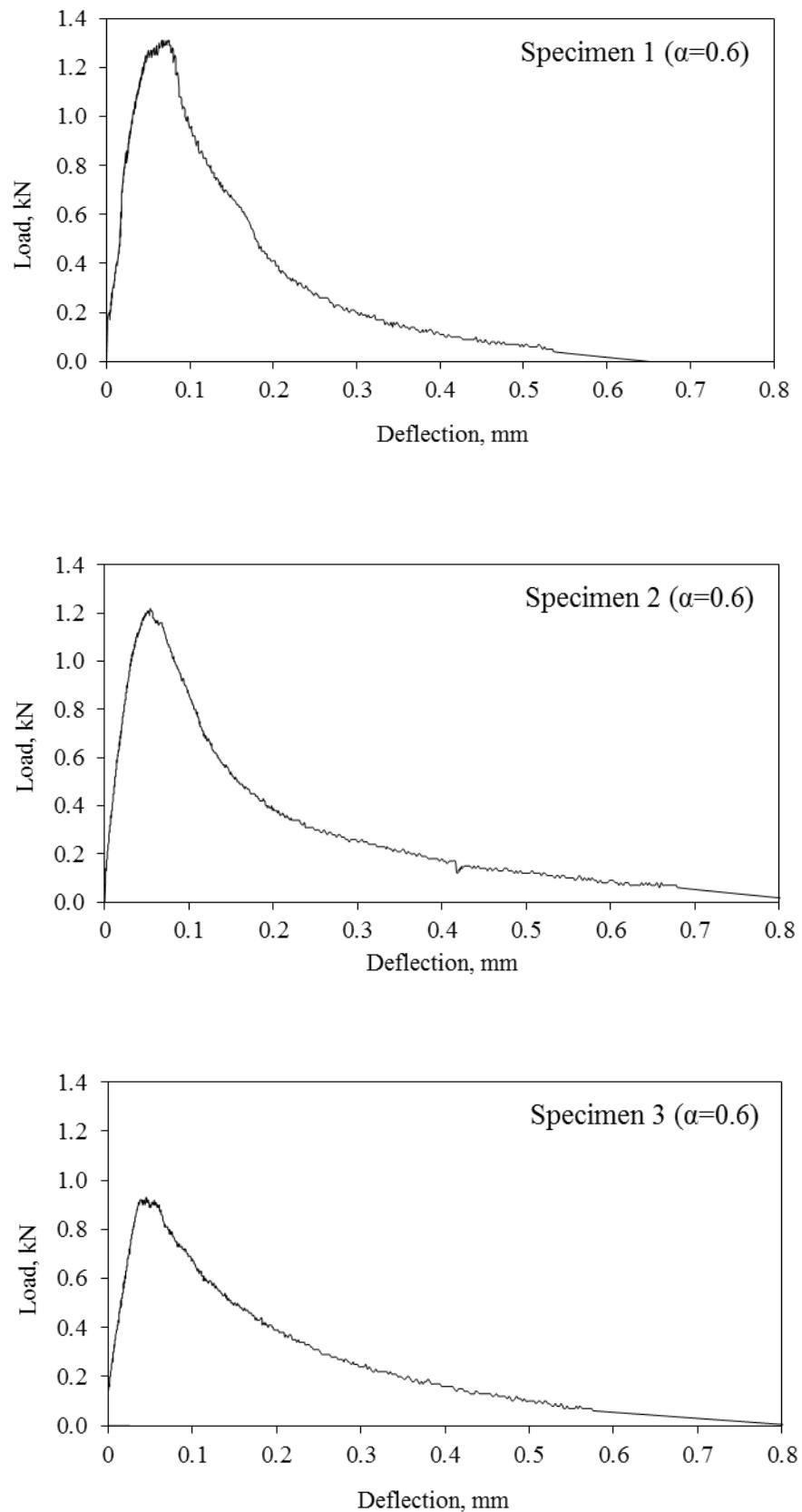
Figure D.1: Experimental load-deflection diagrams for deep notch (a/W = 0.6) specimens of SCC mix 30A

Specimen 1 (α=0.1)

Specimen 2 (α=0.1)

Specimen 3 (α=0.1)
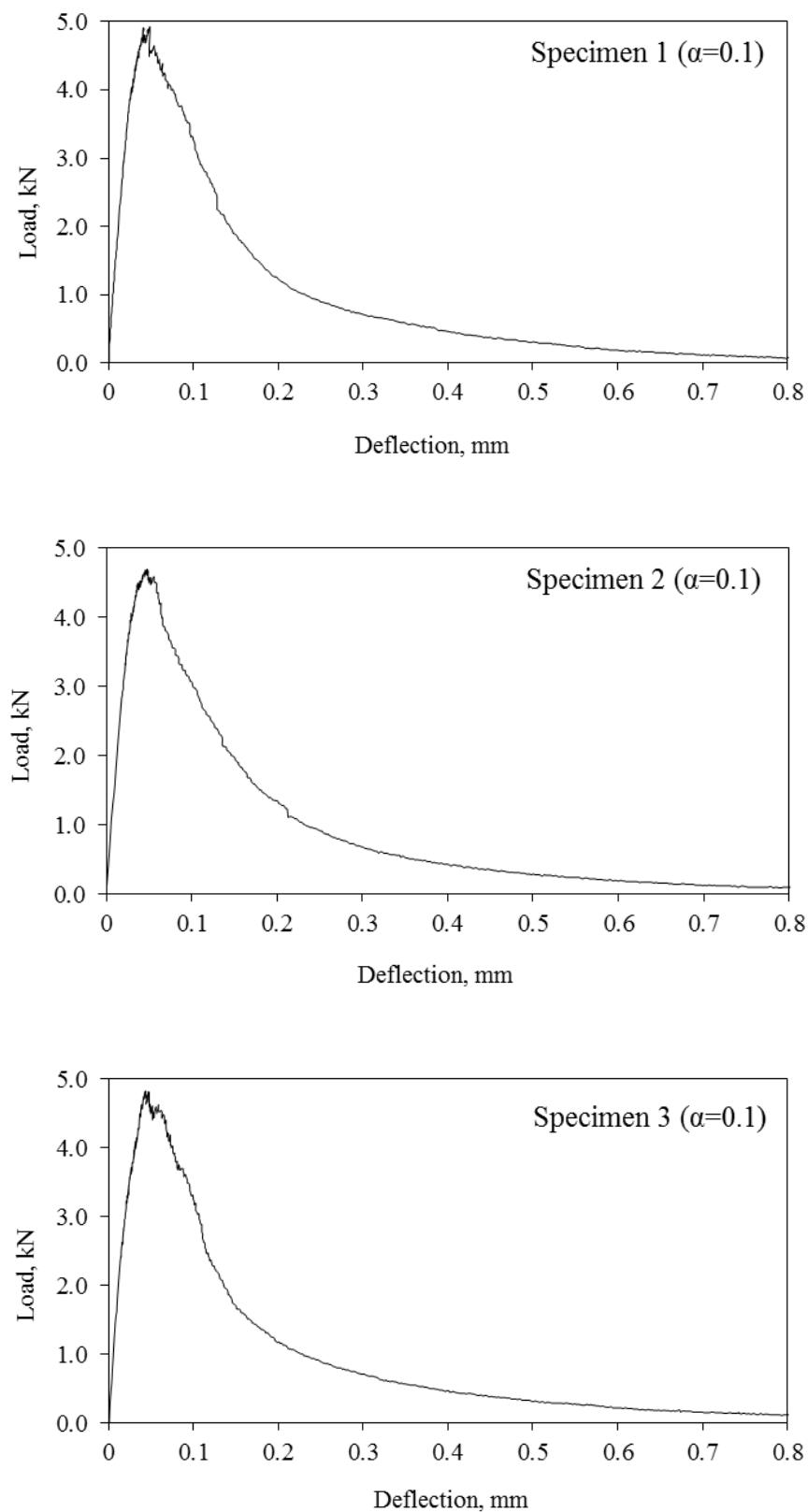
Figure D.2: Experimental load-deflection diagrams for shallow notch (a/W = 0.1) specimens of SCC mix 30A
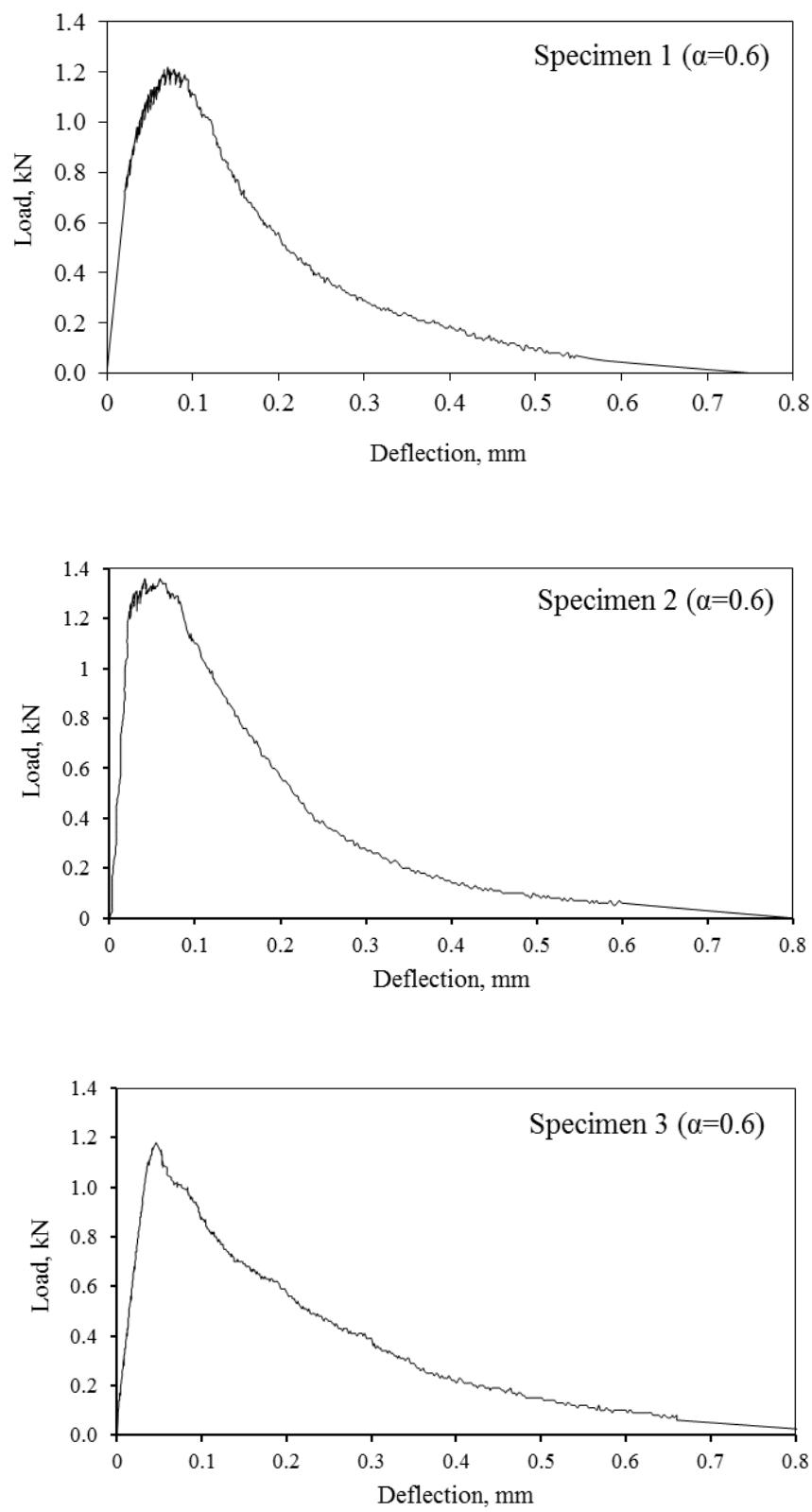
Figure D.3: Experimental load-deflection diagrams for deep notch (a/W = 0.6) specimens of SCC mix 60A
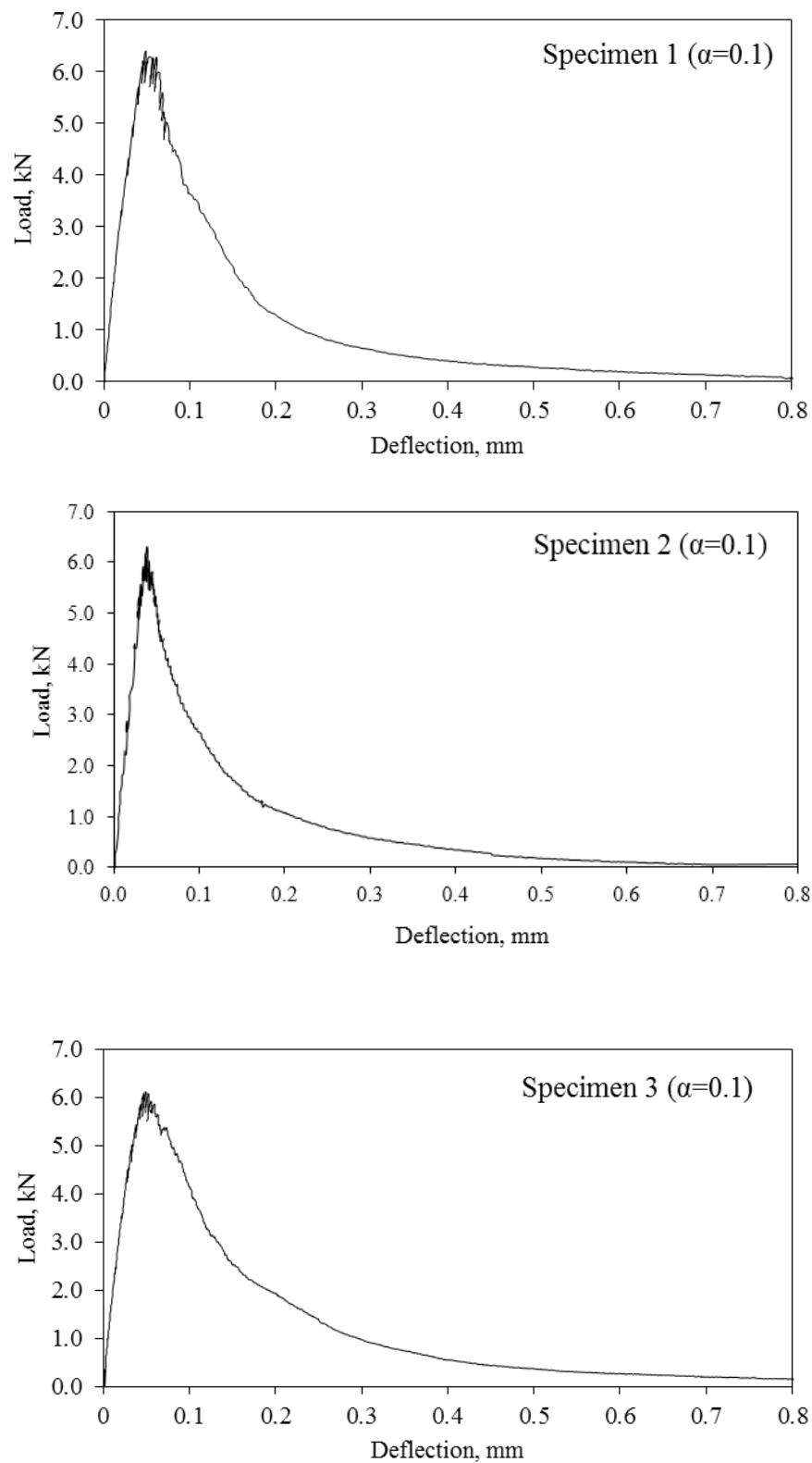
Figure D.4: Experimental load-deflection diagrams for shallow notch (a/W = 0.1) specimens of SCC mix 60A
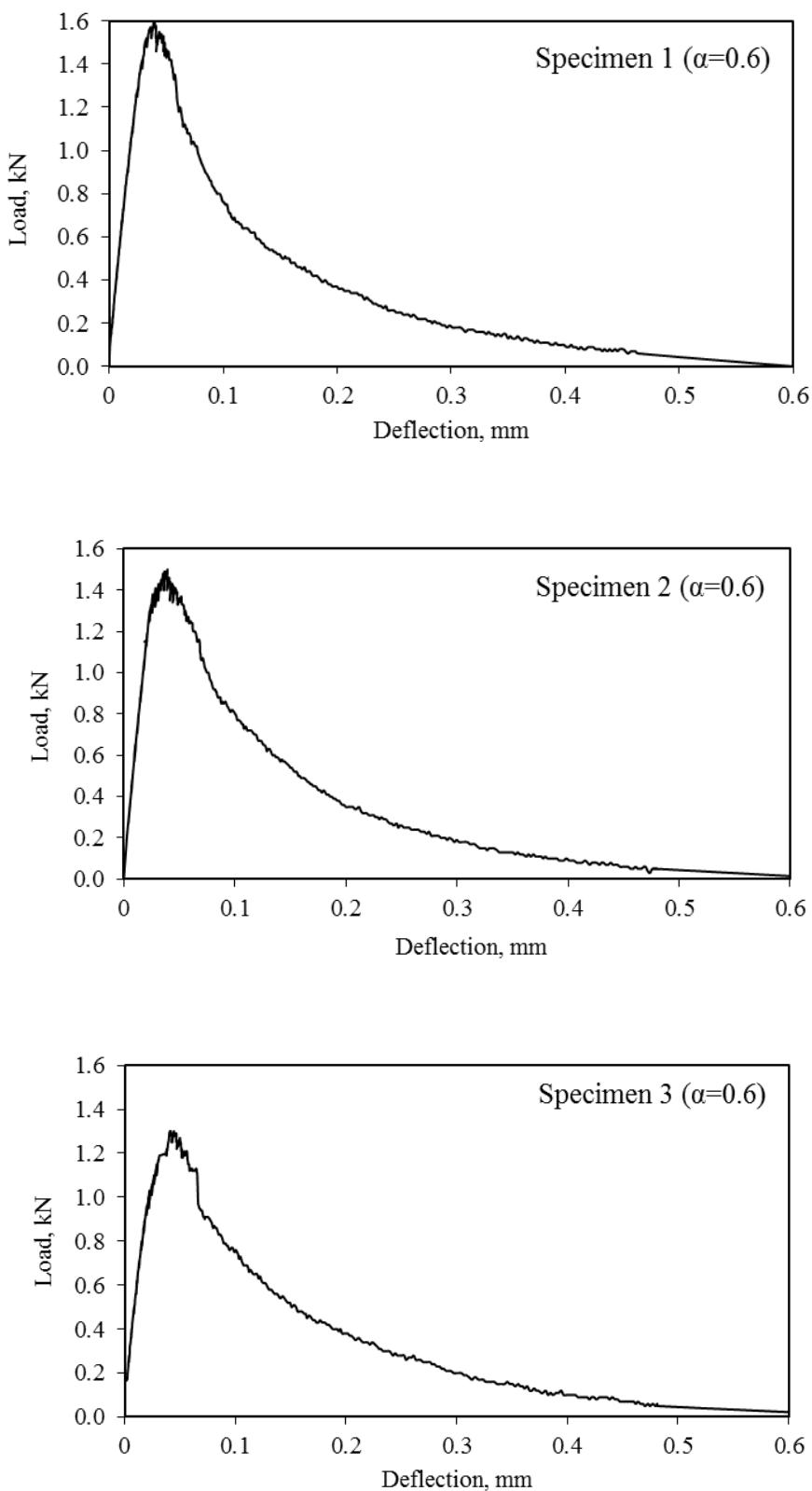
Figure D.5: Experimental load-deflection diagrams for deep notch (a/W = 0.6) specimens of SCC mix 80A
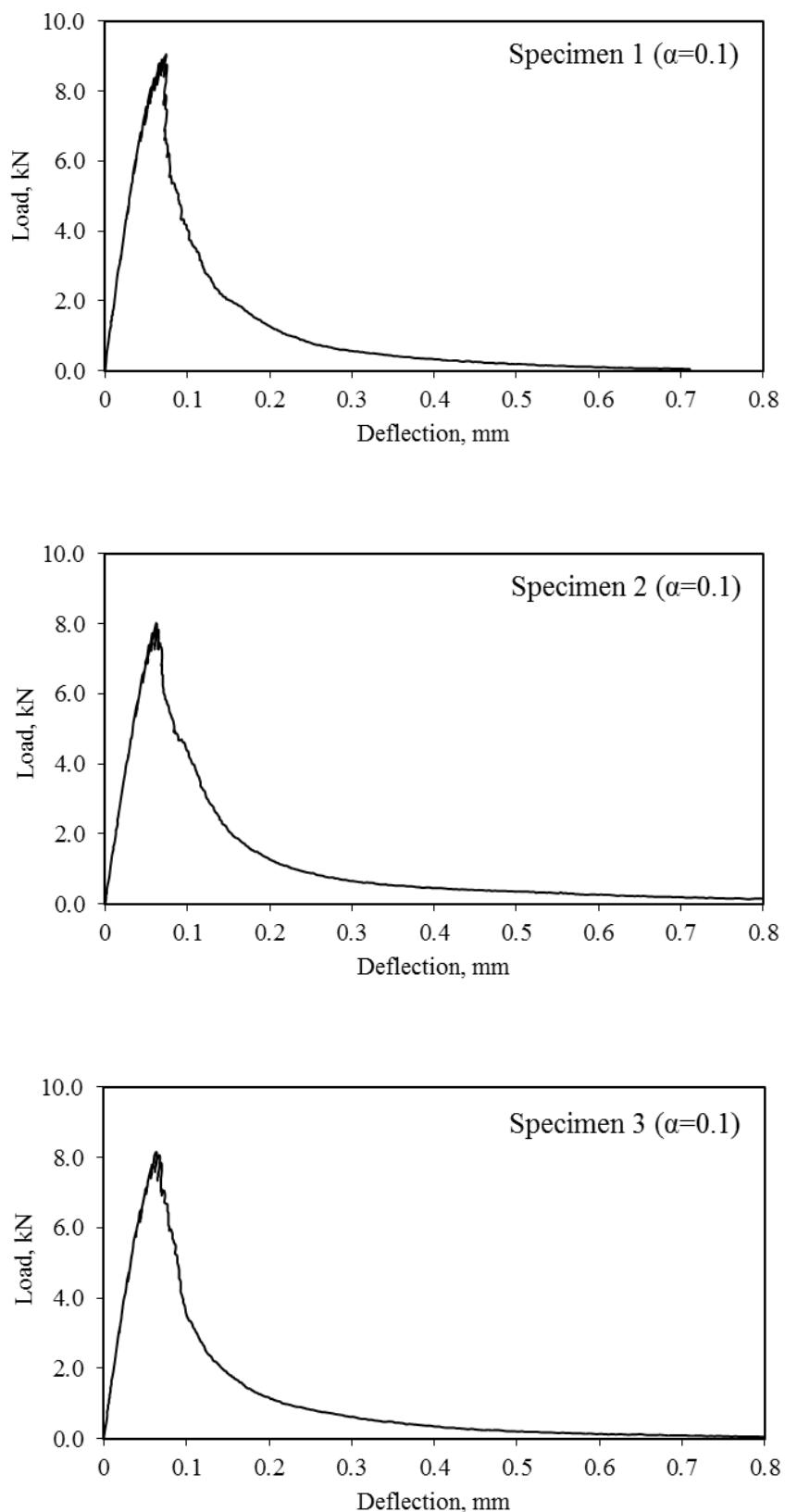
Figure D.6: Experimental load-deflection diagrams for shallow notch (a/W = 0.1) specimens of SCC mix 80A

Appendix E

Experimental load-CMOD diagrams for deep and shallow notched specimens of SCC subjected to TPB test
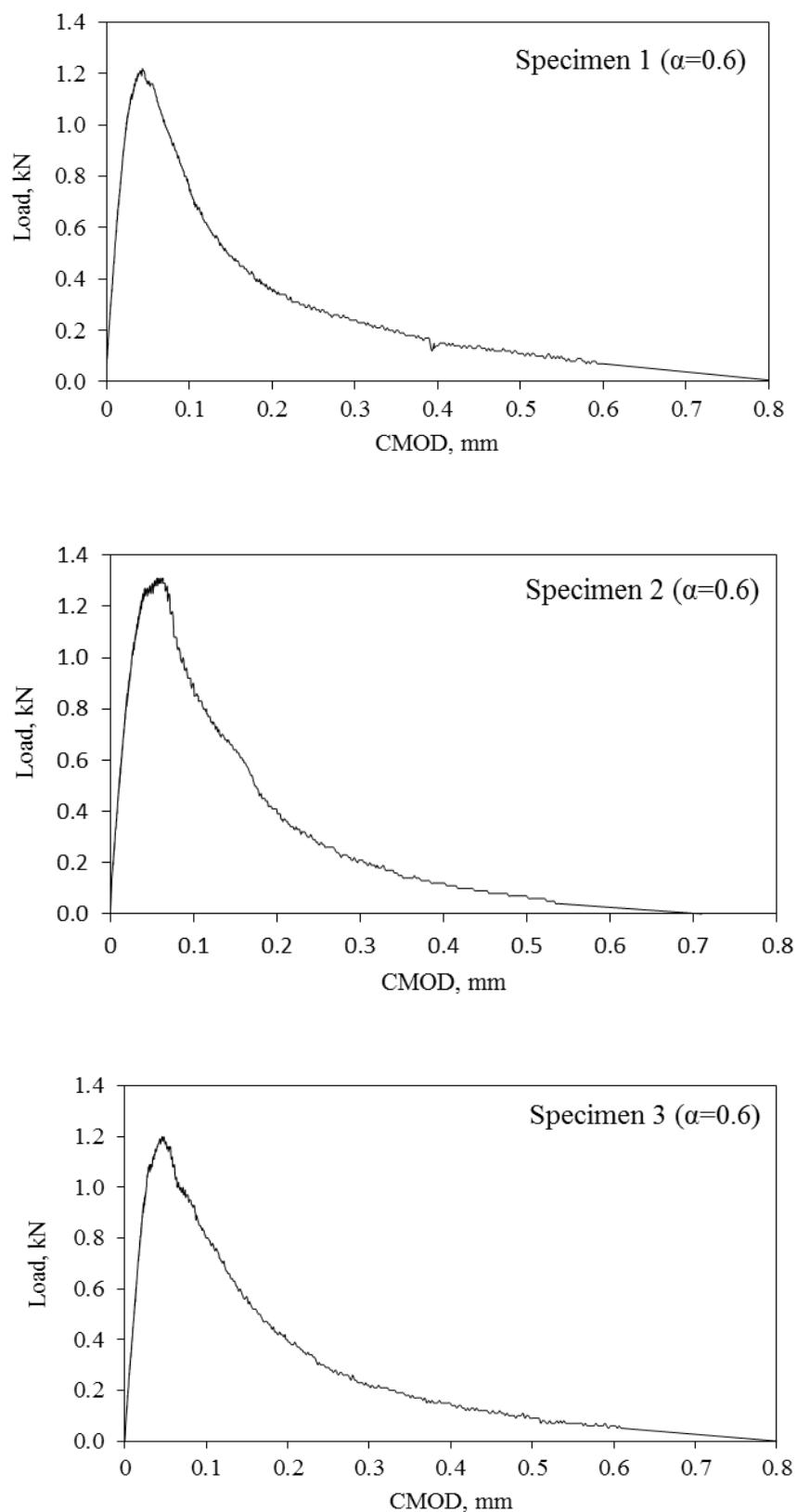
Figure E.1: Experimental load-CMOD diagrams for deep notch (a/W = 0.6) specimens of SCC mix 30A
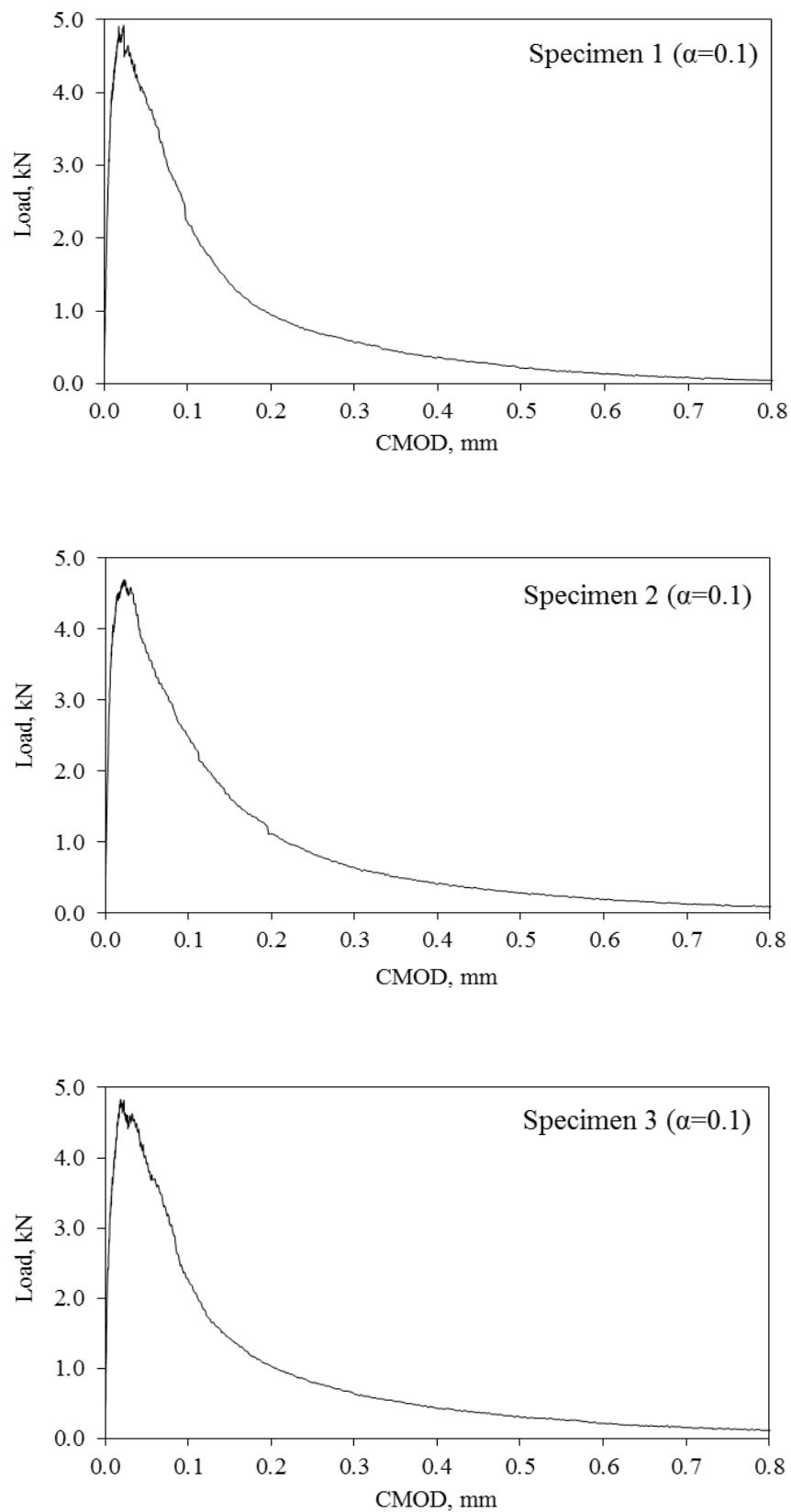
Figure E.2: Experimental load-CMOD diagrams for shallow notch (a/W = 0.1) specimens of SCC mix 30A
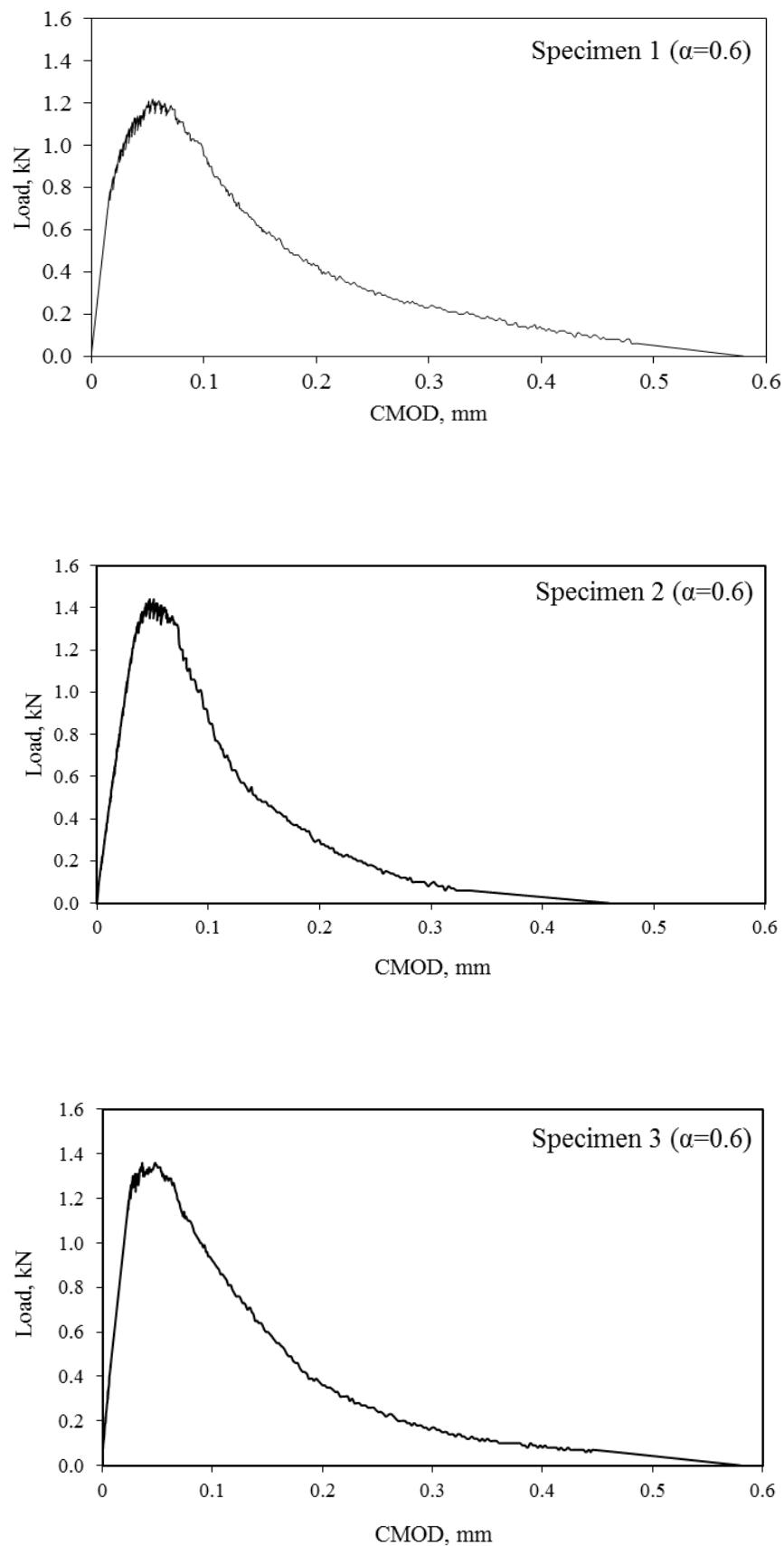
Figure E.3: Experimental load-CMOD diagrams for deep notch (a/W = 0.6) specimens of SCC mix 60A
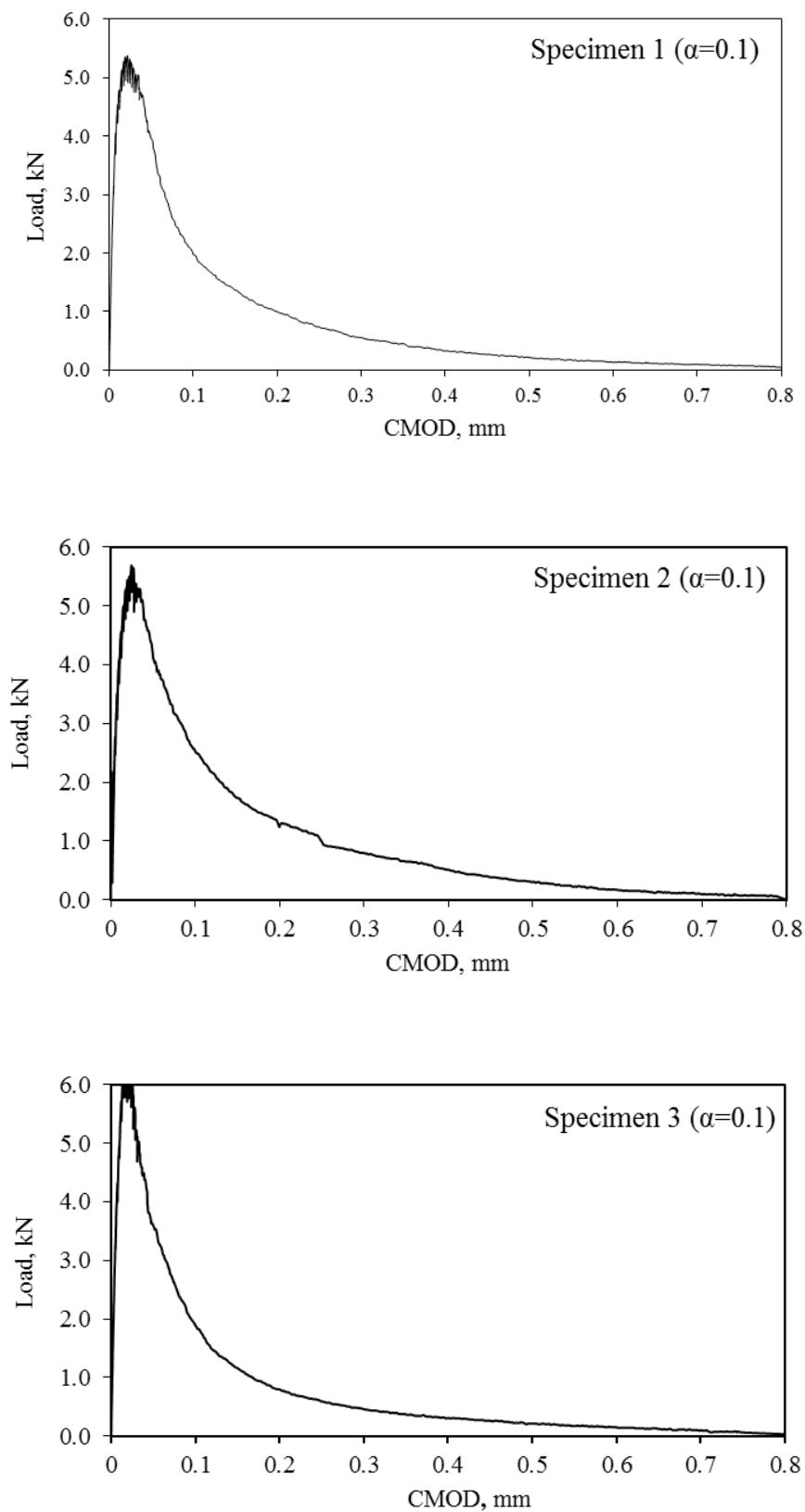
Figure E.4: Experimental load-CMOD diagrams for shallow notch (a/W = 0.1) specimens of SCC mix 60A
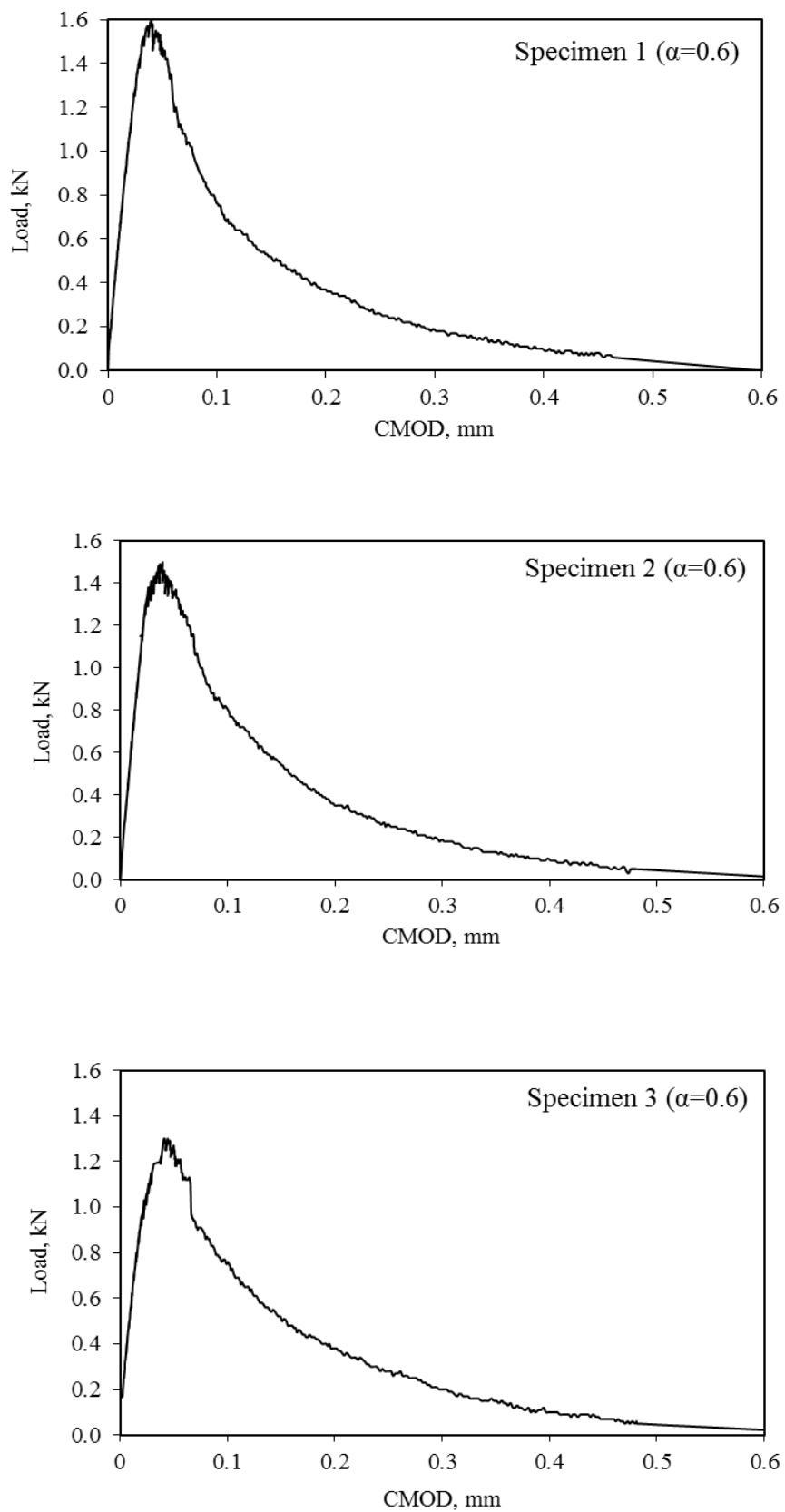
Figure E.5: Experimental load-CMOD diagrams for deep notch (a/W = 0.6) specimens of SCC mix 80A
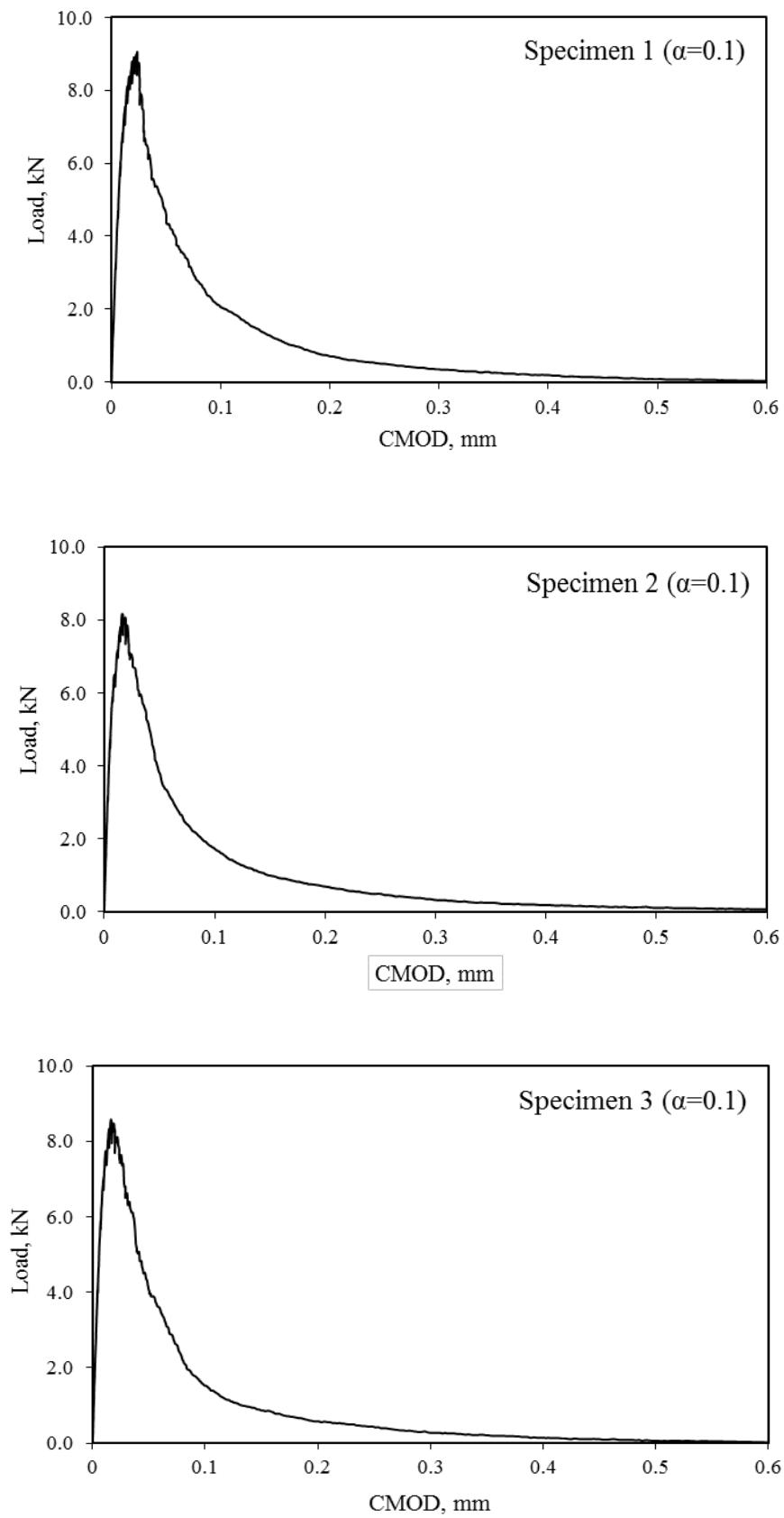
Figure E. 6: Experimental load-CMOD diagrams for shallow notch (a/W = 0.1) specimens of SCC mix 80A

Appendix F

A MATLAB program for determination of the parameters of the bilinear tension softening diagram (TSD)

```
%*********************************************************************
%                         CARDIFF UNIVERSITY
%                       SCHOOL OF ENGINEERING
% A MATLAB code for Determination of the static response of self-
% compacting concrete beams under three-point bending, using a
% bilinear tension-softening (stress-crack opening) relationship
% based on the fictitious crack model.
%*********************************************************************
%     References
% 1. Hillerborg A. (1980). Analysis of fracture by means of the
%    fictitious crack model, particularly for fibre-reinforced
%    concrete, Int J Cement Composites, 2, 177-184.
% 2. Hillerborg A., Modeer M. and Petersson P. (1976). Analysis of
%    crack formation and crack growth in concrete by means of
%    fracture mechanics and finite elements, Cement Concrete
%    Research, 6, 773-782.
% 3. Olesen J.F. (2001). Fictitious crack propagation in fibre-
%    reinforced concrete beams, J Engineering Mechanics, 127, 272-80
%*********************************************************************
%     List of variables
%     Name               Description
%     -----              ------------
%     alp0               Initial notch depth to beam depth ratio
%     db                 beam depth, mm
%     h                  Height of the hinge, mm
%     L                  Span length of the TPB, mm
%     t                  Thickness of the hinge, mm
%     S                  Width of the hinge, mm
%     al, a2, b1 & b2    Parameters for the bilinear relation
%     a1 & a2            1/mm
%     b1 & b2            Dimensionless
%     E                  Young modulus, GPa
%     ft                 Splitting tensile strength, GPa
%     GF                 Specific size-independent fracture energy
%*********************************************************************
%*********************************************************************
% Part one for calculation the shallow notch parameters
%*********************************************************************
%*********************************************************************
```

```matlab
clc
clear all
close all
polyfitOrder = 30;
% Enter the path of the experimental results Excel files of load-
% CMOD curves
v_matpath='C: \Users\Wajde1975\Desktop\ Fracture\80B';
% Enter the maximum displacement of the shallow and deep notches
MaxDisplacement01=0.42;
MaxDisplacement06=0.30;
% Enter the beam dimensions details
L=400;
t=100;
db=100;
a0shallow=10;
a0deep=60;
% Enter the rho value (use 0 for plain concrete or 0.045 for fibre
reinforced concrete)
rho=0;
% Enter the selected sheets numbers for shallow samples
SheetNo1 = [1 2 3 4 5];
% Enter the selected sheets numbers for deep samples
SheetNo6 = [7 8 9 10 11];
% Enter a proposed values of minimum and maximum theta
themin=0;
themax=200;
increment=themax/499;
incrementxq=MaxDisplacement01/499;
% xq is a constant increments in the x-direction of the average
experimental load-CMOD curves
xq = 0: incrementxq:MaxDisplacement01;
% Change the path to the file location
cd(v_matpath)
% Find the excel files in the folder
files = dir ('*.xlsx');
% [status, sheets] = xlsfinfo (filename)
filename = files(1).name;
[AA BB] = size(SheetNo1);
for n=1:BB
% Read Microsoft Excel spreadsheet file
clear subsetA
```

```
sheet = SheetNo1(1,n);
% Enter column range of the Excel sheets
xlRange = 'A:E';
subsetA = xlsread(filename,sheet,xlRange);
%********************************************************************
% Fit curve or surface to data
%********************************************************************
% Enter the column number of the x value (CMOD column in the excel sheet)
x = subsetA (:, 5);
% Enter the column number of the y value (load column in the excel sheet)
y = subsetA (:, 3);
hold on
plot(x,y);
p = polyfit(x,y, polyfitOrder);
f = polyval(p,x);
ff = polyval(p,xq);
% save all the results in one matrix (each column is a excel file)
Final_results(:,n)= ff(1,:);
hold on
end
% find the average of the final matrix
[m z] = size(Final_results);
for i = 1:m
    C(i,1) = mean(Final_results(i,1:z));
end
   plot(xq,C,':.');
   hold on
   plot(x,y,'o');
%********************************************************************
%Except parameters that can be used later on
%********************************************************************
clearvars -except xq C  polyfitOrder a0shallow a0deep db L t rho SheetNo6
v_matpath MaxDisplacement06 themin increment themax
%********************************************************************
a0=a0shallow;
alp0=a0/db;
h=(1-alp0)*db;
s=0.5*h;
%********************************************************************
% Enter a1, a2, b2, ft, E limits values
%********************************************************************
```

```matlab
count = 1;
for a1=1:0.5:50
for a2=0.1:0.05:1.5
for b2=0.1:0.05:0.9
for ft=0.0018:0.0001:0.0048
for E=25:0.5:40
bet1=ft*a1*s/E;
bet2=ft*a2*s/E;
c =(1-b2)*(1-bet1)/(bet2-bet1);
rho=0;
the01=1-rho ;
the12=.5*(1-rho-c+((1-rho-c)^2+c^2/(bet1-1))^0.5);
the23=.5*(rho*(bet2-1)+b2/bet2+(rho^2*(bet2-1)^2+2*rho*(bet2-
1)*b2/bet2+(1-b2)^2/(bet1 -bet2)+b2^2/bet2)^.5);
k=0;
for the=themin :increment: themax
%*******************************************************************
% Alpha & Mu Calculation
%*******************************************************************
% For phase 0
if (0<=the & the<=the01)
alp = 0;
mu = the;
cod = 0;
% For phase I
elseif(the01<the & the<=the12)
bi= 1;
beti = bet1;
alp = 1-bet1-((1-bet1)*((1-rho)/the-bet1))^.5;
mu = 4*(1-3*alp+3*alp^2-alp^3/(1-bet1))*the+(6*alp-3)*(1-rho);
cod = s*ft/E*(1-bi+2*alp*the)/(1-beti);
% For phase II
elseif(the12<the & the<=the23)
bi = b2;
beti = bet2;
alp =1-bet2-(1-b2)/(2*the)-(( 1-bet2)*(( 1-b2)^2/(4*the^2)/(bet1 -bet2)-
bet2+(b2-rho)/the))^.5;
mu = 4*(1-3*alp+3*alp^2-alp^3/(1-bet2))*the+(6*alp-3)*(1-rho)-(((1-
b2)*(3*alp^2-(c/(2*the))^2))/(1-bet2));
cod = s*ft/E*(1-bi+2*alp*the)/(1-beti);
% For phase III
```

```
elseif(the23<the)
bi =0;
beti = 0;
alp = 1 -1 /(2*the)*(1+((1-b2)^2/(bet1-bet2)+b2^2/bet2-4*rho*the)^.5);
mu = 4*(1-3*alp+3*alp^2-alp^3)*the+(6*alp-3)*(1-rho)-
3*alp^2+1/(4*the^2)*(1-b2/bet2)*(1-b2/bet2+c)*(1+bet1*c/(1-
bet1))+(c/(2*the))^2;
cod = s*ft/E*(1-bi+2*alp*the)/(1-beti);
end
k=k+1;
pp(k) = 2/3*ft*h^2*t/L*mu;
m = pp(k)*L/4;
sigm = 6*m/(t*db^2);
cod0 = 4*sigm*a0/E*(0.76-2.28*alp0+3.87*alp0^2-2.04*alp0^3+0.66/(1-
alp0)^2);
CMOD(k) = cod + cod0;
end
AA = [CMOD;pp]';
x = AA(:,1); % the x value
y = AA(:,2); % the y value


% select either spline fit or polyfit (choose one option as shown here)
%******************************************************************

% spline fit option
ff=interp1(x,y,xq,'spline');
%******************************************************************

% poly fit option
% p = polyfit(x,y, polyfitOrder);
% f = polyval(p,x);
% ff = polyval(p,xq);
%******************************************************************
%Check the maximum differences in theoretical and experimental %peak
%load
%************************************************************************H1=ma
x(ff);
H2=max(C);
H3=(H2-H1)/H2*100;
if(-2<=H3 && H3<=2)
```

```
clear Error
[mm nn]= size(xq);
for ii = 1:nn
Error(ii,2) = (ff(1,ii)-C(ii,1))^2;
Error(ii,1) = xq(1,ii);
end
SumError (count,1) = sum (Error(:,2))/nn;
SumError (count,2) = a1;
SumError (count,3) = a2;
SumError (count,4) = b2;
SumError (count,5) = ft;
SumError (count,6) = E;
count = count +1;
end
end
end
end
end
end
EE=sortrows(SumError,[1 6]);
MinERR=EE(1,1);
a1=EE(1,2);
a2=EE(1,3);
b2=EE(1,4);
ft=EE(1,5);
E=EE(1,6);
w1=(1-b2)/(a1-a2);
w2=b2/a2;
sigmaft=a2*(w2-w1);
Gf01=0.5*ft*1000*(w1+sigmaft*w2);
D=[0 w1 w2];
EEE=[1 sigmaft 0];
KneeCoordinatesSHallow= [D; EEE]';
%****************************************************************
%Except parameters that can be used later on
%****************************************************************
clearvars -except sigmaft C xq alp0 E ft db h L t s rho a1 a2 b2 themin
increment themax KneeCoordinatesSHallow w1 w2 Gf01 MinERR SumError
polyfitOrder a0 a0deep SheetNo6 v_matpath MaxDisplacement06 B1
%****************************************************************
bet1=ft*a1*s/E;
```

```
bet2=ft*a2*s/E;
c =(1-b2)*(1-bet1)/(bet2-bet1);
rho=0;
the01=1-rho ;
the12=0.5*(1-rho-c+((1-rho-c)^2+c^2/(bet1-1))^0.5);
the23=0.5*(rho*(bet2-1)+b2/bet2+(rho^2*(bet2-1)^2+2*rho*(bet2-
1)*b2/bet2+(1-b2)^2/(bet1 -bet2)+b2^2/bet2)^.5);
k=0;
%*****************************************************************
%*****************************************************************
% Alpha & MU Calculation
%*****************************************************************
%*****************************************************************
% input theta values
for the=themin :increment:themax
% For phase 0
if (0<=the & the<=the01)
alp = 0;
mu = the;
cod = 0;
% For phase I
elseif(the01<the & the<=the12)
bi= 1;
beti = bet1;
alp = 1-bet1-((1-bet1)*((1-rho)/the-bet1))^.5;
mu = 4*(1-3*alp+3*alp^2-alp^3/(1-bet1))*the+(6*alp-3)*(1-rho);
cod = s*ft/E*(1-bi+2*alp*the)/(1-beti);
% For phase II
elseif(the12<the & the<=the23)
bi = b2;
beti = bet2;
alp =1-bet2-(1-b2)/(2*the)-(( 1-bet2)*(( 1-b2)^2/(4*the^2)/(bet1 -bet2)-
bet2+(b2-rho)/the))^.5;
mu = 4*(1-3*alp+3*alp^2-alp^3/(1-bet2))*the+(6*alp-3)*(1-rho)-(((1-
b2)*(3*alp^2-(c/(2*the))^2))/(1-bet2));
cod = s*ft/E*(1-bi+2*alp*the)/(1-beti);
% For phase III
elseif(the23<the)
bi =0;
beti = 0;
alp = 1 -1 /(2*the)*(1+((1-b2)^2/(bet1-bet2)+b2^2/bet2-4*rho*the)^.5);
```

```
mu = 4*(1-3*alp+3*alp^2-alp^3)*the+(6*alp-3)*(1-rho)-
3*alp^2+1/(4*the^2)*(1-b2/bet2)*(1-b2/bet2+c)*(1+bet1*c/(1-
bet1))+(c/(2*the))^2;
cod = s*ft/E*(1-bi+2*alp*the)/(1-beti);
end
k=k+1;
pp(k) = 2/3*ft*h^2*t/L*mu;
m = pp(k)*L/4;
sigm = 6*m/(t*db^2);
cod0 = 4*sigm*a0/E*(0.76-2.28*alp0+3.87*alp0^2-2.04*alp0^3+0.66/(1-
alp0)^2);
CMOD(k) = cod + cod0;
end
AA = [CMOD;pp]';
x = AA(:,1); % the x value
y = AA(:,2); % the y value
% select either spline fit or polyfit (choose one option as shown here)
%*********************************************************************
% spline fit option
ff=interp1(x,y,xq,'spline');
%*********************************************************************
% poly fit option
% p = polyfit(x,y,polyfitOrder);
% f = polyval(p,x);
% ff = polyval(p,xq);
%*********************************************************************
W1(:,1)=xq;
W2(:,1)=C;
W3(:,1)=ff;
ModelCurve = [xq;ff]';
TestCurve=[W1,W2];
ModelTestCurveShallow = [W1';W2';W3']';
HeaderNames1='xq,PTest,PModel';
% Preferable output sheet name printed here
fileName1 = 'ModelTest01.csv';
outid = fopen(fileName1, 'w+');
fprintf(outid, '%s', HeaderNames1);
fclose(outid);
dlmwrite(fileName1,ModelTestCurveShallow,'roffset',1,'-append',
'precision', 4);
disp(strcat('Generated report ''',fileName1,''''))
```

```
% Preferable output sheet name printed here
filename = 'Parameters.xlsx';
% Desired parameters to be printed in the output sheet
A =
{'a1','a2','b2','w1','w2','Gf01','ft01','E','MinERR';a1,a2,b2,w1,w2,Gf01,
ft,E,MinERR};
B1=[a1,a2,b2,Gf01,ft,E,MinERR];
sheet = 1;
xlRange = 'A';
xlswrite(filename,A,sheet,xlRange)
filename = 'Parameters.xlsx';
A = {'Xknee','Yknee';0,1;w1,sigmaft;w2,0};
sheet = 1;
xlRange = 'J';
xlswrite(filename,A,sheet,xlRange)
%*****************************************************************
%*****************************************************************
%*****************************************************************


% Part two for calculation the deep notch parameters
%*****************************************************************
clearvars -except polyfitOrder MaxDisplacement06 SheetNo6 a0deep db L t s
rho themin increment themax KneeCoordinatesSHallow v_matpath B1
%*****************************************************************
incrementxq = MaxDisplacement06/499;
xq = 0:incrementxq:MaxDisplacement06;
% change the path to the file location automatically
cd(v_matpath)
% find the excel files in the folder
files = dir('*.xlsx');
filename = files(1).name;
[AA BB] = size(SheetNo6);
for n=1:BB
% Read Microsoft Excel spreadsheet file
clear subsetA
sheet = SheetNo6(1,n);
xlRange = 'A:E';
subsetA = xlsread(filename,sheet,xlRange);
%*****************************************************************


% Fit curve or surface to data
```

```
%****************************************************************
% Enter the column number of the x value (CMOD column in the excel
% sheet)
x = subsetA(:,5);
% Enter the column number of the y value (load column in the excel
% sheet)
y = subsetA(:,3);
hold on
plot(x,y);
p = polyfit(x,y,polyfitOrder);
f = polyval(p,x);
ff = polyval(p,xq);
% save all the results in one matrix (each column is a excel file)
Final_results(:,n)= ff(1,:);
hold on
end
% find the average of the final matrix
[m z] = size(Final_results);
for i = 1:m
C(i,1) = mean(Final_results(i,1:z));
end
plot(xq,C,':.');
clearvars -except xq C  polyfitOrder L t s rho db themin increment themax
KneeCoordinatesSHallow a0deep B1
%****************************************************************
% Enter constant values
%****************************************************************
a0=a0deep;
alp0=a0/db;
h=(1-alp0)*db;
% Enter a1, a2, b2, ft, E limits values
count = 1;
for a1=1:0.5:50
for a2=0.1:0.05:1.5
for b2=0.1:0.05:0.9
for ft=0.0018:0.0001:0.0048
for E=25:0.5:40
bet1=ft*a1*s/E;
bet2=ft*a2*s/E;
c =(1-b2)*(1-bet1)/(bet2-bet1);
rho=0;
```

```matlab
the01=1-rho ;
the12=.5*(1-rho-c+((1-rho-c)^2+c^2/(bet1-1))^0.5);
the23=.5*(rho*(bet2-1)+b2/bet2+(rho^2*(bet2-1)^2+2*rho*(bet2-
1)*b2/bet2+(1-b2)^2/(bet1 -bet2)+b2^2/bet2)^.5);
k=0;
for the=themin :increment:themax
%*****************************************************************
% Alpha & Mu Calculation
%*****************************************************************

% For phase 0
if (0<=the & the<=the01)
alp = 0;
mu = the;
cod = 0;
% For phase I
elseif(the01<the & the<=the12)
bi= 1;
beti = bet1;
alp = 1-bet1-((1-bet1)*((1-rho)/the-bet1))^.5;
mu = 4*(1-3*alp+3*alp^2-alp^3/(1-bet1))*the+(6*alp-3)*(1-rho);
cod = s*ft/E*(1-bi+2*alp*the)/(1-beti);
% For phase II
elseif(the12<the & the<=the23)
bi = b2;
beti = bet2;
alp =1-bet2-(1-b2)/(2*the)-(( 1-bet2)*(( 1-b2)^2/(4*the^2)/(bet1 -bet2)-
bet2+(b2-rho)/the))^.5;
mu = 4*(1-3*alp+3*alp^2-alp^3/(1-bet2))*the+(6*alp-3)*(1-rho)-(((1-
b2)*(3*alp^2-(c/(2*the))^2))/(1-bet2));
cod = s*ft/E*(1-bi+2*alp*the)/(1-beti);
% For phase III
elseif(the23<the)
bi =0;
beti = 0;
alp = 1 -1 /(2*the)*(1+((1-b2)^2/(bet1-bet2)+b2^2/bet2-4*rho*the)^.5);
mu = 4*(1-3*alp+3*alp^2-alp^3)*the+(6*alp-3)*(1-rho)-
3*alp^2+1/(4*the^2)*(1-b2/bet2)*(1-b2/bet2+c)*(1+bet1*c/(1-
bet1))+(c/(2*the))^2;
cod = s*ft/E*(1-bi+2*alp*the)/(1-beti);
```

```
end
k=k+1;
pp(k) = 2/3*ft*h^2*t/L*mu;
m = pp(k)*L/4;
sigm = 6*m/(t*db^2);
cod0 = 4*sigm*a0/E*(0.76-2.28*alp0+3.87*alp0^2-2.04*alp0^3+0.66/(1-
alp0)^2);
CMOD(k) = cod + cod0;
end
AA = [CMOD;pp]';
x = AA(:,1); % the x value
y = AA(:,2); % the y value
% select either spline fit or polyfit (choose one option as shown)
%*****************************************************************
% spline fit option
ff=interp1(x,y,xq,'spline');
%*****************************************************************
% poly fit option
% p = polyfit(x,y,polyfitOrder);
% f = polyval(p,x);
% ff = polyval(p,xq);
%*****************************************************************
%Check the maximum differences in theoretical and experimental peak %load
%*****************************************************************H1=ma
x(ff);
H2=max(C);
H3=(H2-H1)/H2*100;
if(-2<=H3 && H3<=2)
clear Error
[mm nn]= size(xq);
for ii = 1:nn
Error(ii,2) = (ff(1,ii)-C(ii,1))^2;
Error(ii,1) = xq(1,ii);
end
SumError(count,1) = sum (Error(:,2))/nn;
SumError(count,2) = a1;
SumError(count,3) = a2;
SumError(count,4) = b2;
SumError(count,5) = ft;
SumError(count,6) = E;
count = count +1;
```

```
end
end
end
end
end
end
EE=sortrows(SumError,[1 6]);
MinERR=EE(1,1);
a1=EE(1,2);
a2=EE(1,3);
b2=EE(1,4);
ft=EE(1,5);
E=EE(1,6);
w1=(1-b2)/(a1-a2);
w2=b2/a2;
sigmaft=a2*(w2-w1);
Gf06=0.5*ft*1000*(w1+sigmaft*w2);
D=[0 w1 w2];
EEE=[1 sigmaft 0];
KneeCoordinatesSHallow=[D;EEE]';
%*****************************************************************
clearvars -except sigmaft C xq alp0 E ft db h L t s rho a1 a2 b2 themin
increment themax KneeCoordinatesDeep w1 w2 Gf01 Gf06 MinERR SumError
polyfitOrder  a0deep KneeCoordinatesSHallow B1
%*****************************************************************
% input a1, a2, b2 values
a0=a0deep;
bet1=ft*a1*s/E;
bet2=ft*a2*s/E;
c =(1-b2)*(1-bet1)/(bet2-bet1);
rho=0;
the01=1-rho ;
the12=.5*(1-rho-c+((1-rho-c)^2+c^2/(bet1-1))^0.5);
the23=.5*(rho*(bet2-1)+b2/bet2+(rho^2*(bet2-
1)^2+2*rho*(bet2-
1)*b2/bet2+(1-b2)^2/(bet1 -bet2)+b2^2/bet2)^.5);
k=0;
% input theta values
 for the=themin :increment:themax
%*****************************************************************
% Alpha & Mu Calculation
%*****************************************************************
```

```matlab
% For phase 0
if (0<=the & the<=the01)
alp = 0;
mu = the;
cod = 0;
% For phase I
elseif(the01<the & the<=the12)
bi= 1;
beti = bet1;
alp = 1-bet1-((1-bet1)*((1-rho)/the-bet1))^.5;
mu = 4*(1-3*alp+3*alp^2-alp^3/(1-bet1))*the+(6*alp-3)*(1-rho);
cod = s*ft/E*(1-bi+2*alp*the)/(1-beti);
% For phase II
elseif(the12<the & the<=the23)
bi = b2;
beti = bet2;
alp =1-bet2-(1-b2)/(2*the)-(( 1-bet2)*(( 1-b2)^2/(4*the^2)/(bet1 -bet2)-
bet2+(b2-rho)/the))^.5;
mu = 4*(1-3*alp+3*alp^2-alp^3/(1-bet2))*the+(6*alp-3)*(1-rho)-(((1-
b2)*(3*alp^2-(c/(2*the))^2))/(1-bet2));
cod = s*ft/E*(1-bi+2*alp*the)/(1-beti);
% For phase III
elseif(the23<the)
bi =0;
beti = 0;
alp = 1 -1 /(2*the)*(1+((1-b2)^2/(bet1-bet2)+b2^2/bet2-4*rho*the)^.5);
mu = 4*(1-3*alp+3*alp^2-alp^3)*the+(6*alp-3)*(1-rho)-
3*alp^2+1/(4*the^2)*(1-b2/bet2)*(1-b2/bet2+c)*(1+bet1*c/(1-
bet1))+(c/(2*the))^2;
cod = s*ft/E*(1-bi+2*alp*the)/(1-beti);
end
k=k+1;
pp(k) = 2/3*ft*h^2*t/L*mu;
m = pp(k)*L/4;
sigm = 6*m/(t*db^2);
cod0 = 4*sigm*a0/E*(0.76-2.28*alp0+3.87*alp0^2-2.04*alp0^3+0.66/(1-
alp0)^2);
CMOD(k) = cod + cod0;
end
AA = [CMOD;pp]';
x = AA(:,1); % the x value
```

```
y = AA(:,2); % the y value
% select either spline fit or polyfit (choose one option as shown)
%********************************************************************
% spline fit option
ff=interp1(x,y,xq,'spline');
%**************************************************************************
**
% poly fit option
% p = polyfit(x,y,polyfitOrder);
% f = polyval(p,x);
% ff = polyval(p,xq);
%******************************************************************
W1(:,1)=xq;
W2(:,1)=C;
W3(:,1)=ff;
ModelCurve = [xq;ff]';
TestCurve=[W1,W2];
ModelTestCurveDeep = [W1';W2';W3']';
HeaderNames1='xq,PTest,PModel';
% Preferable output sheet name printed here
fileName1 = 'ModelTest06.csv';
outid = fopen(fileName1, 'w+');
fprintf(outid, '%s', HeaderNames1);
fclose(outid);
dlmwrite(fileName1,ModelTestCurveDeep,'roffset',1,'-append', 'precision',
4); % increased precision to allow all digits to be saved
disp(strcat('Generated report ''',fileName1,''''))
% Preferable output sheet name printed here
filename = 'Parameters.xlsx';
% Desired parameters to be printed in the output sheet
A
='a1','a2','b2','w1','w2','Gf06','ft06','E','MinERR';a1,a2,b2,w1,w2,Gf06,
ft,E,MinERR};
sheet = 1;
xlRange = 'L';
xlswrite(filename,A,sheet,xlRange)
filename = 'Parameters.xlsx';
A = {'Xknee','Yknee';0,1;w1,sigmaft;w2,0};
B2=[a1,a2,b2,Gf01,ft,E,MinERR];
parametersstar=(B1+B2)/2;
sheet = 1;
```

```
xlRange = 'U';
xlswrite(filename,A,sheet,xlRange)
%*****************************************************************
%*****************************************************************
%*****************************************************************
% This part is to find the unique parameters of hinge model
%*****************************************************************
% Enter constant values
%*****************************************************************
% Input the specific size-independent fracture energy, GF and
% splitting tensile strength, ft values
%*****************************************************************
%GF=0.1469; % Experimental simplified boundary effect method, N/m
%ft=3.12;% Experimental of splitting tensile strength, MPa
%*****************************************************************
a1star=parametersstar (1);
a2star=parametersstar (2);
b2star=parametersstar (3);
Gfstar=parametersstar (4);
ftstar=parametersstar(5)*1000;
w1star=(1-b2star)/(a1star-a2star)
w2star=b2star/a2star
w1=w1star*GF*ftstar/(Gfstar*ft);
sigmaftstar=(w2star-w1star)*a2star;
sigmaftstar2=1-a1star*w1star;
sigmastar=ftstar*sigmaftstar;
secondside=GF*sigmastar*w2star/(a2star*Gfstar*ft);
w2one=(w1+(w1^2+4*secondside)^0.5)/2
w2two=(w1-(w1^2+4*secondside)^0.5)/2
if(w2one>0)
    w2=w2one
end
if(w2two>0)
    w2=w2two
end
a2=a2star
sigmaft=(w2-w1)*a2;
a1=(1-sigmaft)/w1;
% Desired parameters to be printed in the output sheet
myMatrix=[a1star;a2star;ftstar;Gfstar;w1star;w2star;sigmaftstar;a1;a2;ft;
GF;w1;w2;sigmaft]';
```

```matlab
% Preferable output sheet name printed here
fileName = 'Uniqueparameters.csv';
dlmwrite(fileName,myMatrix,'roffset',1,'-append', 'precision', 8);
disp(strcat('Generated report ''',fileName,''''))
%***********************************************************
%***********************************************************
%***********************************************************
% Preferable output sheet name printed here
```

Appendix G

## Simulation results of SCC mixes in 10 and 16-bar J-ring tests
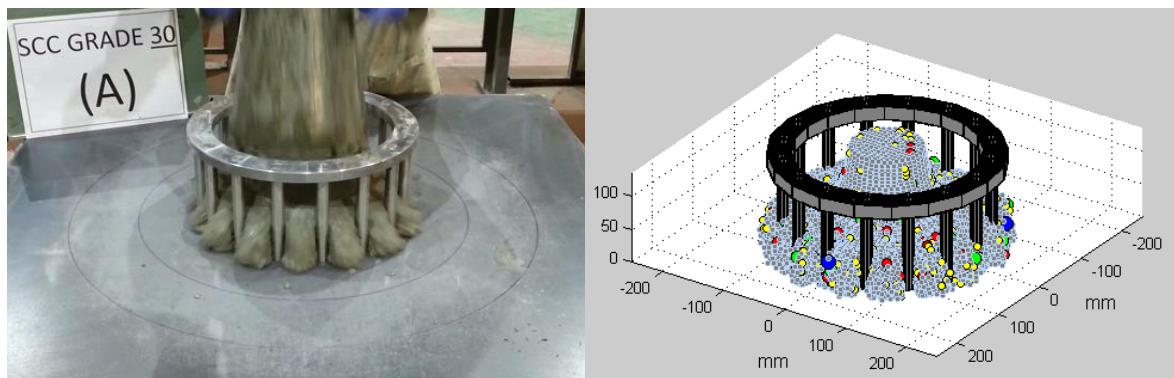
Figure G.1: Flow pattern of SCC Mix30 just after passing through the gaps in 16-bar J-ring test (at 0.2 s)
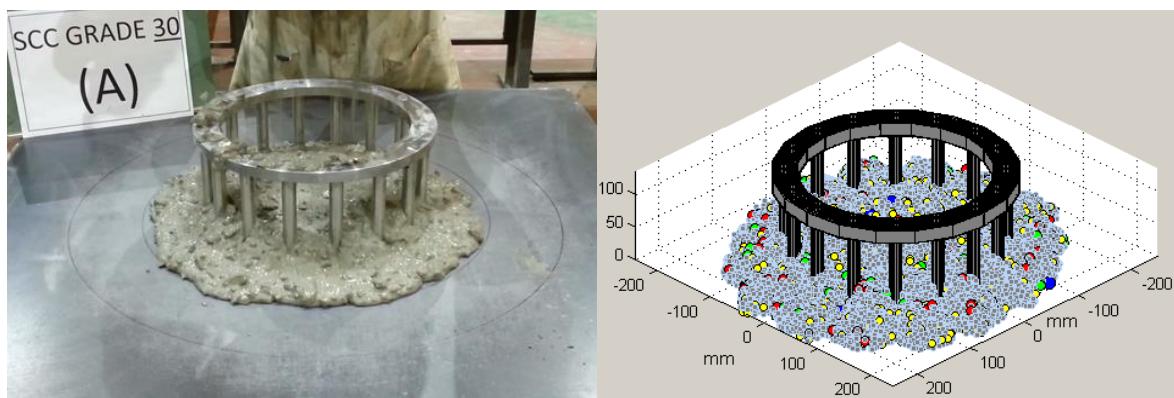

**Figure G.2: Flow pattern of SCC Mix30 at t_{500J} in 16-bar J-ring test (at 0.7 s)**
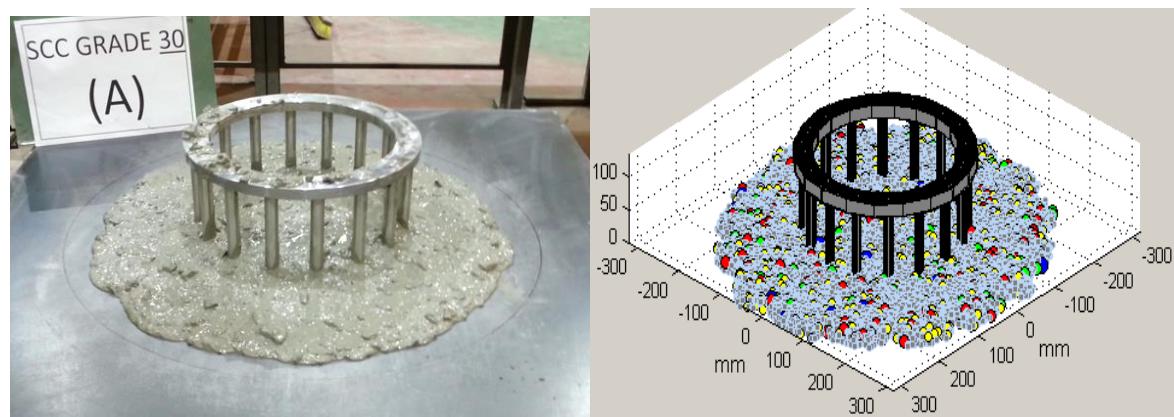
Figure G.3: Flow pattern of SCC Mix30 after it has stopped in 16-bar J-ring test (at 9.0 s)

235
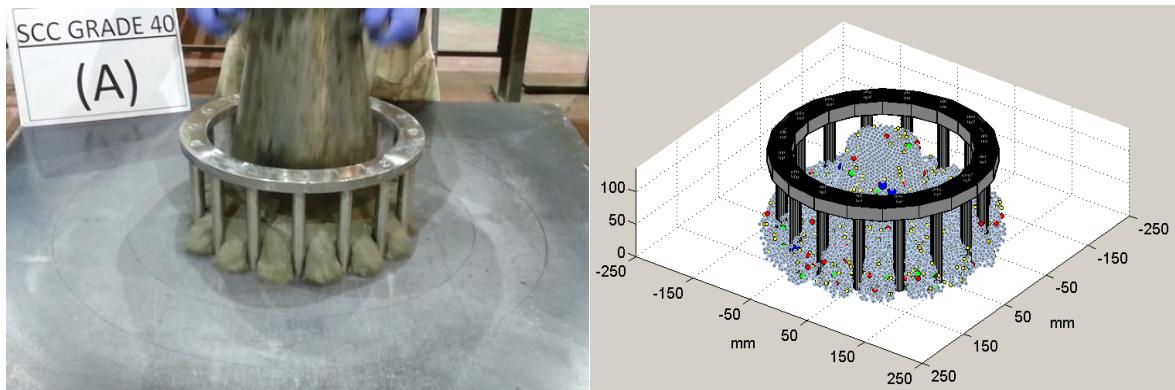
Figure G.4: Flow pattern of SCC Mix40 just after passing through the gaps in 16-bar J-ring test (at 0.3 s)
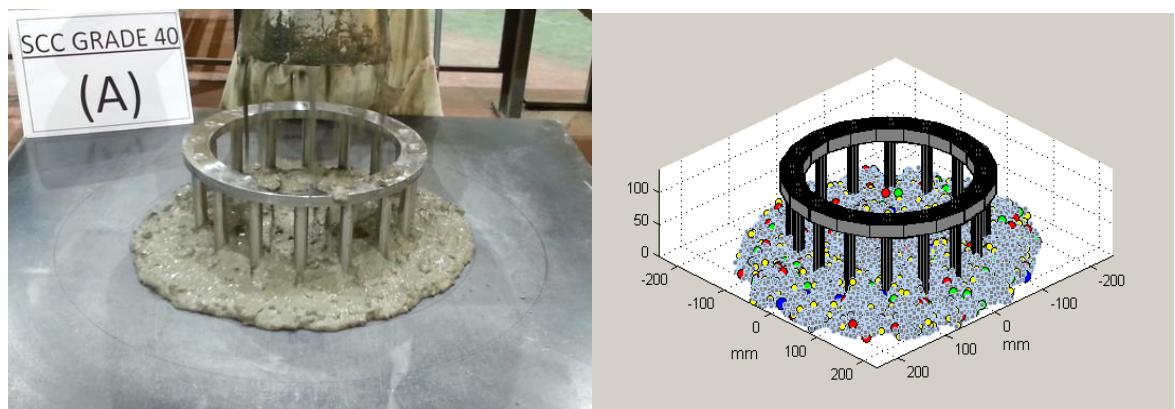
Figure G.5: Flow pattern of SCC Mix40 at t_{500J} in 16-bar J-ring test (at 0.8 s)
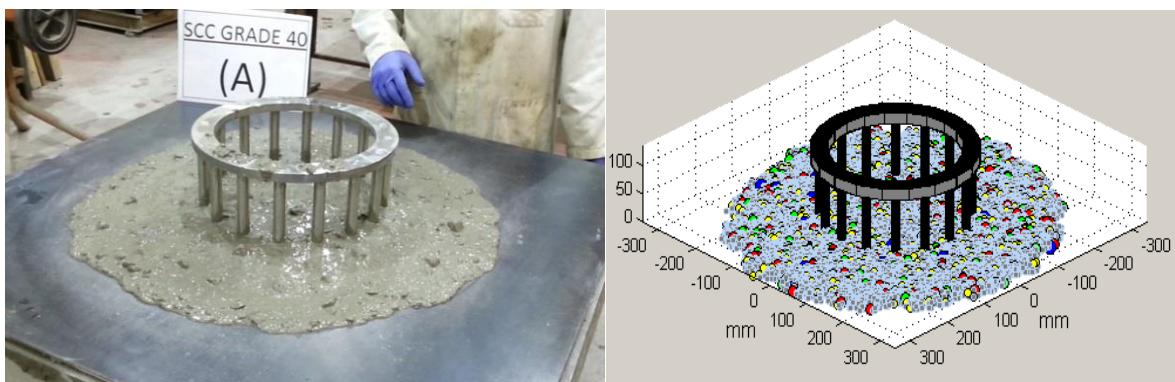
Figure G.6: Flow pattern of SCC Mix40 after it has stopped in 16-bar J-ring test (at 12.0 s)

236
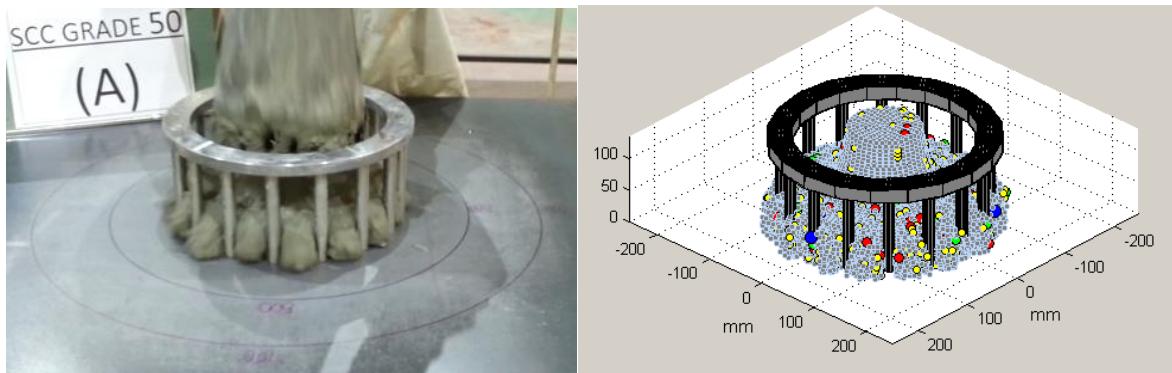
Figure G.7: Flow pattern of SCC Mix50 just after passing through the gaps in 16-bar J-ring test (at 0.4 s)
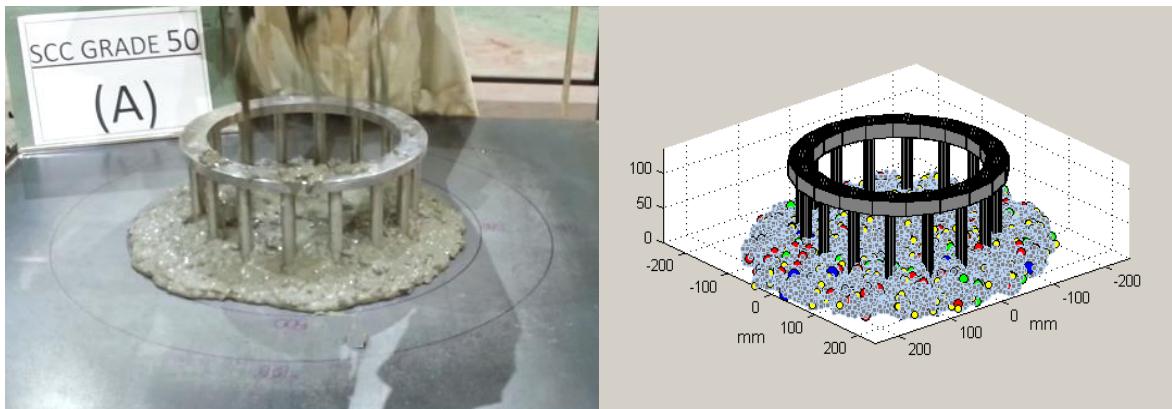
Figure G.8: Flow pattern of SCC Mix50 at t_{500J} in 16-bar J-ring test (at 1.4 s)
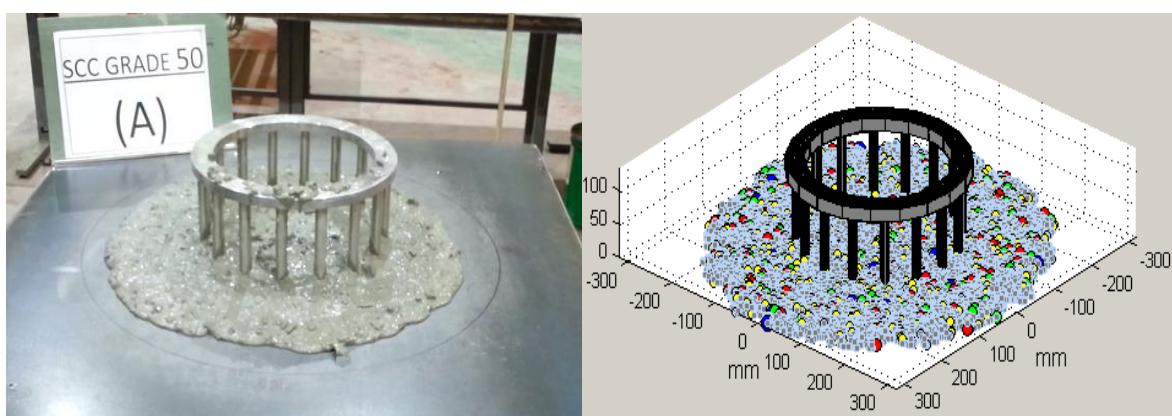
Figure G.9: Flow pattern of SCC Mix50 after it has stopped in 16-bar J-ring test (at 10.0 s)
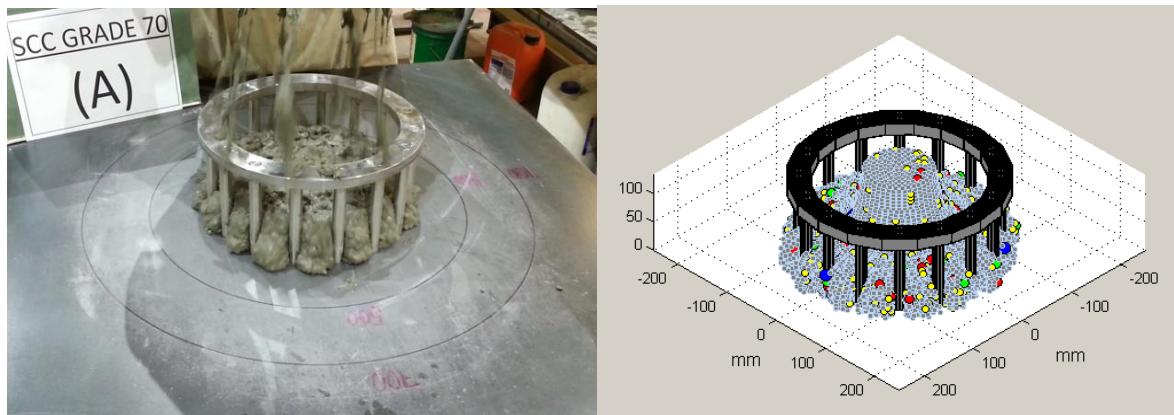
**Figure G.10: Flow pattern of SCC Mix70 just after passing through the gaps in 16-bar J-ring test (at 0.6 s)**
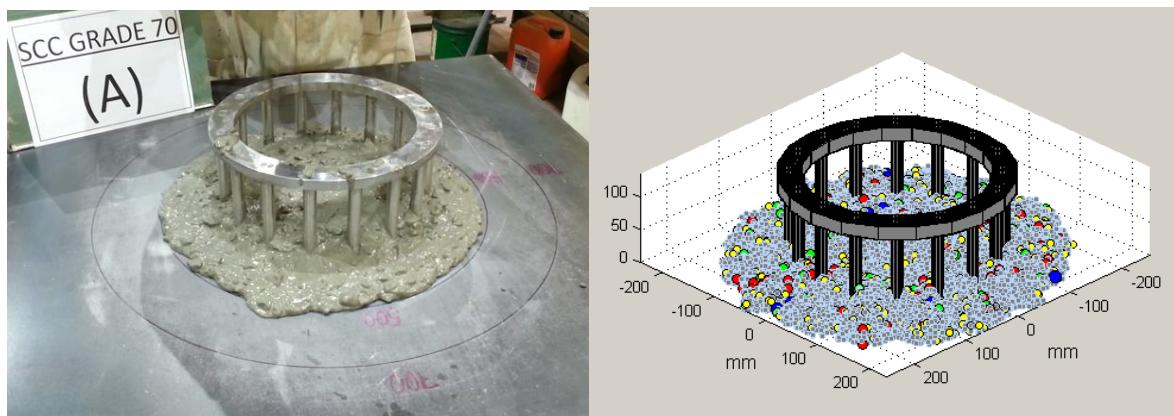
Figure G.11: Flow pattern of SCC Mix70 at t_{500J} in 16-bar J-ring test (at 2.0 s)
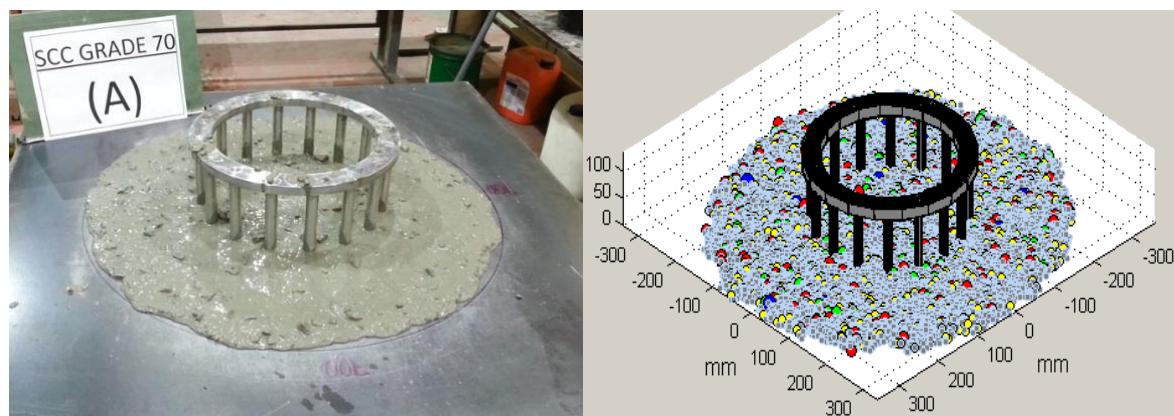
**Figure G.12: Flow pattern of SCC Mix70 after it has stopped in 16-bar J-ring test (at 15.0 s)**
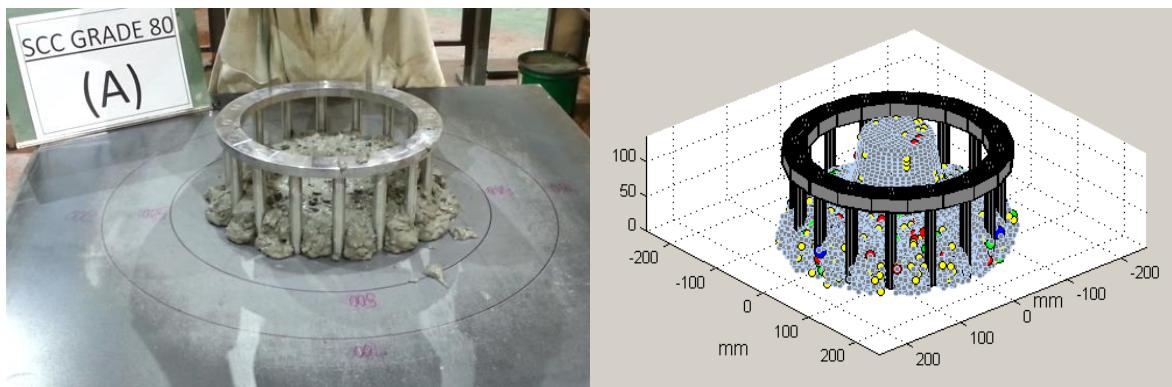
**Figure G.13: Flow pattern of SCC Mix80 just after passing through the gaps in 16-bar J-ring test (at 0.8 s)**
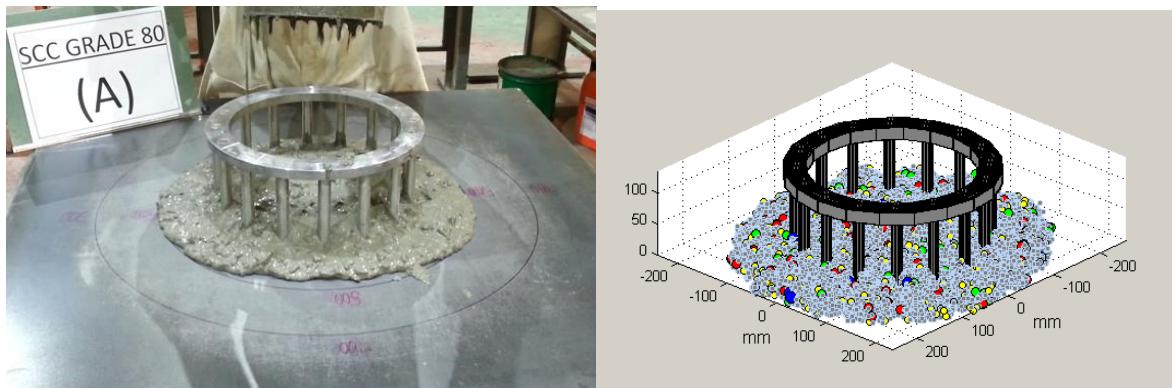
Figure G.14: Flow pattern of SCC Mix80 at t_{500J} in 16-bar J-ring test (at 2.8 s)
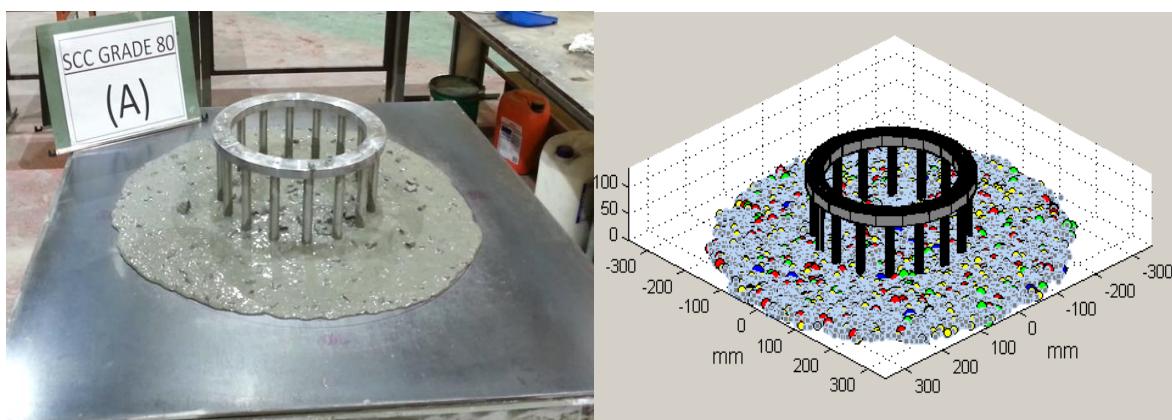
Figure G.15: Flow pattern of SCC Mix80 after it has stopped in 16-bar J-ring test (at 16.0 s)

Table G.1: Simulation and experimental results for SCC mixes of 10 bars J-ring

Mix Designation	Plastic viscosity, Pa s	Yield stress, Pa	t_{500J}, s		Spread diameter, mm	
			experimental	simulated	experimental	simulated
30A	4.63	175	0.6	0.6	665	655
40A	6.84	175	0.7	0.7	710	690
50A	7.84	180	1.4	1.4	660	660
60A	8.18	175	1.5	1.4	640	645
70A	9.32	180	1.8	1.7	700	700
80A	10.47	190	2.4	2.3	705	710
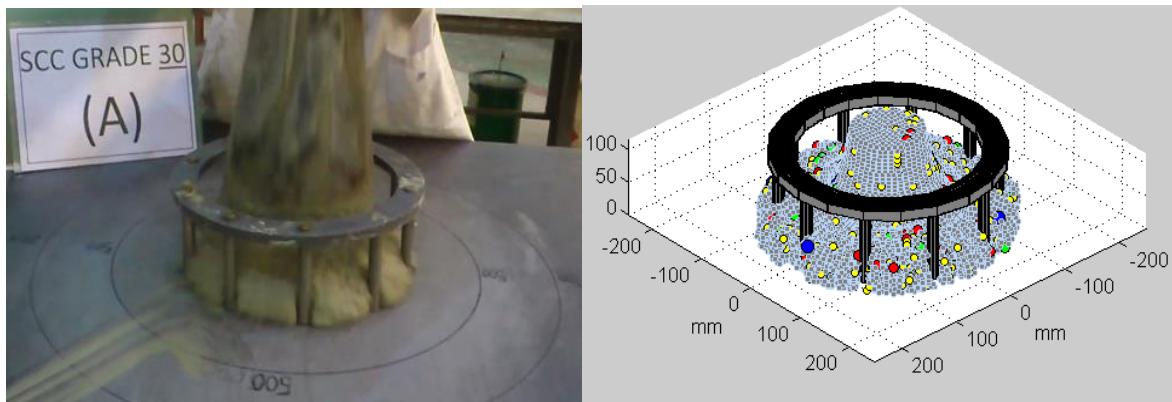
Figure G.16: Flow pattern of SCC Mix30 just after passing through the gaps in 10-bar J-ring test (at 0.2 s)
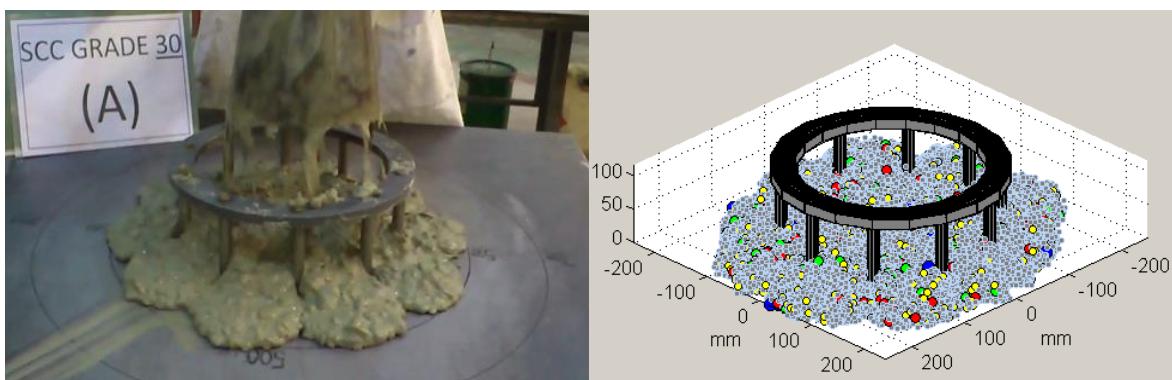
**Figure G.17: Flow pattern of SCC Mix30 at t_{500J} in 10-bar J-ring test (at 0.6 s)**
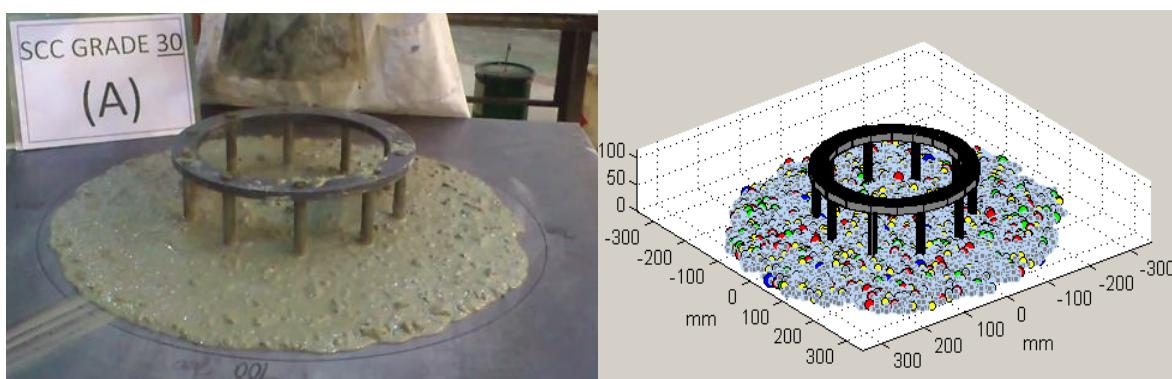
Figure G.18: Flow pattern of SCC Mix30 after it has stopped in 10-bar J-ring test (at 10.0 s)
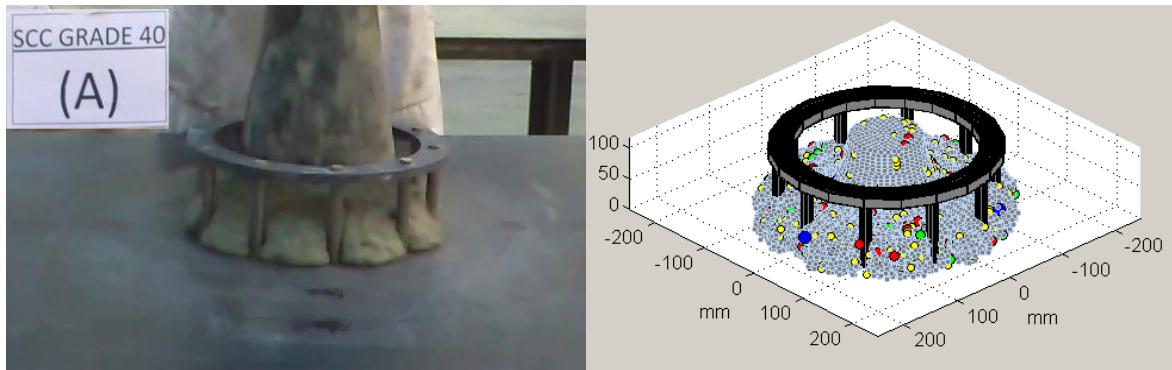
Figure G.19: Flow pattern of SCC Mix40 just after passing through the gaps in 10-bar J-ring test (at 0.3 s)
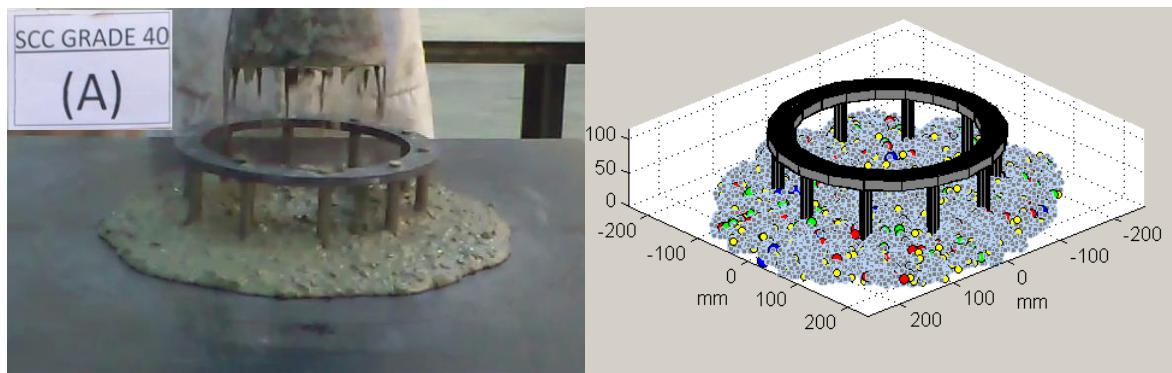

**Figure G.20: Flow pattern of SCC Mix40 at t$_{500J}$ in 10-bar J-ring test (at 0.7 s)**
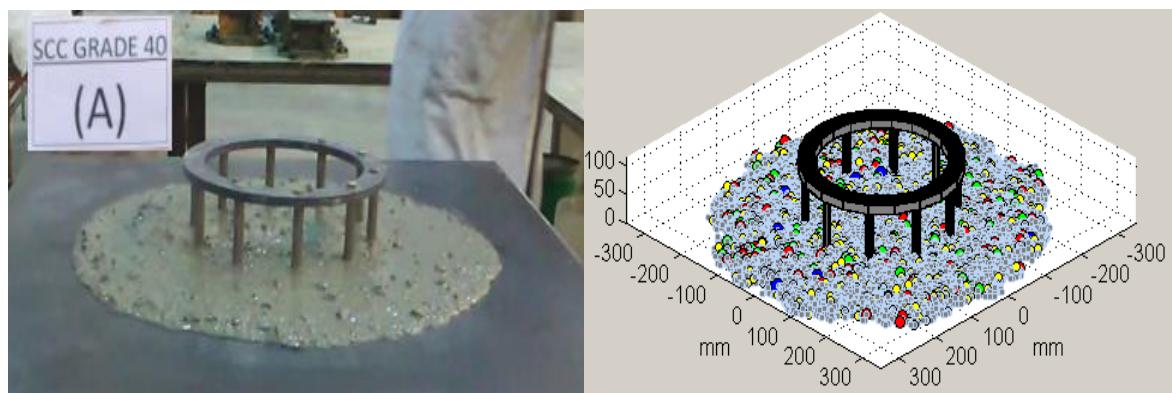
Figure G.21: Flow pattern of SCC Mix40 after it has stopped in 10-bar J-ring test (at 12.0 s)
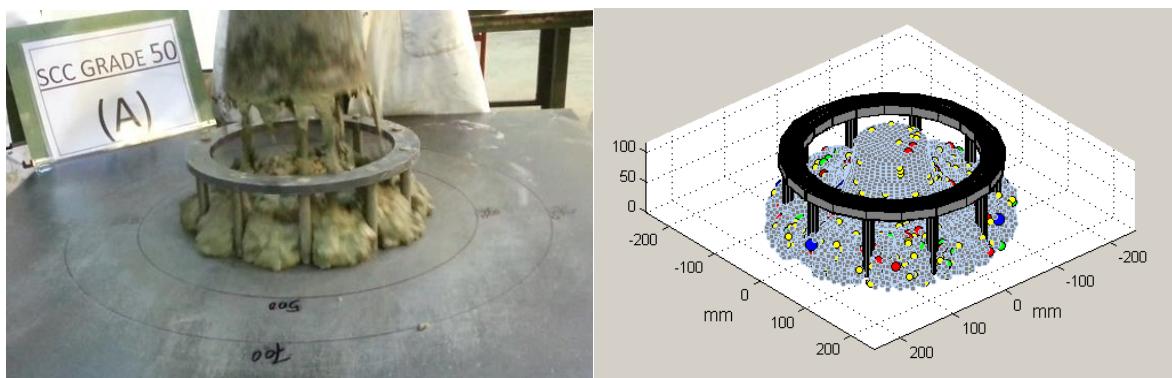
Figure G.22: Flow pattern of SCC Mix50 just after passing through the gaps in 10-bar J-ring test (at 0.4 s)
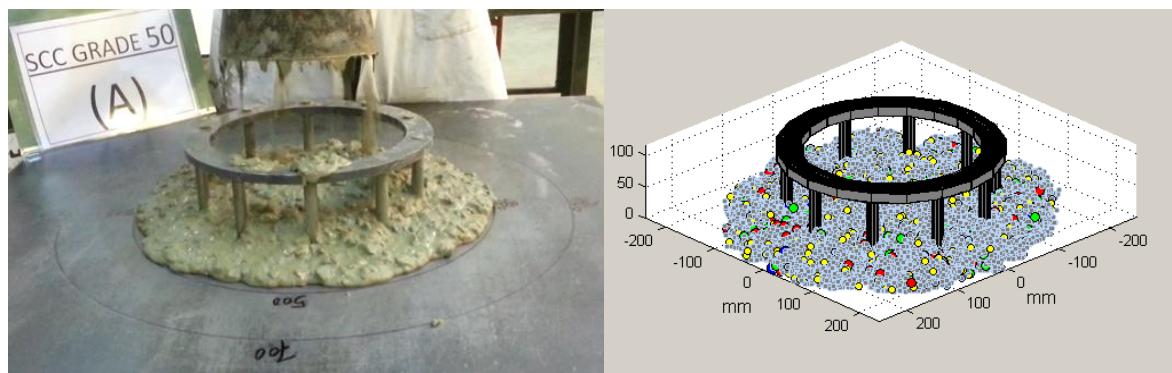
Figure G.23: Flow pattern of SCC Mix50 at t_{500J} in 10-bar J-ring test (at 1.4 s)
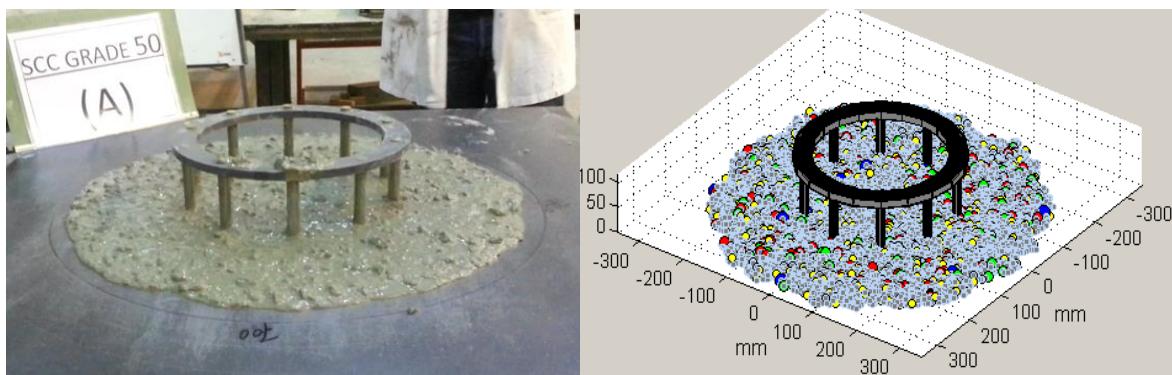
Figure G.24: Flow pattern of SCC Mix50 after it has stopped in 10-bar J-ring test (at 11.0 s)
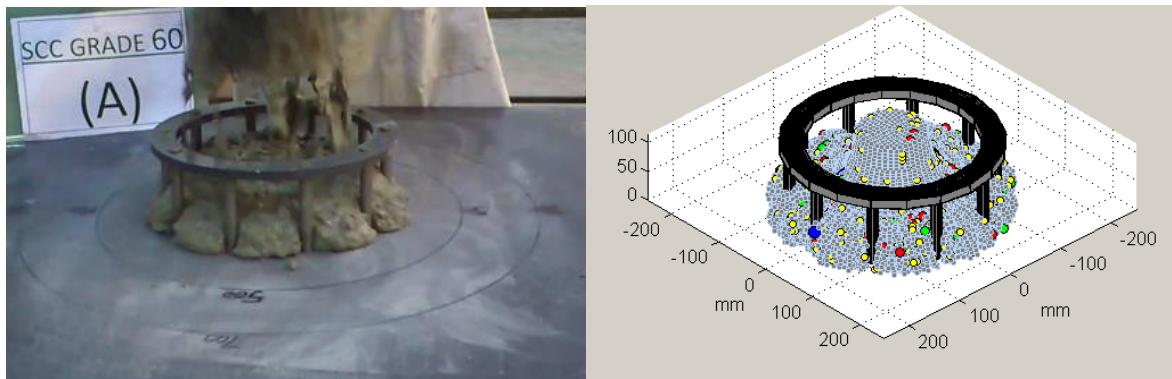
Figure G.25: Flow pattern of SCC Mix60 just after passing through the gaps in 10-bar J-ring test (at 0.4 s)
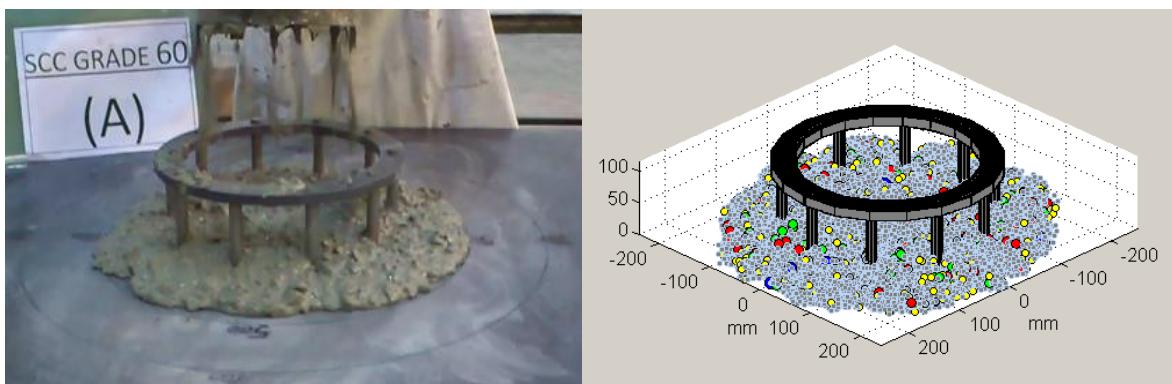
Figure G.26: Flow pattern of SCC Mix60 at t_{500J} in 10-bar J-ring test (at 1.5 s)
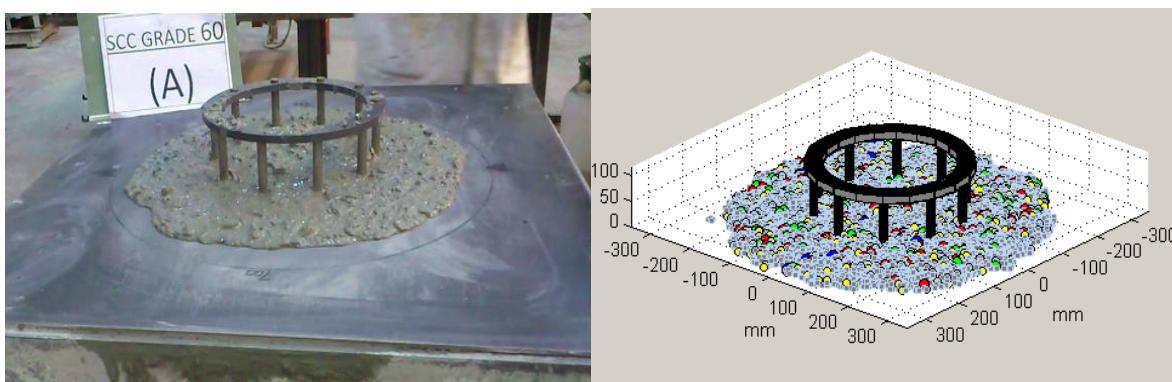
Figure G.27: Flow pattern of SCC Mix60 after it has stopped in 10-bar J-ring test (at 11.0 s)
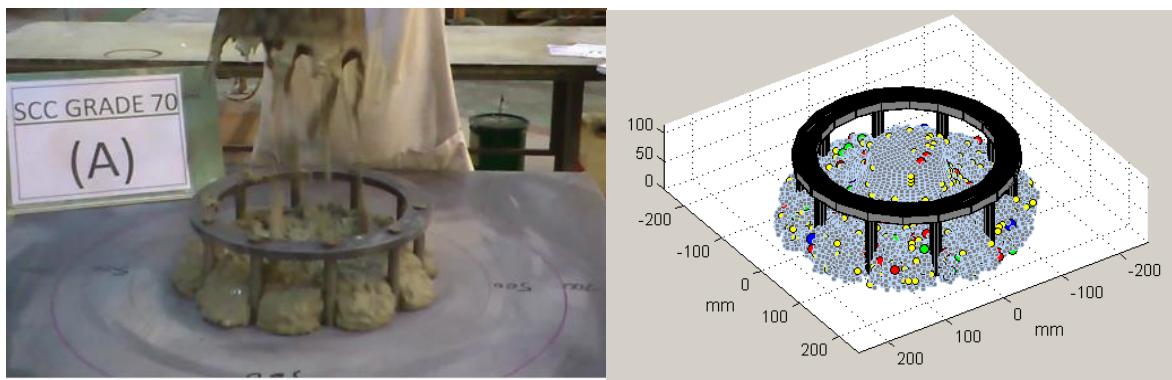
Figure G.28: Flow pattern of SCC Mix70 just after passing through the gaps in 10-bar J-ring test (at 0.6 s)
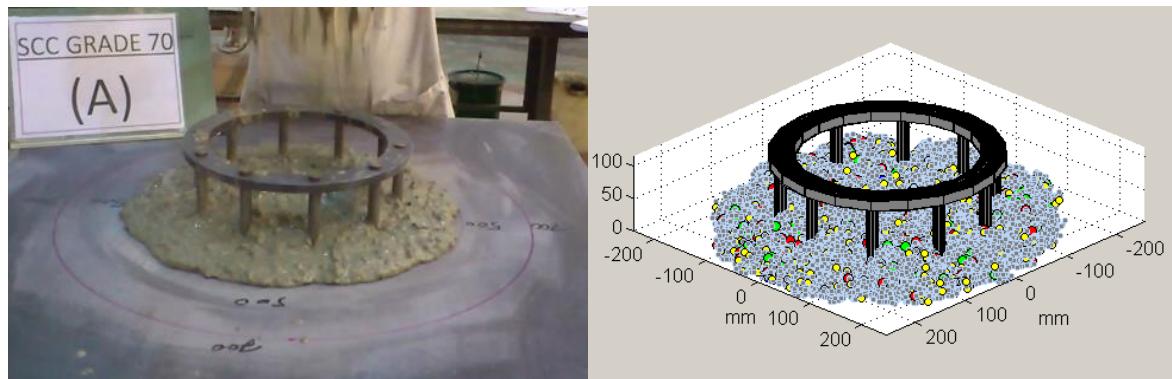
Figure G.29: Flow pattern of SCC Mix70 at t_{500J} in 10-bar J-ring test (at 1.8 s)
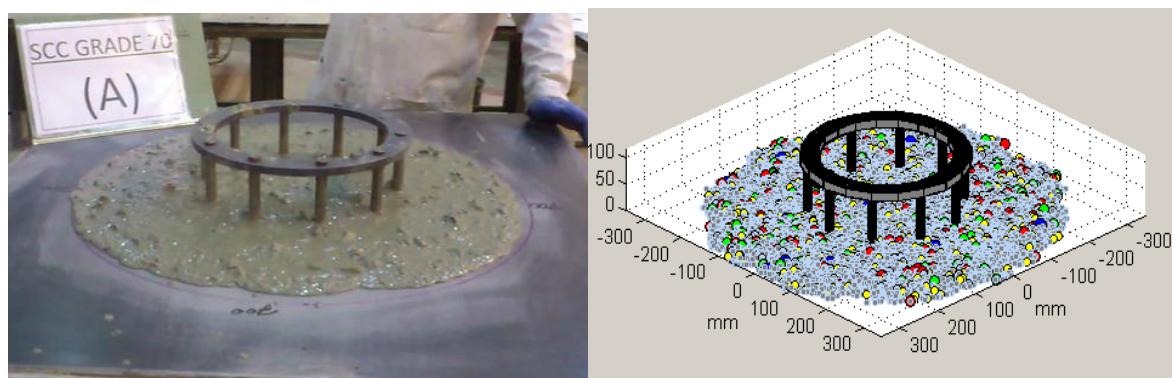
Figure G.30: Flow pattern of SCC Mix70 after it has stopped in 10-bar J-ring test (at 16.0 s)
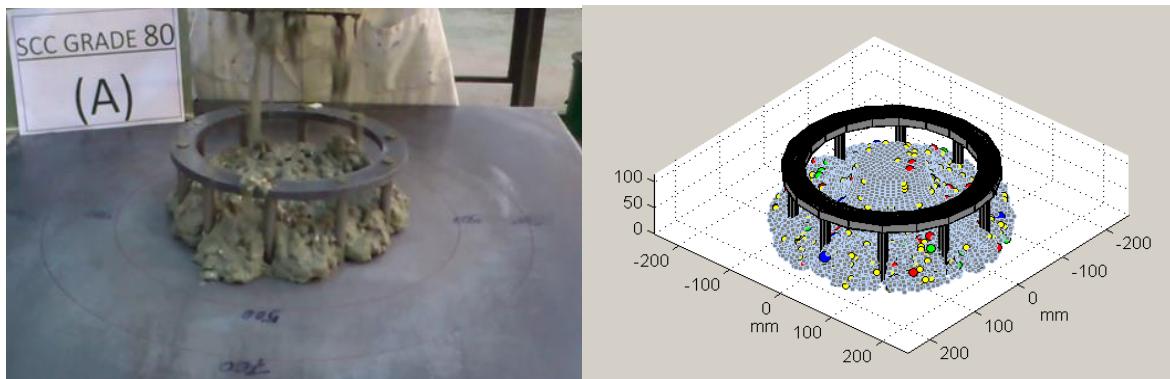
Figure G.31: Flow pattern of SCC Mix80 just after passing through the gaps in 10-bar J-ring test (at 0.7 s)
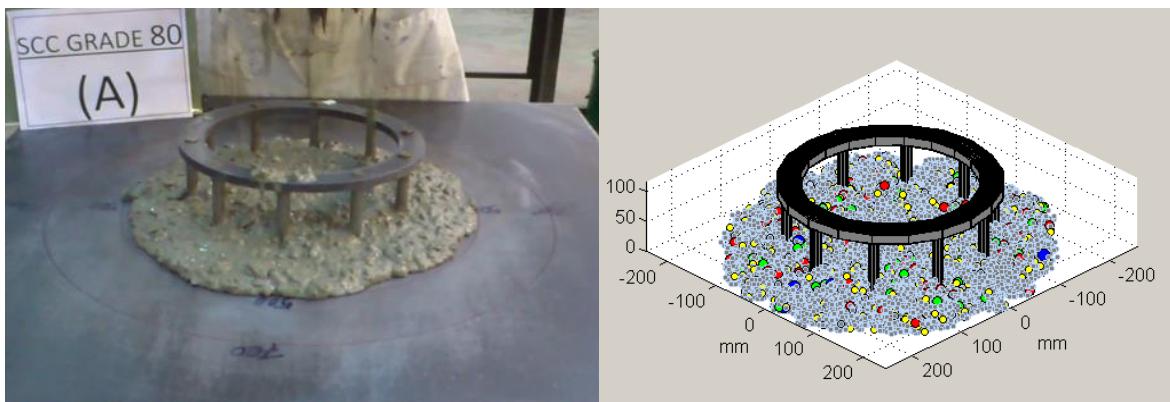
Figure G.32: Flow pattern of SCC Mix80 at t$_{500J}$ in 10-bar J-ring test (at 2.4 s)
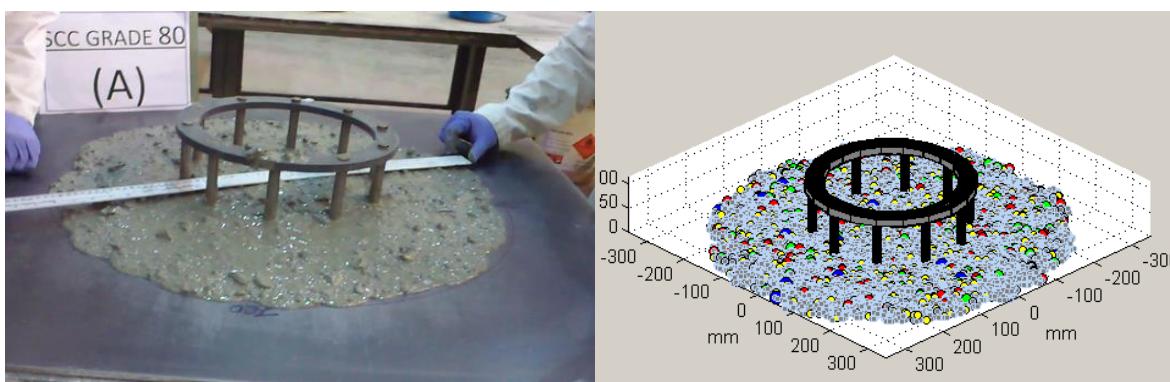
Figure G.33: Flow pattern of SCC Mix80 after it has stopped in 10-bar J-ring test (at 17.0 s)
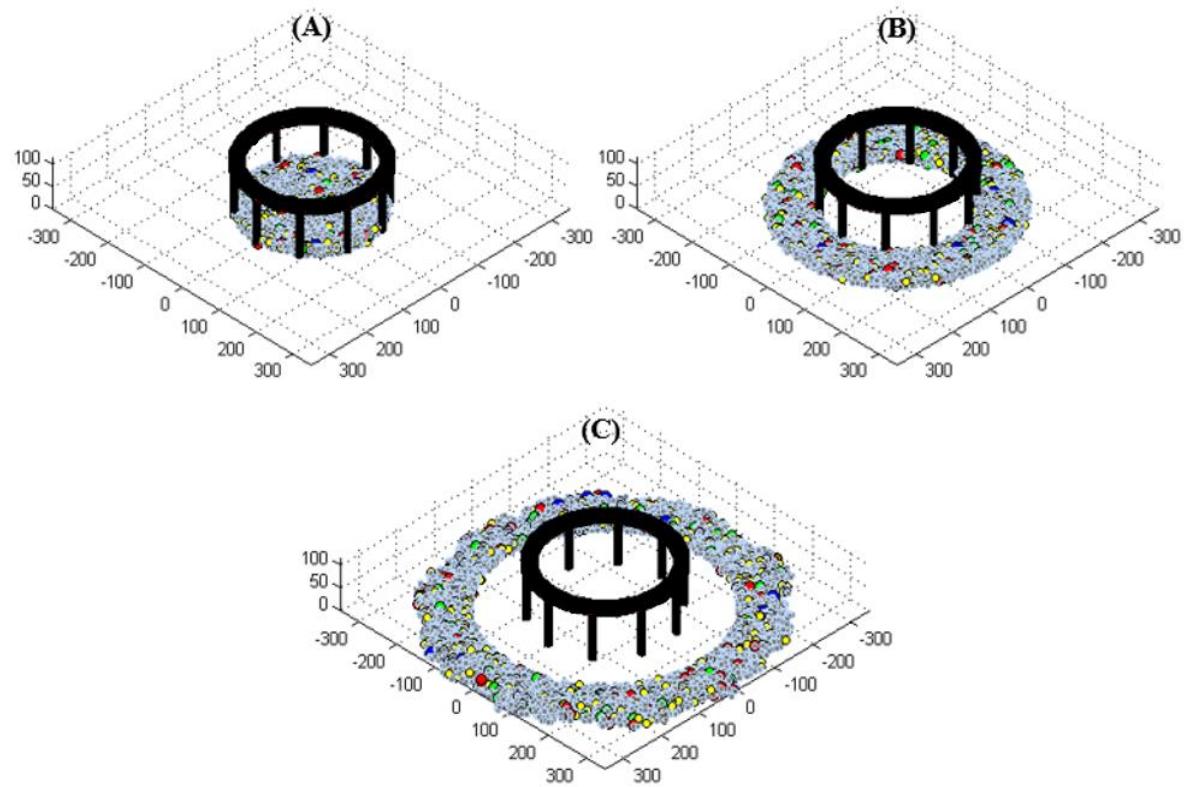
Figure G.34: The three concentric circular regions to evaluate the distribution of coarse aggregates in the J-ring "pancake" of Mix70 in 10-bar J-ring test
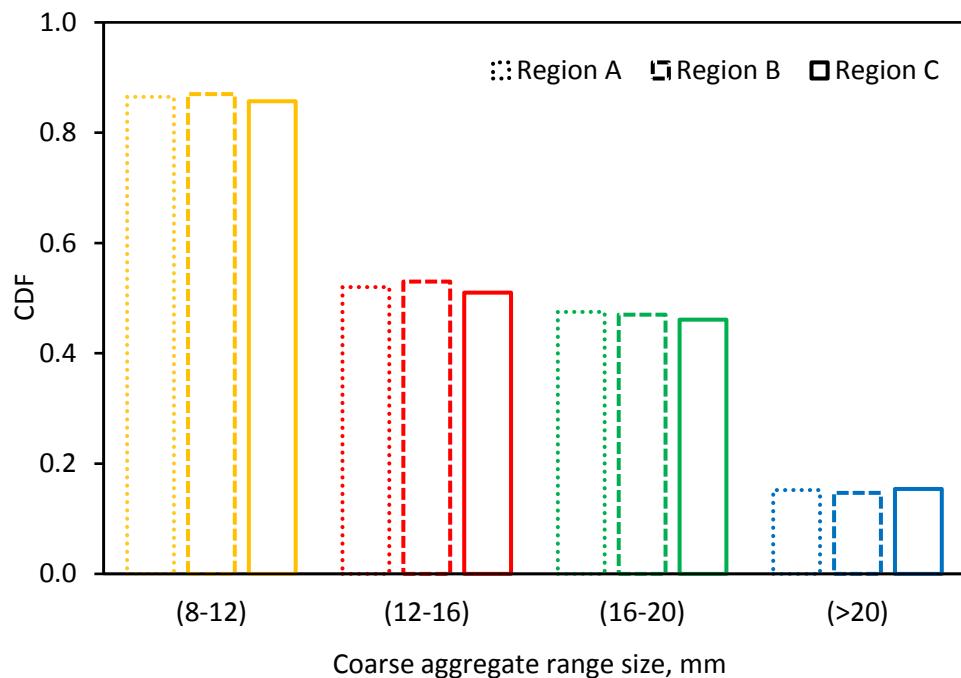
Figure G.35: Coarse aggregate distributions in the three concentric circular regions in 10-bar J-ring test
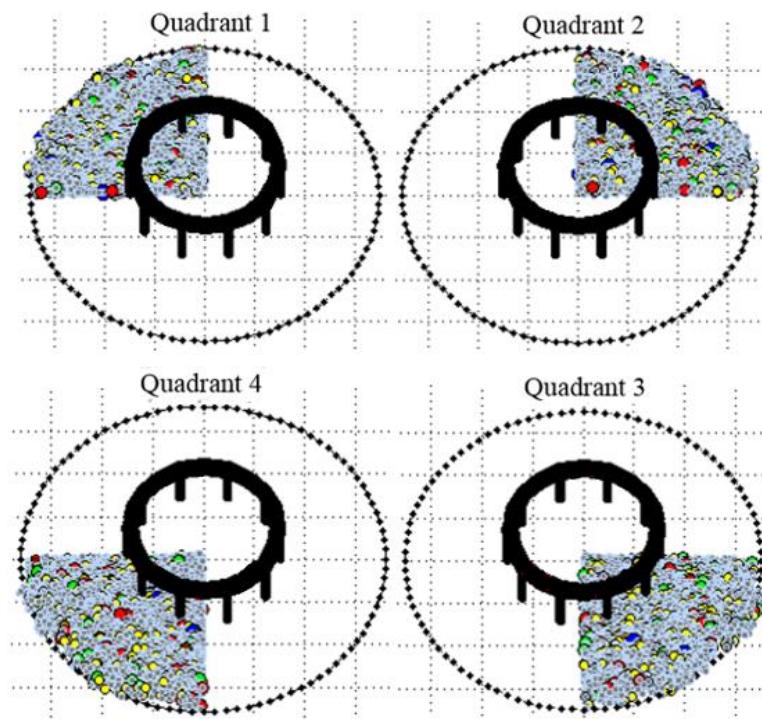
Figure G.36: Four quadrants of Mix60 "pancake" to determine the aggregate distribution (10-bar J-ring test)
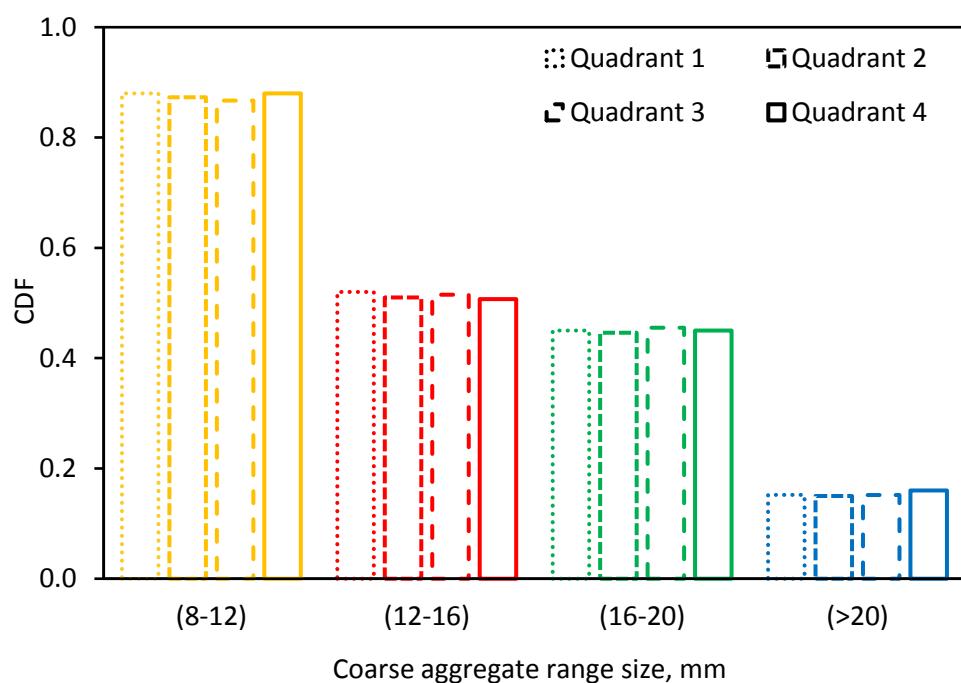

**Figure G.37: Coarse aggregate distributions in the four quadrants (10-bar J-ring test)**
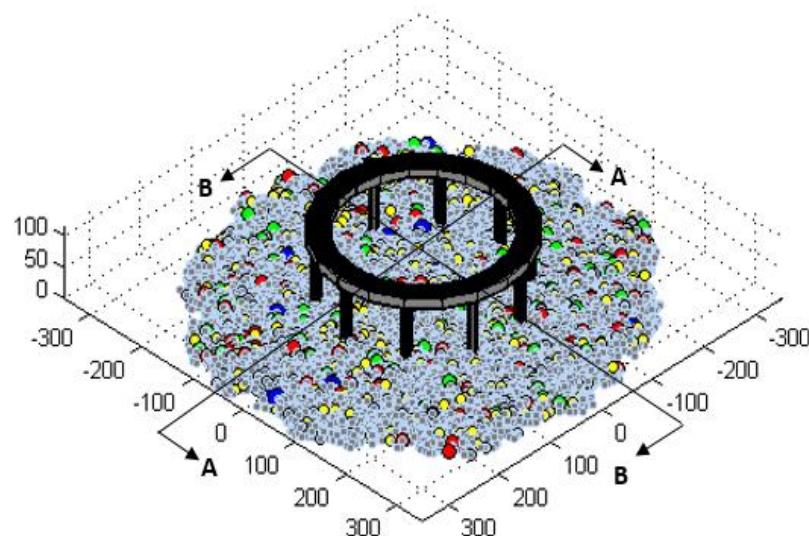
Figure G.38: Flow pattern of SCC (Mix40) showing the large aggregates in 10-bar J-ring test

AA

BB
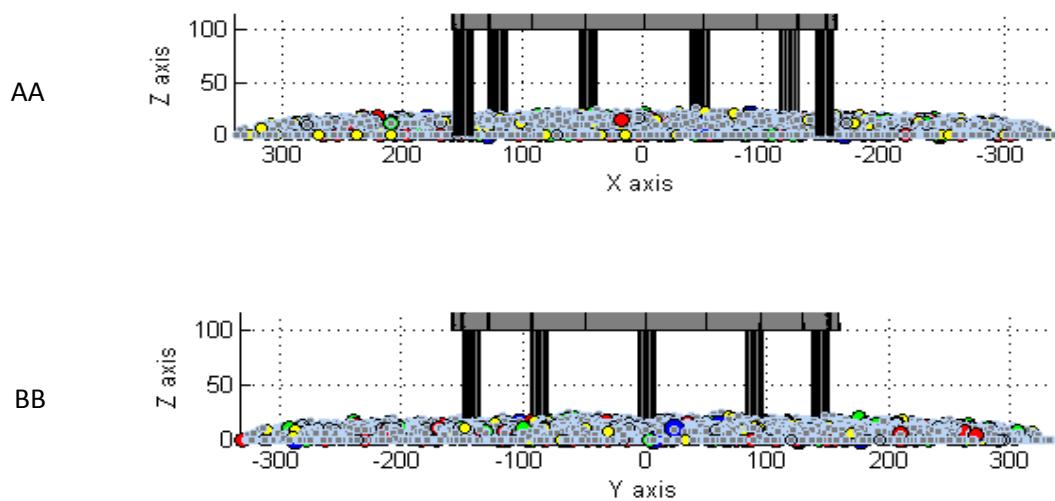
Figure G.39: Coarse aggregate distributions along diametrical cross-sections (AA and BB) of Mix40 "pancake" in 10-bar J-ring test
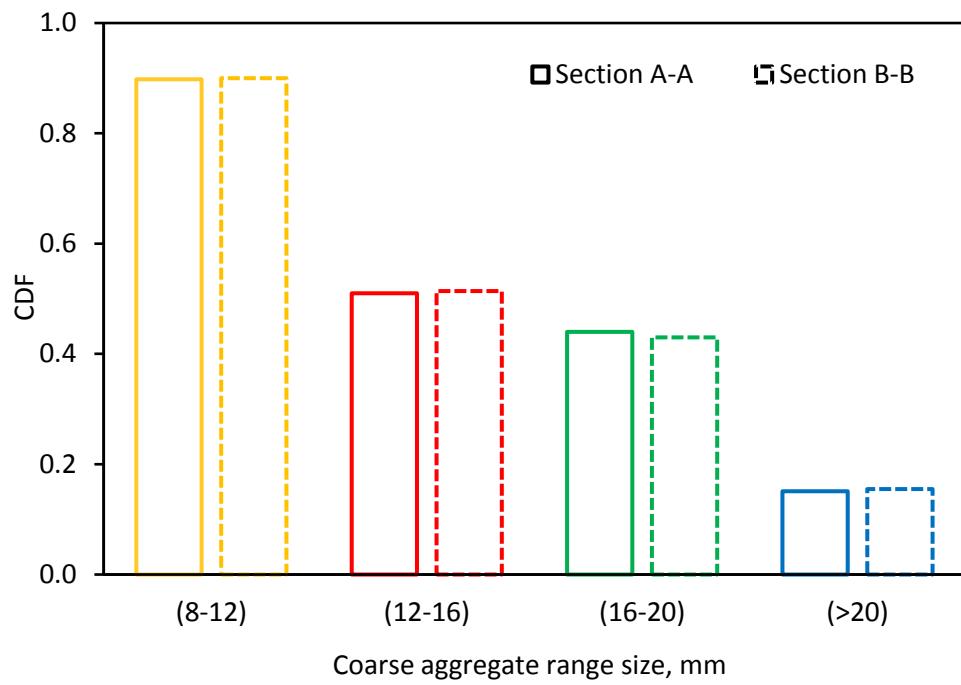
Figure G.40: Coarse aggregate distributions along the diametrical cross-sections (10-bar J-ring test)